Subgrid-scale Modeling of Tsunami and Storm Surge Inundation in Coastal Urban Area

Nobuki Fukui

沿岸市街地を対象としたサブグリッドスケール津波・高潮浸水モデルの開発

論文要旨

日本で危惧されている沿岸災害ハザードとして，津波，高潮，高波があり，特に東京湾，大阪湾，伊勢湾の 3 大湾に隣接する 3 大都市圏において大規模な津波や高潮・高波による浸水災害が想定されている．今後被害が予測される地域に対して長期的な沿岸災害リスク低減に資する防災対策が必要である．

津波と高潮の発生要因はそれぞれ地震，台風であるが，浸水シミュレーションには同一の支配方程式が用いられている．津波や高潮の浸水想定において，一般に浸水計算の中では，市街地における建物や人工構造物を土地利用に応じた Manning の粗度係数のようなグリッド平均値として取り扱われる．しかしながら、市街地に多く存在する建物や橋などの人工構造物により，浸水過程における水位や流速は時々刻々複雑に変化し，これを建物の形状を考慮しない数値モデルで表現するのは難しい．現在では詳細な建物形状データが入手可能になり，解像度 5m 以下の建物形状を高解像度地形として直接計算に反映させた計算が行われ始めているが，大都市などの広い範囲を対象とする場合に計算負荷の増加を伴う．一方，長期の浸水リスク評価には特定シナリオ（入力断層や気象場）を想定した評価が行われているが，リスク評価には地点ごとのハザード強度の確率情報を要するため，多数のシナリオを考慮した確率評価を行う必要があり，リスク評価への高解像度の浸水計算の適用は難しい．従って，従来の数値計算よりも計算負荷を軽減しつつも詳細な建物情報を浸水計算に反映する数値モデルを構築することが求められている．

加えて，津波や高潮による市街地の大規模氾濫は発生時の被害は大きいものの発生頻度が低いため，構築された数値モデルのベンチマークとなるデータが少ないのが現状である．ベンチマークの例として，発生した災害における痕跡調査によって得られる浸水域，遡上高や浸水深が挙げられるが，避難上重要な時々刻々の浸水域の変化や津波の流体力学的特性を把握するために重要な流速を得ることは極めて難しい．

上記背景を踏まえ，長期的な津波や高潮浸水評価の発展に向けて，沿岸市街地の浸水シミュレーションのベンチマークとなるデータの構築と高解像度地形モデルよりも解像度を抑えつつも，計算精度を担保するような市街地の取り扱いの提案を目的とし，以下の 5 項目について検討した．

第一に，市街地を対象とした津波や高潮浸水におけるベンチマークデータの構築として，大型津波再現水槽と和歌山県海南市の沿岸市街地を縮小した模型を用いて，津波・高潮浸水実験を行った．実験では，赤色塗料で染めた水と黄色蛍光塗料で染めたトレーサ粒子により陸上の浸水波の伝播を可視化し，ビデオ画像解析により浸水範囲と流速の平面時系列を推定することに成功した．

第二に，実験によって得られた浸水範囲と流速等を真値として，4 つの異なる 2 次元非線

形長波理論モデルをもとに建物を高解像度地形として入力した浸水計算（建物解像モデル）の精度検証を行った．その結果，いずれの 2 次元非線形長波理論モデルは広域的な浸水過程（浸水深や流速，最大浸水範囲など）は再現可能であるものの，建物の周りの流速や交差点での流れの合流による水位上昇のような局所的な浸水過程はモデル間によってばらつきが現れることがわかった．

第三に，建物を地形として直接解像する高負荷な計算に代わって，粗い計算格子の中で複数建物群に加わる抗力の総和として表現するサブグリッドスケールモデルである平均化個別建物抗力モデル (iDFM: individual Drag Force Model) を開発し，簡易地形を用いた理想化数値実験や実際の津波浸水イベントである東北地震津波の再現計算を宮城県女川町を対象に行い，前述の建物解像モデルを真値とした精度検証を行った．結果として，遡上先端や最大水位，最大流速の解像度依存性を既存の粗度モデルや抗力モデルよりも減少させることに成功した．一方で，建物解像モデルでは建物が水深として入力されるため，建物が流体場に与える影響が質量保存則と運動量保存則ともに考慮できるものの，iDFM では建物が運動量保存則内で流速低減効果として反映されるため，建物による局所的な水位上昇や建物間で発生する縮流の再現などの課題が明らかになった．

第四に，前述の iDFM を高潮モデル SuWAT に適用し，実イベント検証として，2013 年台風 Haiyan によるレイテ島都市域の再現計算を行った．この際，高潮の生起要因の一つである風応力項に着目し，建物情報による風応力項へのフィードバックの有無が氾濫域や浸水深，流速にもたらす差異を検討した．建物情報を有する部分で風応力項を 0 にすることによって遡上先端が汀線側に後退し，流速や浸水深も減少した．結果として，痕跡調査結果との浸水深や浸水範囲の再現性も既存の粗度モデルと比べて向上し，iDFM の高潮浸水計算への適用可能性が示された．

第五に，前述の高潮モデル SuWAT と iDFM に解適合格子法を用いた高潮モデル GeoClaw を結合することにより，日本広域での高潮の発生から市街地の浸水まで効率的に計算する手法を確立した．この手法に基づき，東京の沿岸部である墨田区や江東区を対象に温暖化を想定した台風を用いて高潮浸水計算を行い，iDFM を大都市に適用することで現れる浸水深や流速等の浸水特性を明らかにした．さらに，本研究で行った東北地震津波の再現計算，台風 Haiyan による高潮の再現計算，墨田区や江東区を対象とした仮想高潮実験について，移流項に対する抗力項の寄与率を算定し，移流項に対する抗力項の寄与率は陸域に流入する運動量や質量フラックスの大きさや時間変化によって変化し，津波ではこれらが大きいので寄与率が低くなり，高潮では逆に大きくなることがわかった．また，寄与率はメッシュ内の建物密度によって鋭敏に変化することがわかった．

キーワード

サブグリッドスケール，津波，高潮，浸水，沿岸市街地

福井 信気

Subgrid-scale Modeling of Tsunami and Storm Surge Inundation in Coastal Urban Area

Summary

Coastal disasters are one of the most devastating disasters that occur in Japan, and it is necessary to implement disaster prevention measures that contribute to the long-term reduction of coastal disaster risk in areas where damage is expected in the future. As coastal disasters concerned in Japan, tsunami, storm surge, and extreme waves are exemplified. The wide area inundation in coastal urban area by them are expected in the three major metropolitan areas adjacent to the three major bays of Tokyo Bay, Osaka Bay, and Ise Bay.

The same governing equations are used in numerical models for tsunami and storm surge inundation though the causes of them are different. Currently, detailed building 3D shape dataset is available and numerical simulation using finer grid resolution than 5 m has been conducted by implementing buildings as the high-resolution topography which leads to heavy computational cost. On the other hand, long-term inundation risk assessment is based on specific scenarios. However, since risk assessment requires probabilistic information of hazard intensity for each location, it is necessary to perform probabilistic assessment considering a large number of scenarios, which makes it difficult to apply high-resolution inundation calculations to risk assessment. Therefore, there is a need to construct a numerical model that reflects detailed building information in inundation calculations while reducing the computational load compared to conventional numerical calculations. In addition, there is a lack of benchmark data for numerical models of tsunami and storm surge inundation in urban areas because the frequency of their occurrence is low, although the damage is high. For example, inundation areas, run-up heights and inundation depths obtained by trace surveys can be used as benchmarks, but changes in inundation areas from time to time, which are important for evacuation, and flow velocities, which are important for understanding the hydrodynamic characteristics of tsunamis, are rarely available.

Based on the above background, the author aims to construct benchmark data for coastal urban area inundation simulations and propose a treatment of urban areas that ensures computational accuracy while reducing the resolution compared to high-resolution terrain models, for the development of long-term inundation risk assessment by tsunami and storm surge.

Firstly, a physical modeling of tsunami and storm surge inundation in a coastal city was conducted and the propagation of inundating waves on land was visualized by flowing water dyed with red paint and tracer particles dyed with yellow fluorescent paint, and

the time series of leading edges of inundation and spatial distribution of velocity were successfully estimated by 4K video image analysis.

Secondly, numerical modeling of tsunami inundation in a 3D complex coastal city model including ports and buildings using building-resolving topography in high-resolution grid has been conducted and validated using the dataset of leading edges and limit of inundation, flow velocity and inundation depth obtained from the physical inundation experiment. It was found that the wide area inundation process (inundation depth, flow velocity, limit of inundation, etc.) could be reproduced using any of the models, but the flow velocity around buildings and the water level rise due to the confluence of flows at intersections varied among the models.

Thirdly, as an alternative approach to the building-resolving simulation with heavy computational cost, an subgrid-scale model iDFM focusing on the drag force on buildings to reduce the computational load while ensuring accuracy was developed. As a result, the grid cell size dependency of the limit of inundation, maximum water level, and maximum flow velocity was successfully reduced compared to the existing roughness and drag force models. On the other hand, the accuracy of local phenomena driven by buildings such as surface rising due to blocking and contracting current between structures by the iDFM is clarified as the further challenge.

Fourthly, the iDFM was applied to the historical storm surge inundation targeting coastal urban area. The implementation of the wind drag coefficient in the land side based on the SGS parameters was also proposed and validated using available survey data. As a result, the reproducibility of the inundation depth and the inundation area with the survey results is improved compared with the existing roughness model, and the applicability of iDFM to the storm surge inundation calculation was shown.

Fifthly, an efficient method for calculating storm surge occurrence and urban inundation over a wide area of Japan was developed by combining the storm surge models SuWAT and iDFM with storm surge model GeoClaw based on the adaptive mesh refinement which changes the computational grid cell size spatio-temporally. Using the developed method, storm surge inundation simulations using the iDFM are conducted for large cities and the inundation characteristics by the iDFM was clarified. In addition, the difference of contribution of the drag force term to the advection, which causes the different inundation characteristics in other target areas, was discussed in terms of the land-sea boundary condition and input building information. The contribution of the drag force term to the advection term relatively small when the magnitude and time variation of the momentum and mass fluxes into the land is large. And it was also found that the contribution ratio increased when the density of buildings in the mesh is high.

Keywords

subgrid-scale, tsunami, storm surge, inundation, coastal urban area

Nobuki Fukui

Contents

List of Figures

List of Tables

Chapter 1

Introduction

1.1 Research background and objective

Coastal disasters are one of the most devastating disasters that occur in Japan, and it is necessary to implement disaster prevention measures that contribute to the long-term reduction of coastal disaster risk in areas where damage is expected in the future. As coastal disasters concerned in Japan, tsunami, storm surge, and extreme waves are exemplified. The wide area in coastal urban area are expected to be inundated by them in the three major metropolitan areas adjacent to the three major bays of Tokyo Bay, Osaka Bay, and Ise Bay.

The mega tsunami generated by the 2011 Tohoku Earthquake caused more enormous damage to human lives, coastal structures, and houses than previous expectation. One of the damage characteristics is the large-scale inundation in coastal urban area which had not been observed in historical mega earthquake tsunami (Mori et al., 2013) and it has become necessary to discuss coastal disaster prevention targeting urban area. Therefore, the Central Disaster Prevention Council of the Cabinet Office (2011) has defined two types of tsunamis: L1 tsunamis, which occur about once in a hundred or so years, and L2 tsunamis, which are the largest class of tsunamis that occur about once in a thousand years and cause extensive damage. In the case of the L1 tsunami, coastal structures are designed to protect human lives, residents' property, and governmental facilities and so on, while the disaster reduction countermeasure such as making evacuation plan and city planning is assumed in the case of L2 tsunami. On the other hand, the cause of the storm surge is tropical cyclones and it is assumed that the number of typhoons in the Northwest Pacific decreases but their intensity increases by climate change in high reliability (Knutson et al., 2020). In addition, Special Report on the Ocean and Cryosphere in a Changing Climate by Intergovernmental Panel on Climate Change 2019 (IPCC SROCC) revised the sea level rise projection due to global warming upward and it is expected that extreme sea level rise near shoreline will be more frequent. Hence, it is important that long-term risk assessment and reduction by these two coastal disaster, tsunami and storm surge are quite important to consider the coastal disaster prevention in Japan. It is needed that the modeling of the tsunami inundation process in coastal urban area such as inundation depth, arrival time and so on is important to take countermeasure activities.

The same governing equations are used in numerical models for tsunami and storm surge inundation though the causes of them are different. In Guide to Determining the Potential Tsunami Inundation (MLIT, 2019) and Guide to Creating Storm Surge Inundation Area Maps (MLIT, 2021), the buildings are mainly implemented as grid-averaged value such as roughness coefficient corresponding to land usage in the numerical modeling. However, the water surface elevation and fluid velocity complexly change in spatio-temporal scale during inundation process because of the buildings or other artificial structures. Therefore, it is difficult to express such inundation process using roughness coefficient without considering shapes and spatial layouts of buildings. Currently, detailed building 3D shape dataset such as Plateau (MLIT, 2021) is available and numerical simulation using finer grid resolution than 5 m has been conducted by implementing buildings as the high-resolution topography (Park et al., 2013; Oishi et al., 2016; Yasuda et al., 2021), which leads to heavy computational cost. On the other hand, long-term inundation risk assessment is based on specific scenarios (input faults and meteorological fields). However, since risk assessment requires probabilistic information of hazard intensity for each location, it is necessary to perform probabilistic assessment considering a large number of scenarios, which makes it difficult to apply high-resolution inundation calculations to risk assessment. Therefore, there is a need to construct a numerical model that reflects detailed building information in inundation calculations while reducing the computational load compared to conventional numerical calculations.

In addition, there is a lack of benchmark data for numerical models of tsunami and storm surge inundation in urban areas because the frequency of their occurrence is low, although the damage is high. For example, inundation areas, run-up heights and inundation depths obtained by trace surveys can be used as benchmarks, but changes in inundation areas from time to time, which are important for evacuation, and flow velocities, which are important for understanding the hydrodynamic characteristics of tsunamis, are rarely available. As one of the few examples, Hayashi et al. (2012) succeeded in obtaining the inundation area, wave front velocity, and flow velocity by analyzing the aerial images of the tsunami during the Tohoku Earthquake Tsunami. However, the target area is not the urban area where many buildings are located, but the farmland, and the planar distribution of inundation area and flow velocity in the urban area has not been obtained.

Based on the above background, the author aims to construct benchmark data for coastal urban area inundation simulations and propose a treatment of urban areas that ensures computational accuracy while reducing the resolution compared to high-resolution terrain models, for the development of long-term hazard assessment of tsunami and storm surge.

1.2 Outline of the study

The outline of this thesis is as follows. In Chapter 2, the tsunami inundation experiments are conducted using a large tsunami flume and a physical model of a coastal city in order to visualize the flow of a tsunami during its run-up to the land area and to measure the inundation area and the flat distribution of flow velocity. In Chapter 3, a high-resolution computational tsunami inundation calculation is performed using the obtained experi-

mental results as validation data. In the tsunami inundation calculation, four numerical models based on the nonlinear long wave equation are ensembled to verify the accuracy of these models and to investigate the differences and variations among the models. In Chapter 4, one of the models validated in Chapter 3 is adopted, and a subgrid-scale model focusing on the drag force on buildings is constructed to reduce the computational load while ensuring the accuracy of high-resolution computations using this model as the true value. The subgrid-scale model is constructed by idealized numerical experiments using a simple urban topography, and then by reproducing the Tohoku tsunami as a real event hindcast. In Chapter 5, we apply the subgrid-scale model validated in Chapter 4 to storm surge, where the governing equations are the same. As a real-event validation, we simulate the urban area of Leyte Island caused by Typhoon Haiyan in 2013. In this study, we focus on the wind stress term, which is one of the factors that cause storm surge, and investigate the difference in inundation area, inundation depth, and flow velocity caused by the feedback of building information to the wind stress term. Then, the accuracy of the subgrid-scale model is validated using the true values of inundation depth and inundation area obtained from the damage survey results, and the differences between the subgrid-scale model and the existing roughness model are examined. In Chapter 6, the developed subgrid-scale model is applied to the storm surge inundation calculation for Koto-ku, Tokyo, a large city, and the characteristics given by the subgrid-scale model are clarified when the building density is much larger than that of Onagawa and Leyte Island. Finally, the conclusions of this work are summarized in Chapter 7.

Chapter 2

Physical Modeling of Inundation Using Large Tsunami Flume and Coastal City Model

2.1 Introduction

The inundation of developed urban areas during tsunami attack, with resulting water levels, velocities, and loads, is one of the most important hazard processes to be predicted for coastal planning and design. Large scale tsunami inundations have been reported by numerous destructive mega-earthquakes. In the 2011 Tohoku Earthquake tsunami, inundation was larger than past tsunami events such as Meiji Sanriku Tsunami and infrastructure destruction occurred over a wide area (Mori et al., 2011). Mori et al. (2013) summarized the 2011 Tohoku Earthquake tsunami damages, and differences in local tsunami behaviors such as inundation heights and run-up heights. In order to reduce the number of casualties and infrastructure destruction along coastal regions in future events, understanding tsunami inundation over the built environment or coastal urban cities is very important. The modeling of tsunami inundation processes is essential for designing structures, making evacuation plans, city planning and other activities.

In conventional tsunami inundation simulations, a topography without structural height called "bare-earth" topography has been used, and the structural effect has been indirectly considered by increasing the frictional coefficients according to land usage (e.g. Kotani et al., 1998; Kaiser et al., 2013) with resolutions in the order of 10-100 m, which is much coarser than typical building dimensions (e.g., ASCE, 2016). This approach using bottom friction yields reasonable results, but it is difficult to model detailed inundation processes specific to coastal urban areas, such as flow around multiple buildings. In addition, the drastic development of remote sensing technology, such as LiDAR, enables detailed topographical data to be obtained and can be used to resolve individual buildings with fine resolutions in the order of 1 m (e.g., Verma et al., 2006). Several numerical simulations including structure-resolving topography have been performed with the advancement of computational techniques which will be mentioned in Chapter 3.

On the other hand, validation of local tsunami inundation behavior in real field is

difficult, and observational data is very limited due to the rarity of extreme tsunami occurrence. It is also difficult to measure detailed local phenomena of inundation processes using a physical model due to the complexity of bathymetry, topography, and interaction between tsunami flow and macro roughness elements such as buildings, streets and topographical changes. These complexities induce turbulence, wave breaking, diffraction and other hydrodynamic effects. Additionally, measurements of surface elevations and velocities on land are also difficult due to limitations of a wave flume and in-situ instruments. The objective of Chapter 2 is to discuss macroscopic and local tsunami behavior, tsunami inundation and other hydrodynamic processes on complex land structures in coastal urban areas, and to obtain dataset for numerical model validation for inundations. To achieve the objective, a physical modeling of tsunami inundation in a coastal city was conducted with advanced visualization techniques. After that, the author clarifies the relationships between macroscopic and local characteristics inundation, and complex urban city topography (in particular buildings).

2.2 Laboratory Experiment

The experiments were conducted at the Hybrid Tsunami Open Flume in Ujigawa laboratory, DPRI, Kyoto University (HyTOFU). The flume is 45 m long and 4 m wide, and is capable of generating tsunami-like long-waves or irregular short waves by a combination of water pump, piston-type mechanical wave maker and dam break gate system (Hiraishi et al., 2015). The 70 kW pump can create a change in water level over time similar to a tsunami or storm surge waveform by discharging flow from two 2.0 m $\times$ 0.2 m sized outlets at the flume bed. Maximum pumping capacity is 0.83 m^3/s with a maximum operating time of 1,200 s. The piston type mechanical wavemaker has 2.5 m maximum stroke and up to 2.83 m/s maximum speed. The wave maker itself is capable of generating multiple wave types including solitary waves, and regular or irregular waves up to 2 Hz (Tomiczek et al., 2016).

All experiments employed a wooden city model based on the city center of Kainan, Wakayama, Japan, an industrial city prone to damage from typhoon storm surge, and predicted Nankai Trough tsunamis (Mizobata et al., 2014; Le et al., 2019). The 3D city model, including ports, buildings and houses, was constructed at a scale of 1:250, covering an area of 2 km from east to west and 1 km from north to south (Yasuda et al., 2016). Plan and elevation views of the physical model of Kainan city are shown in Fig. 2.1. The east (inland) side of the model mainly consists of residential areas and mountains with overall higher elevation compared to the coast (west) side. An elevated railway line runs through the city from north to south with a station on the north side of the model. Water was able to flow through the railway line under the bridge, but not the station which was a solid structure. The west (coastal) side of the model mainly consisted of the harbor area, with retail stores and warehouses on the north, oil refineries on the south, and a section of steelworks on the northwest. The only entrance to the port from the deep water region of the model was located at the southwest. The land part of the physical model had a wooden base that was 5.5 cm thick, and was placed on a steel plate 0.8065 m above the bottom of the wave flume, while the bottom of the water region was the steel plate.

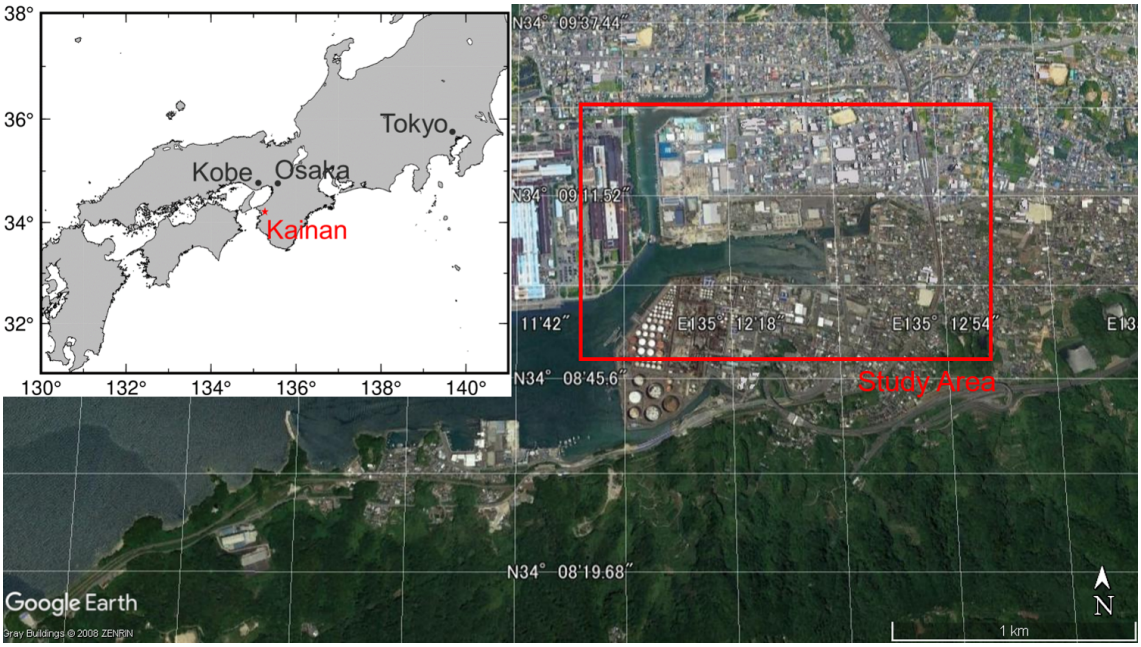

Figure 2.1: Study area of laboratory experiment (Kainan, Wakayama, Japan); map data is from ©Google, 2021 and ©ZENRIN, 2008

A 1:10 planar slope reaching the bottom of the flume was connected to the west of the model. The design water depth for the experiment was 0.877 m.

In total, 12 wave gauges (WG) were set up to cover the flume from offshore to onshore and over the city model to measure wave heights during the experiment. WG1 was set up near the wave maker to provide the initial wave condition for numerical models in Chapter 3. WG2, 3, 6, 9 were placed in the water region of the city model, with all others on normally dry land. The locations of wave gauges are shown in Fig. 2.2, with specific coordinates of each wave gauge listed in Table 2.1. Two acoustic Doppler velocimetry (ADV) devices were set up offshore to measure the velocity of incoming waves.

Visualization of the inundation process across the city model for all cases was recorded by an overhead 4K video camera. For selected cases, fluorescent dye (Sinleuchte red dye) was injected into the water area in the city model prior to the wave forcing so that the leading edge of inundation could be detected in the video images. Particle image velocimetry (PIV) was applied to measure the spatial flow patterns across the city model on several tests using small 5 mm foam particles painted with Sinleuchte fluorescent yellow dye and spread across the model prior to each experiment. Velocity fields were obtained by super-resolution PIV using DynamicStudio software by Dantec Dynamics. Fig. 2.3 shows an example of the visualization of inundation process. The blue and white lines show leading edges of inundation and coastline, respectively. The spatial distribution of velocities are plotted as yellow arrows. The inundated area with red dye and fluid velocities are clearly measured. The measured water velocity over land using PIV is necessary because it is difficult to use in situ instruments such as ADVs in dry or low water level conditions. The estimated flow velocities from PIV combined with the measured velocities from ADV were compared with the results from numerical modeling along with the wave

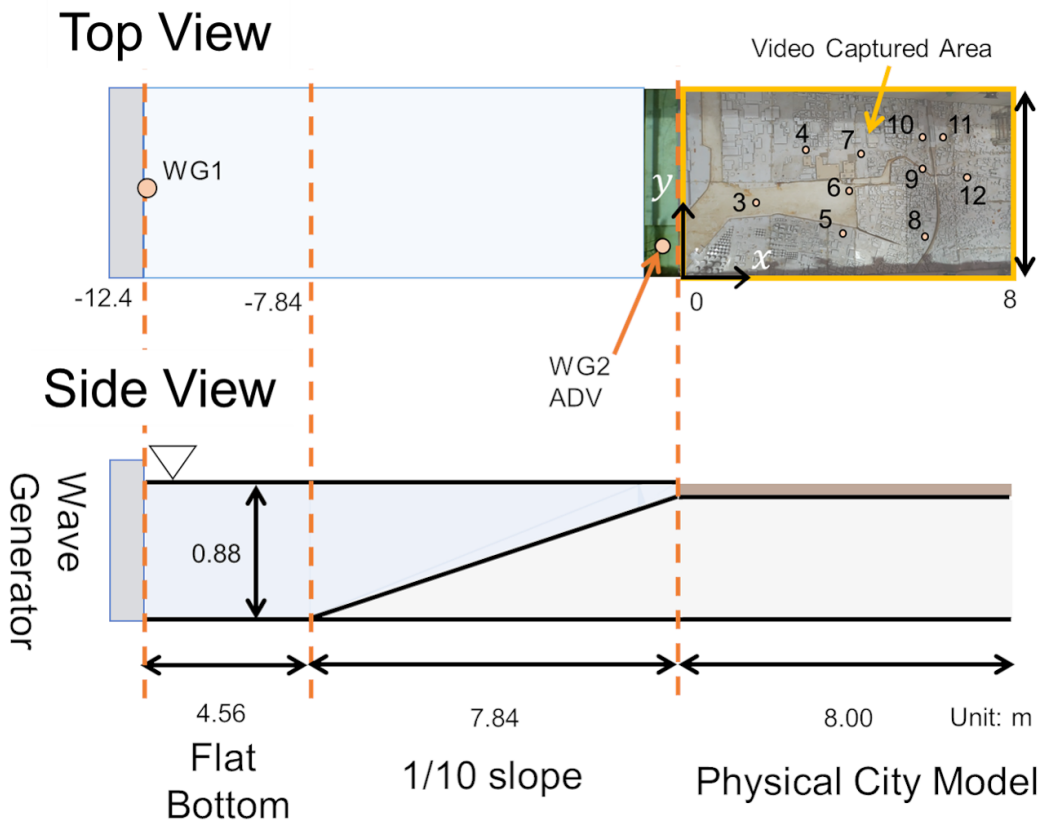

Figure 2.2: Experiment flume layout; (a) top and side view of the experiment flume (circle with number shows each WG location; ADV is installed next to WG2); and (b) elevation in flume and physical city model

Table 2.1: x, y-coordinate of WGs and ADV

measurement	X [m]	Y [m]	Z [m]
WG1	-12.3600	2.0000	-0.8770
WG2	-0.3050	0.8850	-0.0996
WG3	1.4400	1.6830	-0.0439
WG4	2.6400	2.6860	0.0139
WG5	3.2950	0.9050	0.0133
WG6	3.6490	2.0030	-0.0200
WG7	3.7450	2.6480	0.0104
WG8	5.2600	0.9580	0.0159
WG9	5.3460	2.3150	-0.0212
WG10	5.2180	3.1540	0.0067
WG11	5.7130	3.2690	0.0068
WG12	6.4930	2.1450	0.0125
ADV	-0.3050	0.6400	-0.0996

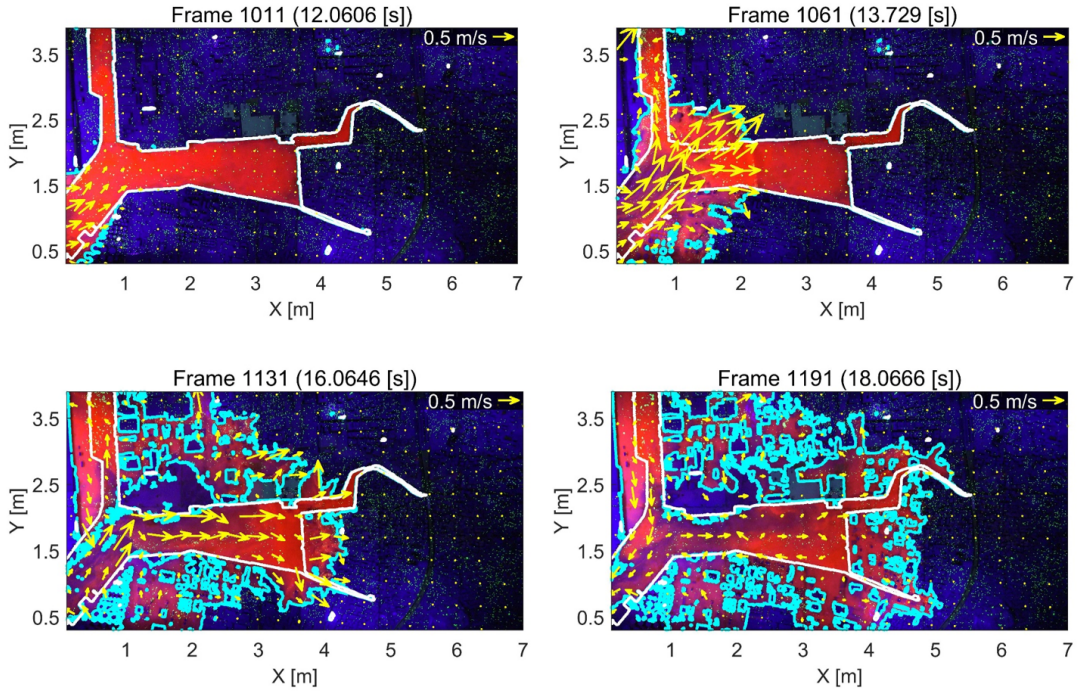

Figure 2.3: Examples of the visualization of inundation process (snapshots of leading edge of inundation (blue line) and esitimated velocity (yellow vectors); time proceeds from upper left to bottom right)

gauge data in Chapter 3.

The experimental conditions are summarized in Table 2.2 and the time series of water surface height in Table 2.2 are shown in Fig. 2.2. Three types of wave generation were conducted; short period wave, long period wave, and simulated tsunami wave as an incident wave, where conditions in each case were determined based on maximum inundation limits in preliminary trials. Short period waves were generated by solitary wave with 0.05 (Case H05) or 0.06 (Case H06) m wave height at WG1 by the piston-type mechanical wavemaker. The duration of the experiment in short period cases is 120 s but the first wave attacking was finished within first 30 s after wave generation. Long period waves were generated by pumping flow with constant discharge $Q = 0.015$ (Case Q0015), 0.020 (Case Q0025), and 0.025 m^3/s (Case Q0025). The maximum wave heights are 0.028, 0.035, and 0.044 m height in Cases Q0015, Q0020, and Q0025, respectively, and the duration of the experiments in long period cases is 420 s. Simulated tsunami wave (Case Nankai 141) was generated by combination of pump- and piston-types wave generator using the predicted Nankai Trough Mega Earthquake tsunami presented by Mizobata et al. (2014). This study used $\sqrt{2}$ times of the estimated tsunami wave height in 1:250 scale, which corresponds to the increase in tsunami wave height if the earthquake's moment magnitude intensity was increased by 0.1. The duration is 720 s. The study focuses Case H05 (short period wave) and Q0025 (long period wave) as main cases.

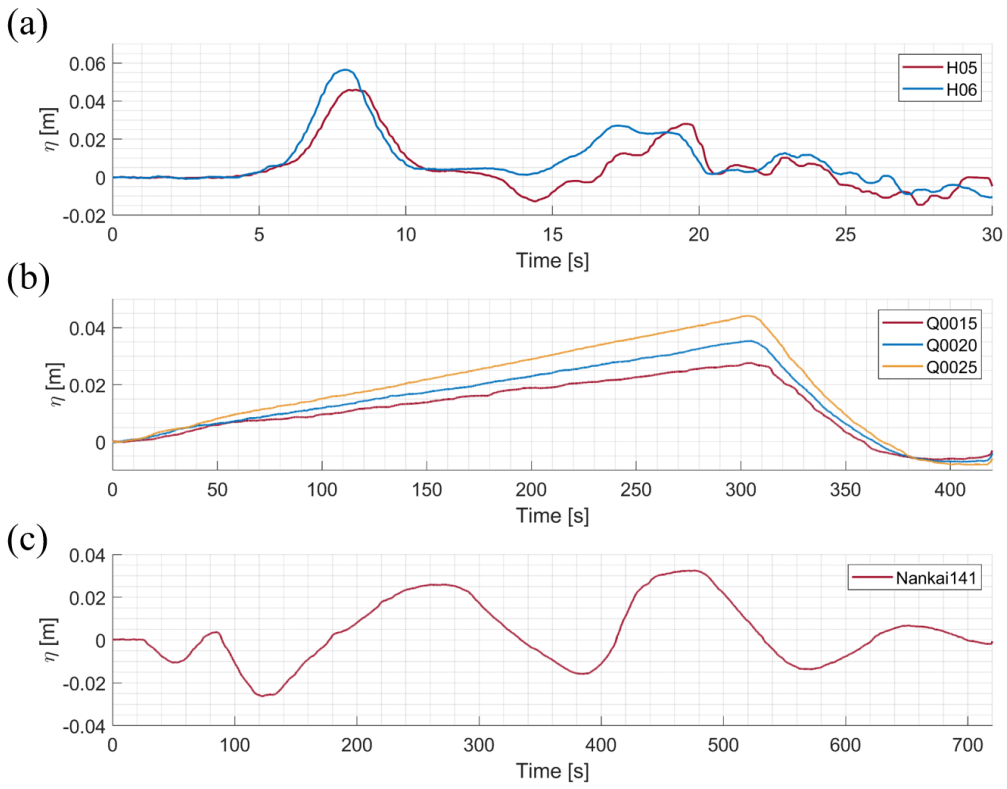

Figure 2.4: Time series of the surface elevation at WG1 for all experimental cases; (a) short wave cases (Cases H05 and H06), (b) long wave cases (Cases Q0015, Q0020, Q0025), and (c) simulated tsunami wave cases (Case Nankai 141)

Table 2.2: List of experimental conditions and measured items

Case Name	Wave Type	Input Wave	Duration	Measured Items	Total number of accetable trials
H05	short period wave	0.05 m height	120 s	Surface elevation Surface fluid velocity Leading edge of inundation	3
H06	short period wave	0.06 m height	120 s	Surface elevation Surface fluid velocity	2
Q0015	long period wave	0.015 m^3/s pumping 0.028 m height	420 s	Surface elevation Surface fluid velocity Leading edge of inundation	1
Q0020	long period wave	0.020 m^3/s pumping 0.035 m height	420 s	Surface elevation Surface fluid velocity	2
Q0025	long period wave	0.025 m^3/s pumping 0.044 m height	420 s	Surface elevation Surface fluid velocity Leading edge of inundation	4
Nankai 141	Simulated tsunami wave	Simulated tsunami wave by Mizobata et al. (2014)	720 s	Surface elevation Surface fluid velocity	2

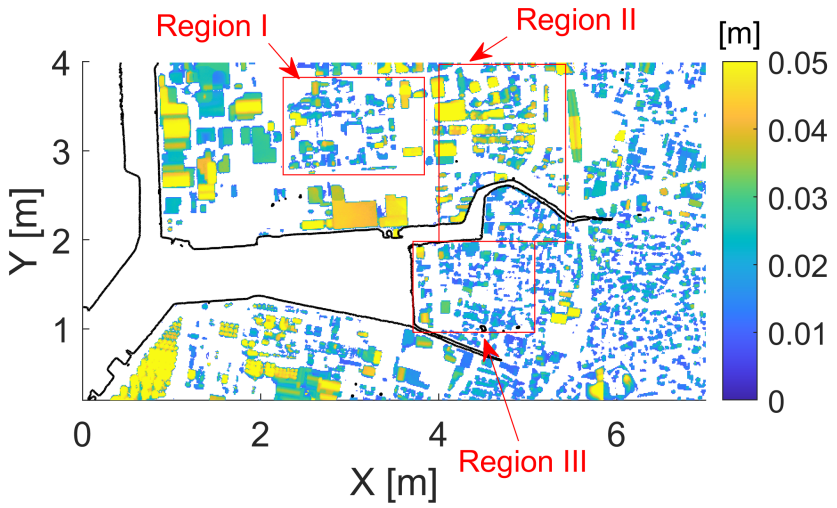

Figure 2.5: Building heights in the physical city model (color) with coastline (black line).

2.3 Experimental results and discussions

This section presents experiment results focusing on spatio-temporal data (i.e. limits of inundation and leading edges of inundation and velocity) and discusses the relationship between buildings (shown in Fig. 2.5) and, macroscopic and local inundation characteristics, in section 2.3.1 and 2.3.2, respectively.

2.3.1 Spatial distributions of velocity and inundation leading edges

Firstly, the short period wave case (Case H05) is examined. Fig. 2.6(a) shows leading edges of inundation corresponding to arrival time of first attack (hereafter arrival time). Fig. 2.6(b) shows spatial distribution of maximum fluid velocity measured by PIV. Here, the relationship of these two results and buildings are discussed. The short period waves have large momentum fluxes from offshore and required time for propagation is approximately 10 to 20 seconds (2.6 to 5.3 min at full scale). The spatial distribution of arrival time depends on shapes and spatial layout of buildings. For example, the Region I (around $X = 2.2$ - 3.5 m, $Y = 2.7$ - 3.5 m shown in Fig. 2.5) in the north area of Kainan has steep gradient of the arrival time. Fig. 2.6(c) shows the mean value of maximum velocities in Regions I-III before or after run-up of buildings or passing the road. The maximum velocity decreases after running up buildings in Region I, where relative difference of maximum velocities before and after run-up is approximately 68% (before building run-up: 1.1 m/s; after building run-up: 0.35 m/s). Then, the author takes a look at the buildings layout. There are buildings with less than 0.04 m (10 m at full scale) but the density of buildings is relatively high. On the other hand, the area with few buildings such as road shown in Fig. 2.6(a) and (b) shows larger maximum velocities than Region I. The relative difference

of maximum velocities is approximately 27% (before passing road: 1.1 m/s; after passing road: 0.81 m/s). This implies that the velocity is reduced by the building blocking appeared and the reduction is large when buildings accumulate in small area. However, such velocity reduction can depend on the the difference of run-up direction and angle of attack. For example, the gradient of the arrival times in Region II (around X = 2.2-3.5 m, Y = 2.7-3.5 m shown in Fig. 2.5) in the middle are of Kainan though the density and number of buildings are same degree as the Region I. Also, relative difference of velocities before and after run-up of buildings (i.e. in ocean and Region II) is 58% (before building run-up: 0.85 m/s; after building run-up: 0.36 m/s) smaller than Region I. The directions in Region I and 2-2 are northeast and east, respectively. Considering the direction of the main flow in the harbour area is east, the velocity reduction is large when the flow direction on the land side is the same as the main flow as in Region II. Moreover, the angle of attack can be another factor of the difference of velocity reduction since the the group of buildings in Region I faces the run-up wave at the southwest corner of the buildings while the one in Region II does at the west lateral side of the buildings. As a future work, it is recommended to quantify the relationship between velocity reduction effect by buildings, and run-up direction and angle of attack to buildings.

Next, long period wave case (Case Q0025) is examined. Fig. 2.7 show arrival time and maximum velocity in the same manner as Fig. 2.6. The limit of inundation extent is larger than Case H05 (all area except the mountain located in southeast) since the transported water mass fluxes are much larger. In this mean, the buildings does not affect the maximum inundation extent. On the other hand, the arrival time is affected by the buildings same as in Case H05. For example, the arrival time exceeds 75 s (approximately 20 min at full scale) in the north part of the Regions 2-3. The run-up flow is blocked by group of buildings and takes roundabout path around them (directions are shown in arrow in Fig. 2.7(a)). The maximum velocity and its direction corresponds to the flow explained in the previous sentence. Approximately 0.2 m/s velocity with northeast direction at X = 5.0 m, Y = 3.0 m is observed in the first wave arrival. However, the arrival time is also affected by the ground elevation more than Case H05 because momentum fluxes are relatively small. For example, slower arrival time (longer than 100 s; 26 min at full scale) is observed in the road mentioned in Case H05, while Case H05 showed the faster inundation speed. The ground elevation at the road is around 0.013-0.015 m, while the one near coastline such as X = 1.0-2.0 m, Y = 2.0-2.5 m is below 0.01 m. But not that the maximum velocity measured at the road is still large compared to the one on the group of buildings in Region I and the building still affects the run-up velocity. Furthermore, the inundation starts from channel placed in southern part of Region III (X = 4.2-5.5 m, Y = 2.0-3.5 m) even though the region is farther from offshore than northwest part such as Region I. One of the reasons is that water level in sea area uniformly rises. Fig. 2.8 shows the comparison of water surface elevations at WGs in harbor or channel (WGs 3, 6, and 9). Note that color indicates case (red: Case H05 and blue: Case Q0025) and marker indicates WG (no marker: WG3, square: WG6, and circle: WG9). The water surface elevation uniformly rises in harbor and water channel in Case Q0025 and other long period wave cases, while it does where the wave arrives in Case H05 and other short period wave cases. Therefore, water overflown from the channel with smaller water storage

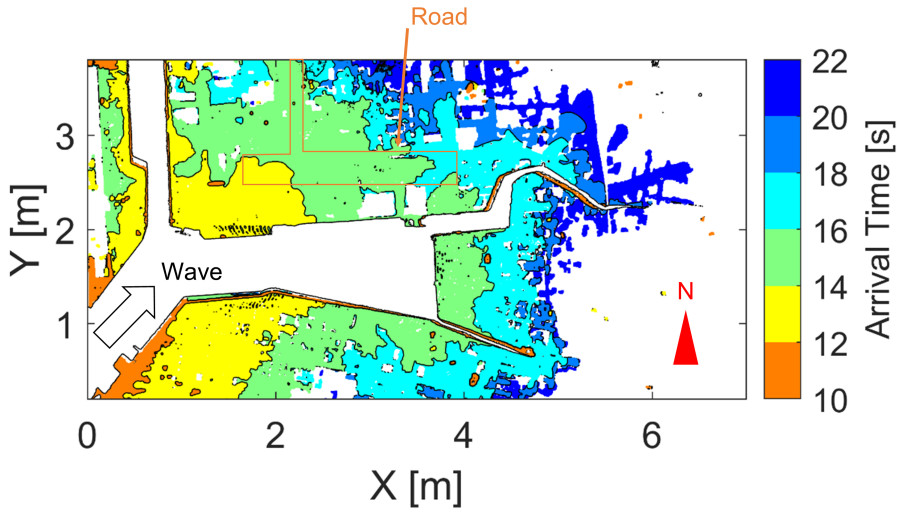

(a) Arrival time

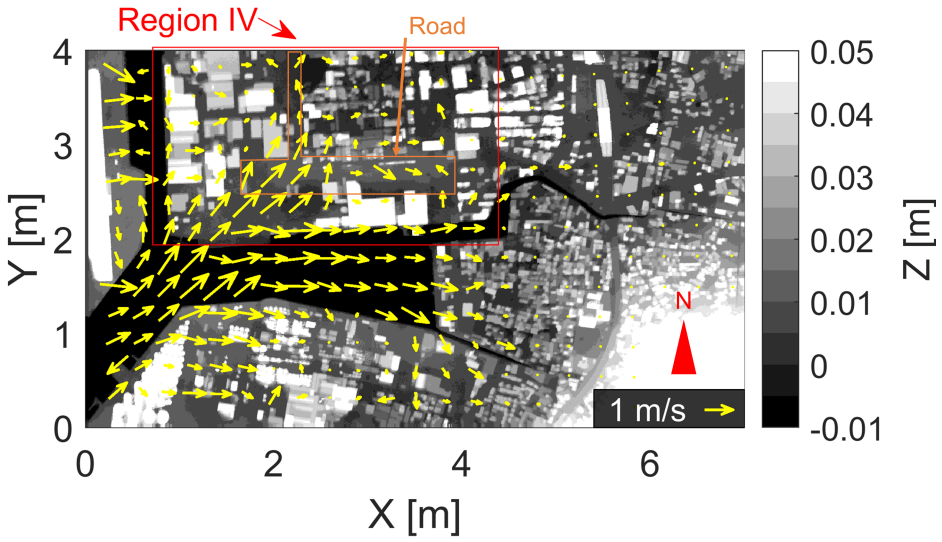

(b) Maximum velocity

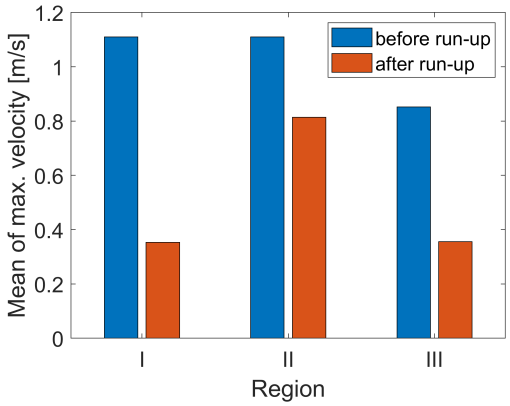

(c) Regional mean of maximum velocities (Regions I-III)

Figure 2.6: Inundation extent according to arrival time elapsed from wave generation and maximum velocity measured in Case H05 ($\eta_0 = 0.05$ m).

capacity than the harbor propagates in land area. These two examples show an aspect of the effect on inundation process by ground elevation as well as buildings.

2.3.2 Relationship between local inundation process and buildings

This section examines and discusses the effect by buildings on the local (range of smaller than 2 m at full scale) inundation process such as flow path and velocity from both qualitative and quantitative aspects. Note that this section focuses on Case H05 since the short period wave case gives clearer effect by buildings due to the larger momentum flux transported from offshore. Firstly, the inundation process is pursued qualitatively. Fig. 2.9 shows the pathlines from near shoreline in Region IV shown in Fig. 2.6(b), where the incident wave arrives from southwest with small wave attenuation and buildings with various shapes are complexly located. The green circle and red triangle show the start and end points of pathlines, respectively. Many pathlines affected by buildings are observed and classified mainly in three patterns.

1. Reflection: run-up flow is reflected and blocked in front of the buildings.
2. Overtopping: run-up flow overtops buildings and keeps propagating.
3. Diffraction: run-up flow is divided by buildings and takes roundabout path around buildings.

However, note that these three flow patterns are mixed up and any of these patterns is dominant focusing on one pathline. Clarifying the condition which flow pattern is dominant is recommended and will be future work. Here, the author discusses each pattern of flow focusing on three example pathlines (PL1-3) shown in Fig. 2.9 using magenta lines and its relationship between buildings (marked in blue boxes in Fig. 2.9). PL1 mainly shows the reflection pattern. The flow in PL1 is reflected by vertical structure in Buildings A and its direction changes from north to south. On the other hand, the flow in PL2 does not overtops one of Buildings B after flowing between buildings. This pattern corresponds to the overtopping pattern. PL3 shows the diffraction pattern twice until the flow stopping by Buildings B and C. The direction of flow in PL3 changes at one of Buildings B from northeast to north. After that, the flow is blocked by Buildings C and propagates along the road. Similar patterns to PL1-3 are observed in Region IV and these three patterns are major in flows.

Secondly, the inundation process is pursued quantitatively focusing on PL2 (overtopping) and 3 (diffraction). Fig. 2.10 shows the time series of fluid velocity on pathlines PL2 and 3. Horizontal axis indicates the elapsed time after wave generation. Left and right axes indicate the fluid velocity and topography elevation on a specific pathline, respectively. Circle with color corresponds to left axis and color shows the flow direction in degree measured from south. Note that the direction larger than 180 degree is seldomly observed. The velocity on PL2 (Fig. 2.10(a)) is approximately 50% decreased at $t = 14$ s because of overtopping the building with 0.025 m height. After that, the velocity increases about 50% and direction changes from 150 to 120 degree. This is because the flow merging with the one from west and momentum flux temporarily increases. Then,

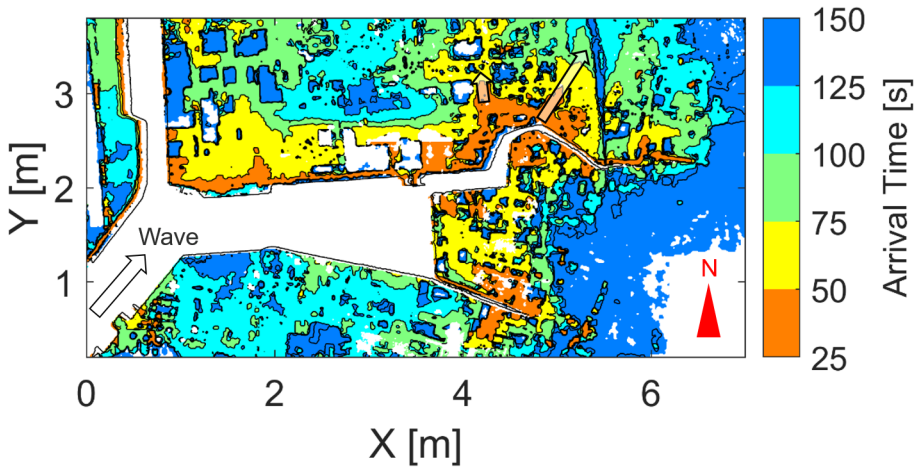

(a) Arrival time

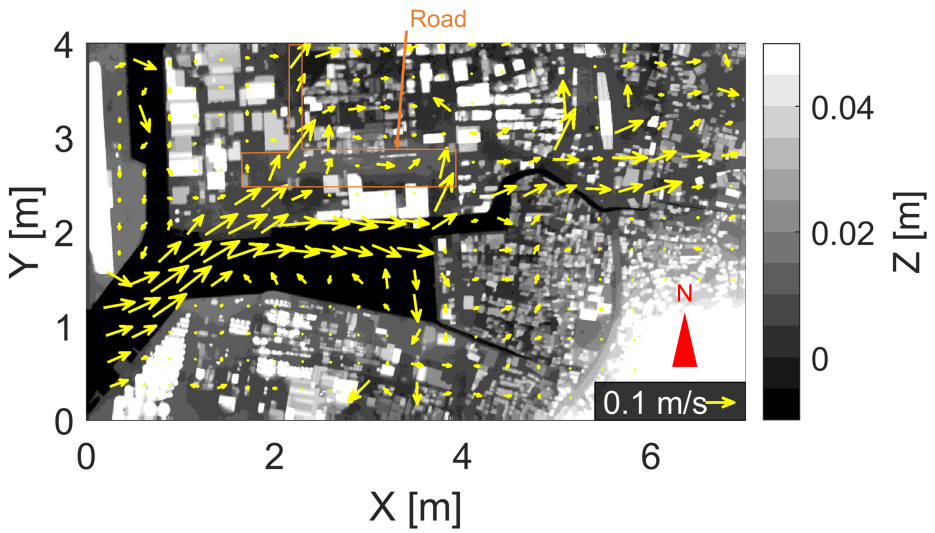

(b) Maximum velocity

Figure 2.7: Inundation extent according to arrival time elapsed from wave generation and maximum velocity measured in Case Q0025 ($Q = 0.025$ m^3/s, $\eta_0 = 0.044$ m).

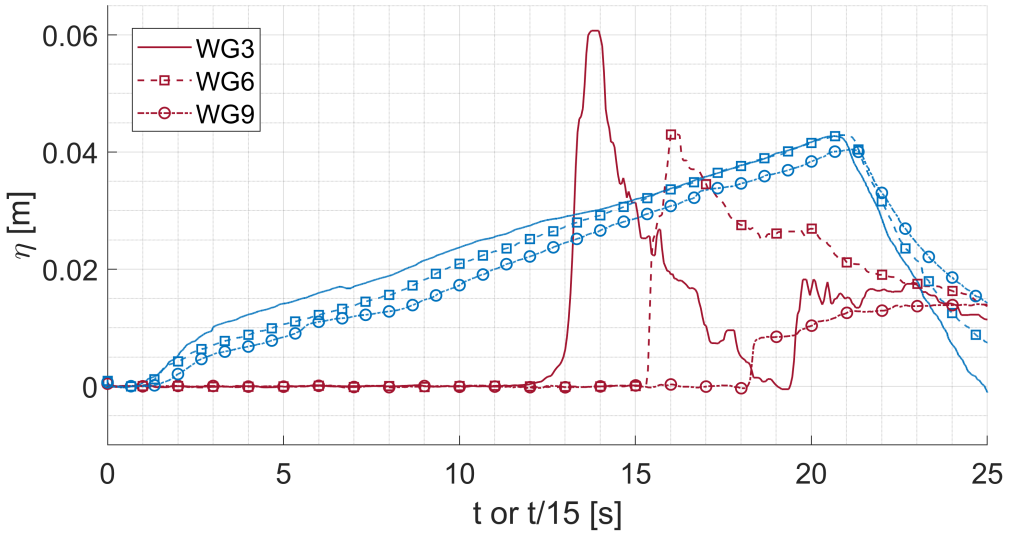

Figure 2.8: Comparison of time series of water surface elevation between Cases H05 (red lines) and Q0025 (blue lines) at WGs 3, 6 (square), and 9 (circle) installed in harbor or water channel; horizontal axis shows the elapsed time from the wave generation (time is divided by 15 for Case Q0025).

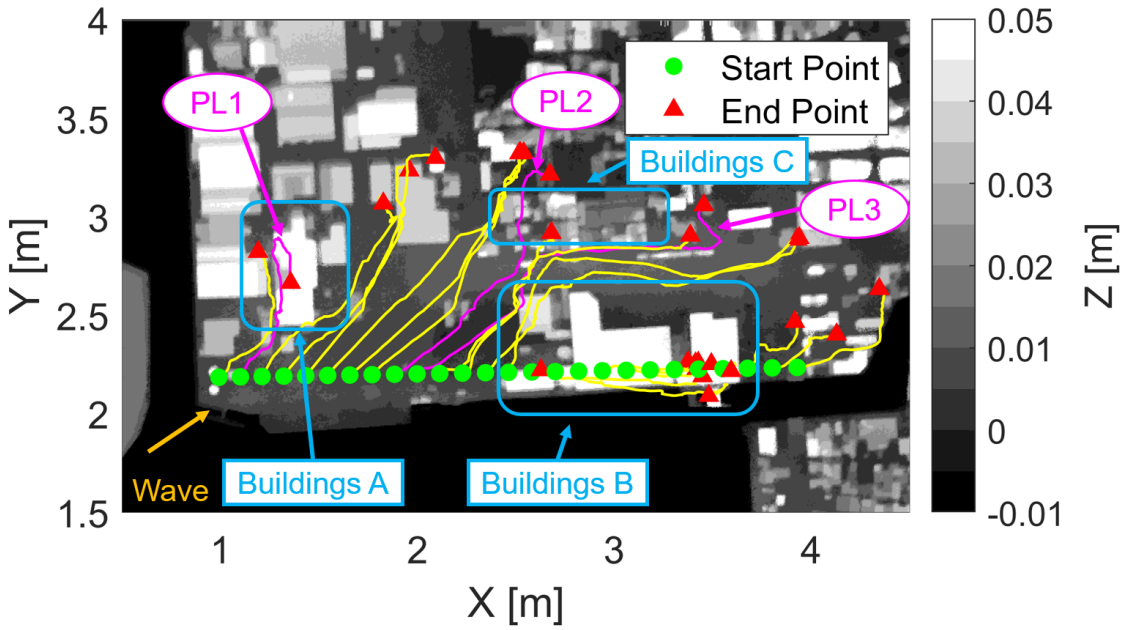

Figure 2.9: Pathlines from near shoreline (Start and end points are marked in green circle and red triangle, respectively); Pathlines PL1 to PL3 mentioned in the section are colored in magenta.

the flow runs up through the gap between each building and collide with a building with relatively high height (0.03 m) in Buildings C. In run-up process along PL2, the velocity decreases and the direction does not vary as long as the flow is not blocked. Therefore, in the overtopping pattern, the magnitude of velocity is reduced rather than flow direction because the buildings work as resistance element. Next, the PL3 is focused. The flow direction is around 135 degree before colliding with Buildings B similarly to other pathlines. However, the direction abruptly changes to 150 degree but the velocity decrease is approximately 25%. After that, the flow runs up in north direction until colliding with Buildings C (t = 14.7 s). The direction changes from 150 degree to less than 90 degree after collision along the road. Thus, in the diffraction pattern, the flow direction is mainly changed. Summarizing this section, three major patterns of flooding wave in land side because of building existence are observed. It is considered that velocity field strongly varies due to buildings complicatedly placed in land side and it is recommended that the spatial layout and shape of building are implemented in numerical simulation of tsunami and storm surge inundation.

2.4 Summary of Chapter 2

Chapter2 conducted physical modeling of inundation using large tsunami flume and in a 3D complex coastal city model which included ports, buildings and a bridge to obtain the benchmark data for further numerical model validations. The experiments used tsunami conditions for a short period wave, long period wave, and simulated tsunami wave by a piston-type wavemaker and pump. The time series of water surface height was measured by 12 WGs covering the flume form offshore to onshore and over the city model. The inundation wave propagation on the land was visualized by 4K video image analysis and the time series of velocity and leading edges of inundation as spatial data which have been measured in few previous researches are measured using PIV and edge detection. The author analyzed obtained experimental results focusing on spatio-temporal data (i.e. limits of inundation and leading edges of inundation and velocity) and discussed the relationship between buildings (shown in Fig. 2.5) and, macroscopic and local inundation characteristics. The summary of Chapter 2 is as follows;

a) The arrival time of first wave was calculated using leading edges of inundation. The spatial distribution of arrival time depends on shapes and spatial layout of buildings regardless of incident wave.

b) If momentum flux transported from offshore is large in short period wave such as Case H05, the arrival time is later according to existence of group of buildings. The maximum velocity decreases after running up buildings after run-up a building accumulating area is approximately 68%, while approximately 27% decrease is observed in the road area without buildings. The strength of velocity reduction by buildings depends on run-up distance and angle of attack of buildings.

c) If momentum flux transported from offshore is small in short period wave such as Case Q0025, the arrival time is affected by topographic characteristics other than

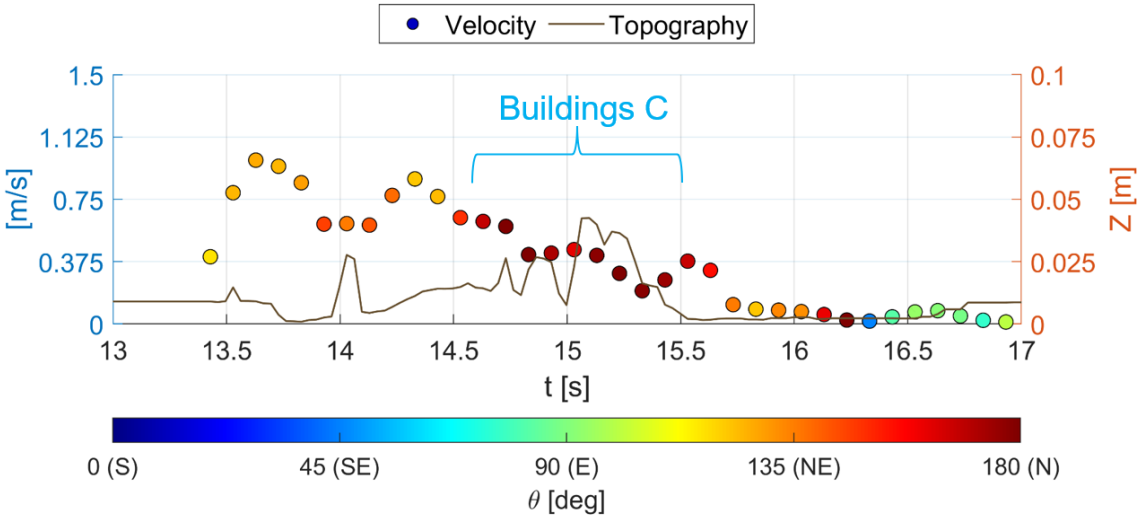

(a) PL2

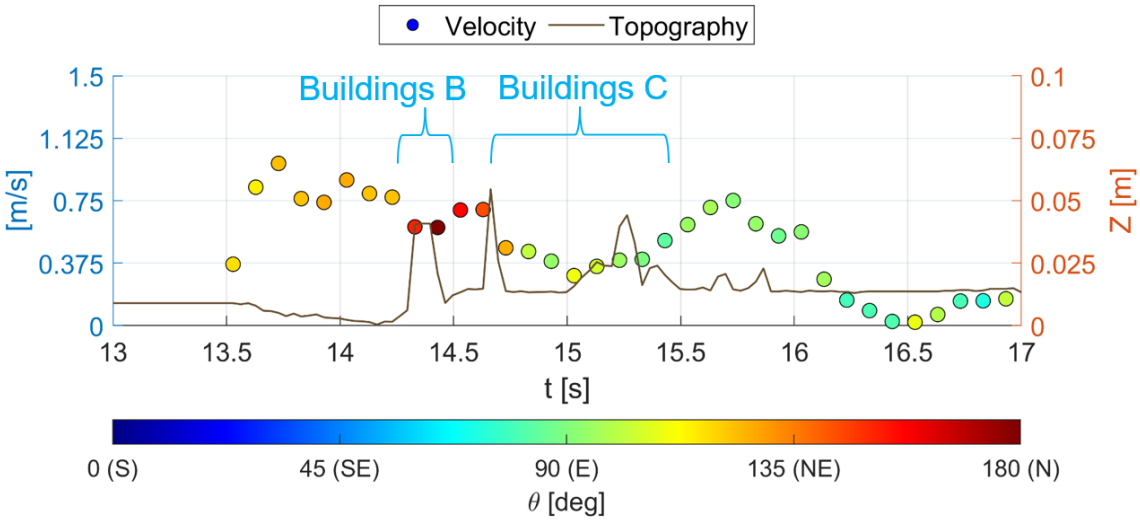

(b) PL3

Figure 2.10: Time series of fluid velocity on pathlines (a) PL2 and (b) PL3 with topography height (left and right axes correspond to velocity and topography height, respectively); color indicates flow direction measured from south direction.

buildings such as ground elevation difference and existence of channelized feature. The road in northern area gave later than 100 s arrival time because of the ground elevation is higher than near coastline. Also, the area close to channel gave earlier than 50 s arrival time even though it was far from offshore.

d) The pathlines and velocities on two representative pathlines were traced using time series of velocity to focus inundation characteristics in local scale. Many pathlines affected by buildings are observed and classified mainly in three patterns; 1) reflection, 2) overtopping, and 3) diffraction. These three flow patterns are mixed up and any of these patterns is dominant focusing on one pathline.

e) The flow pattern of overtopping mainly affects magnitude of velocity, while the one of diffraction affects flow direction.

Chapter 3

High-resolution Simulation of Tsunami Inundation Using Multiple Numerical Models

3.1 Introduction

As a series of the experimental results showed in Chapter 2, macroscopic and local inundation processes such as arrival time and velocity field strongly vary spatially due to buildings complicatedly placed in land side and it is recommended that the spatial layout and shape of building are implemented in numerical simulation of tsunami and storm surge inundation. On the other hand, model uncertainty remains as long as use different numerical models even if the building-resolving simulation is conducted. For example, boundary conditions incorporating building walls, and complex propagation of inundation fronts are all important aspects of the prediction of inundation, and can vary among models. Different numerical models of tsunami simulations are known to produce a range of results for identical inputs, resulting in a range of uncertainty. Lynett et al. (2017) examined the sensitivity of tsunami-generated coastal current predictions for an inter-model set of simulations, and found that shear- and separation-driven currents are quite sensitive to model physics and numerics. The authors concluded that deterministic simulations may be misleading for some aspects of tsunamis, particularly for velocities, and ensemble-based simulations may provide more realistic probabilities of actual conditions (see also Lynett, 2016).

A few studies examined detailed inundation flows in urban areas using building-resolving simulations (e.g., Cox et al., 2008; Park et al., 2013; Prasetyo et al., 2019) as mentioned in Chapter 2. Park et al. (2013) examined flows through an physical model of Seaside, Oregon using a Boussinesq model that directly resolved building footprints. Good agreement was found with a set of 1:50 laboratory experiments, once the friction factor was tuned. Water surface elevations were moderately sensitive to friction, while velocities and momentum fluxes were highly sensitive. In contrast, Prasetyo et al. (2019) did not examine velocities but instead reported arrival times and maximum water surface elevations for a 1:250 scale model of an urban area. While a 2D shallow water model

showed a tendency to underestimate maximum surface elevations and arrival times, a quasi-three-dimensional model gave slightly better agreement with data.

Because of the greatly increased computational cost, Reynolds-Averaged Navier-Stokes (RANS) simulations or Large Eddy Simulations (LES) of tsunamis through built-up environments are less common. The expense and difficulty of simulating large built-up areas with 3D models is clear in the literature, where significant numbers of simulations may be found examining inundation and loading of one or a small number of structures (e.g. Bagherizadeh et al., 2020; Sogut et al., 2020; Sogut et al., 2019; Sarjamee et al., 2017), but notably few studying complex flows around arrays of many buildings. Of these few, Pringgana et al. (2021) examined the influence of onshore structures' orientations and arrangements during a tsunami impact using the numerical method of smoothed particle hydrodynamics (SPH). The authors succeeded in modeling hydrodynamic behavior to a level of detail hitherto unobtainable from physical models. Qin et al. (2018a, 2018b) examined inundation flows with the OpenFOAM model through the same Seaside, Oregon setup as in Park et al. (2013). Key findings were that the flows and water levels could be reasonably predicted by the CFD (Computational Fluid Dynamics) model, and with better accuracy than a shallow water 2D model, but at greatly increased computational cost. Computational expense was large enough that the relatively small town was modeled in sections, and it was suggested that "modeling of an entire town could be computationally impractical". Even with significant increases in available computational power, straightforward simulation of tsunami-like inundation over large built-up areas does not become computationally feasible in the near future. Thus, families of shallow water simulations appear to be likely to continue as the primary computational tool for examining inundation in complex regions.

However, even for nominally similar shallow water models there can exist non-trivial differences in simulations arising from differences in model implementation, particularly for inundation wetting and drying. This provides an additional source of uncertainty in the interpretation of results, and thus it is important to understand the variance in these simulations, and how this relates to the interpretation of model predictions.

The objective of Chapter 3 is to discuss local tsunami behavior, tsunami inundation and other hydrodynamic processes on complex land structures in coastal urban areas modeled by several numerical models of the nonlinear shallow water equations (denoted 2D-SWE hereafter). The experimental results using physical model of a coastal urban city obtained in Chapter 2 is used as a benchmark dataset. A comparison between physical and numerical model results was performed using four different numerical models based on the 2D-SWE. Then, sensitivity of tsunami inundation modeling for water surface elevation, velocities and other tsunami characteristics in urban area has been summarized comparing with physical modeling and numerical results.

Table 3.1: Summary of numerical setup for each model

	TUNAMI-N2	STOC-ML	Subgrid SWE	JAGURS
Abbreviation	TUNAMI	STOC	SGSWE	JAGURS
Governing Eqs.	Depth-Integrated SWE	Velocity-form SWE	Subgrid-Averaged SWE	Depth-Integrated SWE
Spatial Discretization	Finite Difference Method			
Spatial Differentiation	Staggered C-grid			
Temporal Differentiation	Leap-Frog Scheme		Euler-backward scheme	Leap-Frog scheme
Convection Terms	Upwind (1st-order accuracy)			
Other Gradient Terms	Centered (2nd-order accuracy)			
Friction Term	Semi-implicit			
Wet / Dry boundary	Kotani et al. (1998)		Casulli (2009)	Kotani et al. (1998)
Tolerance Depth for Wet / Dry	10^{-10} m	10^{-6} m	0 m	10^{-6} m
Tolerance Depth for Convective Term	10^{-6} m	No	No	10^{-6} m
Maximum velocity limiter	7 m/s	5 m/s	No	$Fr = 2.0$
Roughness coefficient	Water channel ($X = 12.36 - 0.66$ m): 0.025 Physical model ($X = 0.66 - 8.0$ m): 0.013			
Input boundary	$X = -12.6$ m along the left boundary (WG1)			
Boundary conditions	North and South: wall boundary West: inflow boundary East: radiation boundary			

3.2 Numerical Modeling

3.2.1 Numerical Method

In this study, inundation simulations were conducted using four numerical models with different numerical implementations and, to a lesser degree, with different governing equations. The accuracy of the simulation results was compared with experimental results, and the variability among the models was investigated to estimate the uncertainty in numerical simulations. Table 3.1 shows a list of governing equations for each model and other conditions about numerical treatment (e.g. discretization methods for advection term and frictional term, tolerance depth for frictional term). Brief descriptions and relevant references for each of the models are given here:

1. TUNAMI-N2 (Goto et al., 1997): TUNAMI-N2 is a SWE model which has been used to simulate tsunami propagation from offshore to inland areas in Japan and other countries. The governing equations of the models are based on the two-dimensional nonlinear SWE in depth-integrated form, and are discretized in time with explicit leap-frog finite differences.

2. STOC-ML (Tomita et al., 2005): STOC-ML is a multi-layered model with hydrostatic approximation. The governing equations of STOC-ML are the Reynolds-Averaged Navier-Stokes equations, which are different from the other models in this paper. However, the number of vertical layers used here was one and Reynolds stress was ignored in this simulation. Therefore, the governing equations are equivalent to the conventional SWE in velocity form rather than depth-integrated form. In this way it differs from the other models used here.

3. Subgrid SWE model (Kennedy et al., 2019): The subgrid SWE (SGSWE) model developed by Kennedy et al. (2019) uses the grid-averaged SWE in depth-integrated form as the governing equations with closure approximations applied to the subgrid system to enhance the accuracy while saving computational resources. The equations are discretized in time with a Euler-backward finite difference scheme, and in space using a staggered finite difference grid.

4. JAGURS (Baba et al., 2015): JAGURS solves the linear and nonlinear depth-integrated SWE by implementing a staggered-grid, leap-frog finite difference scheme. A nested grid system is adopted to enable higher spatial resolutions in target domains. The code has been parallelized for high-speed computation.

3.2.2 Numerical Setup

Chapter 3 focuses Case H05 (short period wave case) as a main case. Fig. 3.1 shows the measured water surface elevation at WG1 that was used for wave input at the west (ocean) side computational boundary. A free transmission condition was applied at the open boundary in the east side. Boundary conditions for the north and south sides used wall boundaries with slip conditions. Regarding lateral wall effect, the authors checked the velocity and flow direction near the north and south wall boundaries measured by

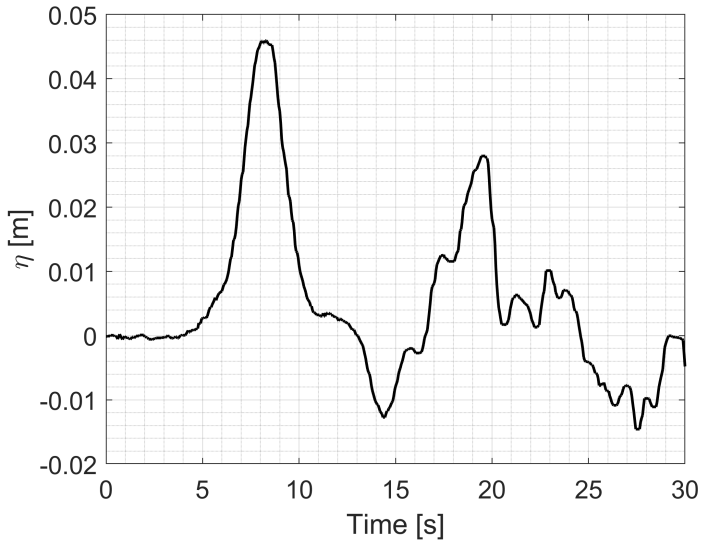

Figure 3.1: Water surface elevation at WG1 near the wave generator used as an incident wave in Case H05.

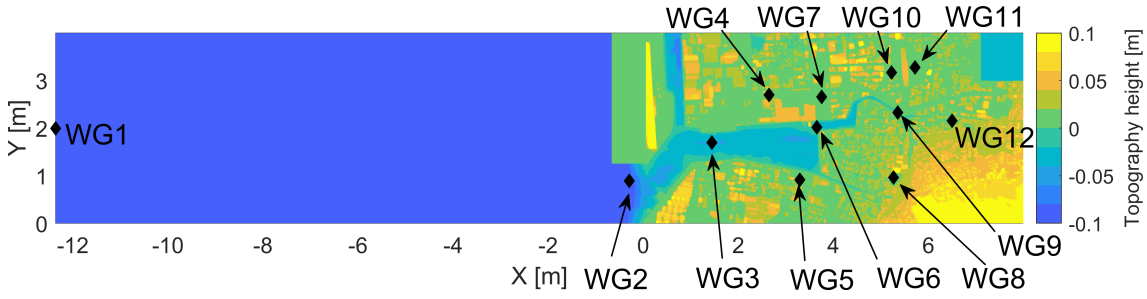

Figure 3.2: Computational domain used in simulation (color shows topography elevation) with each WG location.

PIV. It was confirmed that some wall effects but are limited within 5 cm along the wall. Furthermore, the bottom wall effect may exist since the velocity measured by PIV only shows the one at the top layers. The total computational time was 30 seconds, which allowed inundation by the incident wave to be completed, while not considering waves re-reflecting from the wavemaker. The movie used for a series of the image analyses shows that the reflected wave started to inundate the land area after 25 seconds and contaminate measured data. The author used incident wave data including wave reflection from the wavemaker and removed computational results from 25 s to 30 s.

Figure 3.2 shows the topography and bathymetry in the numerical domain. Elevation data for the domain of the physical city model ($X \geq 0.0$ m) was created by interpolating scanned point cloud data into a regular grid. Point data was obtained with a laser scanner (Leica BLK360) set up at three locations in the basin, with results combined into one dataset. As for the grid size, the convergence tests changing grid size 1.0 and 0.5 cm was conducted before main computations and there were no significant differences of maximum

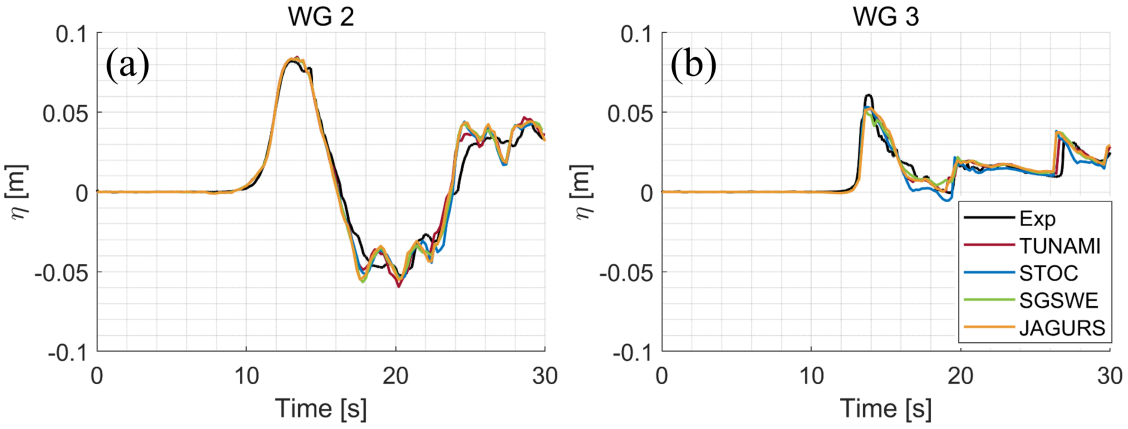

Figure 3.3: Time series of water surface elevation at (a) bay mouth (WG2) and (b) center of the port (WG3); color shows models or experiment (black: experiment, red: TUNAMI, blue: STOC, green: SGSWE and yellow: JAGURS).

surface elevation and velocity between two different grid size cases. Thus, 1.0 cm grid resolution was chosen to reduce computational time, which resulted in a domain of 2037 × 400 points. Bottom roughness was based on the Manning model with roughness coefficients of $n = 0.025$ m$^{-1/3}$s for $X < 0.66$ m and $n = 0.013$ m$^{-1/3}$s for the domain of physical city model ($X > 0.66$ m) based on the land usage following Kotani et al. (1998). The Manning ' s roughness for the physical model area is smaller than the one for the ocean bottom since the value of 0.010-0.013 m$^{-1/3}$s for Manning roughness is recommended for artificial channel made by smooth wood (e.g. Chow, 1959). Note that the model input (bathymetry, incident wave, roughness, and etc.) is confirmed to be unified and no self-filtering schemes to handle the large gradient of bathymetry due to buildings is implemented for all the numerical models (TUNAMI, STOC, SGSWE, and JAGURS).

3.3 Results

This study uses two types of data, point gauge and spatial data, and compares model results both between each other and to laboratory results. The magnitude and time of maximum surface elevation at selected locations are examined for point data. In addition to the arrival time, wave front velocity, fluid velocity and surface elevation (maximum value and time series) will be examined in the spatial data by visualization analysis of laboratory experiments.

3.3.1 Model variation and accuracy of water surface height at WGs

Fig. 3.3 shows the surface elevation at WGs 2-3 installed at the entrance and center of the port (locations in Fig. 3.2) for confirmation of the incident wave condition. All models show good agreement with experimental data at WG2. However, for all models the maximum surface elevation is about 0.01 m (15 - 20%) smaller than the measurement at WG3, although the absolute magnitude is small. This may either be caused by attenuation

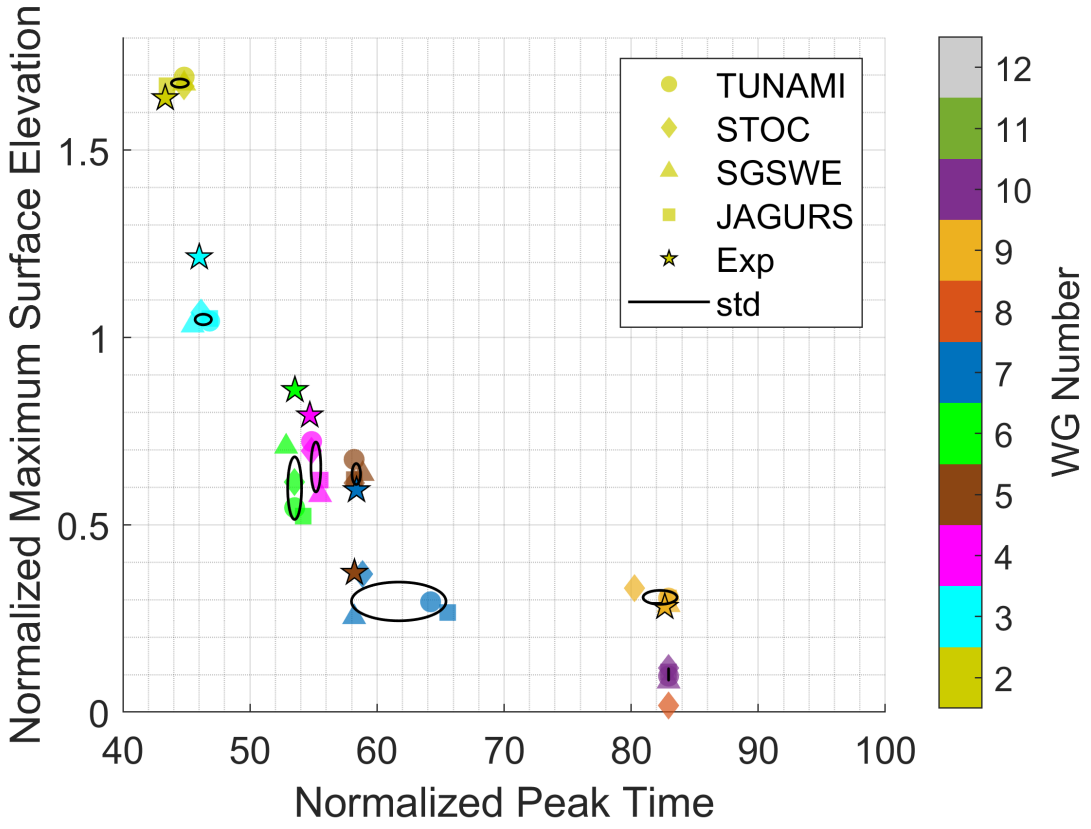

Figure 3.4: Maximum surface elevation at each WG and its appearance time (peak time) normalized by the incident wave in Case H05; Marker (circle: TUNAMI, diamond: STOC, triangle: SGSWE, square: JAGURS and star: experiment) color shows WG number and black ellipsoid shows standard deviation.

near the entrance of the port by sea bottom friction that is larger than the physical experiment, more likely from dispersive effects not included in these hydrostatic models, or wall effects in experiment. Since the results on land tend to be underestimated due to the influence of these biases of incident waves, this should be considered. Figure 3.4 shows the relationship between modeled maximum surface elevations and their peak times. The surface elevations and times are normalized by incident wave conditions as

$$\bar{\eta} = \eta/\eta_0 \tag{3.1}$$

$$\bar{T} = T/T_0 \tag{3.2}$$

where $\eta_0 = 5.0$ cm (wave height at WG1), $T_0 = \sqrt{h/g}$ s, $h = 0.877$ m (depth of the wave flume), $g = 9.81$ m/s^2, respectively. All the models show similar tendencies where they tend to underestimate the maximum surface elevation. The ellipsoids in Fig. 3.4 show the mean (center of ellipsoids) and standard deviation (radii) of maximum water surface elevation and time of peak water levels for the four model results at each gauge location. It is observed that the larger deviations are observed at locations further inland (WG 4, 5, 7) and in very shallow inundation depths (WG 6, 9) while differences are smaller in deeper

water (WG 2-3). Focusing on gauges in inundated regions, WG4 (road in flat area), and WG 7 (intersection of buildings) give about 4.7 and 3.7 times larger standard deviation in surface elevation than WG3 (in the port). It is also observed that arrival times of the peak inundation also have a large standard deviation (about 5.8 times larger than WG3). Both WG4 and WG7 are installed on a wide road but large buildings on both sides of the road complicate simulations. Furthermore, WG7 is at a location where two major inundation wave fronts merge from the west and the south. The complexity of inundation appears to be a major reason why model variations here are larger than in deep inundation areas. More detailed inundation processes around the intersection will be presented in the following section.

3.3.2 Model variation and accuracy in spatio-temporal distribution of inundation

Numerical results about the spatial (or spatio-temporal) data are discussed to examine the inter-model variation. To estimate model uncertainty for any computed property, the relative magnitude of inter-model variation of each value is defined as

$$v = \sigma/\mu \tag{3.3}$$

where v is the variation, σ is model standard deviation and μ is model mean value.

Maximum inundation depth and spatial extent are two important measures for tsunami intensity, and are widely used for tsunami hazard maps. Fig. 3.5 shows the model mean and standard deviation of the maximum inundation depth in each grid. The inundation limit of the tsunami leading edge from the experimental data is also shown in Fig. 3.5(a). The overall inundated area from model results matches well with the experimental data, and thus the inundation limits can be reproduced by the numerical models. Focusing on the maximum inundation depth, the mean value of the inundation tends to be larger at areas close to the original shoreline. For instance, deeper inundation depths of more than 0.03 m (7 m at full scale) are recorded in the north nearshore area ($X = 1 - 2$ m and $Y = 2 - 2.5$ m). The inundation depth in the middle nearshore area ($X = 3.8 - 4$ m and $Y = 1 - 2$ m) is also recorded as more than 0.05 m (12.5 m at full scale) depth. The inter-model variation of inundation depths in the models changes significantly depending on areas but shows some general patterns. Overall, large areas of the model results show standard deviations smaller than 0.004 m (1 m at full scale) but some areas have larger deviation. Specifically, the nearshore north ($X = 1 - 2$ m and $Y = 2 - 2.5$ m) and south ($X = 1 - 2$ m and $Y = 1 - 1.2$ m) areas show large deviations (more than 0.006 m; 1.5 m in real scale) of maximum inundation depth. These are near the locations of first inundation, and the large variation appears to be related to the dynamic wetting, drying, and propagation of the large amplitude wave front. In these areas, the inter-model variation, v, is 0.17 and 0.24 on average in the nearshore north and south, respectively.

Figure 3.6 shows the model mean and standard deviation of the maximum fluid velocity in the same format as Fig. 3.5. The mean value of the velocity unsurprisingly tends to be larger at areas close to the original shoreline likewise the inundation depth. Furthermore, the velocity is locally amplified at the roads or small alleys between buildings. For example,

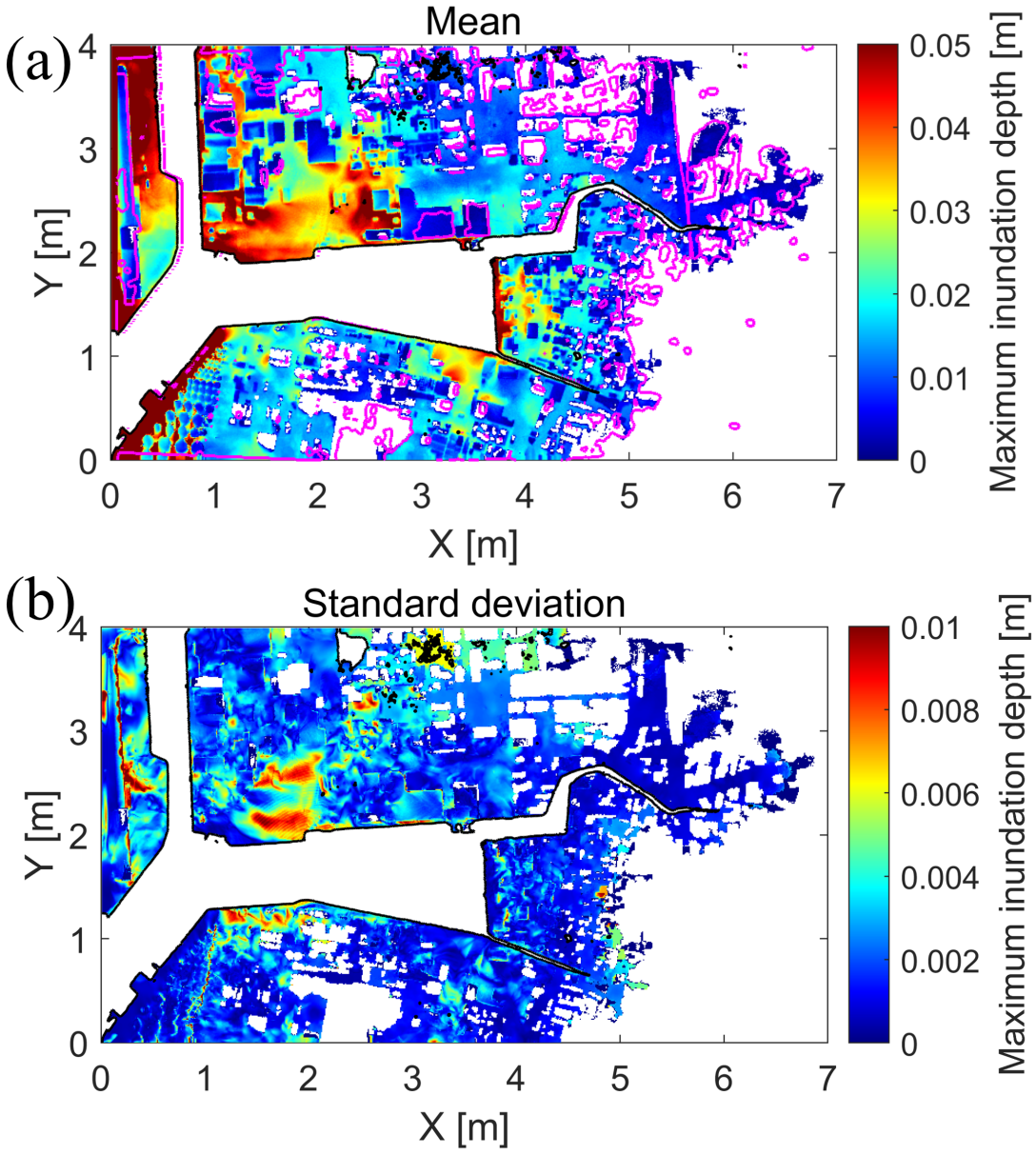

Figure 3.5: (a) Inter-model mean and (b) standard deviation of maximum inundation depth (magenta line shows the maximum inundation leading edge observed in the experiment).

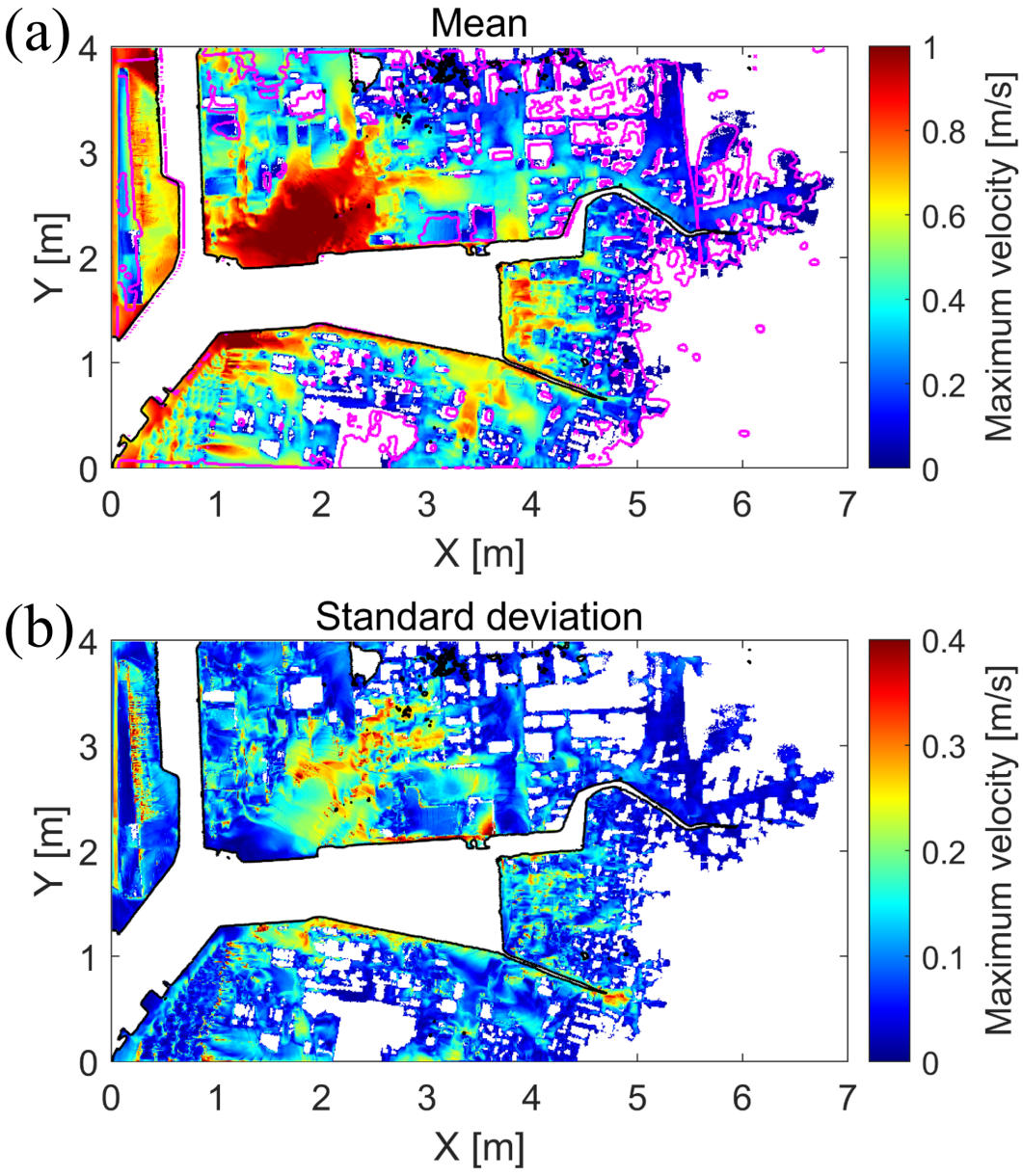

Figure 3.6: (a) Inter-model mean and (b) standard deviation of maximum velocity (magenta line shows the maximum inundation leading edge observed in the experiment).

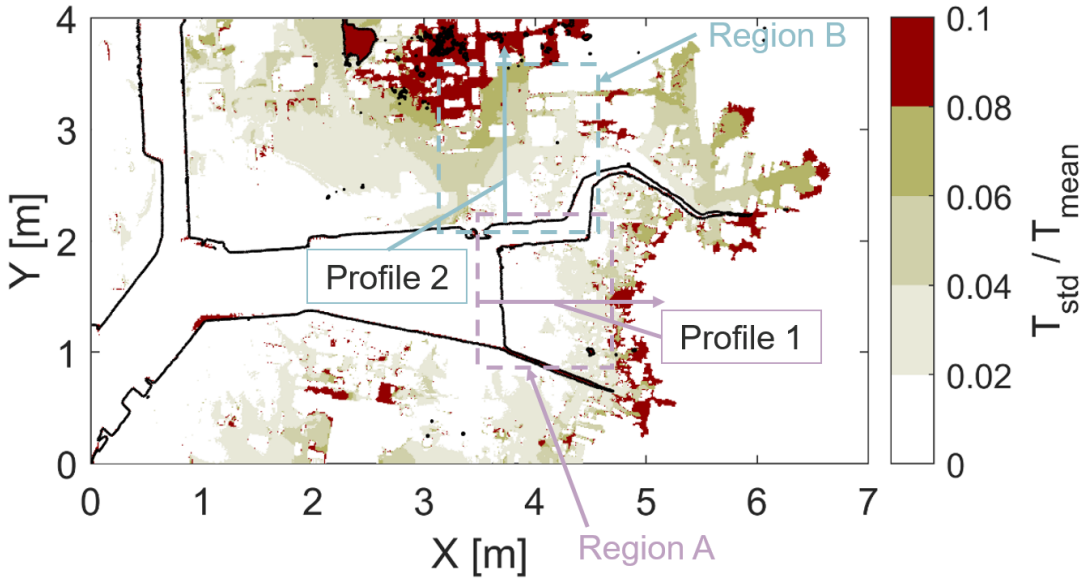

Figure 3.7: Spatial distribution of variation (ratio of model standard deviation to mean) of arrival time (black line shows shoreline).

in the middle nearshore area ($X = 3.8-4$ m and $Y = 1-2$ m), the mean value of velocity is 0.5 m/s (7.9 m/s at full scale) but more than 0.8 m/s (12.6 m/s at full scale) is also observed between the buildings. The large standard deviation of the velocity is also given in the road or small alley between buildings and approximately more than 0.3 m/s (4.74 m/s at full scale) is recorded in the middle nearshore area ($X = 3.8-4$ m and $Y = 1-2$ m). In addition, the nearshore north ($X = 1-2$ m and $Y = 2-2.5$ m) and south ($X = 1-2$ m and $Y = 1-1.2$ m) areas show large deviations similarly to the inundation depths (more than 0.35 m/s; 5.53 m/s in real scale). The inter-model variation, v, is 0.54, 0.17 and 0.33 on average in the nearshore middle, north and south, respectively.

Arrival time of the inundation front is important in tsunami inundation modeling for evacuation planning (e.g. Wang et al., 2016). Inundation front propagation is a complex function of the detailed numerical wetting and drying choices combined with implementation of convective momentum, surface gradients, building boundaries, and other aspects near the moving wet-dry front. The spatial distribution of inundation arrival time variation is shown in Fig. 3.7. Arrival time inter-model variations near the harbor and close to shorelines are uniformly small, with large areas showing $V < 0.04$. Inland, a larger variation is observed as the run-up distance is long and inundation depends not only on direct distance from the shoreline but also on potentially complex flow paths. For example, for Region A in Fig. 3.7, the dimensionless variation is $V < 0.02$ near the shoreline, while in Region B, the variation exceeds 0.04 around $X = 3.5$ m and $Y = 2.2$m even though the direct distance from the shoreline is short. This appears to be because inundation here comes overland from the west, and has already travelled a long distance over land.

To investigate the major factors causing differences in model inundation arrival times, wave front velocities from models and experiments are compared along a one-dimensional

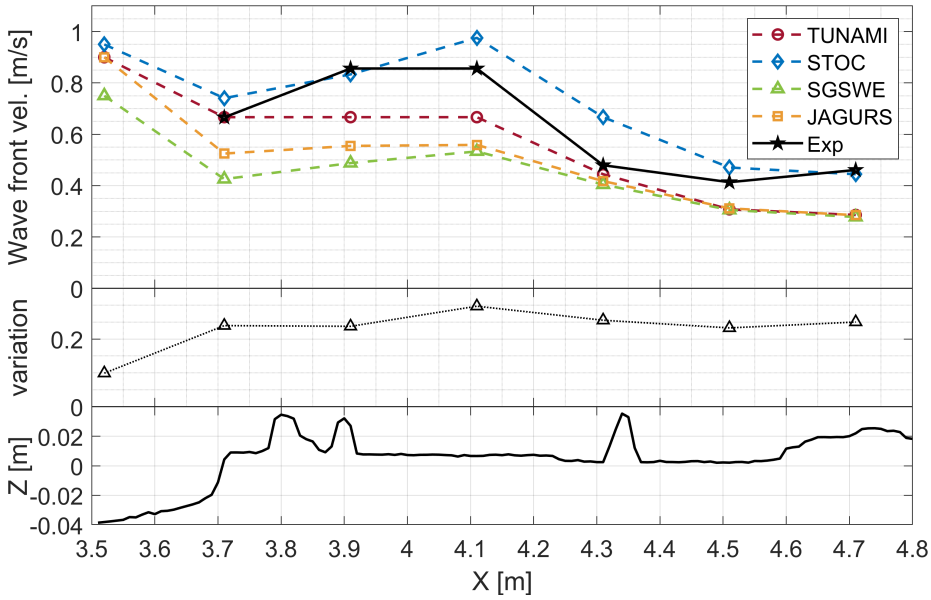

Figure 3.8: Wave front velocities by models (top), their variation (middle) and topographical change (bottom) at Profile 1 shown in Fig. 3.7; dashed lines show numerical results and black solid line shows experimental results.

transect. The inundation leading edge is detected at grid cell where the inundation depth changes from zero to any positive value. The wave front velocity is calculated as the ratio of the displacement of them to the time required. Figure 3.8 shows laboratory and model inundation front velocities along Profile 1 (shown in Fig. 3.7). Note that both sea and land are included in this transect. The results show that the difference of inundation front velocity among the four models is more than twice as large inland when compared to flow in the harbor. This inland speed variation is around 20 - 30% of the inter-model mean. The different models have very consistent tendencies: STOC gives the fastest speeds and TUNAMI, JAGURS and SGSWE follow in order. All the models show similar tendencies but STOC and TUNAMI give closest agreement with the experimental result. The inundation front velocity from STOC is closest to the experiment (within 15% error) in the plain area (e.g. $X = 3.9 - 4.1$ m) while TUNAMI is the most accurate around buildings ($X = 3.7 - 3.9$ m). These results show the blocking effect by buildings is well modeled by TUNAMI and the contraction flow is well modeled by the STOC. However, all models except STOC underestimate the wave front velocity behind the first group of buildings ($X = 3.9 - 4.3$ m) and the error ranges about 10% to 40%. Observed variations of the inundation front velocity are mainly caused by the variation of the fluid velocity in inundated areas which, along with maximum elevation variation, will be discussed in the next paragraph.

Maximum fluid velocities and surface elevations along Profiles 1 and 2 represent another road for comparison. Fig. 3.9 inter-compares model results for maximum surface elevations, and for maximum velocities while including PIV results from laboratory experiments. For

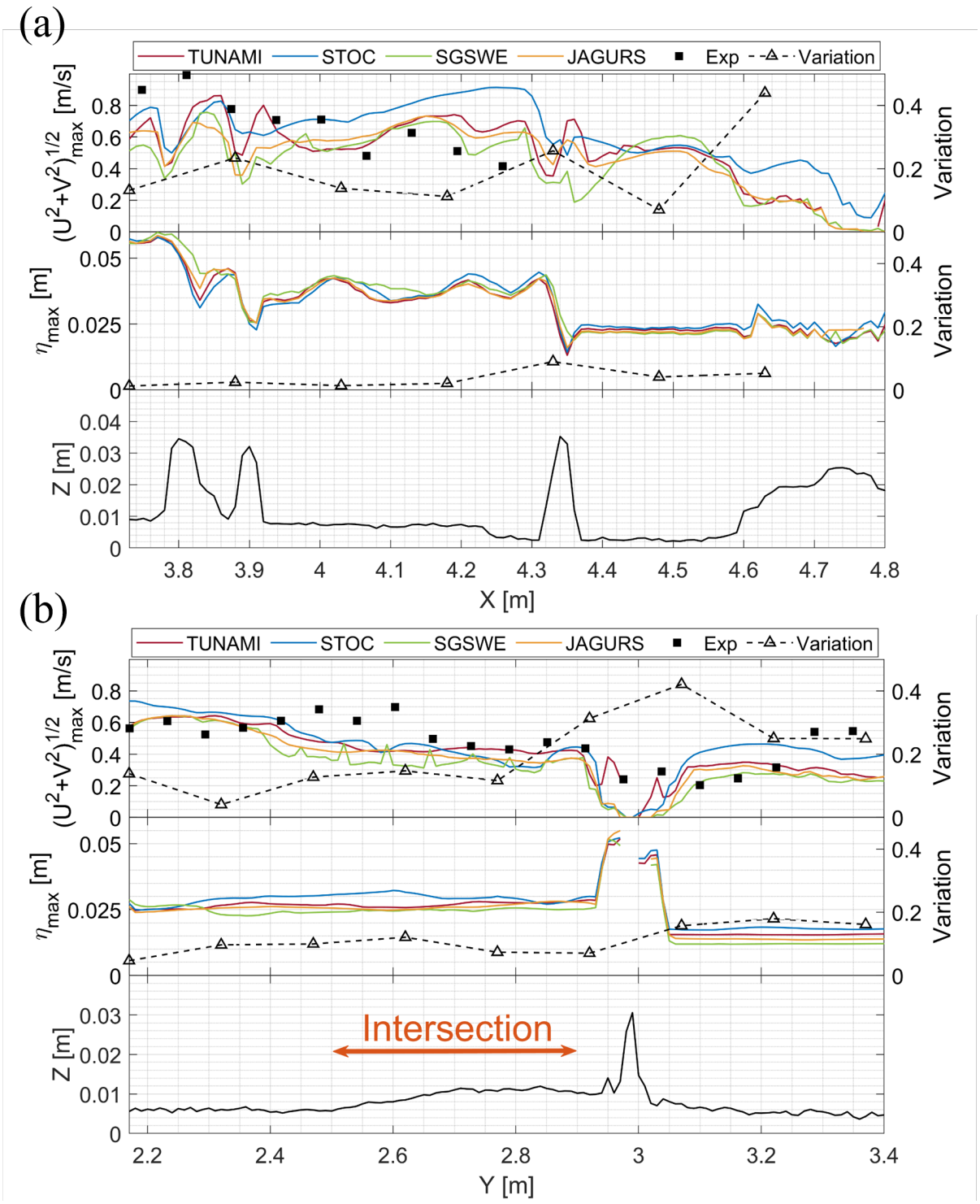

Figure 3.9: Maximum velocity magnitude (upper), surface elevation (middle), and topographical change (bottom) at Profiles 1 (middle part of city) and 2 (north part of city) shown in Fig. 3.7; solid line shows numerical results, black rectangle shows experimental results and black dashed line shows inter-model variation.

laboratory data, only high reliability (high particle density) PIV results were included. In Profile 1 (Fig. 3.9(a)), all model velocities show similar trends, with reasonably good agreement with the experiment and between each other. However, as with inundation front velocities, the magnitudes of maximum current velocities differ. The maximum current velocity modeled by STOC is the largest and TUNAMI, JAGURS and SGSWE follow in decreasing order as found for inundation front velocity. The inter-model variation of the maximum current velocity is more than twice as large as that of surface elevation. Furthermore, it is observed that the maximum current velocity variation is large around buildings. Specifically, the inter-model velocity variation is 0.50 at $X = 3.88$ m and 4.35 m where relatively large buildings are located. However, the author should be careful in ascribing significance to the large variation at $X = 4.63$ m since the velocity is much smaller than other areas. The source of the velocity difference will be examined in the Discussions section.

The inter-model comparison in Profile 2 is shown in Fig. 3.9(b). Note that both maximum current velocity and surface elevation are similar in each model but model velocity magnitudes follow the same trends as in Profile 1. There are two characteristic areas to be discussed: a road intersection at $X = 2.5 - 2.9$ m, and a building area at $X = 3.0$ m. In particular, the intersection shows different characteristics than other locations. Here, the maximum current velocity variation is 0.18 and larger differences from experimental results are observed. Note that the variation of maximum current velocity is similar between the intersection ($X = 2.5 - 2.9$m) and shoreline ($X = 2.2$ m) but each model gives quite different values at the intersection while all models except STOC are quite close to each other and to measured values at the shoreline. Once again, the variation for maximum surface elevation is smaller than that for maximum current velocity. However, the velocity variation is still larger than Profile 1 even though the number of buildings is smaller. One of the reasons is that flow here comes from two directions, and flow at the intersection from the west direction blocks the flow from the south direction. The results above show that the maximum current velocity is quite sensitive to the model used. Possible reasons for such variation of this and other properties will be considered in the Discussions section.

Next, the author examines spatio-temporal uncertainty focusing on the leading edge of inundation. Figure 3.10 shows a time series of inundation leading edge every 0.2 s from the start of the inundation in Region A. Note that time steps shown on the title represent the elapsed time from the wave arrival at the shoreline. Little difference in inundation leading edge is observed before the arrival at the first group of buildings X (shown in Fig. 3.10 by orange box). However, the difference gradually increases after passing buildings X. The STOC and TUNAMI models are closer to the experiment than the SGSWE and JAGURS. After passing the second group of buildings Y (yellow box in Fig. 3.10), leading edges from STOC and the experiment are furthest while the ones by other models are underestimated. At the final snapshot (1.0 s), differences between models are maximum and the leading edge of the inundation front varies from 4.2 - 4.4 m. The STOC model shows the fastest inundation, with laboratory experiments, TUNAMI, JAGURS and SGSWE following in decreasing order, consistent with previous analyses. The same analysis was performed in Region B and a smaller variation of the inundation leading edge is observed (not shown). Such difference depends on the cross-shore velocity, and will be discussed in detail later.

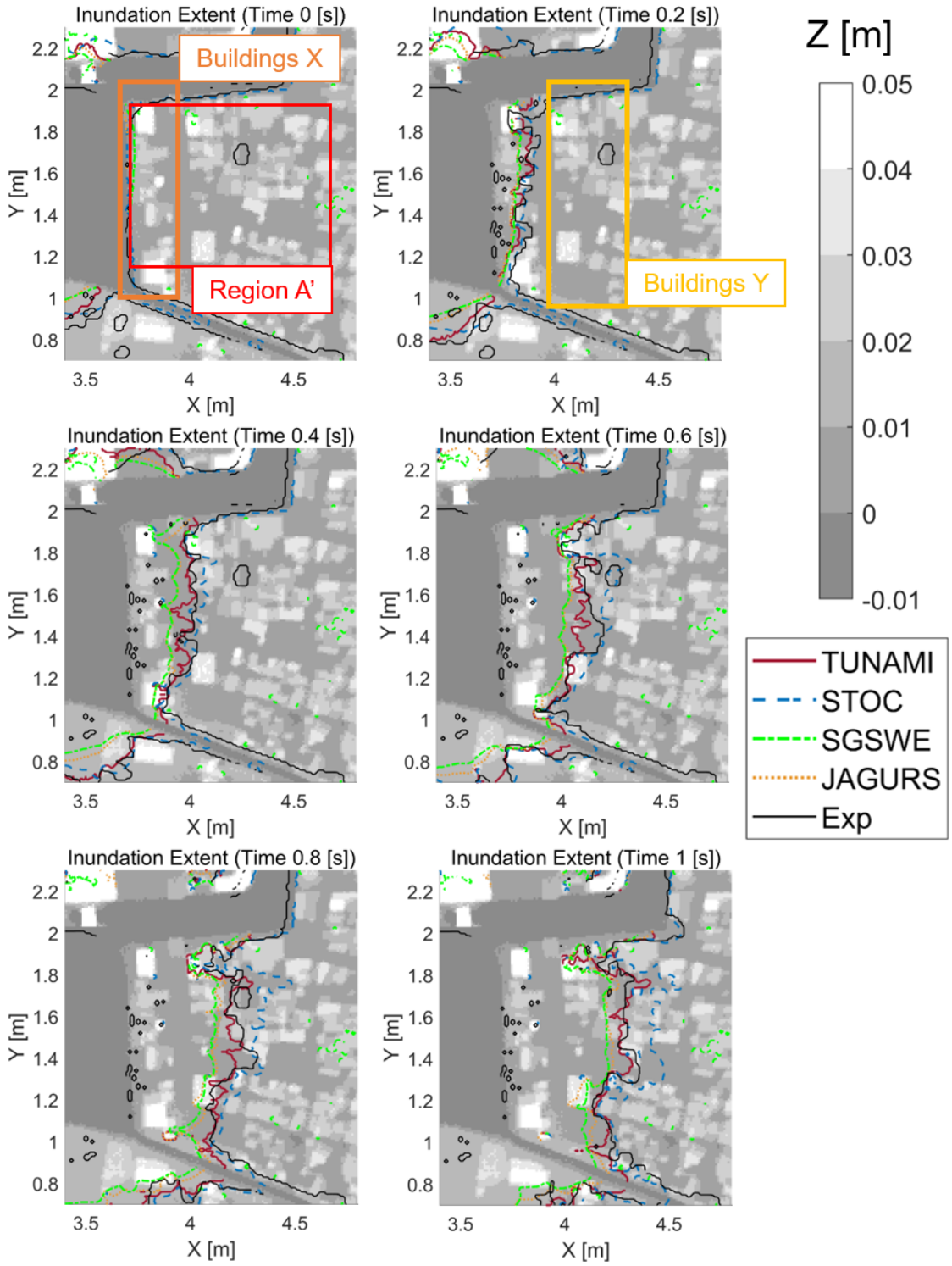

Figure 3.10: Inundation leading edge (color corresponds to Fig. 3.3) in time series at Region A shown in Fig. 3.7 from the starting time of inundation (a: 0 s, b: 0.2 s, c: 0.4 s, d: 0.6 s, e: 0.8 s, and f: 1.0 s after starting inundation); colored boxes show groups of buildings X and Y where flow arrives first and second, respectively.

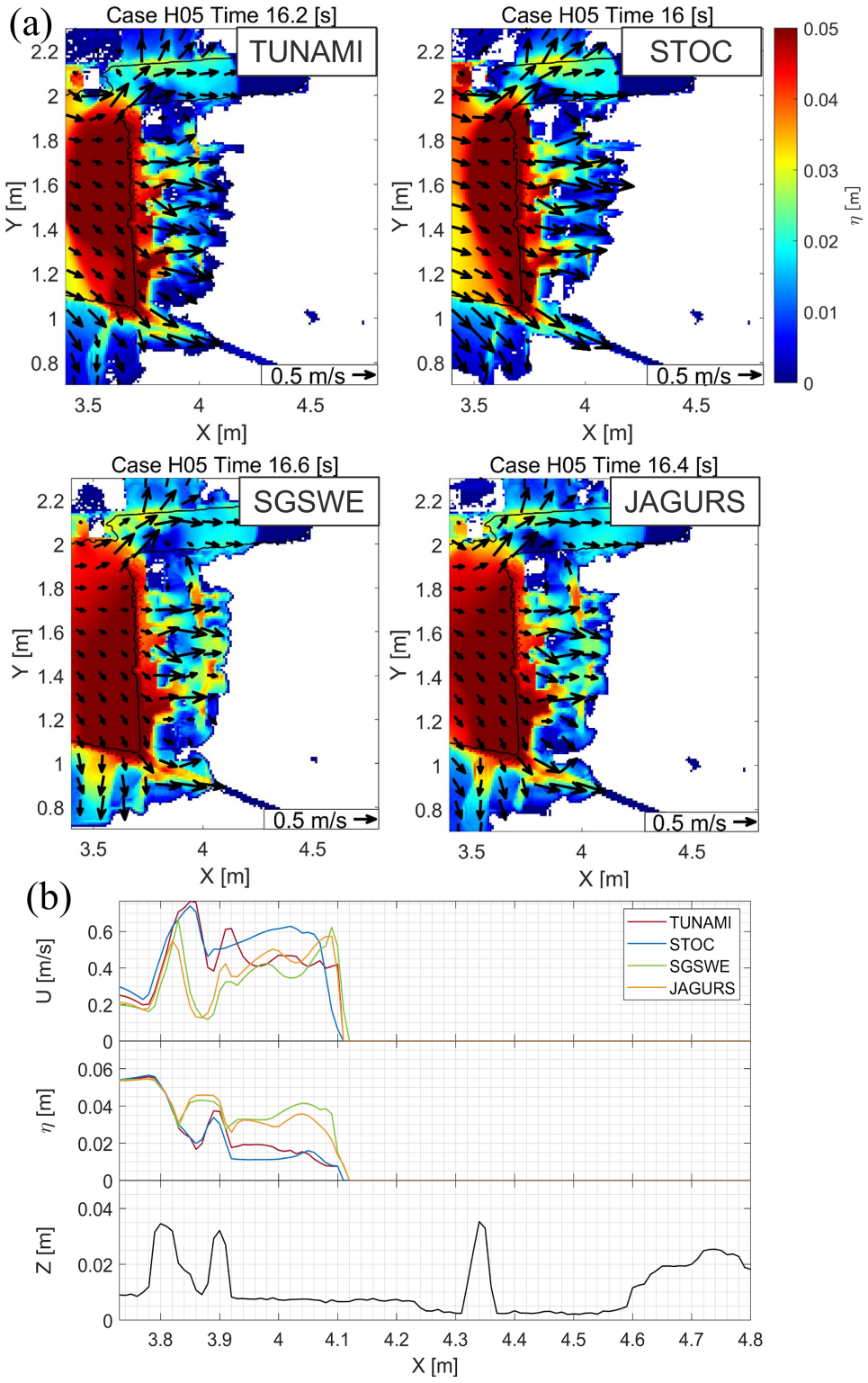

Figure 3.11: Model difference of snapshot of inundation process in Region A when modeled flow arrives at Buildings Y; (a) Snapshot of surface elevation and current (top left: TUNAMI, top right: STOC, bottom left: SGSWE and bottom right: JAGURS) and (b) Cross-sectional change of cross-shore velocity (top) and surface elevation (middle) and topographic change (bottom) along Profile 1 shown in Fig. 3.7 (color corresponds to Fig. 3.3).

To investigate the inter-model differences of the inundation process in detail, the spatio-temporal change of the surface elevation and velocity in the model are shown in Fig. 3.11. Fig. 3.11(a) shows the snapshots of the surface elevation and velocity in Region A when the modeled inundation leading edge arrives at the second group of buildings Y given by the yellow box in Fig. 3.10(a). These arrival times are different in each model and reflect differences in inundation velocities. The results of TUNAMI and STOC show similar tendencies for surface elevation: the total inundation area with depths greater than 0.01 m is smaller for these models than for SGSWE and JAGURS. The local variations of surface height along the buildings and channels differ model by model. Fig. 3.11(b) shows cross sections of the cross-shore velocity and surface elevation at the same time as Fig. 3.11(a) along Profile 1. The cross-shore velocity is also divided into the same groups as Fig. 3.11(a). The values near the first group of buildings are close to each other between the TUNAMI and STOC models, and their difference is within 5%. However, STOC gives about 30% larger cross-shore velocity near the inundation leading edge ($X = 4.0 - 4.1$ m) than TUNAMI. STOC tends to give large velocity in small areas surrounded by buildings such as roads. The SGSWE and JAGURS are close to each other in the whole area along Profile 1 and their difference is within 10%. Also, the cross-shore velocities modeled by the SGSWE and JAGURS are smaller than the TUNAMI and STOC around the first group of buildings. For the surface elevation, patterns for each model are more visible. TUNAMI and STOC show a gentle slope of surface elevation near the leading edge ($X = 4.0 - 4.1$ m) while SGSWE and JAGURS show steeper slopes. There is about 55% difference in the surface elevation between the two groups.

Finally, the author examines spatial-temporal uncertainty focusing on the inundation for merging flow. Fig. 3.12 shows the difference of the merging flow at the intersection in Region B. Times are different for each model, and were chosen so that in each model the inundation leading edge arrives at the north side of the intersection as flow merges. Note that the surface elevation at velocity when the two flows from south and east direction merge are shown. There is a noticeable difference of velocity and surface elevation between the models especially around the intersection (marked with red circle). For example, the TUNAMI and STOC give around 0.023 m surface elevation while the SGSWE and JAGURS give around 0.015 m. The current velocity and direction also differ. TUNAMI and JAGURS show flow in the north direction but not STOC. SGSWE also shows north direction flow but some velocity direction is different (northwest direction). The major flow direction is determined by the blocking effect by the flow from the west direction. Larger current velocity from the west direction gives a larger blocking effect for the flow from the south direction.The larger blocking effect leads to local amplification of surface elevation. A series of the differences of inundation process is mainly due to the arrival time of the flow from the west direction since the variation is at least 1.5 times larger than that from the south direction. Such inter-model variations of the arrival time give the difference of momentum fluxes transported from the west direction and strength of the blocking effect. Factors of the variation of the detailed inundation process with a series of analyses will be shown in the Discussions.

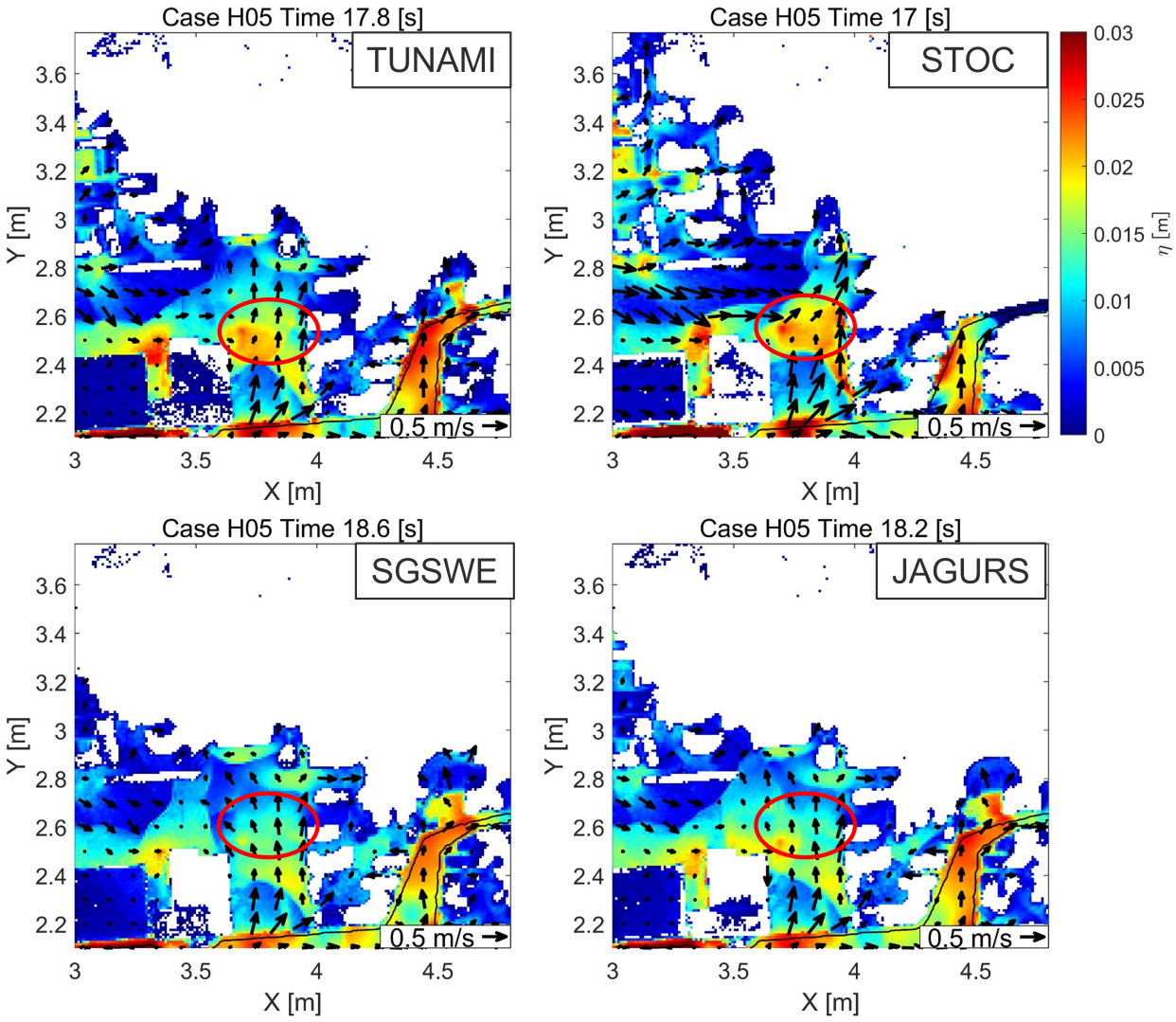

Figure 3.12: Model difference of the snapshots of surface elevation and current velocity in Region B shown in Fig. 3.7 when the flows from both South and West directions merge (top left: TUNAMI, top right: STOC, bottom left: SGSWE and bottom right: JAGURS).

3.4 Discussions

The author here investigates the reproducibility of the tsunami inundation experiments using four different numerical models. It is clear that all numerical models can reproduce the inundation process overall but the detailed local behavior of hydrodynamic quantities such as surface elevation at intersections or velocity around buildings vary between models. Here, the source of the differences in numerical models and results is discussed in detail based on the inter-model comparison. There are four main factors causing the variation in numerical results among the four models: 1) differences in advection term and temporal discretization, 2) bottom friction term discretization, and 3) wet/dry boundary conditions, and 4) differences in formulations of governing equations (velocity, depth-integrated form, subgrid, conservative or non-conservative form). Fundamental discretization schemes for bottom friction and advection terms are similar between each model but there are differences of detailed treatments. It is not clear how such differences affect the variations of inundation processes but this is one of the main reasons of presented variation of numerical results.

A small variation of velocity and surface elevation is observed in the offshore area away from the port and only SGSWE showed slightly slower propagation speed. Here, the effect of the friction term is minor for tsunami propagation offshore since the effect of advection term is small in the offshore area. Differences here probably results from the backward Euler time-stepping in SGSWE vs the leapfrog scheme in the other models. However, the velocity variations between models are much larger on inundated land regions. Focusing on the area scale, the inter-model variation in inundation leading edge in Region B is smaller than Region A. Such differences in the inundation leading edge in each region depend on the cross-shore velocity. The major flow direction in Region A is the same as in offshore (east direction) while the flow direction in Region B is perpendicular to the one in offshore (north direction). Therefore, the cross-shore velocity at the shoreline is larger in Region A than Region B and it indicates that the larger velocity gives the larger variation.

This tendency might be explained by the differences of advection terms and wet/dry boundary condition considering the effect of the friction term is minor based on the discussion in the previous paragraph. A major source is the difference of advection term since magnitudes are proportional to the square of the current velocity and it is relatively larger when the current velocity is larger. The wet/dry boundary condition also contributes to the variation. The same wet/dry conditions (Kotani et al., 1998) are used in the TUNAMI, STOC and JAGURS but the detailed treatment in source codes is different in each model even though the scheme used is the same. For instance, the application phase of the wet/dry condition is different. TUNAMI and JAGURS apply the wet/dry condition before computation of discharge while STOC does it after computation of velocity in whole the domain.

The effects of tolerance water depth for wet/dry on inundation by the numerical models is small compared to the tsunami scale, as the detailed differences of the wet/dry boundary scheme in their source codes give large variation of the surface elevation and wave front velocity. Such differences in surface elevation give variation of the current velocity since the

Table 3.2: Summary of calibrated coefficient (λ and ξ) for each empirical fragility model

	λ	ξ
EF1	1.58	0.41
EF2	1.73	0.42

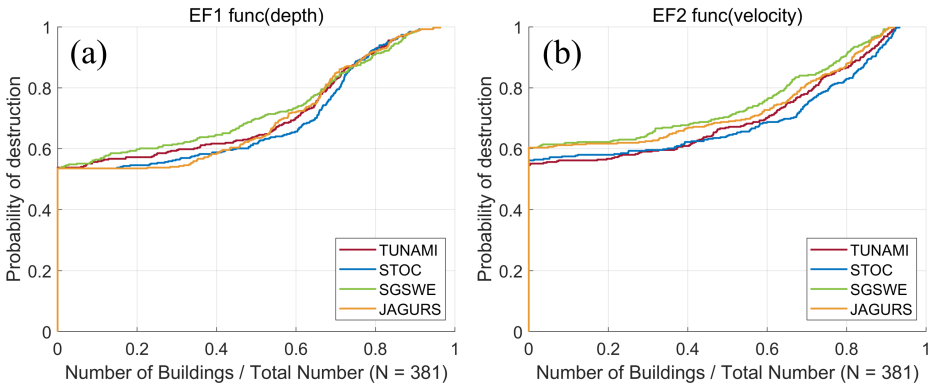

Figure 3.13: Predicted probability of building destruction by different models and building ratio out of 381 buildings in total corresponding below a certain probability by two empirical fragility functions (a: EF1 using inundation depth and b: EF2 using fluid velocity; color shows model differences and corresponds to Fig. 3.3).

current velocity arises from the gradient of surface elevation. Once the velocity variation occurs, the advection term evaluation gives large variation since the advection term is proportional to the square of the velocity. However, a detailed mechanism is not clearly shown and further investigation using simpler topography such as uniform slope is needed. Finally, the velocity difference gives the variations of wave front velocity and arrival time.

Moreover, it is also important that the arrival time difference gives a further difference in the local inundation process. Region B is a good example for indicating this point. Two flows in the west and south directions merge at the intersection in Region B. Arrival of the flow from the south direction does not vary due to the small cross-shore velocity explained above but the one from the west direction is quite different between each model since the cross-shore velocity has the same direction as the main flow. The discrepancy of the merge time creates the local difference of surface distribution and current velocity. The earlier arrival time gives a large blocking effect by the flow from the west direction to the one from the south direction, which the large surface elevation around the intersection is calculated as explained in Section 3.3.2. Based on the discussions presented in the previous paragraph, the detailed differences of treatment of the advection term and wet/dry boundary condition give variation of the current velocity on the land and the errors between each model are accumulated as the run-up distance is longer due to the iteration process for solving the advection term using the current velocity in previous time step. Moreover, abrupt topographic changes such as buildings also enlarge the variation of the surface elevation and current velocity.

The variations in the maximum inundation depths and fluid velocities observed in the

inter-model comparison also affect the building damage fragility assessment calculated from these tsunami intensity factors. Here, the sensitivity analysis to the variations of these two intensities is given using fragility models by Hayashi et al. (2013). The fragility model calculates the probability of destruction using either maximum inundation depth or maximum fluid velocity, and was developed using linear regression combined with results of numerical modeling for the validation of the tsunami front and flow velocities in the 2011 Tohoku Earthquake Tsunami. (Other literature on this topic are exemplified in Suppasri et al., 2013, Charvet et al., 2015, etc.). The probability of the destruction $P_D(x)$ is found by

$$P_D(x) = \Phi\left[\frac{\ln x - \lambda}{\xi}\right] \tag{3.4}$$

where Φ represents the standardized normal distribution function, and x stands for the tsunami intensity measure (e.g. maximum inundation depth or fluid velocity), λ and ξ represent calibrated coefficients for each intensity measure (each value is shown in Table 3.2). Hayashi et al. (2013) assumed three different structure types are assumed: RC, steel and wooden; steel is assumed in this comparison since no detailed data about the structures in Kainan is available. The functions using only maximum inundation depth and fluid velocity are denoted as EF1 and EF2, respectively. The tsunami intensity measures at the grid points around the buildings are collected and averaged. After that, the probability of the destruction for each building using the collected intensity measures was calculated following Eq. 3.4. Then, the number of buildings below a specific probability of the destruction was calculated. Fig. 3.13 shows the model variations of the probabilities of building destruction for each different model. Both EF1 (depth) and EF2 (velocity) show inter-model fragility variations to some extent. However, EF2 gives larger differences especially when the probability of destruction is high (more than 0.6). Meanwhile, EF1 shows somewhat smaller inter-model variation for each building v_b, particularly for high probabilities of damage. Note that v_b is calculated by the following formula:

$$v_b = \frac{\sqrt{\frac{1}{N_b}\frac{1}{N_{\mathrm{model}}}\sum_{j=1}^{N_{\mathrm{model}}}\sum_{i=1}^{N_b}(P_{D,i,j} - P_{D,i,\mathrm{mean}})^2}}{P_{D,\mathrm{all-mean}}} \tag{3.5}$$

where N_b (= 381) is the number of buildings, N_{model} (= 4) is the number of SWE models, $P_{D,i,j}$ denotes the probability of the destruction for the i-th building estimated by the j-th SWE model, and $P_{D,\mathrm{all-mean}}$ denotes the arithmetic average of the probability for all SWE models and buildings. For overall predictions, the EF1 model shows inter-model variation in damage state probability $v_b = 0.16$, compared to $v_b = 0.20$ for the EF2 model. The results above indicate that inter-model variation leads to significant differences in predicted damage and higher sensitivity of the fragility is given by the fluid velocity than the inundation depth.

Furthermore, the scaling effect including surface tension and friction is assessed using

Table 3.3: Summary of values to calculate dimensionless quantities (Bo, We, Re, and Fr)

	Name	Value
g	Gravitational acceleration	9.81 m/s^2
ρ	Water density	1000 kg/m^3
ρ_a	Air density	1.29 kg/m^3
$\Delta\rho$	Difference of density	1000 kg/m^3
L	Characteristic length	0.05 m (average building width in physical model)
U	Characteristic velocity	Average value of maximum velocity in Region A'
γ	Surface tension	0.0728 N/m
ν	Kinematic viscosity	10^{-6} m^2/s

Table 3.4: Summary of the calculated dimensionless quantities (Bo, We, Re, and Fr); upper and lower numbers show values at experimental and full scale, respectively

	TUNAMI	STOC	SGSWE	JAGURS	Exp.
Bo	336.45	336.45	336.45	336.45	336.45
	2.10×10^7	2.10×10^7	2.10×10^7	2.10×10^7	2.10×10^7
We	170.08	275.79	128.29	153.49	198.45
	1.11×10^7	1.72×10^7	0.96×10^7	0.80×10^7	1.24×10^7
Re	22504	29264	19304	21687	22992
	8.90×10^7	1.16×10^7	7.63×10^7	8.57×10^7	9.09×10^7
Fr	0.64	0.84	0.55	0.62	0.66
	0.64	0.84	0.55	0.62	0.66

dimensionless quantities, Bo, We, Re, and Fr, which are defined as follows;

$$Bo = \frac{\Delta \rho g L^2}{\gamma} \tag{3.6}$$

$$We = \frac{\rho U^2 L}{\gamma} \tag{3.7}$$

$$Re = \frac{UL}{\nu} \tag{3.8}$$

$$Fr = \frac{U}{\sqrt{gL}} \tag{3.9}$$

where each variable and its value are summarized in Table 3.3. The calculated dimensionless quantities in Region A' (shown in Fig. 3.10(a) by red box) are summarized in Table 3.4. Note that the values of Fr do not change between experimental and full scale since the experiment follows the Froude similitude. Bo and We related to surface tension are approximately $O(10^2)$, which indicates that the contribution of the surface tension to the gravity and inertial forces may be still small though there is large difference between experimental and full scales. The experimental and numerical results showed approximately $O(10^4)$ and $O(10^7)$ for Re, respectively. Then, the contribution of the viscosity to the inertial force is still negligible. Indeed, the drag coefficient for a circular cylinder, C_D, is approximately 1.0 and 0.75 in the case of $Re = O(10^4)$ and $O(10^7)$, respectively (e.g. Roshko, 1961). Therefore, the range of resistance force differences by buildings between the experimental and full scales is within 25%.

In summary, overall characteristics of inundation processes such as the inundation depth, surface elevation and current velocity can be modeled by presented multi-model inundation simulation. However, a range of the variation of detailed inundation process exemplified by merging, blocking and so on specifically in city areas such as buildings, bridges and intersections still remains. The author believes that uncertainty of the simulated results by model difference needs to be considered if the numerical simulation of urban inundation is performed since such inter-model variation of inundation depth or velocity gives significant differences in building fragility assessment. Moreover, the scaling effect induced by surface tension and etc. on the magnitude of the surface elevation and fluid velocity can be still small for this experimental case though there are large difference of dimensionless quantities between experimental and full scale. However, the further study about quantifying scaling effect is still recommended.

3.5 Summary of Chapter 3

This study conducted physical and numerical modeling of tsunami inundation in a 3D complex coastal city model including ports and buildings. Experiments used tsunami conditions of a solitary wave by piston type wave maker, and constant flow and realistic long period tsunami waveforms by pump. Time series of tsunami wave height were measured by 12 wave gauges covering the flume from offshore to onshore and over the city model. Tsunami inundation propagation on the land was recorded by an overhead 4K video camera. Fluorescent dye was used to detect the leading edge of inundation. PIV was applied to measure the spatial flow pattern and velocity field were obtained. This study

also ran and compared numerical simulations among four different models based on various forms (depth-integrated, velocity-form, or subgrid-averaged) and numerical schemes of the nonlinear shallow water equations. The sensitivity of tsunami inundation simulations in urban areas has been discussed by comparing the simulations with the physical experiment results for the case of solitary wave condition. The summary of Chapter 3 is as follows;

a) Overall characteristics of inundation processes such as the inundation depth, surface elevation and current velocity could be modeled by presented multi-model inundation simulation. All models can reproduce the inundation process overall but the detailed local processes such as surface elevation at intersection or velocity around buildings vary in each model.

b) The variation of results was confirmed in detailed inundation process as exemplified by merging, blocking and so on specifically in city areas such as buildings, bridges and intersections.

c) Fundamental discretization schemes for bottom friction and advection terms are the same between each model but there are differences of detailed treatments on their coding. Difference in surface elevation gives variation of the current velocity since the current velocity is gradient of the surface elevation. Once the velocity variation occurs, the advection term evaluation gives large variation since the advection term is proportional to the square of the velocity. Considering that the tolerance water depth for wet/dry is small compared to the tsunami scale, the detailed differences of the wet/dry boundary scheme in their source codes give large variation of the surface elevation and wave front velocity.

d) The arrival time difference gives a further difference in the local inundation process. The detailed differences of treatment of the advection term and wet/dry boundary condition give variation of the current velocity on the land and the errors between each model are accumulated as the run-up distance is longer due to the iteration process for solving the advection term using the current velocity in previous time step. Artificial topographic changes such as buildings also enlarge the variation of surface elevation and current velocity.

e) Chapter 3 confirmed the importance of considering uncertainty of the modeled results due to model difference in tsunami inundation simulation targeting coastal urban areas. The results indicate that inter-model variation leads to significant differences in predicted damage and the use of velocities to compute fragility has higher sensitivity to model implementation than using inundation depth.

Chapter 4

Subgrid-scale Modeling of Tsunami Inundation Over Coastal City

4.1 Introduction

A series of the multi-model building-resolving inundation simulation using four different 2D-SWE models in Chapter 3 showed the 2D-SWE model could reproduce the inundation process overall but the detailed local processes such as surface elevation at intersection or velocity around buildings varied in each model. The shown results confirmed the importance of multi-model ensemble simulation even for building-resolving inundation simulations. Hereafter, the author defines such building-resolving approach used in Chapter 3 as structure resolving model (SRM). The SRM using 2D-SWE still needs finer resolution less then the order of 10 m, while the practical approach using bare-earth topography uses the order of 100 m resolution. The ensemble inundation simulation using the SRM focusing on a specific region and scenario is feasible since the number of ensembles is small. However, a practical tsunami simulation that allows the coarser spatial resolution (e.g., 30 m) is still required as an alternative to the SRM when numerous ensemble cases are needed, as in probabilistic tsunami hazard assessments (e.g., Mueller et al., 2015; Goda et al., 2015; Miyashita et al., 2020), because the use of high-speed computers such as supercomputers is limited.

Several treatments of built-up areas as subgrid-scale (SGS) models have been proposed to overcome this computational cost issue. For instance, Aburaya and Imamura (2002) and Imai et al. (2013) proposed a combined equivalent roughness model (CERM) using the bottom friction calculated according to the building width and building coverage in a computational grid, in which drag force acting on a building was determined using the Morison's equation. Adriano et al. (2016) examined the CERM by performing a tsunami simulation at a 5 m resolution for Onagawa in the case of the 2011 Tohoku tsunami and compared simulation data obtained using a building-resolved digital surface model (i.e., SRM) with the survey data. The CERM achieved similar performance to the SRM in terms of reproducing the interpreted flow depths, but a slight delay in arrival time was observed.

On the other hand, the use of drag force models (DFMs) of built-up areas was proposed (e.g., Oishi et al., 2016; Fukui et al., 2019). Buildings were assumed to be the resistance element with the drag force acting on buildings in the DFM. Oishi et al. (2016) examined the DFM at 5 m resolution by comparing it with the SRM at 0.556 m resolution using a supercomputer for the estuary of the Hei River, Iwate Prefecture in the Tohoku case. They showed that an optimal calibration of drag coefficients would minimize the errors in the arrival time of the leading edge between the SRM and DFM. Fukui et al. (2019) conducted tsunami simulations using the DFM in a physical inundation experiment of Onagawa by Prasetyo et al. (2019) as a benchmark problem. In that study, the drag coefficient was assumed to be an exponential function of the Reynolds number Re, and the importance of its adequate calibration was confirmed, as in Oishi et al. (2016). However, there remained uncertainty in the modeled inundation process associated with the grid size; in the DFM, it was assumed that only one building exists in the grid cell, ignoring the spatial layout of the building. Therefore, consideration of detailed topographical properties and careful evaluation of inundation characteristics are required.

Chapter 4 aims to improve the grid size dependency by modifying the DFM and to investigate the error characteristics between the modified DFM and high-resolution (HR) tsunami inundation simulation using the SRM. The modified DFM incorporates spatial information about multiple structures, which has not been considered in previous studies. To evaluate the effectiveness of the SGS models, inundation depth, arrival time, and inundation limit using complex urban topography has been mainly discussed in previous studies. This study examines the fluid velocity, which is directly affected by SGS model implementation, as well as inundation depth and inundation limit, starting from the simple urban topography to more complex one. This work is organized as follows. Section 4.2 presents the modified DFM to reduce the grid size dependency. In Section 4.3, an idealized numerical experiment using simple topography and building data is performed to examine the detailed inundation process, whereas Section 4.4 presents a numerical experiment using the SRM for Onagawa in the 2011 Tohoku case. Section 4.5 presents discussions about the similarity and difference of model performance focusing on velocity reduction effect by buildings, and further improvement of the presented model. Finally, conclusions are presented in Section 4.6.

4.2 individual Drag Force Model (iDFM)

4.2.1 Governing equations and urban roughness formulations

The 2D-SWE in Eqs. (4.1-4.2) are typically used for tsunami inundation simulation and the authors use the numerical code TUNAMI-N2 (Goto et al., 1997) based on NSWEs:

$$\frac{\partial \eta}{\partial t} + \frac{\partial M}{\partial x} + \frac{\partial N}{\partial y} = 0 \tag{4.1}$$

$$\frac{\partial M}{\partial t} + \frac{\partial}{\partial x}\left(\frac{M^2}{D}\right) + \frac{\partial}{\partial y}\left(\frac{MN}{D}\right) = -gD\frac{\partial \eta}{\partial x} - R_x \tag{4.2}$$

$$\frac{\partial N}{\partial t} + \frac{\partial}{\partial x}\left(\frac{MN}{D}\right) + \frac{\partial}{\partial y}\left(\frac{N^2}{D}\right) = -gD\frac{\partial \eta}{\partial y} - R_y \tag{4.3}$$

where, t is the time; η is the sea surface elevation; M and N are the components of the depth-integrated velocity in the x- and y-directions, respectively; g is the gravitational acceleration; h is the still water depth; D is the total water depth ($= \eta + h$); and R_x and R_y are the representative resistance forces in the x- and y-directions, respectively, due to roughness and topographical changes, such as Manning ' s coefficient n corresponding to land usage (e.g., Kotani et al., 1998; Kaiser et al., 2013):

$$R_x = \frac{gn^2 M\sqrt{M^2+N^2}}{D^{7/3}} \tag{4.4}$$

$$R_y = \frac{gn^2 N\sqrt{M^2+N^2}}{D^{7/3}} \tag{4.5}$$

In DFMs, resistances by artificial structures are considered in the drag force term, and R_x and R_y are rewritten as

$$R_x = \frac{gn^2 M\sqrt{M^2+N^2}}{D^{7/3}} + \frac{F_D^x}{\rho} \tag{4.6}$$

$$R_x = \frac{gn^2 N\sqrt{M^2+N^2}}{D^{7/3}} + \frac{F_D^y}{\rho} \tag{4.7}$$

The iDFM is an SGS model that calculates the drag force acting on multiple structures in a computational grid cell and feeds it back to the mean flow field. The drag force is calculated as the sum of the forces applied to individual structures and is given by Eqs. (4.8) and (4.9):

$$\frac{F_D^x}{\rho} = \sum_{k=1}^{N_b} \frac{1}{2} C_D A_{x,k} M \frac{\sqrt{M^2+N^2}}{D^2} \frac{d}{D} \frac{1}{\Delta x \Delta y} \tag{4.8}$$

$$\frac{F_D^y}{\rho} = \sum_{k=1}^{N_b} \frac{1}{2} C_D A_{y,k} N \frac{\sqrt{M^2+N^2}}{D^2} \frac{d}{D} \frac{1}{\Delta x \Delta y} \tag{4.9}$$

where N_b is the number of buildings in a computational grid cell;$A_{x,k}$ and $A_{y,k}$ denote the projected areas of individual (k-th) structures out of N_b in a computational grid cell in the x- and y-directions, respectively; Δx and Δy are the spatial grid sizes in the x- and y-directions, respectively; $C_D = f(Re, \mathbf{l}, S_f)$ is the drag coefficient; $\mathbf{l}$ is the characteristic length of the obstacle in the SGS; and S_f is the coefficient representing the building shape. Because it is difficult to implement the effect of S_f it is not implemented in this study. The inundation state (i.e., fully submerged or partially submerged) is incorporated by the effective depth d, representing the water depth of the area on which the drag force acts. d is given by:

$$d = \begin{cases} h & (D \geq h_{b,k}) \\ D & (D < h_{b,k}) \end{cases} \tag{4.10}$$

Originally, the sum of the drag forces needs to be calculated from individual structural information (i.e., $A_{x,k}$, $A_{y,k}$, and $h_{b,k}$). However, this approach is not practical when the number of structures is large. Therefore, the iDFM model adopts the grid-averaged values

for the projected areas and characteristic building heights, which are given by:

$$\bar{A}_x = \frac{1}{N_b}\sum_{k=1}^{N_b} A_{x,k} \tag{4.11}$$

$$\bar{A}_y = \frac{1}{N_b}\sum_{k=1}^{N_b} A_{y,k} \tag{4.12}$$

$$\bar{h}_b = \frac{1}{N_b}\sum_{k=1}^{N_b} h_b \tag{4.13}$$

Using Eqs. (4.11-4.13), Eqs. (4.8-4.10) can be approximated as

$$\frac{F_D^x}{\rho} = N_b \times \frac{1}{2} C_D \bar{A}_x M \frac{\sqrt{M^2+N^2}}{D^2}\frac{d}{D}\frac{1}{\Delta x \Delta y} \tag{4.14}$$

$$\frac{F_D^y}{\rho} = N_b \times \frac{1}{2} C_D \bar{A}_y N \frac{\sqrt{M^2+N^2}}{D^2}\frac{d}{D}\frac{1}{\Delta x \Delta y} \tag{4.15}$$

$$d = \begin{cases} \bar{h}_b & (D \geq \bar{h}_b) \\ D & (D < \bar{h}_b) \end{cases} \tag{4.16}$$

$\bar{A}_x$, $\bar{A}_y$, $\bar{h}_b$, and $\bar{N}_b$ are called SGS parameters in this report, and the next section presents the calculation process using HR building shape data.

4.2.2 Calculation process of subgrid-scale parameters

The SGS parameters are calculated according to the following procedures, which are depicted in Fig. 4.1(a).

1. Acquisition of HR building shape data
2. Calculation of h_b, A_x, and A_y for the individual buildings
3. Counting of the number of individual buildings N_b in a computational grid cell
4. Averaging of the individual h_b, A_x, and A_y values in a computational grid cell

The first step entails obtaining building shape data (3D coordinates of the building vertices) that are processed using 3D data or HR digital surface model that includes building height data in the topography. The second step involves calculating h_b, A_x, and A_y from the obtained building shape data. h_b and widths in the x- and y-directions, k_x and k_y, respectively (see the upper part of Fig. 4.1(b)), are given by

$$h_b = \max(z_v) - \min(z_v) \tag{4.17}$$

$$k_x = \max(x_v) - \min(x_v) \tag{4.18}$$

$$k_y = \max(y_v) - \min(y_v) \tag{4.19}$$

where x_v, y_v, and z_v denote the 3D Cartesian coordinates of the building vertices and $\max(\cdot)$ and $\min(\cdot)$ are the maximum and minimum values, respectively. Note that the

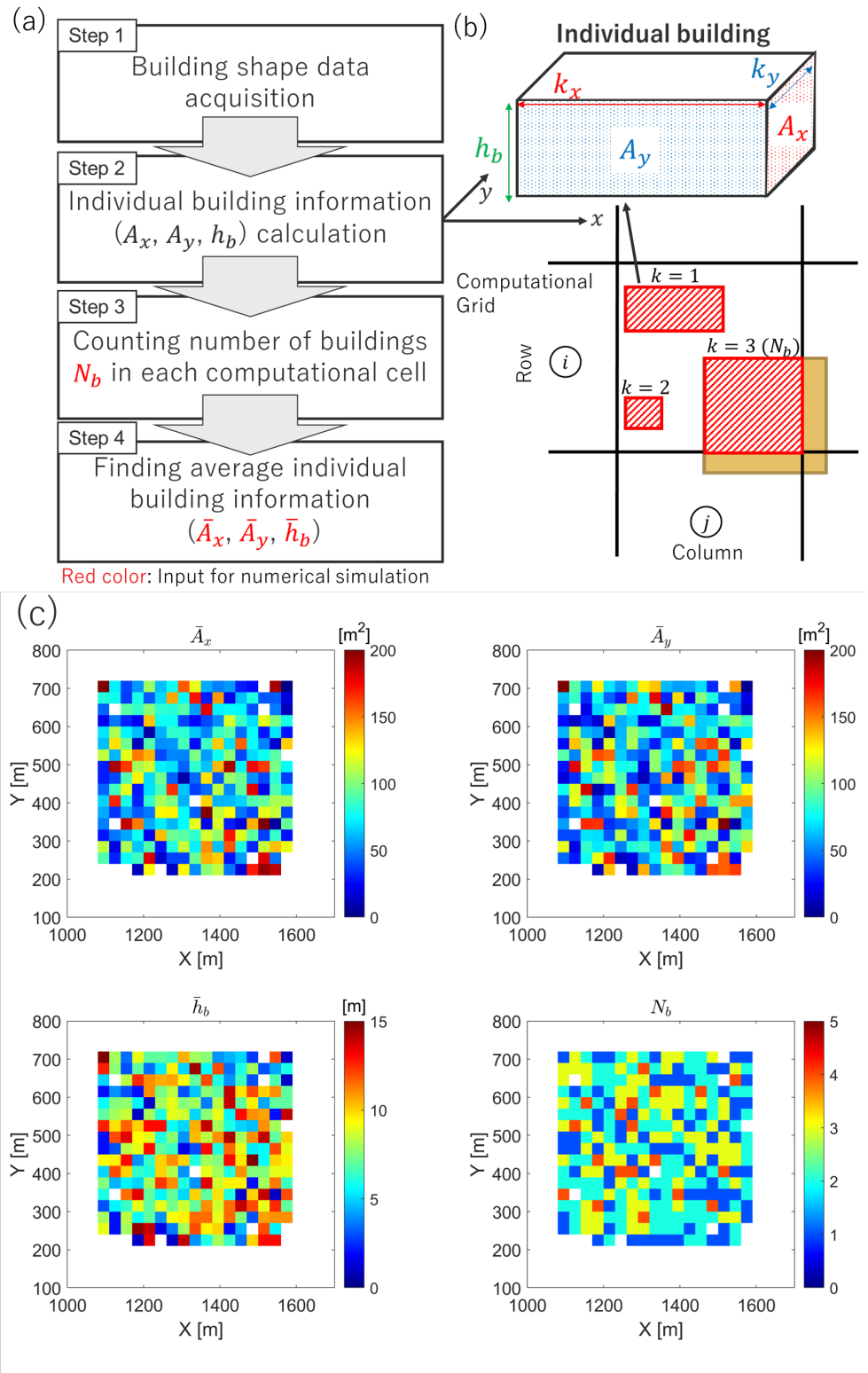

Figure 4.1: Summary of the upscaling scheme for iDFM; (a): flow chart of the calculation of the SGS parameters and individual drag force in tsunami simulation, (b): schematic view of the individual building and the method of counting buildings in each computational grid cell, and (c): sample spatial distributions of SGS parameters (i.e., projected areas in each direction, characteristic height, and number of buildings)

iDFM assumes that the building shapes are rectangular prisms. Then, A_x and A_y are calculated using

$$A_x = k_y h_b \tag{4.20}$$

$$A_y = k_x h_b \tag{4.21}$$

The third step involves determining N_b in the computational grid cell using image analysis of the projection view of the buildings from the top (the lower part of Fig. 4.1(b) shows a schematic view of the building edge detection process). The building boundary edges in the 2D coordinates are captured by the Canny method (Canny, 1986), and the number of edges is equal to N_b. The criteria for counting buildings are as follows.

1. If the building edge is fully contained in a computational grid cell, the building is counted (see the buildings with $k = 1$ and 2 in Fig. 4.1(b)).

2. If the building edge is partially contained in a computational grid cell, the building is counted when the intersection of the building and computational grid size (red shaded area in Fig. 4.1(b)) is larger than 20% of the footprint area of the building (see the building with $k = 3$ in Fig. 4.1(b)).

The fourth step is cell-averaging of the individual h_b, A_x, and A_y values using Eqs. (4.11-4.13). Figure 4.1(c) shows an example of the calculated SGS parameters, which are input into the numerical computation.

4.3 Idealized numerical experiment using simple urban topography

This section presents several idealized numerical experiments that are conducted to test the performance of the iDFM and previously presented models before the iDFM is applied to a realistic tsunami inundation simulation (Section 4.4).

4.3.1 Numerical setup

Figure 4.2 shows the basic setup of the numerical experiment. The computational domain consists of an oceanside area with a 10 m uniform water depth and a floodplain with a group of buildings (total 625 buildings) on 0 m ground elevation with respect to the undisturbed sea surface. Fig. 4.2(a) illustrates the bathymetry and topography of the entire domain. Five idealized layouts of the buildings are considered in an urban setting (X = 1,000-1,700 m), and Table 4.1 summarizes the basic topographic setup. The regular locate case considers buildings with a uniform width (5 m $\times$ 5 m) and height (6 m) that are arranged in 25 rows of 25 buildings (625 buildings in total). Roads between buildings in both the x- and y-directions are 10 m wide. To consider non-uniform road map, the building layout was randomly changed. The coordinates of the bottom-left corner are determined to be 1100-1700 and 100-600 in the x- and y-directions, respectively, following the discrete normal distribution with 1 m interval. The building width and

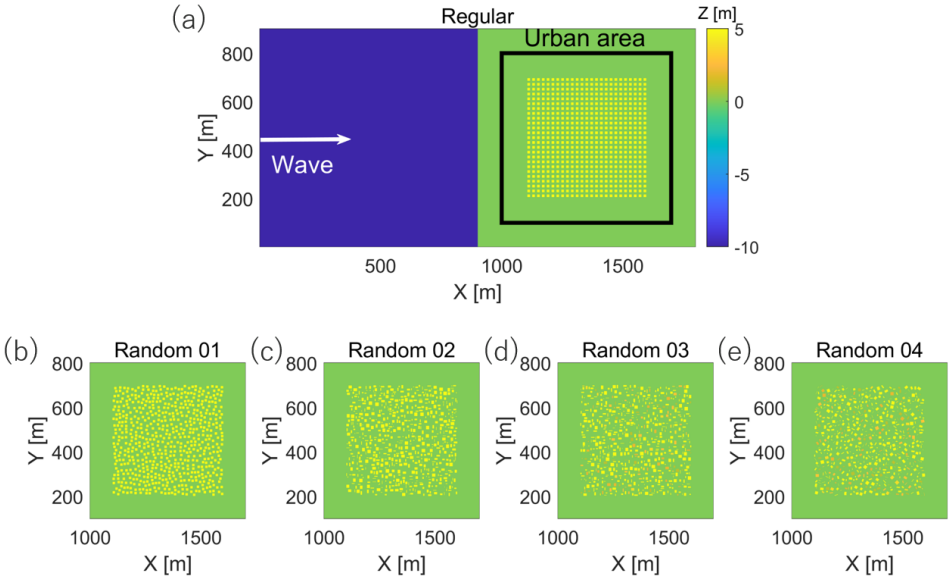

Figure 4.2: Computational domain and building layout used for (a): Regular (uniform shape and regular array), (b): Random 01 (uniform shape and random array), (c): Random 02 (random width and location), (d): Random 03 (random width, height and location), and (e): Random 04 (random width, height, angle of attack and location) (color shows bathymetry and topography elevation)

Table 4.1: Topographic setup in idealized numerical experiment

Urban model	Regular	Random 01	Random 02	Random 03	Random 04
Building width	10 m	10 m	1-15 m (Random)	1-15 m (Random)	1-15 m (Random)
Building height	6 m	6 m	1-15 m (Random)	1-15 m (Random)	1-15 m (Random)
Building location	Uniform	Random	Random	Random	Random
Angle of attack	0 °	0 °	0 °	0 °	-180 ° -180 ° (Random)
Number of buildings	625 (25 rows × 25 columns)				

Table 4.2: Numerical setup of the idealized numerical experiment

	iDFM	DFM	CERM	SRM
Governing equations	Depth-integrated SWE			
Discretization	Finite difference method			
Spatial Differentiation	Staggered C-grid			
Temporal Differentiation	Leap-frog scheme			
Convection Terms	Upwind (first-order accuracy)			
Other Gradient Terms	Centered (second-order accuracy)			
Friction Term	Semi-implicit			
Duration [s]	Wave S075: 200 Wave L15: 3000			
Integration time step [s]	0.05	0.05	0.05	0.025
Grid cell size [m] (Number of cells)	20 (45×90 cells), 30 (30×60 cells), 40 (23×45 cells), and 50 (18×36 cells)			1 (900×1800 cells)
Roughness coefficient [$m^{-1/3}s$]	0.025	0.025	Imai et al. (2013)	0.025
Drag coefficient	Eq. (4.22)			
Wet/dry boundary	Kotani et al. (1998)			
Input boundary	$X = 0$ m along the left boundary			
Boundary conditions	North and South: wall boundary West: inflow boundary East: radiation boundary			

Table 4.3: Summary of mean and standard deviation of calculated SGS parameters in urban area in the case of Regular and Random 04

(a) Regular gridded: Regular

Δx [m]	$\bar{A}_x$ [m^2]		$\bar{A}_y$ [m^2]		$\bar{h}_b$ [m]		N_b	
	Mean	Std.	Mean	Std.	Mean	Std.	Mean	Std.
20	60.00	0.00	60.00	0.00	6.00	0.00	1.00	0.00
30	60.00	0.00	60.00	0.00	6.00	0.00	2.16	1.07
40	60.00	0.00	60.00	0.00	6.00	0.00	3.70	0.73
50	60.00	0.00	60.00	0.00	6.00	0.00	6.25	1.80

(b) Random gridded: Random 04

Δx [m]	$\bar{A}_x$ [m^2]		$\bar{A}_y$ [m^2]		$\bar{h}_b$ [m]		N_b	
	Mean	Std.	Mean	Std.	Mean	Std.	Mean	Std.
20	80.15	55.70	78.52	55.90	7.93	4.24	1.22	0.43
30	81.53	46.18	80.57	46.10	7.95	3.41	2.14	0.90
40	78.43	37.40	77.37	37.33	7.77	2.64	3.48	1.33
50	79.34	27.84	77.26	26.71	7.91	2.11	5.56	1.43

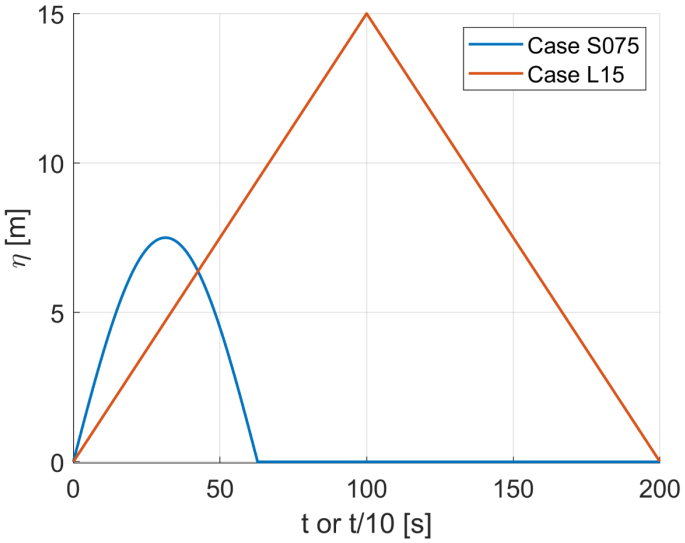

Figure 4.3: Incident wave for the idealized numerical experiment (blue: Wave S075 and red: Wave L15); note that time scale is divided by 10 for Wave L15.

height are randomly changed for the random cases as shown in Table 1. Note that the SGS models (i.e., the iDFM, DFM, and CERM) use bare-earth topography with 20-50 m resolution, which does not have building information, whereas the SRM uses structure-resolved topography at 1 m resolution. The SGS parameters are calculated as described in Section 2.1 and previous studies (DFM: Fukui et al., 2019 and CERM: Imai et al., 2013). Fig. 4.1(c) shows the spatial distribution characteristics (A_x, A_y, h_b, and N_b) in the Random 04 case at 30 m resolution. Table 4.2 summarizes the other numerical setups (e.g., discretization methods for the advection and frictional terms and tolerance depth for the frictional term). Table 4.3 summarizes the mean and standard deviation of the SGS parameters for each grid size in the Regular and Random 04 cases. A_x, A_y, and h_b are quite similar among the different grid sizes, but N_b increases as the grid size increases. Regarding C_D used in the SGS models, there have been a few studies on C_D estimation targeting tsunamis, and its empirical values are in the order of 0.1 or 1.0 (e.g., 3.3 in Aburaya and Imamura, 2002; 3.0 in Imai et al., 2013; and 0.5 in Adriano et al., 2016). Here, the approach of Fukui et al. (2019) is adopted, in which the drag coefficient is given as a function of Re:

$$C_D = a \exp(\lambda b Re) + c \tag{4.22}$$

where a = 9.1481, b = -0.0867, λ = 0.005, and c = 0.75. Note that c, which is the lower limit of the drag coefficient, is changed from 0.25 to 0.75 as Re is larger than the order of 10^7 on the full scale and C_D is constant (Roshko, 1961). Regarding the offshore boundary condition, this study assumes two types of incident waves, as shown in Fig. 4.3: 1) a sinusoidal wave with a 7.5 m wave height and 126 s period (Wave S075) and 2) a triangular wave with a 15 m wave height and 4,000 s period (Wave L15). These incident waves resemble waves generated in the physical experiment performed by Prasetyo et al. (2019). Waves S075 and L15 correspond to solitary and hydraulic bore waves, respectively.

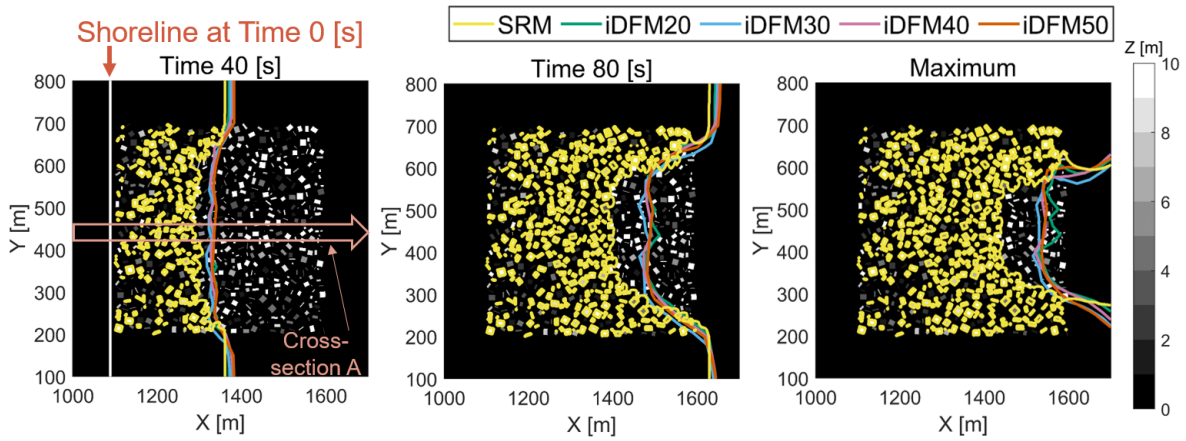

(a) Wave S075 case: ($\eta = 7.5$ m, $T = 136$ s)

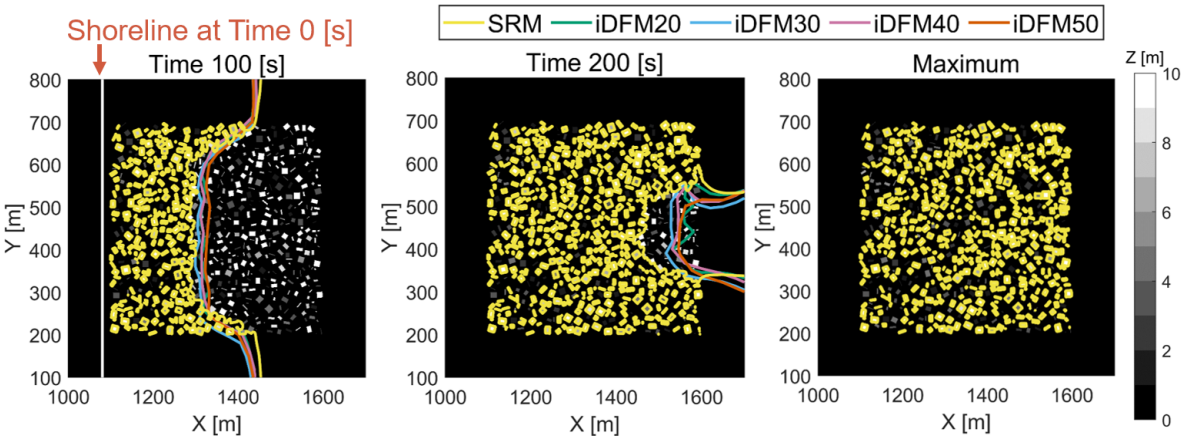

(b) Wave L15 case: ($\eta = 15$ m, $T = 4{,}000$ s)

Figure 4.4: Time series of the inundation leading edge since inundation starts modeled by the iDFM (colors indicate the cell sizes for computation or the SRM; green: $\Delta x = 20$ m, cyan: $\Delta x = 30$ m, magenta: $\Delta x = 40$ m, red: $\Delta x = 50$ m, and yellow: SRM) in the Random 04 topography.

4.3.2 Results

The analysis yields spatial data to quantify the model performance over a wide range. Firstly, the temporal changes of the inundation leading edge and overall inundation limits are examined. Surface elevation (or inundation depth) and tsunami arrival time were exemplified as indices for tsunami intensity in previous studies. In this paper, the maximum surface elevation and fluid velocity ($= \sqrt{U^2 + V^2}$), where U and V are the velocities in the x- and y-directions, respectively) are discussed as representative tsunami intensity. The performance is examined based on 1) the accuracy compared to SRM and 2) the solution convergence depending on the grid cell size, as described in the following section. Section 4.3.3 mainly discusses the Random 04 case and results for other cases are separately reported in Appendix.

Figures 4.4(a) and (b) show the leading edges of inundation every 40 or 100 s from the arrival of the wavefront in front of the buildings, and the inundation in the cases of

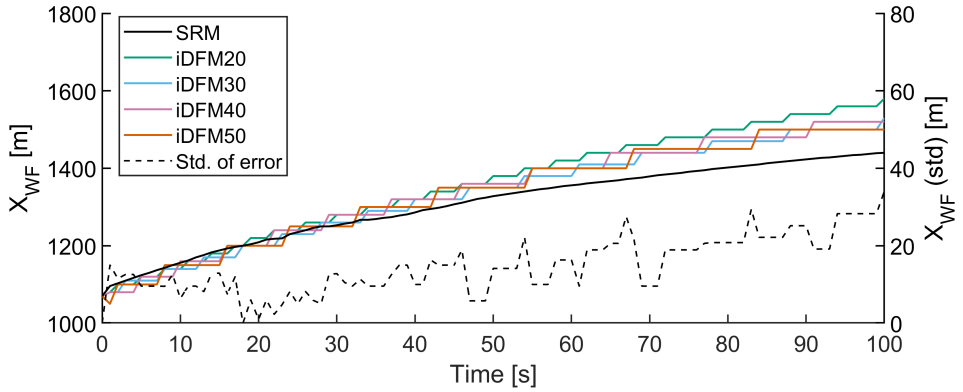

(a) Wave S075 case: ($\eta = 7.5$ m, $T = 136$ s)

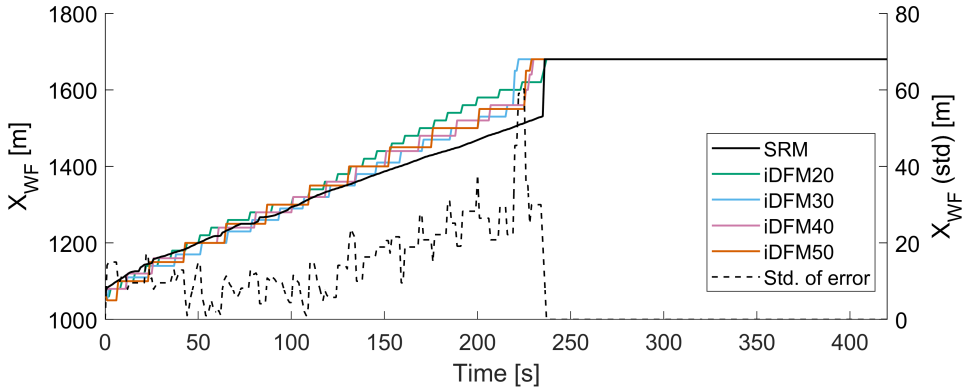

(b) Wave L15 case: ($\eta = 15$ m, $T = 4{,}000$ s)

Figure 4.5: Time series of the $x-$coordinate of the wavefront X_{WF} at Cross-section A shown in Fig. 4.4(a) modeled by the iDFM in the resolutions of $\Delta x = 20$ (green), 30 (blue), 40 (magenta), and 50 m (red), and SRM in $\Delta x = 1$ m (black); dashed line shows the standard deviation of the error or X_{WF} between the SRM among four cases of different resolutions.

Waves S075 and L15 modeled by the iDFM and SRM, respectively; refer to Figs. A. 1-4 for other cases (Regular or Random 01-03) in Appendix. Note that the entire domain is inundated in the case of Wave L15. In both cases (Waves S075 and L15), the inundation leading edges modeled by the iDFM are close to those obtained from the SRM until the middle of the group of buildings is inundated (specifically, at 40 and 100 s for Waves S075 and L15, respectively). However, the wavefront velocity obtained by the iDFM gradually overestimates that of the SRM (80 or 200 s after the arrival of Waves S075 and L15, respectively), and the inundation edges resulting from the iDFM reach farther from the shoreline than those from the SRM for Wave S075.

Regarding the solution convergence by grid cell size, there are minor differences between resolutions. Figure 4.5 shows time series of the x-coordinate of the wavefront X_{WF} on the center cross-section at $Y = 450$ m (Cross-section A) shown in Fig. 4.4(a) to quantify how much inundation leading edges modeled by the iDFM change for different resolutions. The iDFM by each resolution shows similar error characteristics between the SRM. The

error is within approximately 50 m when time is shorter than 50 s, while the error increases gradually after 50 s. The standard deviation of X_{WF} is around 20 m and lower than 40 m for Wave S075, which means there is difference of X_{WF} as long as one or two grid cell size among four resolutions. Besides, the case of Wave L15 shows the similar tendency to Wave S075. The error between SRM is relatively small until 100 s when the mean value of X_{WF} is lower than 1,400 m (middle of the group of buildings) in each resolution. The standard deviation of X_{WF} is around 20 m until 100 s but it increases up to around 30 m when whole the domain is inundated for Wave L15. A large standard deviation of 60 m after 220-230 s is due to the difference of the arrival time of leading edge at the end of the buildings (X = 1,600 m). Still, the grid cell size dependency is insignificant in this idealized numerical experiment.

Next, detailed tsunami intensities obtained from the iDFM and SRM are compared and differences (error characteristics) are examined by focusing on the case of Δx = 30 m, where the ratio of grid size to the characteristic building width $\Delta x/k_x$ is 3. Fig. 4.6(a) compares the spatial distributions of the maximum inundation depth (the first and second panels from left show the results obtained from the iDFM in Δx = 30 m and SRM, respectively) in Wave S075. Note that the SRM results are upscaled at the same resolution as the iDFM according to the cell average (the raw results are provided in the third panel from left of Fig. 4.6(a)), and the surface elevation and velocities at grids including the structures for the SRM are excluded because the SGS models cannot solve the structure overtopping. The fourth panel from left of Fig. 4.6(a) depicts the relative differences between the two models (iDFM-SRM). The iDFM and SRM show similar spatial patterns in the maximum surface elevation. Specifically, the calculated values are large at closer distances from the shoreline. This result indicates that both models can express the surface increase due to the structural blocking effect to some extent. However, compared with the SRM, the iDFM approximately underestimates the surface elevation by 30% in front of the group of buildings (X = 1,000-1,100 m), and overestimates it by more than 50% in the middle of the building (X = 1,300-1,500 m). Figures 4.6(b) provides a similar comparison of the maximum fluid velocity. The velocities of both the iDFM and SRM tend to be large in nearshore areas (X = 1,000-1,200 m), and their attenuation is observed in the group of buildings. The relative difference between them in the group of buildings is approximately 17.5%, and the iDFM can capture the velocity reduction effect. However, there are some situations where the results from iDFM become relatively inaccurate. For example, when localized flow, such as contracting current between buildings, is dominant in the computational grid cell, the relative error is large. Specifically, at the front (X = 1,100-1,200 m) or lateral side (Y = 200 or 700 m) of the group of buildings, many shrinkage flows between buildings are observed, and the relative difference between the iDFM and SRM exceeds 30%.

Figures 4.7(a) and (b) compare the maximum surface elevation and fluid velocity in the case of Wave L15, respectively (the figure layout is the same as that in Fig. 4.6). Similar to Wave S075, the overall spatial pattern of the iDFM results is close to that of the SRM results, and the relative error between the iDFM and SRM is 9.4% on average. Note that much larger mass fluxes are transported from offshore than in the case of Wave S075 because the wave period is longer and the entire computational domain is inundated

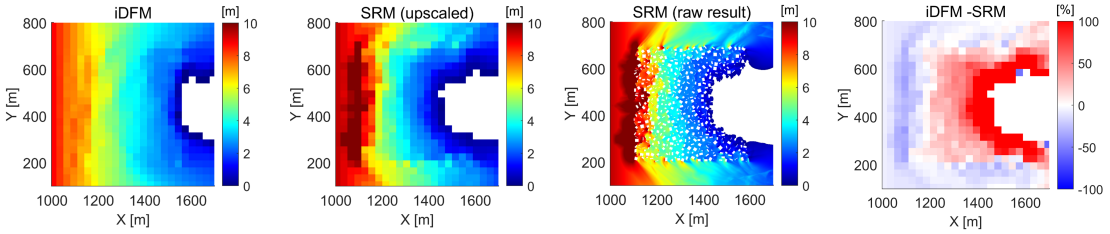

(a) Maximum surface elevation

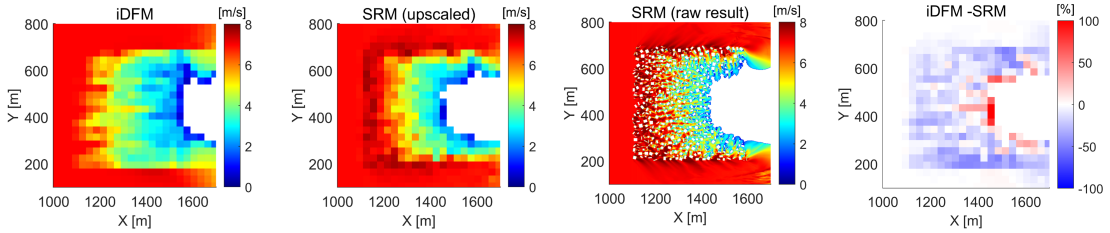

(b) Maximum fluid velocity

Figure 4.6: Difference of (a) maximum surface elevation and (b) maximum fluid velocity between the iDFM ($\Delta x = 30$ m) and SRM results with the Random 04 topography in the Wave S075 case (1st panel from left: iDFM, 2nd panel: cell-averaged value for SRM, 3rd panel: raw results of SRM, and 4th panel: error between iDFM and SRM).

uniformly. In terms of velocity, the number of grid cells overestimated by the iDFM is increased compared to that in the case of Wave S075 (approximately 25% increase; Wave S075: 402 cells and Wave L15: 503 cells), especially near the center of the group of buildings, resulting in the relative error of 22% on average, which is smaller than Case S075. For other cases (Regular or Random 01-03), refer to Figs. A. 5-12.

Figure 4.8(a) shows the spatial distributions of maximum surface elevation (top), maximum fluid velocity (middle), and topographic change (bottom) along Cross-section A in Fig. 4.4(a) in the case of Wave S075. The previous SGS models are also included for comparison. Regarding the maximum fluid velocity, larger differences are observed among the SGS models and the iDFM achieves the best result. For instance, in the middle of the group of buildings, the iDFM produces a velocity less than 4 m/s, although DFM and CERM yield 6 m/s, which indicates that the velocity reduction effect of the buildings by the iDFM is larger than those of the DFM and CERM. The reduction effects of the SRM and iDFM are similar, and the difference between them is less than 21% in an inundated area modeled using both approaches. All the SGS models, including the iDFM, show similar cross-sectional tendencies in terms of the maximum surface elevation. The modeled flow is attenuated owing to the presence of buildings, which serves as a resistance element. In contrast, the SRM shows a local rise at the forefront of the group of buildings (X = 1000-1150 m), which does not appear in the SGS models. The difference between the SRM and iDFM is approximately 1-2 m (20%). However, the other points in the rear of the cross-section are similar, and the iDFM can reproduce more realistic inundation characteristics.

Fig. 4.8(b) presents the spatial distributions of maximum surface elevation and fluid velocity along Cross-section A for Wave L15. There are no major differences in the maxi-

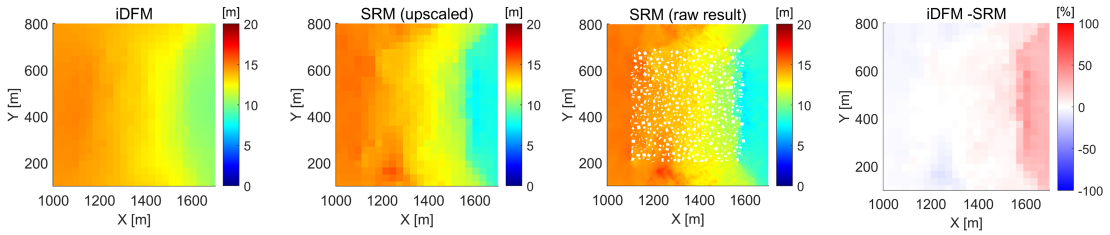

(a) Maximum surface elevation

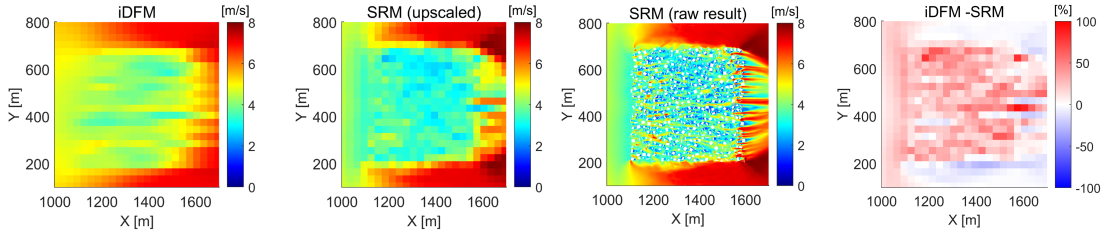

(b) Maximum fluid velocity

Figure 4.7: Difference of (a) maximum surface elevation and (b) maximum fluid velocity between the iDFM ($\Delta x = 30$ m) and SRM results with the Random 04 topography in the Wave L15 case (1st panel from left: iDFM, 2nd panel: cell-averaged value for SRM, 3rd panel: raw results of SRM, and 4th panel: error between iDFM and SRM).

Table 4.4: Mean and standard deviation, and variation (ratio of standard deviation to mean) of RMSEs among whole the layouts (Regular and Random 01-04) in specific grid size Δx for the iDFM

	Surface elevation			Fluid velocity		
Δx [m]	Mean	Std.	Var.	Mean	Std.	Var.
20	0.13	0.042	0.32	0.12	0.0052	0.044
30	0.14	0.043	0.31	0.11	0.0067	0.058
40	0.14	0.045	0.32	0.13	0.0062	0.049
50	0.15	0.049	0.32	0.12	0.0078	0.063

mum surface elevation among the four models, as shown in Fig. 4.8(a), and all SGS models exhibit consistent results except for the right edge of the domain. In contrast, the differences in fluid velocity are large. Similar tendencies are observed in the SRM and iDFM results, and the difference between them is less than 29%. All SGS models display small spatial changes of velocities in the group of buildings, but the magnitudes are different: approximately 5 m/s for the iDFM and CERM and approximately 7 m/s for the DFM. The observed differences can be attributed to the evaluation of the drag force term, calculated as the velocity reduction effect, in different methods. In the iDFM and DFM, the drag force term is inversely proportional to the grid cell size and total water depth. On the other hand, the friction term in the CERM is proportional to the total water depth. Therefore, Wave L15, which provides a longer period and higher wave height, leads to a larger friction term in the CERM and smaller drag force terms in the iDFM and DFM. The DFM provides a smaller drag force than the iDFM because the structural information for the DFM is smoothed when the grid cells are large.

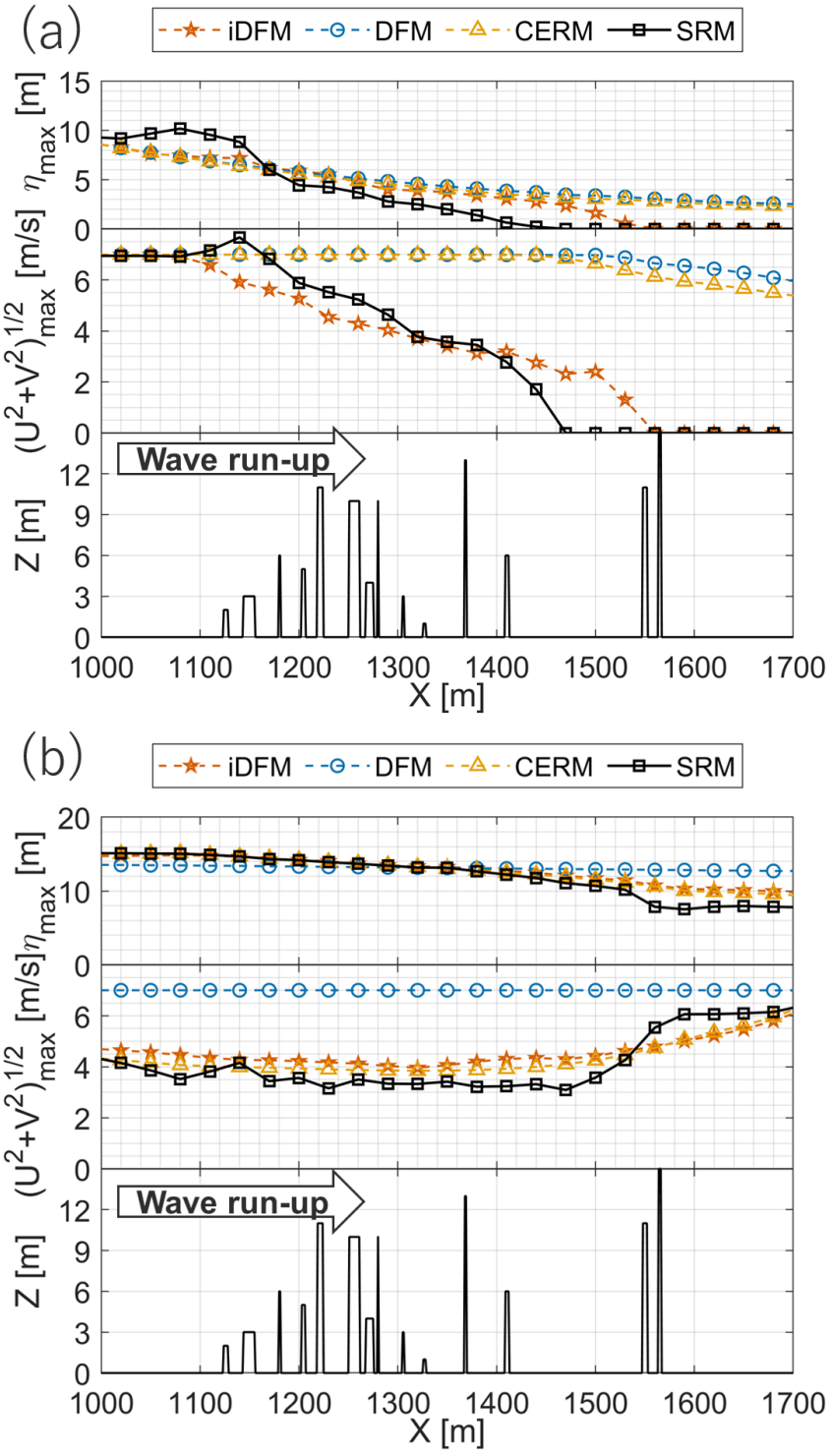

Figure 4.8: Maximum surface elevation and current velocity in Cross-section A in Fig. 4.4(a) and topographic change in the Random 04 topography (colors indicate models; red: iDFM, blue: DFM, yellow: CERM and black: SRM for $\Delta x = 30$ m); (a): Wave S075 ($\eta = 7.5$ m, $T = 136$ s) and (b): Wave L15 ($\eta = 15$ m, $T = 4000$ s)

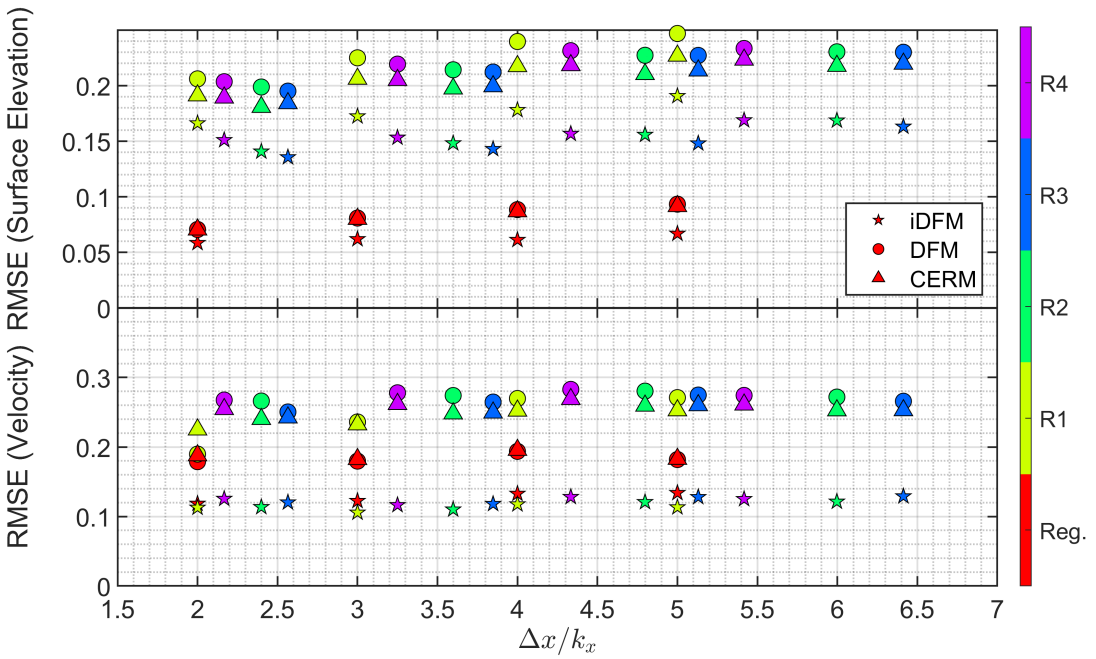

Figure 4.9: Relationship between the RMSE of the maximum surface elevation and current velocity between the SRM in the Wave S075 case and ratio of grid size to characteristic building width (markers indicate models; star: iDFM, circle: DFM and triangle: CERM, and colors indicate used building layouts)

Moreover, the differences in the error characteristics between different grid sizes and building layouts are examined using the root mean square error (RMSE) of the maximum surface elevation and fluid velocity as representative measures. The RMSEs of the maximum surface elevations and fluid velocities in the urban area between each SGS model and the SRM are calculated to check the solution convergence depending on the grid cell size. Fig. 4.9 shows the relationship between the RMSE and grid cell size in the case of Wave S075. Note that maximum surface elevation and fluid velocity are normalized by the incident wave (i.e., $\eta = 7.5$ m and $U = \sqrt{gh}$, where $g = 9.81$ m/s^2 and $h = 10$ m) and the grid cell size is normalized by the mean width of buildings as a characteristic width. The RMSEs of both the surface elevation and fluid velocity are within 0.3 (2.25 m and 2.97 m/s for surface elevation and fluid velocity, respectively). On average, the RMSEs of maximum surface elevation and fluid velocity reduced by 25% and 49% on average from other SGS models, respectively, which shows improvement from previous SGS models. The RMSE increases as the grid cell size increases for all SGS models, but the iDFM is less sensitive to the grid cell size dependency. In particular, the RMSE of the maximum fluid velocity obtained by the iDFM when the cell width ratio is more than 5 is 48% smaller than those of the other SGS models on average.

In addition, the influence of the building layout on the RMSEs of the iDFM is large for the surface elevation but small for the fluid velocity. The variations (the ratio of the standard deviation σ to mean μ) of the RMSE of the surface elevation and fluid velocity among whole the layouts (Regular and Random 01-03) in each grid size are shown in

Table 4.4. For instance, the variations in the case of $\Delta x = 30$ are 0.31 ($\mu = 0.14$ and $\sigma = 0.043$) and 0.058 ($\mu = 0.11$ and $\sigma = 0.0067$), respectively. Regarding the surface elevation, the buildings are aligned so that the flow between buildings is less obstructed by other buildings; therefore, the surface elevation on the inland side is larger than it is in the other cases. Consequently, the RMSE for the iDFM is small because the iDFM tends to provide a large surface elevation on the inland side. On the other hand, the velocity is reduced by the buildings as macroscopic obstacles, and the RMSE for the iDFM overall is small even though localized contracting flow occurs.

In conclusions, a series of performance evaluations for the idealized numerical experiment revealed that the iDFM can reproduce the overall inundation processes and that the grid cell size dependency is reduced compared to other SGS models. However, there is still discrepancy between the iDFM and SRM, and the differences reported in Section 4.3 are mainly due to the differences in the building feedback process, which will be discussed in Section 4.5.

4.4 Application to the historical 2011 Tohoku tsunami

This section describes an application of the SGS models to Onagawa during the 2011 Tohoku tsunami as a historical event. Onagawa is located in the northern part of the Tohoku region and was severely damaged by the tsunami. The maximum tsunami height at the bay mouth was 14 m, and the maximum run-up height was 35 m there (Mori et al., 2011). These tsunami inundation height characteristics are typical along the Sanriku ria coastal area (Mori et al., 2011). The town center of Onagawa, which was devastated, was one of the most populated areas of the Sanriku coast, and caused a total of 816 fatalities, with additional 125 missing (12% of the total population) and 3,888 damaged houses (85% of all houses) (Suppasri et al., 2013). Onagawa is selected as the target area because of the topographic characteristics, locations of the houses and buildings near the coast, and sizes of the surrounding hills.

4.4.1 Numerical setup

Table 4.5 summarizes the basic numerical setup used for the computations, and the overall settings, such as the governing equations, discretization scheme, and wet/dry boundary condition, are the same as in the idealized numerical experiment (Table 4.2). The iDFM, DFM, and CERM are used as SGS models, as in the idealized numerical experiment but results modeled by the iDFM will be focused on in this section. The tsunami source model is developed by referring to the fault plane geometry, such as the trench location, top-fault depth, strike, and dip considered by Satake et al. (2013). The fault plane model covers an area of 650 km $\times$ 250 km and has a constant strike of 193 $^\circ$ and variable dip angles, gradually steepening from 8 $^\circ$ to 16 $^\circ$ along the down-dip direction (Goda et al., 2015). Kinematic rupture processes are considered in the source model by Satake et al. (2013). The vertical seafloor displacements are calculated using the formulae of Okada (1985) and Tanioka and Satake (1996), which assume that the vertical seafloor displacement is identically translated to the sea surface, representing the initial condition of the tsunami

Table 4.5: Setup of the Onagawa case

	SGS models	SRM
Tsunami source model	Satake et al. (2013)	
Duration [h]	1 (only the first wave attack is considered)	
Integration time step [s]	0.1	0.025
Nesting domain and resolution	D1 (Δx = 1350 m), D2 (Δx = 450 m), D3 (Δx = 150 m), D4 (Δx = 50 m), and D5 (Δx = 20 or 30 m)	D1 (Δx = 1350 m), D2 (Δx = 450 m), D3 (Δx = 150 m), D4 (Δx = 50 m), D5 (Δx = 10 m), and D6 (Δx = 5 m)
Grid size at final domain [m]	20, 30, or 50	5

propagation model. The duration of the numerical simulation was 1 h (i.e., 14:46-15:46 JST) because this study is mainly focused on the first wave attack. The integration time step is determined based on the satisfaction of the CFL condition (0.1 s and 0.025 s are adopted for the SGS models and SRM, respectively).

As the input data for the tsunami simulations, the Miyagi prefectural government provided a dataset containing bathymetry and topography information, coastal/riverside structures, such as breakwaters and levees, and roughness coefficients (Manning coefficient). However, this study does not implement breakwaters and levees to ignore grid cell size dependency of offshore water surface elevation on layout of the coastal structures. The data are constructed in the form of nested grids (1350-450-150-50-10-5 m) covering the entire geographical region of Tohoku. Figs. 4.10(a)-(d) show some of the constructed computational domains. Two different topographies are employed for the last domains of the SGS and SRM models (see Figs. 4.10(c) and (d)). The SGS models adopt a bare-earth topography and do not include structures on the land. Note that the elevation data representing buildings are removed by median filtering (e.g., Fukui et al., 2019) and cell-averaged into 20, 30, and 50 m meshes. Meanwhile, the SRM uses the HR digital surface model (DSM), representing building information as part of the land elevation. The HR DSM is constructed by combining 3D building shape data and topography at 5 m resolution. The SGS parameters for the iDFM are calculated using the 3D building shape data shown in Fig. 4.11(a). Figs. 4.11(b)-(e) depict the spatial distribution of the SGS parameters at 30 m resolution. Grid cells with $\bar{A}_x$ and $\bar{A}_y$ of 100-200 m^2 constitute the majority of the cells in Onagawa. However, several commercial facilities with tall building heights and long widths are located close to the shoreline in the southern area of Onagawa, which provide large values of $\bar{A}_x$ and $\bar{A}_y$ (more than 300 m^2).

4.4.2 Results

The same evaluation process as the idealized numerical experiment is applied to this realistic tsunami case and focuses on the results modeled by the iDFM at Δx = 30 m, which is the resolution practically used in Japan for tsunami inundation simulation because

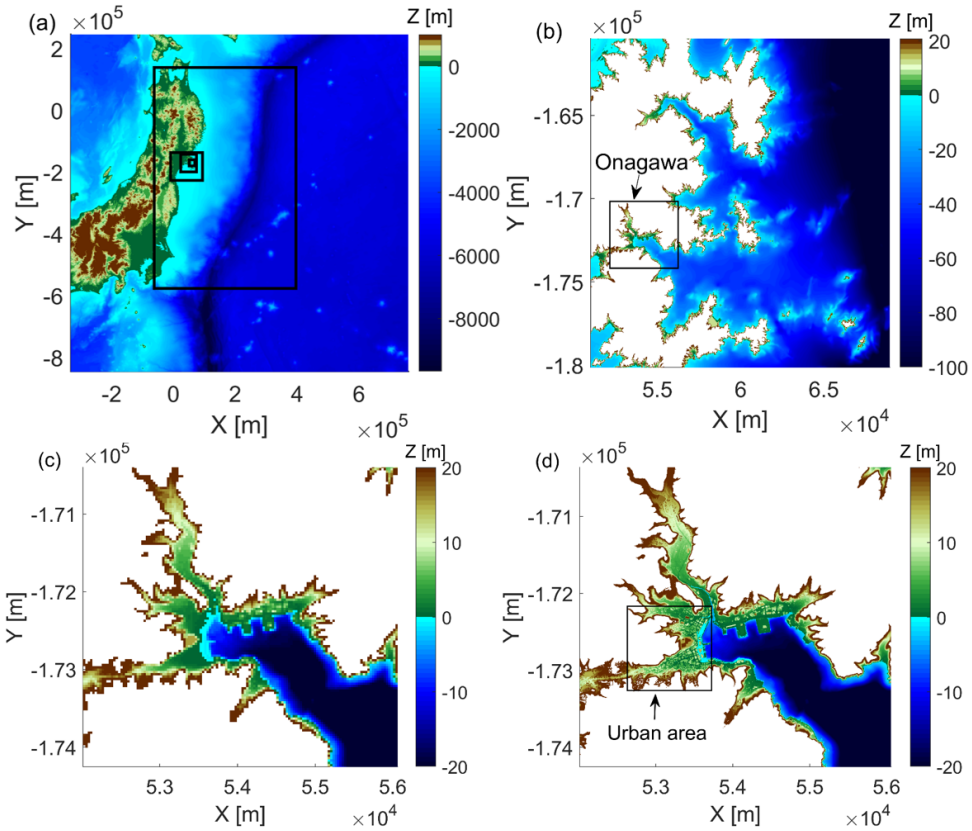

Figure 4.10: Topography used in the numerical simulation; (a) D1 (Δx = 1350 m; black boxes show nested domains), (b) D5 (Δx = 30 m), (c) Onagawa area in D5 (Δx = 30 m) shown by black box, and (d) Onagawa area in D6 (Δ x = 5 m)

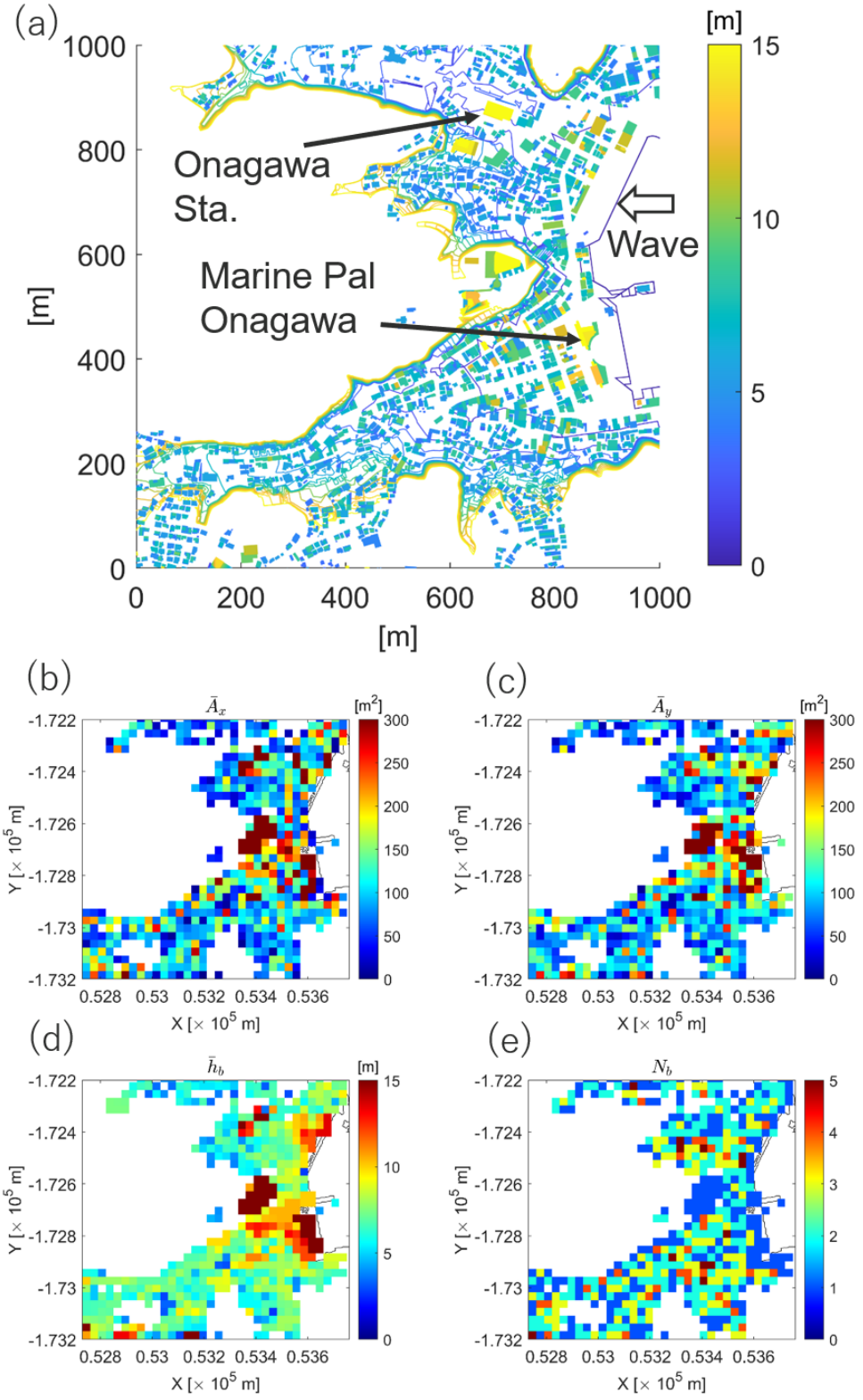

Figure 4.11: Building information data in Onagawa; (a) Spatial distribution of 3D building shape data (colored polygons) with topography (color contour lines) and (b) $\bar{A}_x$, (c) $\bar{A}_y$, (d) $\bar{h}_b$, and (e) N_b calculated using $\Delta x = 30$ m in the Onagawa urban area shown in Fig. 4.10(d)

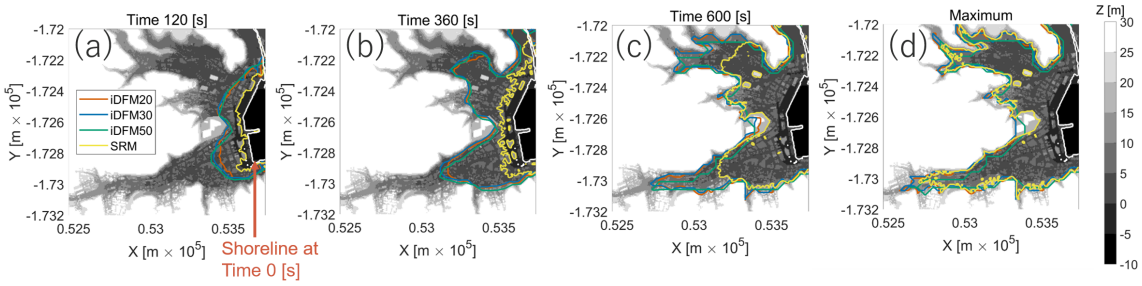

Figure 4.12: Inundation leading edge for t = (a) 120, (b) 360, and (c) 600 s and (d) maximum state (colors indicate used models; red: iDFM in Δx = 20 m, blue: iDFM in Δx = 30 m, green: iDFM in Δx = 50 m, and yellow: SRM; color contour in the background shows topography)

the results based on Δx = 20 and 50 m are similar to 30 m.

Firstly, the inundation leading edge and limits are examined, as shown in Fig. 4.12. Snapshots of the inundation leading edges at 120, 360, and 600 s after the tsunami wave arrives at the shoreline are presented. The iDFM shows a similar inundation process regardless of the resolution, as in the ideal numerical experiment. However, different wave propagation speeds are observed compared to the SRM. The wavefront modeled by the iDFM arrives at the inland area 360 s after the tsunami wave arrives at the shoreline, and the inundation area reaches the maximum approximately 600 s later. On the other hand, the wavefront modeled by the SRM remains around buildings close to the shoreline 360 s after the tsunami wave arrives at the shoreline. The inundation area reaches the maximum approximately 400 s after it does in the iDFM. This discrepancy is mainly caused by the difference in the fluid velocity near the shoreline. The current SGS model estimates smaller velocity reduction effects by structures than the SRM, which will be discussed in the following two paragraphs.

Fig. 4.13 shows the maximum surface elevation and fluid velocity modeled by the iDFM (Δx = 30 m) and SRM. Note that the SRM results are upscaled at the same resolution as the iDFM results based on the cell average (the third panel from the left of Fig. 4.13(a) shows the raw results), and the maximum surface elevation and fluid velocity on the structures for the SRM are excluded because the SGS models cannot solve structure overtopping. Differences less than 30% are observed between the iDFM and SRM in terms of the maximum surface elevation. These differences are relatively small, noting that for this historical tsunami case, a large mass flux is transported from offshore, and every area in Onagawa is inundated, as described in Section 4.3.2. However, the iDFM is prone to overestimate the maximum surface elevation in the northern area of Onagawa because the blocking effect of large structures (Onagawa station, shown in Fig. 4.11(a)) is strong in the SRM. Such differences are also observed in the idealized numerical experiment (Section 3) and will be discussed further in Section 4.5. Regarding the maximum fluid velocity, the SRM shows strong velocity reduction, similar to that of Wave L15 in Section 4.3, which leads to the overestimation by the iDFM. This effect is especially notable in the area close to the shoreline, where several commercial facilities are located. Specifically, differences of

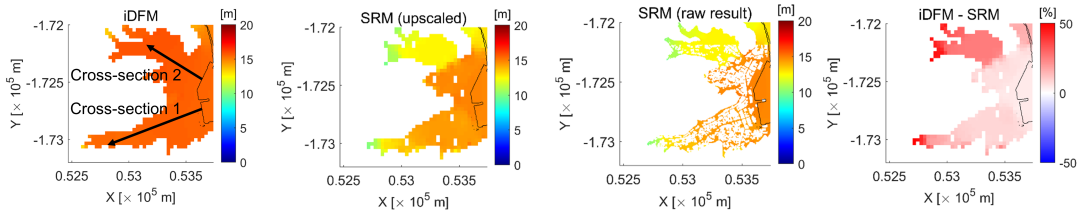

(a) Maximum surface elevation

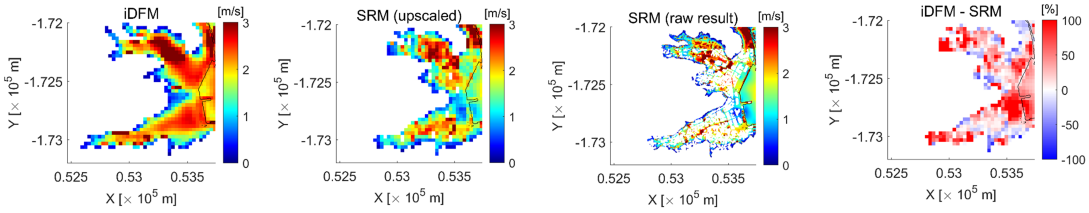

(b) Maximum fluid velocity

Figure 4.13: Spatial distributions of maximum surface elevation and velocity (1st panel from left: iDFM, 2nd panel: cell-averaged value for SRM, 3rd panel: raw results of SRM, and 4th panel: error between iDFM and SRM).

more than 100% between the iDFM and SRM are observed around the large commercial buildings (Marine Pal Onagawa in Fig. 4.11(b)). Such overestimation of the velocity leads to a difference in the inundation leading edge.

Two representative profiles (Cross-sections 1 in the southern region and 2 in the northern region of Onagawa) in Fig. 4.13(a) are examined in Fig. 4.14. Note that the figure layout is similar to Fig. 4.8, but the wave run-up direction is reversed. The effect of buildings on the maximum surface elevation is small when the tsunami height is significantly greater than the building height. All SGS models give a surface elevation of 15 m, whereas the SRM yields 12-14 m (approximately 30% difference) along each cross-section. Focusing on the maximum fluid velocity, all SGS models show similar trends along each cross-section. The difference between the iDFM and SRM appears mainly near large structures taller than 10 m. For example, in Cross-section 1, a maximum of 175% overestimation between the iDFM and SRM is observed near Marine Pal Onagawa (run-up distance X_R = 30-100 m; note that the building shape does not appear in the bottom panel). In Cross-section 2, there is a group of residential buildings approximately 10 m high near the shoreline and Onagawa train station has a height of 20 m. Approximately, 83% and 100% overestimations are observed around these buildings and Onagawa Station, respectively. The major sources of the errors in the maximum surface elevation and fluid velocity are common because the fluid velocity is given by the gradient of the surface elevation. This point is further discussed in Section 4.5.

4.5 Discussion

This study revealed that the iDFM can reproduce overall inundation processes, such as the inundation limit and the maximum water depth. Under ideal conditions (Section 4.3), the

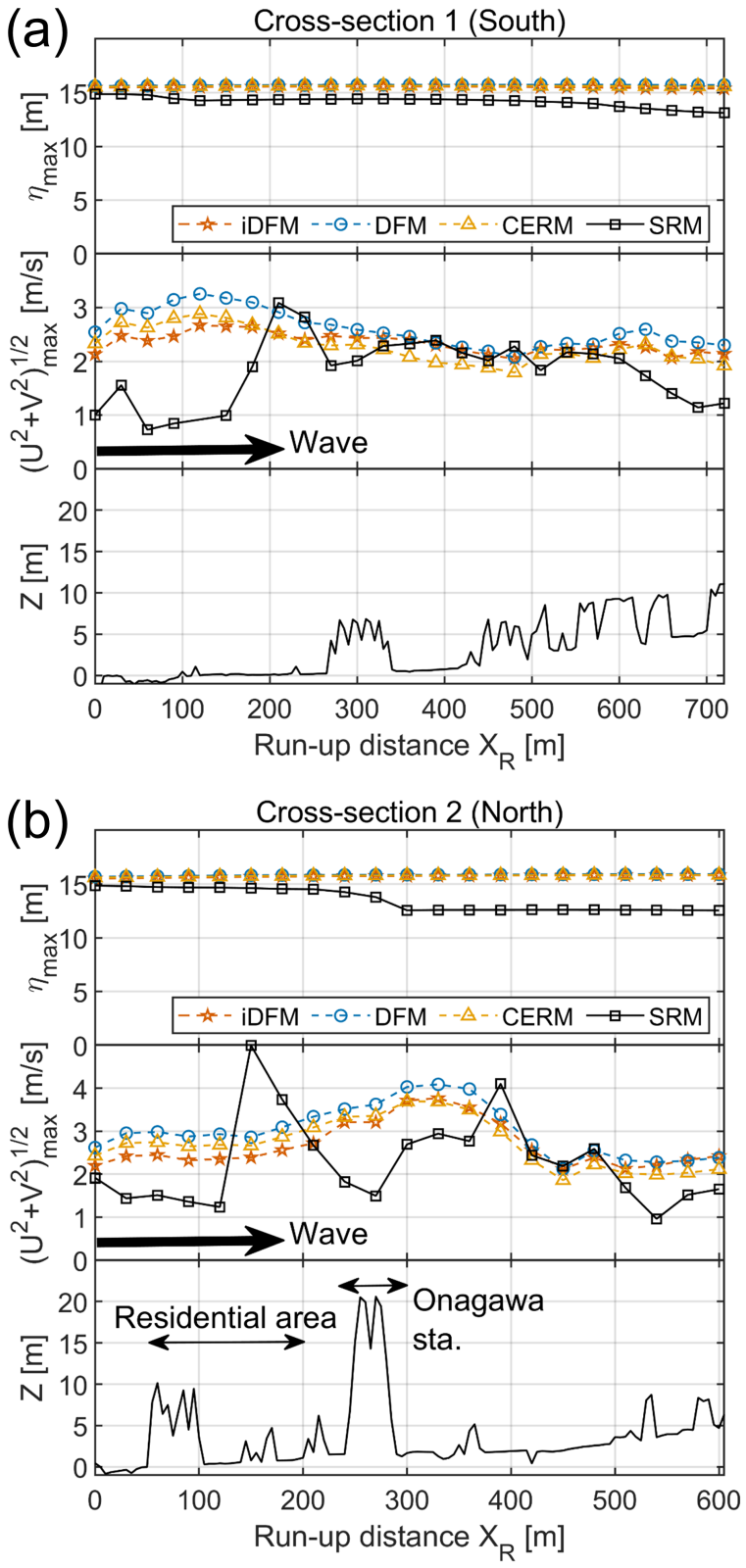

Figure 4.14: Spatial distributions of maximum surface elevation (top panel), current velocity (middle) and topography along two sections shown in Fig. 4.13(a) (colors indicate models; red: iDFM, blue: DFM, yellow: CERM and black: SRM for $\Delta x = 30$ m); (a): Cross-section 1 and (b): Cross-section 2

iDFM successfully improved the accuracy of the temporal progression of the inundation leading edge and maximum fluid velocity. However, the results differed from those of the SRM, especially in the realistic tsunami case (Section 4.4). This section discusses 1) the differences in the velocity reduction effect between the iDFM and SRM, 2) the differences in the error characteristics between the idealized numerical experiment and realistic tsunami case, and 3) possible future improvements of SGS modeling.

The velocity reduction due to the presence of structures is different between the SRM and iDFM because the structures are treated as part of topography in SRM while the structural effects are represented by the grid-based friction parameters in iDFM. In the SRM, the structure information is fed back to the water depth because the structure height is treated as ground elevation. Then, the total water depth is smaller over built-up areas than the areas without structures, and the structural effect is considered in the mass conservation and wet/dry boundary scheme. Therefore, the surface elevation is calculated by considering the structure and specific effects reproduced by structures, such as blocking and contracting current between buildings. The fluid velocities (i.e., discharge fluxes in the governing equations) are estimated based on the spatial gradient of the surface elevation at the same time step. For example, the surface elevation in front buildings is large when inundation flow is blocked by buildings and the fluid velocity is negligible because the spatial gradient of the surface elevation is small, as observed in the historical tsunami case. On the other hand, the structural information feedback process is simplified for the iDFM. The iDFM (and other SGS models) adopts bare-earth topography, which does not treat the structures as ground elevation. Because of such treatment, the mass conservation and wet/dry boundary schemes do not consider structural effects, such as blocking. Instead, the structures are evaluated as resistance elements in momentum conservation, which reduces the fluid velocity, and the surface elevation could differ from that obtained using the SRM.

It is inferred that the difference in the velocity reduction effect described above can explain the error characteristics of the maximum surface elevation and velocities observed in the idealized numerical experiment and historical tsunami simulation. The differences in the maximum surface elevation in front of the group of buildings were observed in the numerical experiment, mainly in the Wave S075 case, and the historical tsunami case. One of the reasons of the differences is due to the reproducibility of the water level rise caused by the blocking by the group of buildings described in the previous paragraph. Regarding the maximum fluid velocity, two main types of error characteristics were observed: 1) overestimation due to the blocking effect and 2) underestimation due to the contracting current between buildings. The former characteristics appeared mainly in the Wave L15 case for the numerical experiment and the historical tsunami case, as described in Sections 3.2 and 4.2. The error in the surface elevation causes the spatial gradient error, which leads to a fluid velocity error. The latter characteristics appear mainly in the Wave S075 case in the numerical experiment because larger momentum fluxes are transported from offshore. The fluid velocity between buildings is approximately 43% different from that in the case of Wave L15.

The effect of the error of the maximum surface elevation and fluid velocity between the SRM on the inundation leading edge and the limit of inundation extent tends to depend

on the Froude number Fr of the run-up flow during the inundation, which is defined as:

$$Fr = \frac{\sqrt{U^2 + V^2}}{\sqrt{gD}} \tag{4.23}$$

Using Fr, the drag force term in the iDFM can be transformed into:

$$F_D = KC_D Fr^2 \tag{4.24}$$

where K is a parameter determined by the shape of the structure, such as the projected area. Assuming that C_D is almost constant (in this study, 0.75) because the Reynolds number is larger than the order of 10^6, the Froude number affects the drag force term. Fr was calculated to be greater than 0.4 in both the Wave S075 and L15 cases in the idealized numerical experiment, whereas Fr is at most 0.25 for the realistic tsunami case. Therefore, when Fr is large, the drag term, which is an effect of velocity reduction, increases, and the run-up velocity decreases, resulting in a run-up process similar to that in the SRM. However, when Fr is small, the value of the drag term is insufficient, and the tsunami moves faster than it does in the SRM.

Finally, future approaches of improving the iDFM are mentioned based on the previous discussions. The major difference between the iDFM and SRM lies in whether the vertical height of the structure is reflected in the mass conservation law as the water depth. To address this issue, the effect of the structure can be included as an additional term in the mass conservation law. An example of an additional term is the porous term (e.g., Kennedy et al., 2019). When applied to the iDFM, a term that is a function of the height of a representative building or the occupancy rate in a mesh can be considered, but this subject remains a topic for future works.

4.6 Summary of Chapter 4

Chapter 4 proposed a new drag-force-type model of macroscopic roughness by buildings, called the iDFM, focusing on a complex coastal urban topography including ports, buildings, and houses for depth-averaged NSWE models based on previous models, such as the DFM (Fukui et al., 2019) and CERM (Aburaya and Imamura, 2002; Imai et al., 2013). The iDFM adopts the total sum of the drag force acting on individual buildings in a computational grid cell to reduce the grid cell dependency observed in the DFM. As a performance evaluation, idealized numerical experiments using simple urban topography with several spatial building layout patterns and hindcast experiments targeting a historical tsunami inundation event for the 2011 Tohoku tsunami were conducted, and the results were compared with those of an HR tsunami simulation using building-resolved topography (i.e., the SRM). The major conclusions are as follows.

a) In general, the iDFM (and other SGS models) takes into account the effect of structures as resistance elements that reduce the fluid velocity in momentum conservation. On the other hand, the SRM evaluates this effect as topography and feeds it back not only into the momentum conservation but also into the mass conservation and wet/dry boundary conditions. Therefore, the iDFM can model the overall inundation characteristics, such as the inundation limits, but not local phenomena driven

by structures, such as surface rising due to blocking and contracting current between structures.

b) In the idealized numerical experiment, the RMSEs of maximum surface elevation and fluid velocity reduced by 25% and 49% on average from other SGS models, respectively, which showed improvement from previous SGS models. Moreover, the limits of inundation or time series of inundation leading edges showed good agreement with the SRM even when the grid resolution is coarser.

c) In historical tsunami case, the iDFM underestimated velocity reduction due to the buildings near shoreline and it gives overestimation of leading edges of inundation. Such observed differences in the error characteristics between the idealized numerical experiment and historical tsunami case (Onagawa case) may be due to the difference in Fr during the tsunami run-up.

Future research in this area should focus on further model improvement, considering the feedback by structures in mass conservation and the wet/dry boundary conditions.

Chapter 5

Subgrid-scale Modeling of Storm Surge Inundation

5.1 Introduction

It is important to evaluate the hazard of the inundation caused by not only tsunamis but also storm surges in terms of the inundated area and height, and quantify the protective effective of breakwaters. Although the frequency of storm surge inundation in urban areas is higher than that of tsunamis, there are still few data that can be used as verification data. Therefore, the number of study focusing on the storm surge inundation over coastal city is still few. Here, two examples of high-resolution storm surge inundation simulation are introduced. Blumberg et al. (2015) has developed and validated high-resolution, hydrodynamic model that encompasses the urban coastal waters of New Jersey along the Hudson River Waterfront opposite New York City, New York for simulating inundation during Hurricane Sandy. A square model grid (Δx = 3.1 m) combined with a high-resolution lidar elevation dataset permits a street-by-street focus to inundation modeling. Validation against 56 watermarks and 16 edgemarks provided via the USGS and through an extensive crowdsourcing effort consisting of photographs, videos, and personal stories shows that the model is capable of computing overland water elevations quite accurately throughout the entire surge event. A series of validation showed fine performance (the correlation coefficient between the watermark observations and the model results is 0.92 and the standard deviation of the residual error is 0.07 m) and the model applicability to suggestion of location of prevention facility could be built. Takagi et al. (2015) has conducted the building-resolving simulation (Δx = 10 m) using Delft3D-FLOW validated by their own field investigation targeting downtown Tacloban in Leyte Island, the Philippines. A series of their works showed that flow velocities along the street in Tacloban downtown reached up to 7 m/s due to flow contraction along the high-density blocks of houses, and water surface elevations reached their peaks in just 10 min. In addition, it has been concluded that pedestrian evacuation in the middle of a storm surge generated by a strong typhoon is a high-risk behavior as a key finding. These two works showed the building-resolving storm surge inundation simulation in high-resolution gave reliable results to some extent. However, similarly to tsunami, a practical storm surge simulation

that allows the coarser spatial resolution than the order of 10 m is still required as an alternative to the introduced building-resolving simulation (i.e. SRM) when numerous ensemble cases are still needed. Unfortunately, the SGS models such as the iDFM targeting on the storm surge inundation have not been discussed and roughness distribution according to land usage is still used in the practical simulation.

The cause of the storm surge is the low pressure due to typhoons or exclusive cyclones, while the cause of the tsunami is earthquake. These two phenomena are totally different but the governing equations are the same (here 2D-SWE). Therefore, the iDFM presented in Chapter 4 can be implemented in the storm surge simulation using 2D-SWE.

Chapter 5 aims to examine the applicability of the iDFM to storm surge inundation targeting wider range of domain size than the one used in high-resolution simulation. The huge storm surge inundation event in coastal city, Tacloban, Palo and Tanauan, in Leyte island caused by typhoon Haiyan in 2013 is used as a case study and the available field survey data (inundation depth and limit of inundation) is used for the validation. In addition, the virtual tsunami inundation simulation based on the historical tsunami in 2012 is conducted to discuss the different and common points of model performance of the iDFM compared to Onagawa case presented in Chapter 4.

5.2 Typhoon Haiyan

Typhoon Haiyan (Yolanda in local name) striking the Philippines, Vietnam, and nearby areas in November 2013, was an extremely intense tropical cyclone, which has been so-called as a super typhoon. The minimum central pressure of the Haiyan was 895 hPa, and the maximum gust peak speed was over 90 m/s (Mori et al., 2014). Typhoon Haiyan was the 11th typhoon of such minimum central pressure recorded in the last 30 years in the western North Pacific Ocean and was the most powerful typhoon to make landfall to date (Lin et al., 2014; Schiermeier, 2013).

Typhoon Haiyan gave catastrophic not only human but also economic damage to Leyte and Samar due to the above mentioned extensive intensity. National Disaster Risk Reduction and Management Council (NDRRMC; as of 6 March, 2014) reported that 6245 persons were killed, 28,626 were injured and 1039 are still missing over the entire Philippine. On the other hand, around 34,366 million pesos (775 million USD) of total economic loss associated with infrastructure and agriculture was estimated (TIME, 2013). Japan Society of Civil Engineers (JSCE) and Philippine Institute of Civil Engineers (PICE) jointly carried out a field survey (Tajima et al., 2014). The survey revealed a clear contrast of inundation characteristics. While the inner part of San Pedro bay showed relatively high inundation heights, the east coast of Leyte also had comparably high inundation height even outside the San Pedro Bay (Tajima et al., 2014). In particular, Tacloban, Palo and Tanauan, which are built-up areas in the west coast of San Pedro Bay, recorded 25 m, 17 m, and 15 m, respectively (Tajima et al., 2014).

Several studies regarding evaluation of the typhoon intensity characteristics or coastal hazard assessment induced by Haiyan have been conducted. Mori et al. (2014a, 2014b) conducted the numerical experiments validated by the field survey results of Tajima et al.

Table 5.1: Summary of computational setup for the WRF in the case of WRF-0550

	D1	D2
Target typhoon	Typhoon Haiyan	
Period	00:00, 5th, Nov., 2013-00:00, 10th, Nov., 2013 UTC	
Horizontal resolution	3 km	1 km
Horizontal grids	1334 × 667	1501 × 703
Vertical resolution	56 layers	
Initialization of SST	MGDSST by MRI	
Initialization of Atmos.	NCEP FNL	
Spectrum Nudging (SN)	ON (every 3600 second)	OFF
Cumulus convection scheme	OFF	
Cloud microphysics scheme	WSM 6-class graupel scheme (Hong and Lim, 2006)	
PBL scheme	YSU scheme (Hong and Lim, 2006)	

(2014) using the Weather Research and Forecasting (WRF) model (Skamarock et al., 2008) and the coupled Surge, WAve and Tide model referred to as SuWAT (Kim et al., 2015) for atmospheric and storm surge models, respectively. The authors showed the coherent structure of the storm surge profile due to the specific bathymetry of Leyte Gulf and the Philippines Trench as a major contributor to the disaster in Tacloban, and indicated the sensitivity of storm surge forecast.

5.3 Setup of the storm surge inundation simulation

5.3.1 Atmospheric model

The storm surge simulation needs pressure and wind speed fields caused by a typhoon to calculate pressure-driven and wind-driven surges. Here, the author uses the WRF model to simulate atmosphere including pressure and wind speed induced by Haiyan. The author follows the numerical setup utilized the case of WRF-0550 in Mori et al., (2014a), which is summarized in Table. 5.1. A single-moment six-category microphysics scheme was used for cloud microphysics, and no cumulus cloud parameterization was applied. The Yonsei University (YSU) scheme was adopted as the planetary boundary layer (PBL) scheme. The domain size of the WRF was approximately 4000 × 2000 km mainly centered at 130 °E and 10 °N, and sensitivity to domain size was examined in advance. The initial, lateral, and sea surface boundary conditions for WRF were taken from the Final Operational Global Analysis by National Centers for Environmental Prediction and Japan Meteorological Agency's (JMA) Global Spectral Model. The downscaling of the typhoon by NWP could not control the track; therefore, data assimilation using spectral nudging (SN) was configured to use wavenumber 3 relative to domain size, and lower components of analysis data were applied for several runs of the WRF simulations.

5.3.2 Storm surge model

Storm surge was simulated using the SuWAT. In SuWAT, surge and wave modules are applied to numerical domains that are nested in parallel using the Message Passing Interface (MPI) standard. The surge module in SuWAT solves the depth-integrated NSWE by using the staggered-C grid in space and the leapfrog method in time:

$$\frac{\partial \eta}{\partial t} + \frac{\partial M}{\partial x} + \frac{\partial N}{\partial y} = 0 \tag{5.1}$$

$$\begin{aligned}\frac{\partial M}{\partial t} + \frac{\partial}{\partial x}\left(\frac{M^2}{D}\right) + \frac{\partial}{\partial y}\left(\frac{MN}{D}\right) = fN - gD\frac{\partial \eta}{\partial x} + \frac{D}{\rho}\frac{\partial P}{\partial x} + \frac{1}{\rho}(\tau_s^x - R_x + F_R^x) \\ + A_h\left(\frac{\partial^2 M}{\partial x^2} + \frac{\partial^2 M}{\partial y^2}\right)\end{aligned} \tag{5.2}$$

$$\begin{aligned}\frac{\partial N}{\partial t} + \frac{\partial}{\partial x}\left(\frac{MN}{D}\right) + \frac{\partial}{\partial y}\left(\frac{N^2}{D}\right) = -fM - gD\frac{\partial \eta}{\partial y} + \frac{D}{\rho}\frac{\partial P}{\partial y} \\ + \frac{1}{\rho}(\tau_s^y - R_y + F_R^y) + A_h\left(\frac{\partial^2 N}{\partial x^2} + \frac{\partial^2 N}{\partial y^2}\right)\end{aligned} \tag{5.3}$$

in which P is the atmospheric pressure, f is the Corioris parameter, A_h is the horizontal eddy diffusions and other notations correspond to Chapter 4. F_R^x and F_R^y represent the components of the depth-averaged wave-induced radiation stress:

$$F_R^x = -\frac{\partial S_{xx}}{\partial x} - \frac{\partial S_{xy}}{\partial y} \tag{5.4}$$

$$F_R^y = -\frac{\partial S_{yx}}{\partial x} - \frac{\partial S_{yy}}{\partial y} \tag{5.5}$$

where the wave-induced radiation stresses are represented by

$$S_{xx} = \rho g \iint \left[\frac{C_g}{C}\cos^2\theta + \frac{C_g}{C} - \frac{1}{2}\right] E d\sigma d\theta \tag{5.6}$$

$$S_{xy} = \rho g \iint \left[\cos\theta \sin\theta\right] E d\sigma d\theta \tag{5.7}$$

$$S_{yy} = \rho g \iint \left[\frac{C_g}{C}\sin^2\theta + \frac{C_g}{C} - \frac{1}{2}\right] E d\sigma d\theta \tag{5.8}$$

in which C and C_g are the wave celerity and group velocity, σ and θ are the angular frequency and the wave direction, and E is the energy density spectrum, respectively. The depth-averaged wave radiation stress estimated from SWAN is included in the momentum equations that are solved by the surge modules. $\boldsymbol{\tau_s} = [\tau_s^x, \tau_s^y]$ denotes the wind stress usually represented as follows;

$$\boldsymbol{\tau_s} = \rho_a C_w \boldsymbol{W}|\boldsymbol{W}| \tag{5.9}$$

where ρ_a is the density of air, C_w is the wind drag coefficient, and $\boldsymbol{W} = [W_x, W_y]$ is the wind speed at 10 m height.

5.3.3 Numerical setup of the storm surge model

Table.5.2 describes the summary of the computational setup. The computational duration is 5 days (from 00:00 UTC on November 5th to 00:00 UTC on November 10th in 2013) using 0.2 second time increment. This study uses four domain nesting (grid spacing $\Delta x =$ 2430 m, 810 m, 270 m, and 90 m in D1 to 4). The computational domains use General Bathymetric Chart of the Oceans (GEBCO, 2014) and LiDAR data as bathymetric and topographic data shown in Fig. 5.1, respectively. Fig. 5.1(b) shows the last domain (i.e. D4) targeting San Pedro Bay and its coastal regions, which contain three urban areas, Tacloban, Palo, and Tanauan mentioned in Section 5.2.1. As for the treatment of urban areas in D4, the cases of iDFM use the sum of drag forces applied to individual buildings in each grid cell (same as Chapter 4), whereas the CNTL use the manning's coefficient 0.040 in land following the previous researches (Takagi et al., 2015; Kim et al., 2017) since the land usage data is not available.

The SGS parameters (i.e. $\bar{A}_x$, $\bar{A}_y$, $\bar{h}_b$ and N_b) shown in Fig. 5.2 are calculated following the methods mentioned in Chapter 4 based on the building shape data obtained in OpenStreetMap, which is an editable map database built and maintained by volunteers and distributed under the Open Data Commons Open Database License. Unfortunately, the dataset is not as it is in 2013 but 2021, but the author confirmed the building layouts in Tacloban, Palo and Tanauan do not change so much based on aerial photographs before Haiyan landfall in Google Earth. The building height is assumed as 3 m (single-story building, if building width is less than 10 m), 6 m (two-story building, if building width is more than 10 m), or 10 m (large factory or shopping mall, if building width is more than 100 m) since the building height data is not included in the building shape data. The building drag coefficient follows the setup in Chapter 4. The SuWAT uses the wave model of Simulating Waves Nearshore (SWAN, Booij et al., 1999), is used to calculate radiation stress and wind drag coefficient in ocean. The astronomical tidal effects are excluded from the simulation for simplicity since the expected tidal level at 0:00 am on November 8th was 0.15 m (Mori et al., 2014).

Table 5.3 shows the implement of wind drag coefficient C_w in SuWAT. In ocean, C_w is calculated as the wave dependent C_w by Janssen (1989) in SWAN. On the other hand, C_w in land uses the linear function of the magnitude of wind speed at 10 m height, $U_{10} = |\boldsymbol{W}|$, proposed by Honda and Mitsuyasu (1980);

$$C_w = \begin{cases} (1.29 - 0.024\,U_{10}) \times 10^{-3} & (U_{10} < 8\,[\mathrm{m/s}]) \\ (0.581 + 0.063\,U_{10}) \times 10^{-3} & (U_{10} \geq 8\,[\mathrm{m/s}]) \end{cases} \tag{5.10}$$

However, the Honda-Mitsuyasu's function (hereafter denoted as HM-function) was derived from experimental work targeting wind wave growth in ocean. Furthermore, the wind speed reduction by obstacles such as buildings on land is not implemented in atmospheric model when the spatial resolution is much coarser than building dimensions (e.g. $\Delta x >$ the order of 1 km). Therefore, the implementation of the feedback of buildings to wind stress term is needed to model the wind-driven surge on land areas. This study uses four different options for the implement of C_w to evaluate the effect of such feedback of buildings to wind stress term. The case of CNTL and iDFM-WDON use HM-function in all land mesh grid not considering the effect of buildings. The case of iDFM-WDBuildSub

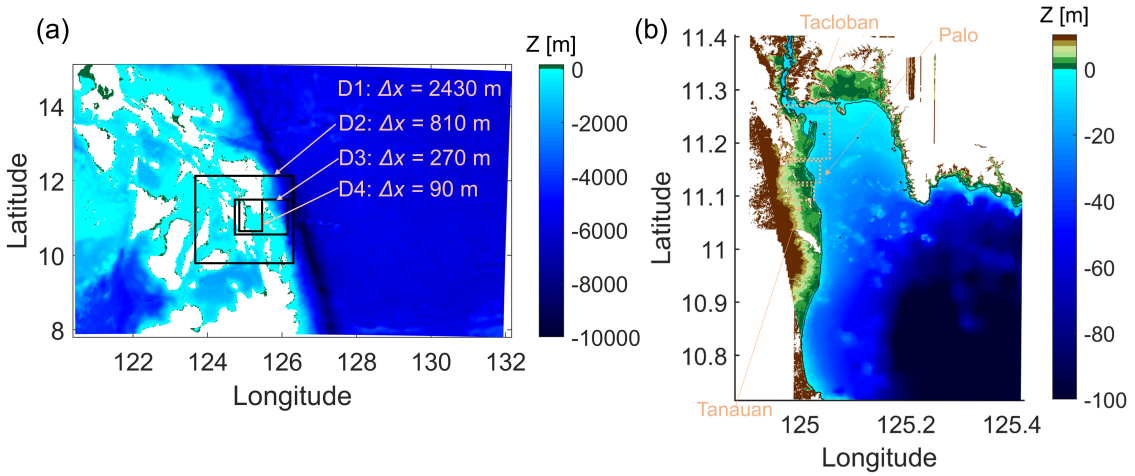

Figure 5.1: Topography and bathymetry in (a): D1 (Philippine Sea, $\Delta x = 2430$ m) and (b): D4 (Leyte Gulf, $\Delta x = 90$ m); black boxes show the nested area D2-4.

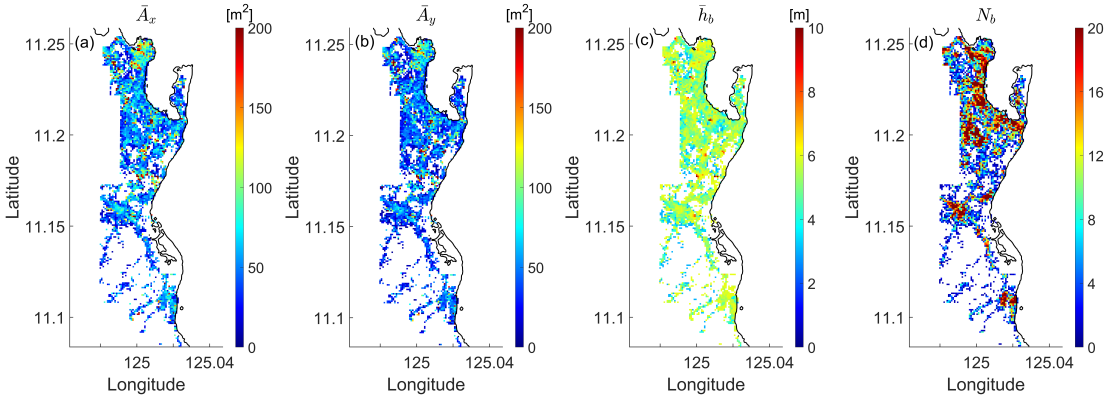

Figure 5.2: SGS parameters in $\Delta x = 90$ m in target area; (a): $\bar{A}_x$ and (b): $\bar{A}_y$, and (c): $\bar{h}_b$, and (d): N_b (black line shows shoreline).

Table 5.2: Summary of computational setup for iDFM and CNTL

	iDFM	CNTL
Period (YYYY/MM/DD hh:mm)	2013/11/05 00:00 - 2013/11/10 00:00 UTC	
Time step Δt	0.2 s	
Horizontal resolution Δx	2430 m (D1) 810 m (D2) 270 m (D3) 90 m (D4)	
Manning's coefficient n	0.025 (all area)	0.040 (land) 0.025 (ocean)
Wind drag coefficient C_w	Table. 5.3	
Building drag coefficient C_D	Eq. (4.22)	Not implemented
Wave model	SWAN (Booij et al., 1999)	
Tide model	Not implemented	

Table 5.3: Treatment of wind drag coefficient C_w in SuWAT

Case Name	C_w in land	C_w in ocean
CNTL	Honda and Mitsuyasu (1980)	Janssen (1989) (Wave induced drag force)
iDFM-WDON	Honda and Mitsuyasu (1980)	
iDFM-WDBuildSub	Honda and Mitsuyasu (1980) ($D \geq \bar{h}_b$)	
	0 ($D < \bar{h}_b$)	
iDFM-WDBuildAll	Honda and Mitsuyasu (1980) ($N_b = 0$)	
	0 ($N_b \geq 1$)	
iDFM-WDOFF	0	

uses HM-function when building is submerged (i.e. $D \geq \bar{h}_b$) and zero wind stress when building is not submerged. The case of iDFM-WDBuildAll use HM-function where no building exists (i.e. $N_b = 1$) and zero wind stress where at least one building exists.

5.4 Results and discussions

5.4.1 Atmospheric field modeled by WRF-0550

The author confirms accuracy of atmospheric field modeled by WRF model (WRF-0550) before evaluating storm surge inundation. Fig. 5.3(a) shows a comparison of the typhoon track with JMA best track. Markers show the location of center of the typhoon at the specific time. Both WRF-0550 output and JMA best track show the landfall at 0:00 UTC, 8th Nov. on Leyte island although there approximately -0.25 degree bias of track. Fig. 5.3(b) shows the time series of the typhoon intensity (i.e. sea surface pressure, SLP) compared with JMA best track data. Regarding the SLP, the WRF-0550 gives close value to the observation in landfall date (0:00 UTC, 8th Nov.) and its error is approximately 10 hPa though it overestimates at highest intensity. Thus, the accuracy of atmospheric field by WRF-0550 is still enough to simulate the storm surge inundation.

5.4.2 Effect of wind stress term implementation corresponding to building information

Next, the effect of the difference of C_w and improvement on the storm surge model results are discussed. The survey results by Tajima et al. (2014) (here inundation limits) are used to discuss model accuracy. The spatial inundation characteristics such as limits of inundation, inundation depths, or current velocities are mainly examined following Chapters 3 and 4. Figs. 5.4(a) and (b) show the differences of maximum inundation extents in the cases of iDFM-WDON (hereafter "iDFM-" is omitted), WDBuildSub, WDBuildAll, WDOFF, and survey results in Tacloban, and Palo · Tanauan area, respectively. Note that the survey data is shown only in Tacloban area. All cases modeled by the iDFM overestimated the limit of inundation in Tacloban area. However, the extent of overestimation by WDBuildSub, WDBuildAll, and WDOFF is larger than WDON, which indicates the possibility of model improvement using C_w implementations (Note that WDBuildSub gives

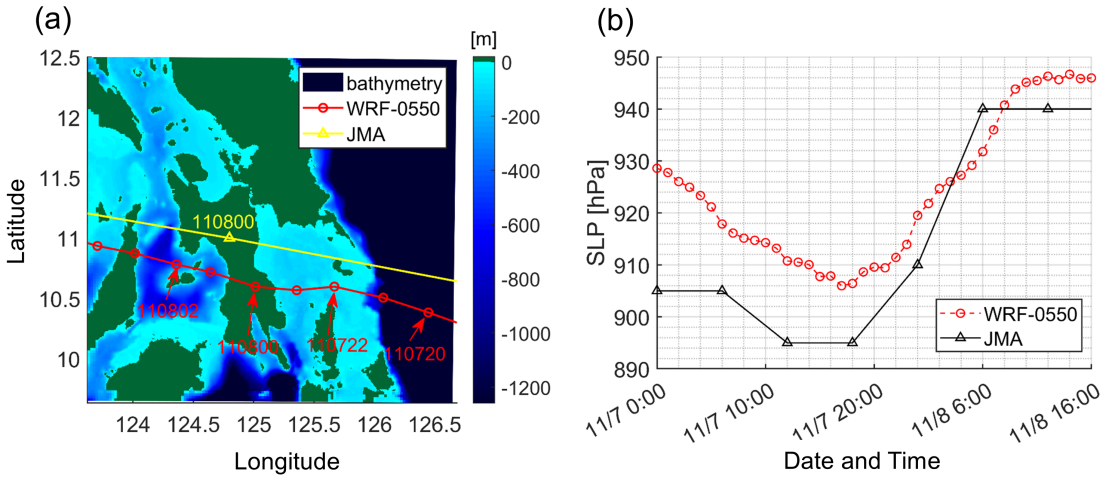

Figure 5.3: Meteorological information of typhoon Haiyan; (a): comparison of TC track between WRF-0550 (red) and JMA best track (yellow) with bathymetry (color contour), and (b): Time series of minimum SLP by WRF-0550 result (red dash line) and JMA best track data (black line).

the same result as WDBuildAll in Tacloban area). As explained in Section 5.3.3, the wind speed field on land area calculated by WRF basically does not include the feedback from the buildings and vegetation because of the coarse resolution. Therefore, the calculated wind stress term can larger than real as long as any correction based on building information is not done because the wind speed can overestimate. The differences among WDBuildSub, WDBuildAll, and WDOFF are small in Tacloban area. Here, most inundated grid cells have at least one building (i.e. $N_b \geq 1$). It is considered that the condition of $C_w = 0$ can be fulfilled during whole the inundation process for these three cases. On the other hand, Palo & Tanauan area gives different tendencies, where the results except WDOFF are similar and wider area than WDOFF. Wide area in Palo & Tanauan area is covered with the numerous plantation farms and the number and density of buildings is lower than Tacloban area. Hence, the feedback on the wind stress term from buildings is smaller, which can be the reason of small differences among WDON, WDBuildAll and WDBuildSub while WDOFF gives smaller limit of inundation. Still, the centers of Palo and Tanauan (annotated in Fig. 5.4(b) with arrow) accumulate buildings, and WDBuildAll and WDBuildSub show smaller limit than WDON in the backside of the centers (i.e. the east side).

Next, the spatial distributions of inundation depths and maximum velocities are examined. Fig. 5.5 show the absolute and relative differences between WDBuildSub or WDBuildAll, and WDON. These two cases, WDBuildSub and WDBuildAll, show similar difference between WDON, where the absolute and relative difference are within 0.25 m and 10%, respectively near shoreline. The relative difference is larger as the distance from the shoreline is longer. In both WDBuildSub and WDBuildAll cases, more than 30% relative difference is observed. Fig. 5.6 show the differences of maximum fluid velocities in the same format in Fig. 5.5. The absolute and relative difference are within 0.25% m/s

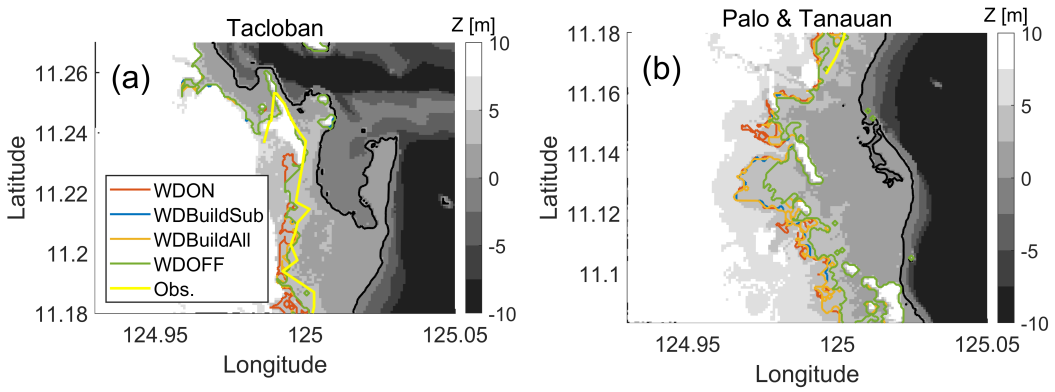

Figure 5.4: Comparison of inundation limits between implement of wind in land validated by observation by Tajima et al., 2014 in (a): Tacloban and (b): Palo · Tanauan areas. Note that WDBuildAll and WDBuildSub give the same result in Tacloban area.

and 15% on average near shoreline, though the area without buildings locally show larger velocities than WDON in both cases. The relative differences near limit of inundation is larger similarly to the inundation depth, which causes the smaller inundated area. A series of consideration shows that the influence by the implementation of wind stress change based on building information is large for velocity near limits of inundation, and such velocity reduction leads to smaller inundated area. Furthermore, the inundation limit in Tacloban area is closer to the observation than WDON, which shows the potential of the model improvement. The further challenge is estimation of the wind speed reduction ratio by buildings in storm surge model since the proposed implementation allows only zero wind stress term. Following discussion will use WDBuildSub case as the physically most sophisticated case.

5.4.3 Validation of iDFM and CNTL run based on survey results

Next, the iDFM (WDBuildSub) is validated compared with the observation and CNTL. Fig. 5.7 shows the limits of inundation modeled by the iDFM (red line) and CNTL (blue line) with observation (yellow line). The iDFM approach shows the smaller limit than the CNTL in Tacloban area, and the model accuracy is improved very well. The reason of such improve can be both the wind stress and velocity reduction by building feedback and the quantitative analysis of the velocity will be done. On the other hand, the difference of the limit of inundation in Palo & Tanauan area between iDFM and CNTL is smaller than Tacloban area.

Next, the maximum inundation depths are examined. Figs. 5.8(a) and (b) show the spatial distribution of maximum inundation depths from iDFM and CNTL. Relatively large inundation depths (more than 3 m) are observed near shoreline from both cases. However, the values of inundation depths decrease near run-up limits. Further analysis of the spatial distribution of them will be discussed referring to several representative cross-section along run-up direction in next subsubsection. Overall model performances of iDFM and CNTL are examined using observed inundation depths at 15 survey points (Tajima et

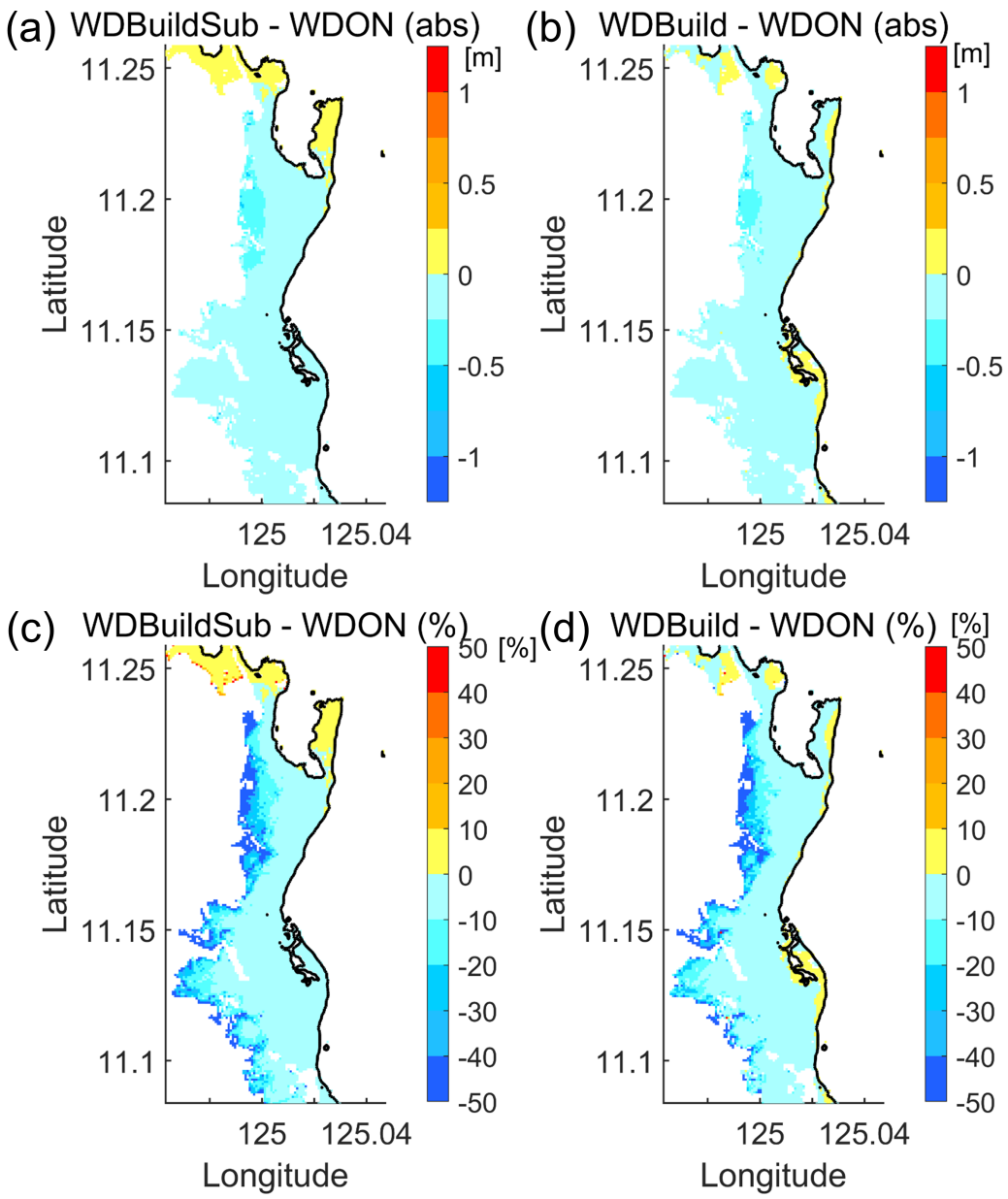

Figure 5.5: Absolute differences of maximum inundation depths (a: WDBuildSub - WDON and b: WDBuild - WDON), and relative differences (c: WDBuildSub - WDON and d: WDBuild - WDON).

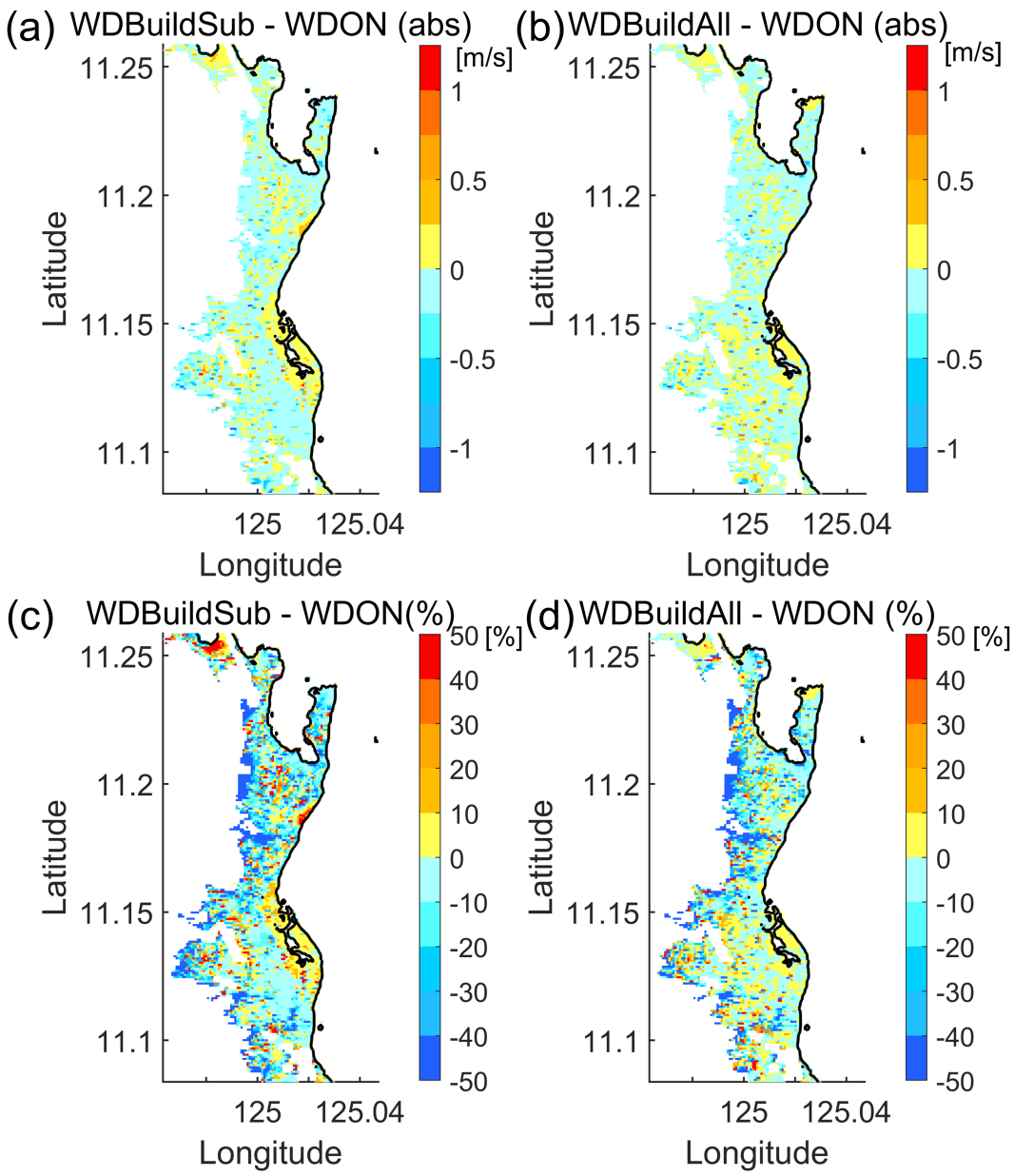

Figure 5.6: Absolute differences of maximum fluid velocities (a: WDBuildSub - WDON and b: WDBuild - WDON), and relative differences (c: WDBuildSub - WDON and d: WDBuild - WDON).

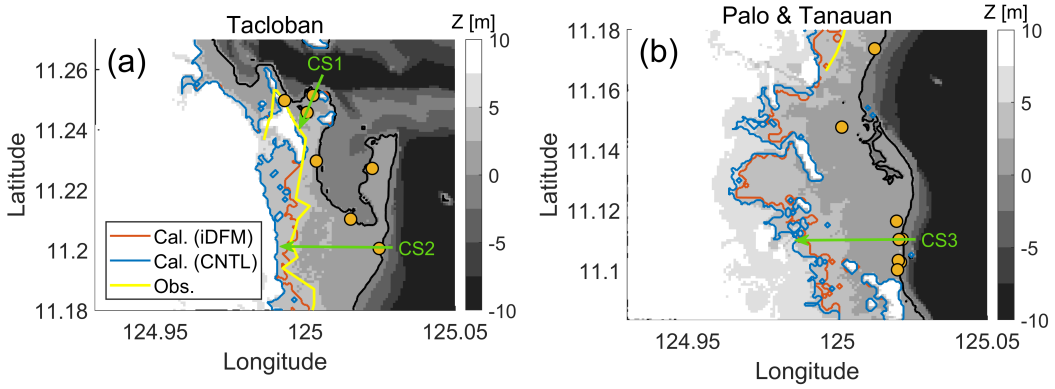

Figure 5.7: Comparison of inundation limits between iDFM (WDBuildSub; red line) and CNTL (blue line) in land validated by observation by Tajima et al. (2014) in (a): Tacloban area and (b): Palo · Tanauan area.

al., 2014) shown in Fig. 5.8(a). Note that survey points with low reliability or according to wave overtopping are excluded from the analysis. Fig. 5.8(c) shows inundation depths at each point. The root mean square error (RMSE) and average relative error (RERR) were calculated and shown as follows;

$$RMSE = \sqrt{\sum_{i=1}^{n_{obs}} \frac{(\hat{D}_i - D_i)^2}{n_{obs}}} \tag{5.11}$$

$$RERR\,[\%] = 100 \times \frac{1}{n_{obs}} \sum_{i=1}^{n_{obs}} \frac{|\hat{D}_i - D_i|}{\hat{D}_i} \tag{5.12}$$

where n_{obs}, $\hat{D}_i$, and D_i denote the number of survey points, observed inundation depth at i-th point, and calculated inundation depth at i-th point, respectively. The difference between iDFM and CNTL is within 0.2 m in all the points since most points are located near shoreline. Points 1-8 in Tacloban area shows less than 0.5 m error for iDFM at Points 1, 3, 5, and 7 (5/8 points). Points 2, 4, 6 shows approximately 1.0 m error, which can be caused by survey error and measurement error of topography. Points 9-15 in Palo · Tanauan area show less accurate due to the same reason as Points 2, 4, 6. In addition, the Points 11-13, and 15 were observed from watermarks on buildings in urban area in Tanauan, which also can contribute to the error. RMSE and RERR are approximately 0.84 m and 20%. A series of analyses showed that the accuracy of inundation depth near shoreline for iDFM and CNTL is enough.

5.4.4 Model difference between iDFM and CNTL run

This subsection focuses model difference of inundation characteristics between iDFM and CNTL. Fig. 5.9 shows the comparison of time series of inundation leading edges between iDFM (red line) and CNTL (blue line) every 20 minutes after 23:00, 7th Nov (inundation starting time). Little difference is observed within 40 minutes after inundation start except the center of Tanauan area. After that, the difference of leading edges gradually increases.

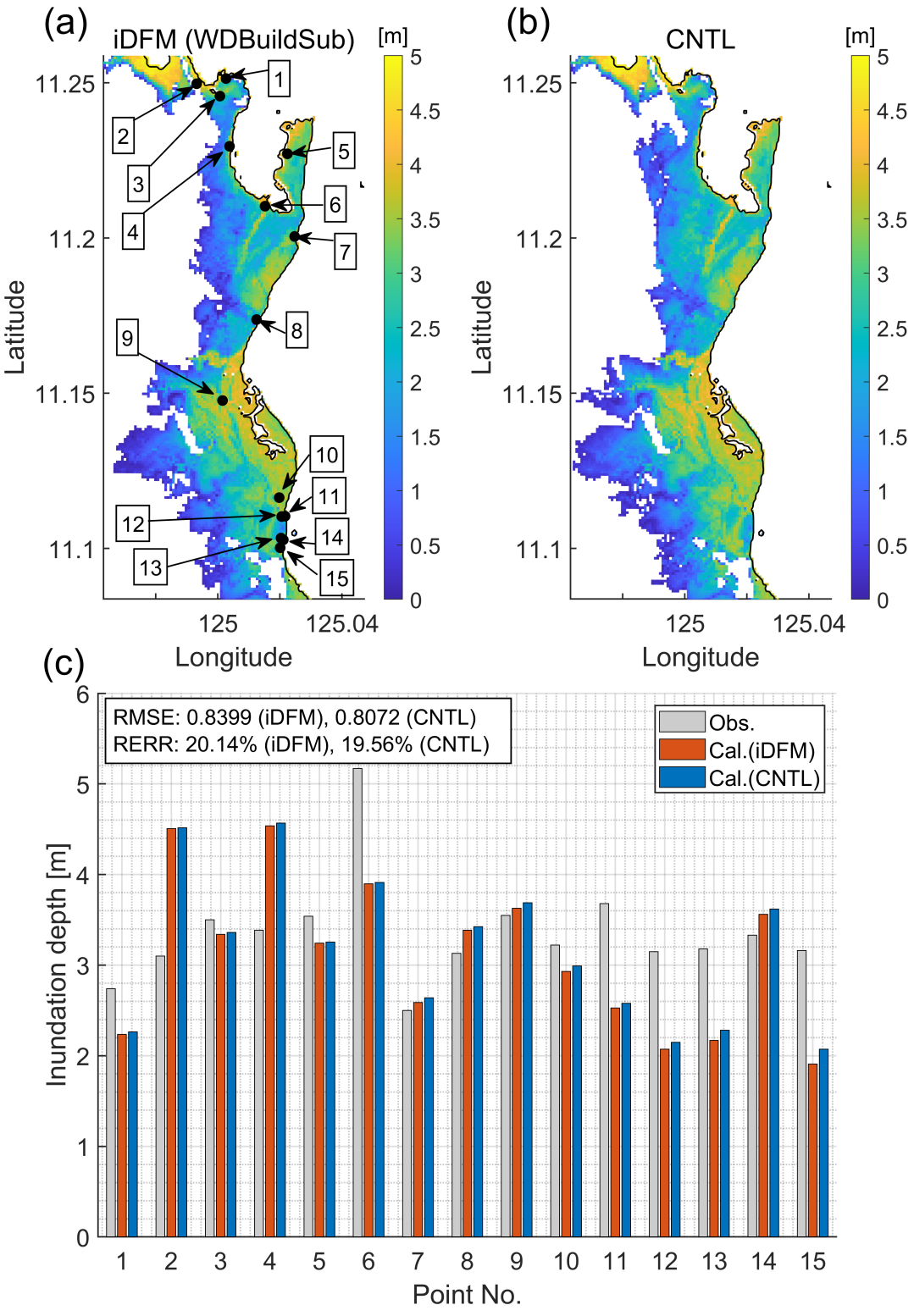

Figure 5.8: Maximum inundation depths between (a): iDFM (WDBuildSub) and (b): CNTL, and (c): comparisons at 15 observation points by Tajima et al., 2014.

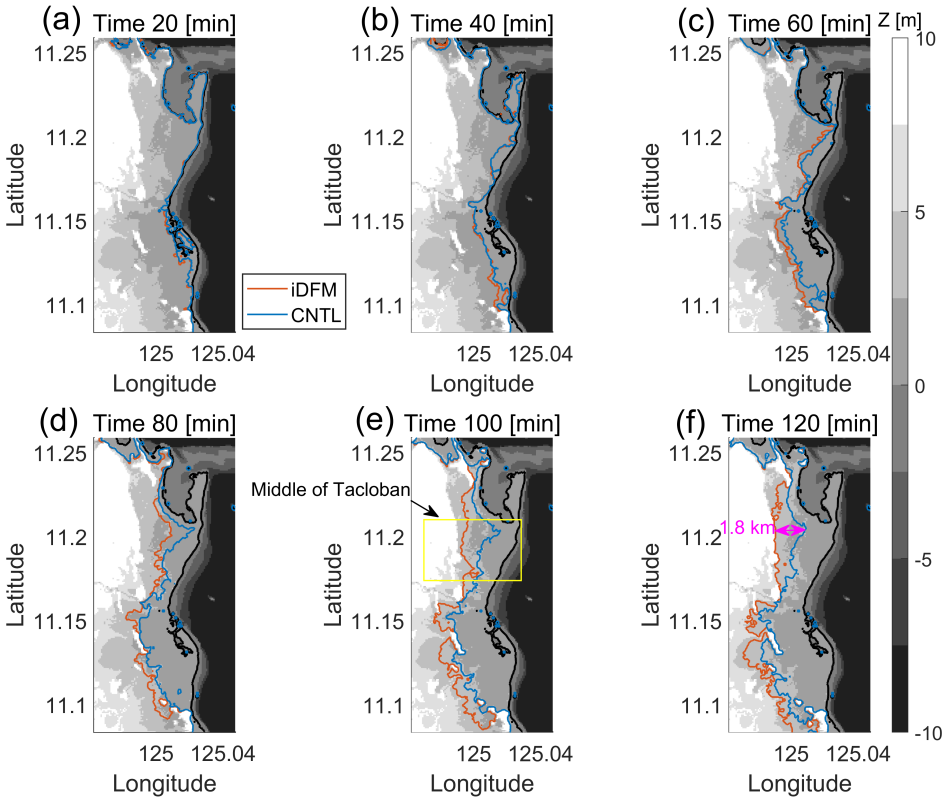

Figure 5.9: Comparison of inundation leading edges between iDFM (WDBuildSub; red line) and CNTL (blue line) every 20 minute; (a): 20 min, (b): 40 min, (c): 60 min, (d): 80 min, (e): 100 min, (f): 120 min after 2013/11/07 23:00 UTC.

In particular, the middle of Tacloban area (shown in Fig. 5.9(e)) shows significant differences and the distance between two run-up limits (iDFM and CNTL) is approximately 1.8 km 120 minutes (shown in Fig. 5.9(f)) after the inundation start.

Next, the spatial distribution of the maximum inundation depth is compared for iDFM and CNTL. Figs. 5.10(a) and (b) show the absolute and relative difference of maximum inundation depths between the iDFM and CNTL. The absolute and relative differences with less than 0.25 m and 10% are widely distributed near shoreline as shown in previous subsubsection. However, larger differences are observed in the inland area. In particular, the middle of Tacloban area (shown in Fig. 5.9(f)) shows more than 1 m and 50% differences. On the other hand, the downtown area in north of Tacloban shows smaller differences than the middle area. Both two areas explained the previous sentence area are filled with grid cells with building, which implies that inundation depth (or water surface elevation) is not sensitive to inundation depth near shoreline.

Figure 5.11 shows the spatial distributions of maximum fluid velocity by each model (a: iDFM and b: CNTL) and their differences (c: absolute difference and d: relative difference). The iDFM shows different contrast for velocity in Tacloban or Palo · Tanauan area. The cells with velocity less than 0.5 m/s are majority in Tacloban area, while the ones with velocity more than 1 m/s are majority in Palo · Tanauan area. The cells

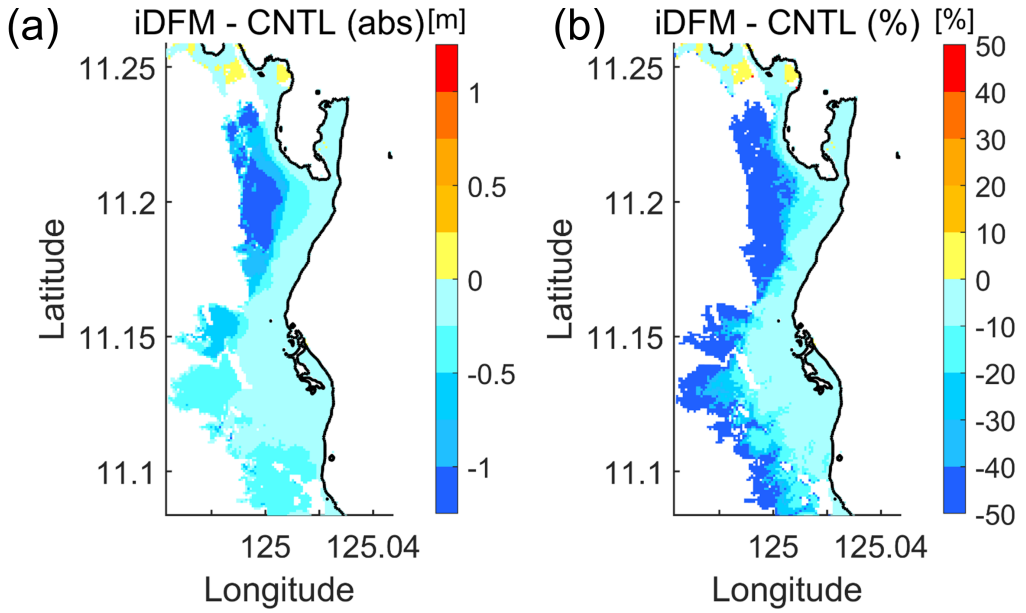

Figure 5.10: Difference of maximum inundation depths between iDFM (WDBuildSub) and CNTL (a: absolute difference and b: relative difference).

with velocity more than 1 m/s are majority in whole the area in the CNTL. Next, the absolute and relative differences are calculated in the same manner as the Fig. 5.10. The spatial pattern of the velocity reduction is similar to the spatial pattern of the number of buildings N_b. The gray contour indicates the area with $N_b = 5$ and the inside of this contour shows relatively large number of buildings are placed. The grid cells with more than 0.5 m/s and 50% velocity reduction such as whole area of Tacloban area and centers of Palo and Tanauan are mainly distributed in the gray contour. From obtained results, it is shown that the fluid velocity modeled by the iDFM are more affected by the buildings than the maximum inundation depth. In addition, observed slower inundation speed by the iDFM than the CNTL can be caused by the velocity reduction by buildings and its extent is large where buildings are numerously placed.

A series of examination of spatial distributions implies that the velocity reduction by the building resistance (i.e. drag force) in the equation of momentum conservation is accumulated as the run-up distance is longer. As a result of velocity reduction, the amount of inflow volume in the inland decreases, which causes the maximum inundation depth reduction near limit of the inundation. To confirm the hypothesis, the maximum inundation depth and fluid velocity on three representative cross-section along the run-up direction shown in Fig. 5.7. Fig. 5.12 shows comparison of inundation depth (1st row), maximum fluid velocity (2nd row), SGS parameters:$\bar{A}_x$ and N_b (3rd row), and ground elevation (4th row) along the run-up distance whose origin is at shoreline. Note that several grid points located in the sea (elevation is lower than zero) are also shown and maximum inundation depth is maximum surface elevation from mean sea level there. CS1 in the downtown area in the north of Tacloban has 450 m run-up distance since the run-up flow stops in front of the hill higher than 10 m. The difference of the inundation depths between CNTL is almost zero and the accuracy compared to the observation is within 0.5

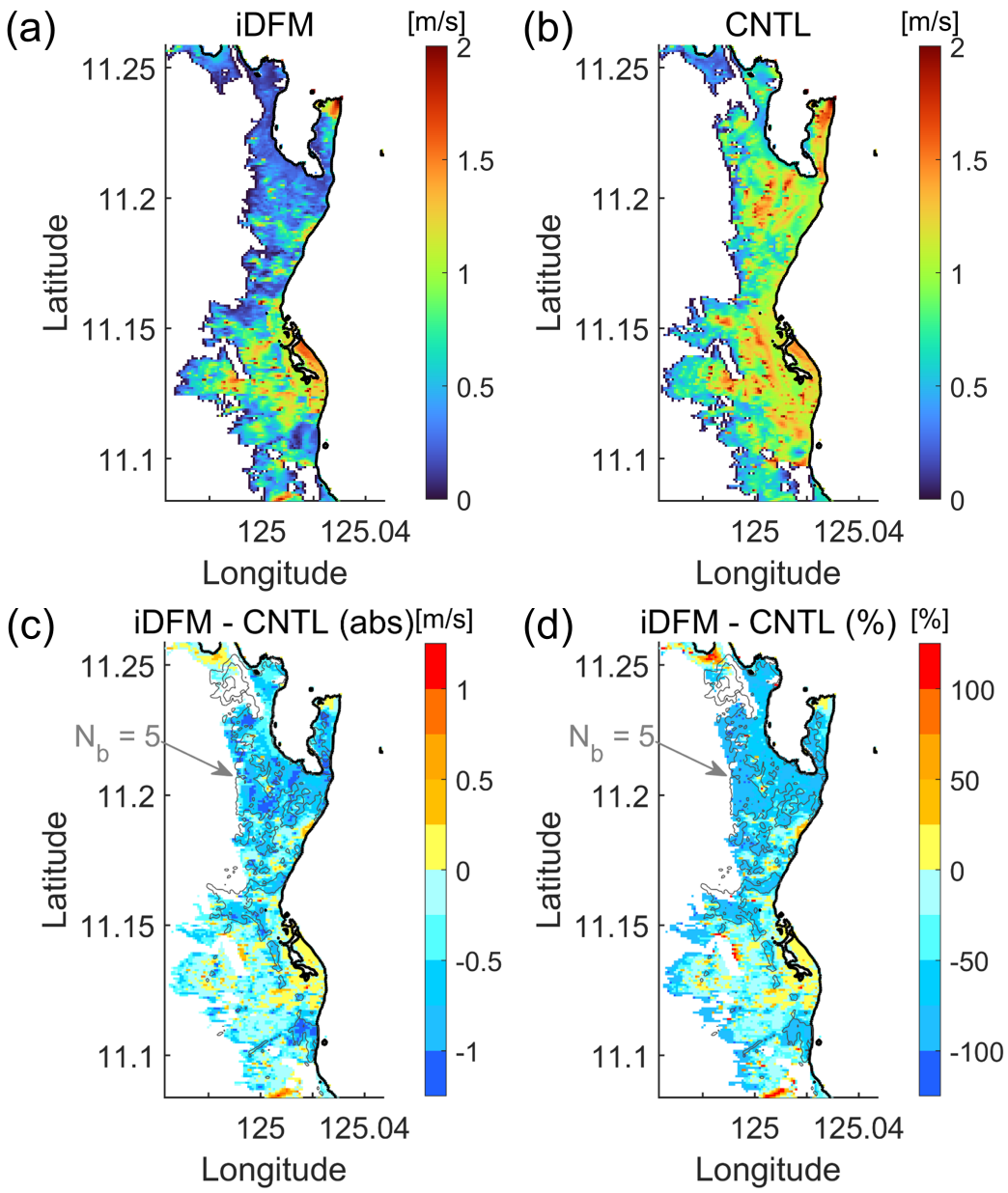

Figure 5.11: Maximum fluid velocities modeled by (a): iDFM (WDBuildSub) and (b): CNTL, and (c): absolute and (d): relative differences, respectively (black and gray line shows shoreline and contour of $N_b = 5$).

m. Beside, the iDFM gives approximately 50% smaller velocity than the CNTL especially where buildings exist. CS2 in the middle of Tacloban area shows different characteristics from CS1 since the maximum run-up distance is much larger than CS1. The difference of maximum inundation depth is still less than 0.5 m up to 1800 m run-up distance. However it gradually increase and the difference is more than 1.0 m near run-up limit. This is the different point from CS1. The velocity difference is clearer than the inundation depth and the iDFM gives more than 50% smaller velocity than the CNTL consistently from the shoreline to limit of run-up. Finally, CS3 in the center of Tanauan is examined. CS3 also showed the different characteristics from CS2 though the maximum run-up distance is similar. The little difference of maximum inundation depth is observed along whole the cross-section, while the velocity difference corresponds to the SGS parameters;$\bar{A}_x$ and N_b until the run-up distance is shorter than 1400 m. The reason of these characteristics can be that the resistance by building drag force is small due to low number of the building number and run-up flow from south direction which is not affected by buildings merges in the inland area.

A series of the analyses showed as follows

- The accuracy of the limit of inundation and maximum inundation depth modeled by the iDFM is adequate compared to the survey data.
- The inundation depth (or surface elevation) is not sensitive to the SGS parameters but the maximum fluid velocity is near shoreline.
- The inundation depth and velocity near run-up limit decrease compared to the CNTL because the velocity reduction by buildings is iterated in every time step in momentum conservation as the run-up distance is longer.
- Such velocity reduction makes large difference in leading edges of inundation and this can result in large difference of arrival time.

5.4.5 Tsunami simulation targeting typhoon Haiyan storm surge height

The storm surge inundation characteristic and accuracy modeled by the iDFM has been discussed in Section 5.4 by comparing the survey data and the roughness model used in previous study.

(1) Numerical setup

The tsunami height is assumed based on SRCMOD (Mai and Thingbaijam, 2014), which records historical earthquake rupture models all over the world, since mega earthquake tsunami has not attacked the Leyte island. The author adopted the 2012 East of Sulangan Earthquake for base of the virtual earthquake, where the source parameters (moment magnitude M_w, fault length L, fault width W, mean fault slip D_a, dip, strike and rake) are summarized in the first row in Table.5.4. Note that the author does not assume subfault for simplicity and use mean slip. The initial tsunami height is generated using the formulae of Okada (Okada, 1985) and Tanioka and Satake (1996) in the same manner in Chapter 4. This section changes M_w to 9.03 so that the time series of the tsunami height at the point near Tacloban matches storm surge height as much as possible. Fig. 5.13(a) and (b) show

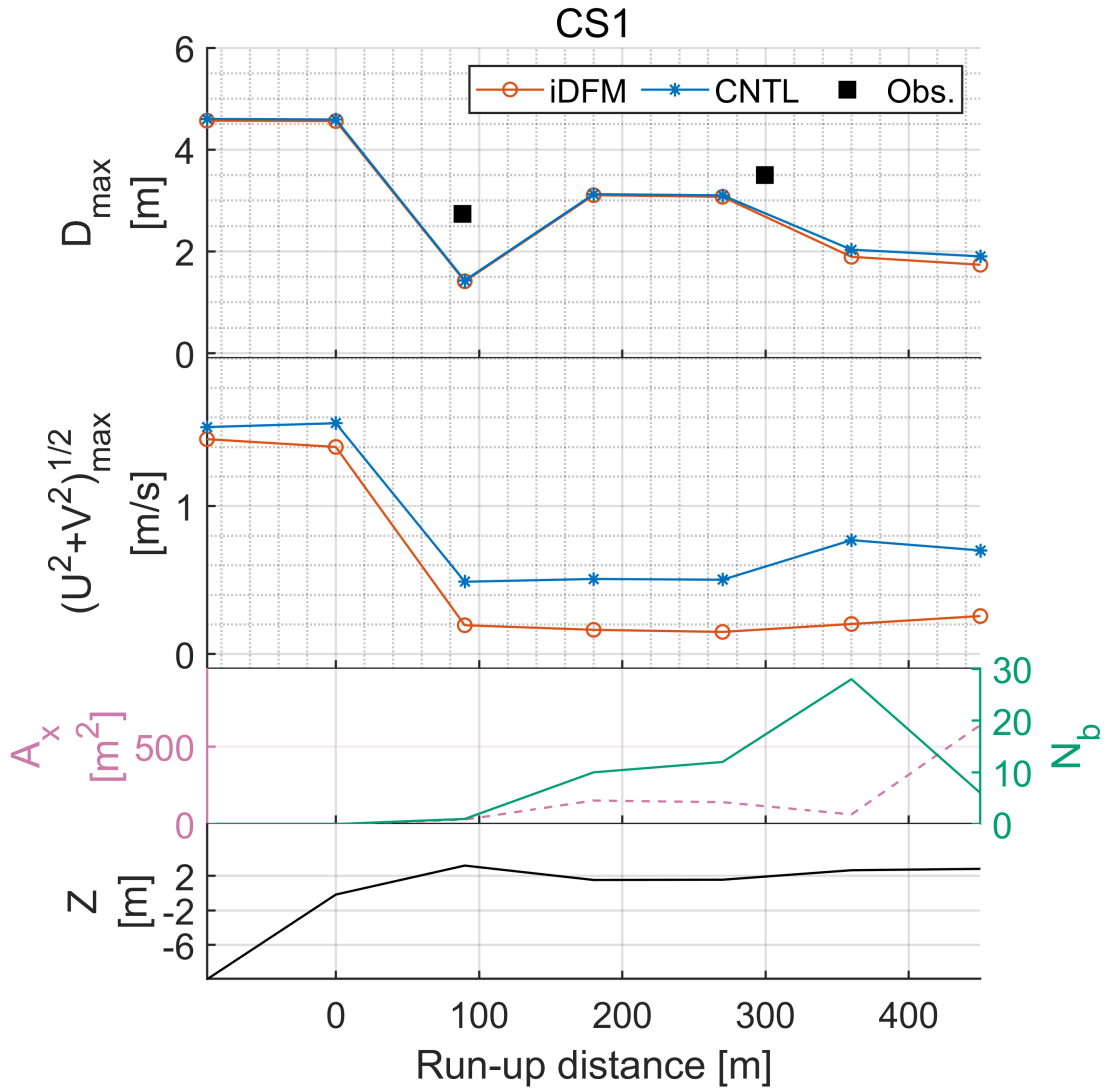

(a) CS1

Figure 5.12: Maximum inundation depths (1st panel), velocities (2nd panel) between iDFM (WDBuildSub, red) and CNTL (blue) along (a): CS1, (b): CS2, (c): CS3 shown in Figure 5.7 with SGS parameters; $\bar{A}_x$ and N_b (3rd panel) and topography (4th panel); Run-up distance is 0 m at shoreline.

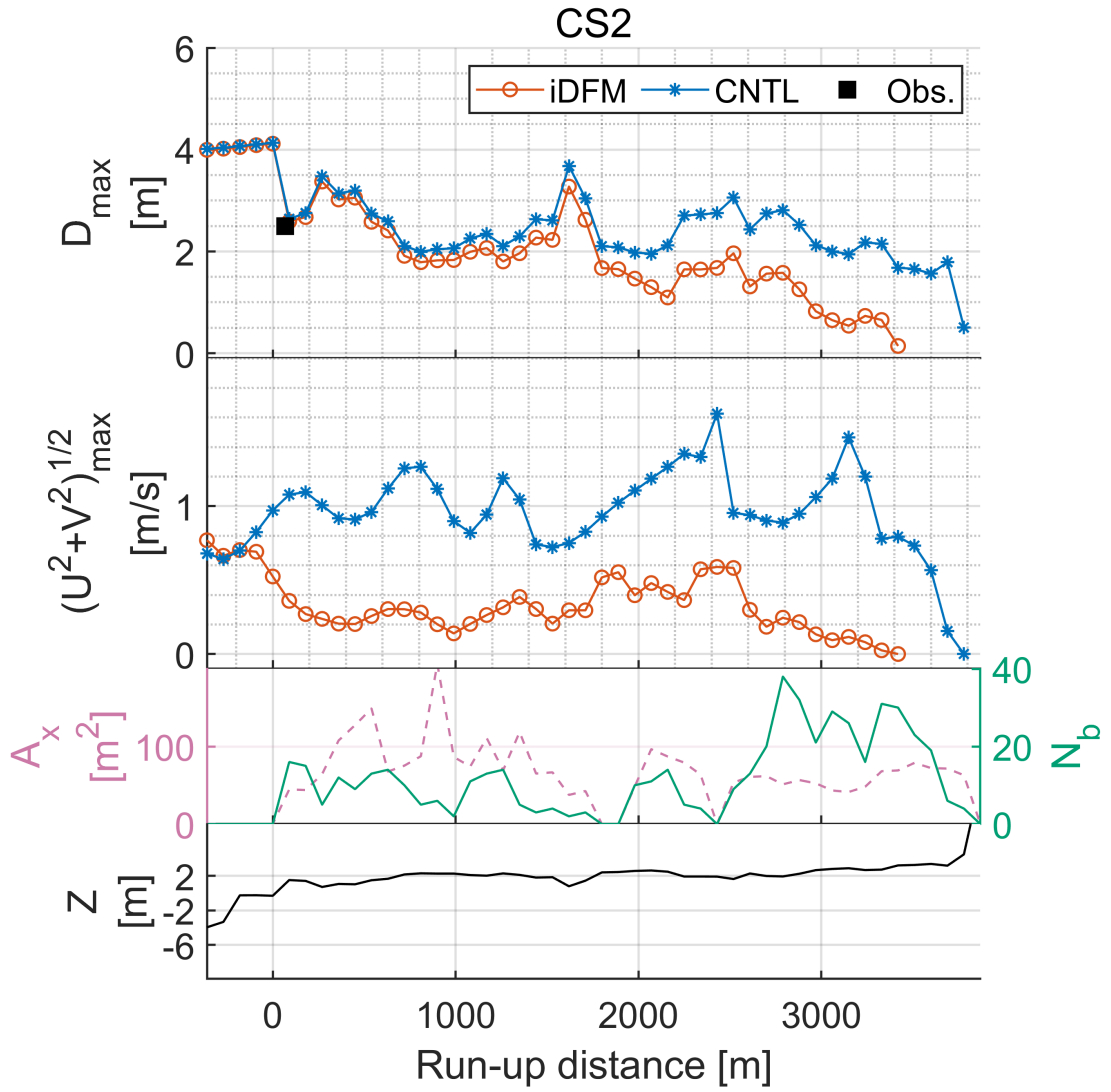

(b) CS2

Figure 5.12: Maximum inundation depths (1st panel), velocities (2nd panel) between iDFM (WDBuildSub, red) and CNTL (blue) along (a): CS1, (b): CS2, (c): CS3 shown in Figure 5.7 with SGS parameters; $\bar{A}_x$ and N_b (3rd panel) and topography (4th panel); Run-up distance is 0 m at shoreline (continued).

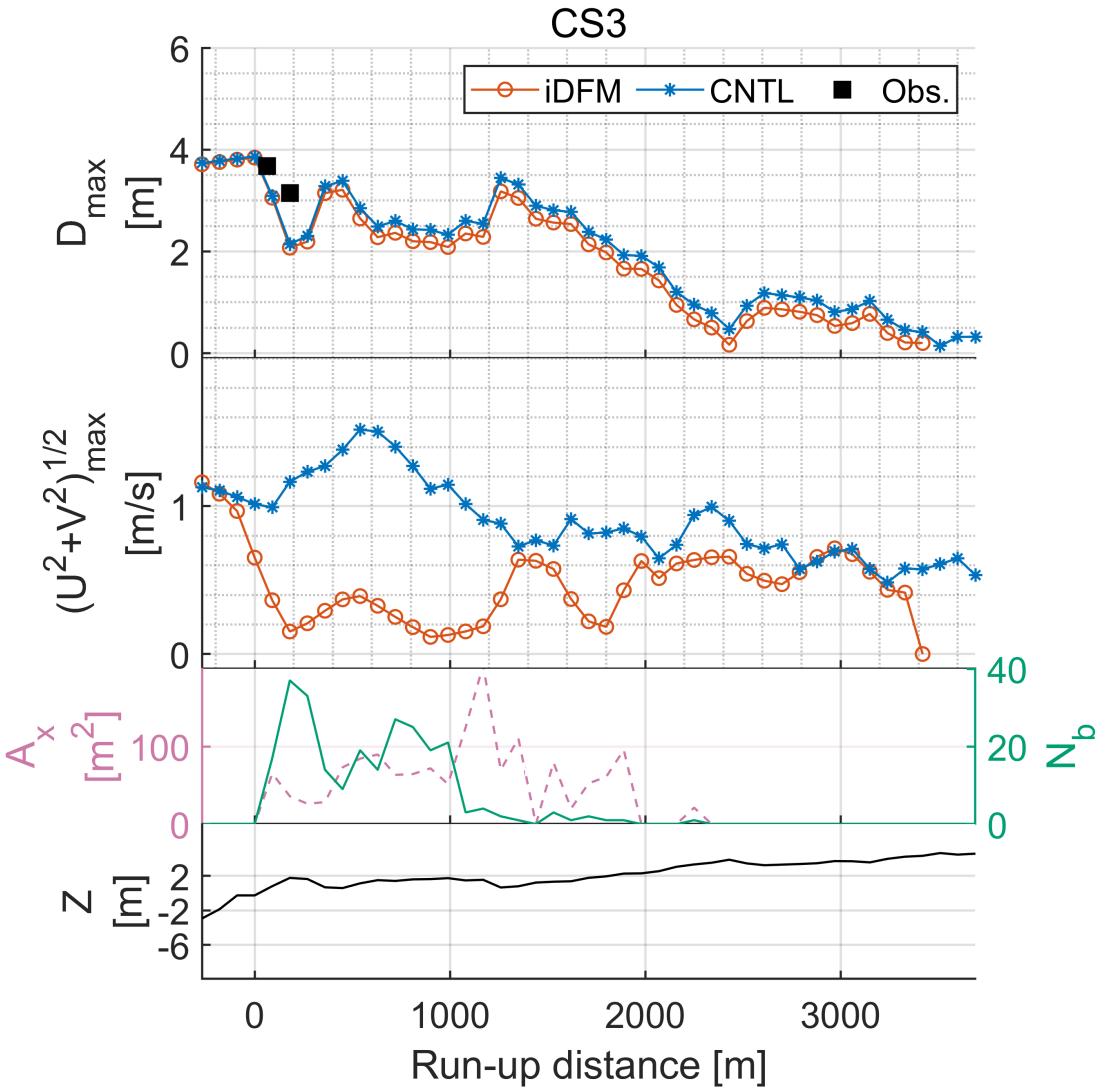

(c) CS3

Figure 5.12: Maximum inundation depths (1st panel), velocities (2nd panel) between iDFM (WDBuildSub, red) and CNTL (blue) along (a): CS1, (b): CS2, (c): CS3 shown in Figure 5.7 with SGS parameters; $\bar{A}_x$ and N_b (3rd panel) and topography (4th panel); Run-up distance is 0 m at shoreline (continued).

Table 5.4: Fault model data used in this study

Case Name	Mw	L [km]	W [km]	D_a [m]	Dip [deg]	Strike [deg]	Rake [deg]
Mw759 (Original)	7.59	128.00	90.00	0.42	45.77	345.75	56.16
Mw903	9.03	582.60	223.70	6.26			

Table 5.5: Scaling law of the fault width W, length L, mean slip D_a proposed by Goda et al. (2016). Note that random variable ϵ_W, ϵ_L, and ϵ_{D_a} are ignored for simplicity in this study.

Equations
$\log_{10} W = -1.7030 + 0.4488 M_w + 0.2053 \epsilon_W$
$\log_{10} L = -2.0106 + 0.5289 M_w + 0.1741 \epsilon_L$
$\log_{10} D_a = -3.3625 + 0.4606 M_w + 0.3250 \epsilon_{D_a}$

the time series of the surface elevation (time axis is normalized in Fig. 5.13(b)) at Station 4 near Tacloban and where the maximum wind stress is relatively small (see Fig. 5.13(c)). The fault length, width, and mean slip are calculated using the scaling relationship (see Table.5.5) proposed by Goda et al. (2016). Recalculated source parameters are summarized in Table.5.4 and generated initial tsunami height is shown in Fig. 5.14. The numerical model of tsunami propagation adopts TUNAMI-N2 (Goto et al., 1997) same as Chapters 3-4. The other setups such as topography, spatial resolution, time increment, and SGS parameters follow the storm surge simulation.

(2) Model difference between iDFM and CNTL

Figure 5.15 shows the comparison of maximum inundation depths between the iDFM and CNTL in the same format as Fig. 5.11. Note that the gray contour shows the area where $N_b = 5$. Basically, it is observed that the iDFM shows smaller inundation depth than the CNTL likewise the storm surge. The absolute and relative difference of inundation depth is within 0.5 m and 15% except near limit of inundation. However, the both absolute and relative differences have no relationship between one of the building information N_b. On the other hand, Fig. 5.16 shows the comparison of maximum velocity. Both absolute and relative difference is negative where the grid cells are surrounded by gray contour. This explains that the velocity reduction effect by buildings is applied where the number of building N_b is relatively high.

Figures 5.17 and 5.18 show the the comparisons of maximum inundation depth and velocity in Onagawa case between the iDFM and CNTL. Note that reference computation for the CNTL using the same setup in Chapter 4 except roughness coefficient in land area has been done to fix the condition for roughness coefficient in land area with the Tacloban case. The red contour shows the $\bar{A}_x = 100$ m^2. Similarly to Fig. 5.15, the both absolute and relative differences have no relationship between the one of the building information $\bar{A}_x$. However, larger absolute and relative differences in the area with $\bar{A}_x / ge 100 \mathrm{m}^2$ and the velocity reduction effect by buildings is applied where the projected area of buildings

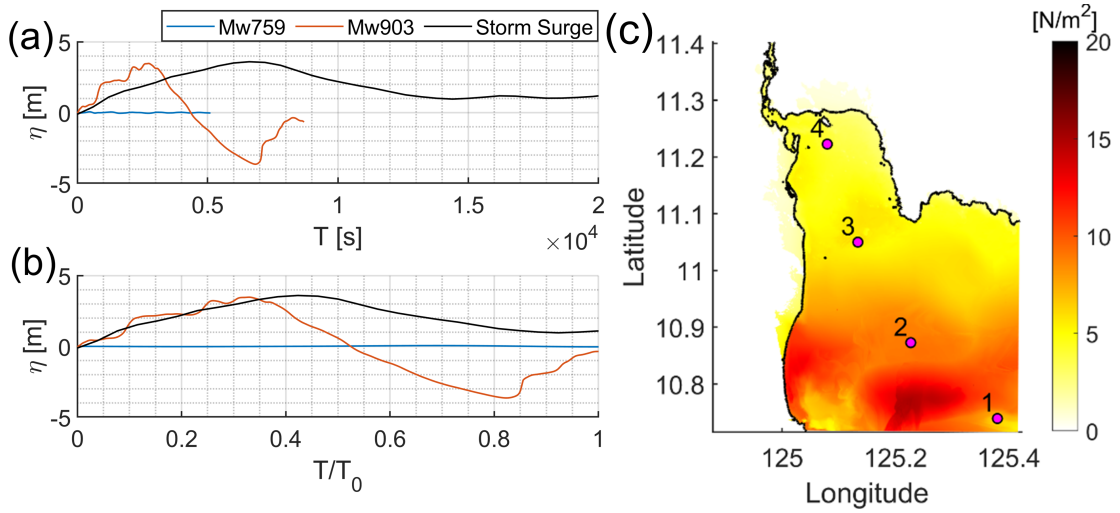

Figure 5.13: Time series of surface elevation at Station 4 (a: time is not normalized, b: time is normalized by period) and (c): maximum wind stress.

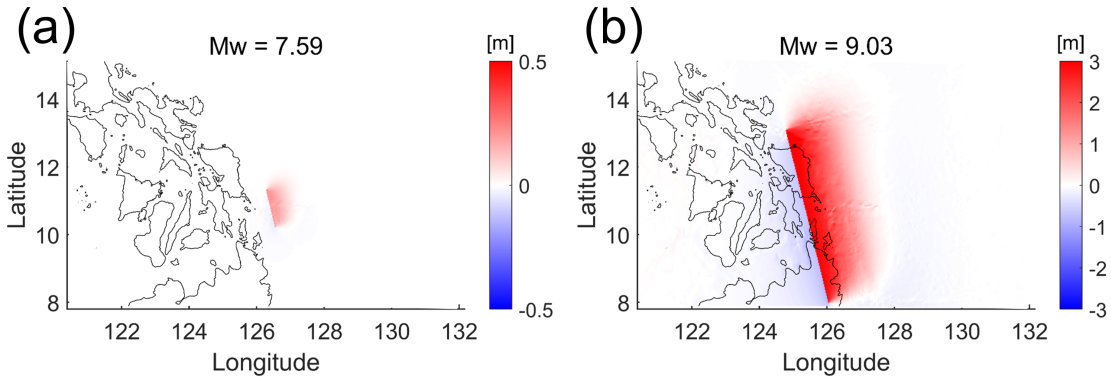

Figure 5.14: Initial tsunami height calculated by slip by Okada (1985) together with the equation by Tanioka and Satake (1996) in the cases of (a): $M_w = 7.59$ (original) and (b): $M_w = 9.03$ (targeting typhoon Haiyan).

(i.e. size of the building) is relatively high.

The results of these two cases show that even when the target domain and incident conditions are changed, the iDFM changes the feedback by buildings in the form of velocity reduction effect compared to the roughness model, and the velocity decreases corresponding to the mesh where the building information exists. The spatial pattern of the velocity reduction depends on the building information, which depends on how many buildings are included in the target area. In the case of Tacloban, most of the buildings are smaller in size (i.e., projected area) than those of Onagawa, but the number of buildings is large and dense in the mesh, so the spatial pattern of flow reduction is dominated by the spatial pattern of the number of buildings. On the other hand, in Onagawa, the size of each building is larger than that of Tacloban, but the number of buildings is smaller, so the spatial pattern of flow velocity reduction is dominated by the spatial pattern of projected area.

5.5 Summary of Chapter 5

Chapter 5 presented the application of the iDFM developed in Chapter 4 to the historical storm surge inundation (typhoon Haiyan case) targeting coastal urban area in Philippine. The implementation of the wind drag coefficient C_w in the land side based on the building information (i.e. SGS paramters) was also proposed and validated using available survey data. After that, the inundation characteristics such as limit of inundation, inundation depth, and velocity modeled by the iDFM with new implantation of C_w are examined in comparison with the survey data and the roughness model used in previous studies. In addition, to clarify the difference of characteristics between Onagawa case in Chapter 4, the virtual tsunami inundation simulation using the iDFM was conducted. The summary of Chapter 5 is as follows;

a) The influence by the implementation of wind stress change based on building information is large for velocity in grid cells near limits of inundation, and such velocity reduction leads to smaller inundated area. The inundation limit in Tacloban area is close to the observation, which shows the potential of the model improvement.

b) The maximum fluid velocity near shoreline is sensitive to the SGS parameters rather than the inundation depth (or surface elevation). On the other hand, the inundation depth and velocity near run-up limit decrease compared to the CNTL because the velocity reduction by buildings is iterated in every time step in momentum conservation as the run-up distance is longer. Such velocity reduction makes large difference in leading edges of inundation and this can result in large difference of arrival time.

c) The velocity reduction effect corresponding to the building existence is observed in the virtual tsunami case and it is consistent with Onagawa case. The amplitude of reduction is larger where the number of buildings N_b is large in Tacloban case but the amplitude is larger where the projected area $\bar{A}_x$ or $\bar{A}_y$ is large.

Chapter 6 examines the storm surge inundation characteristics modeled by the iDFM in

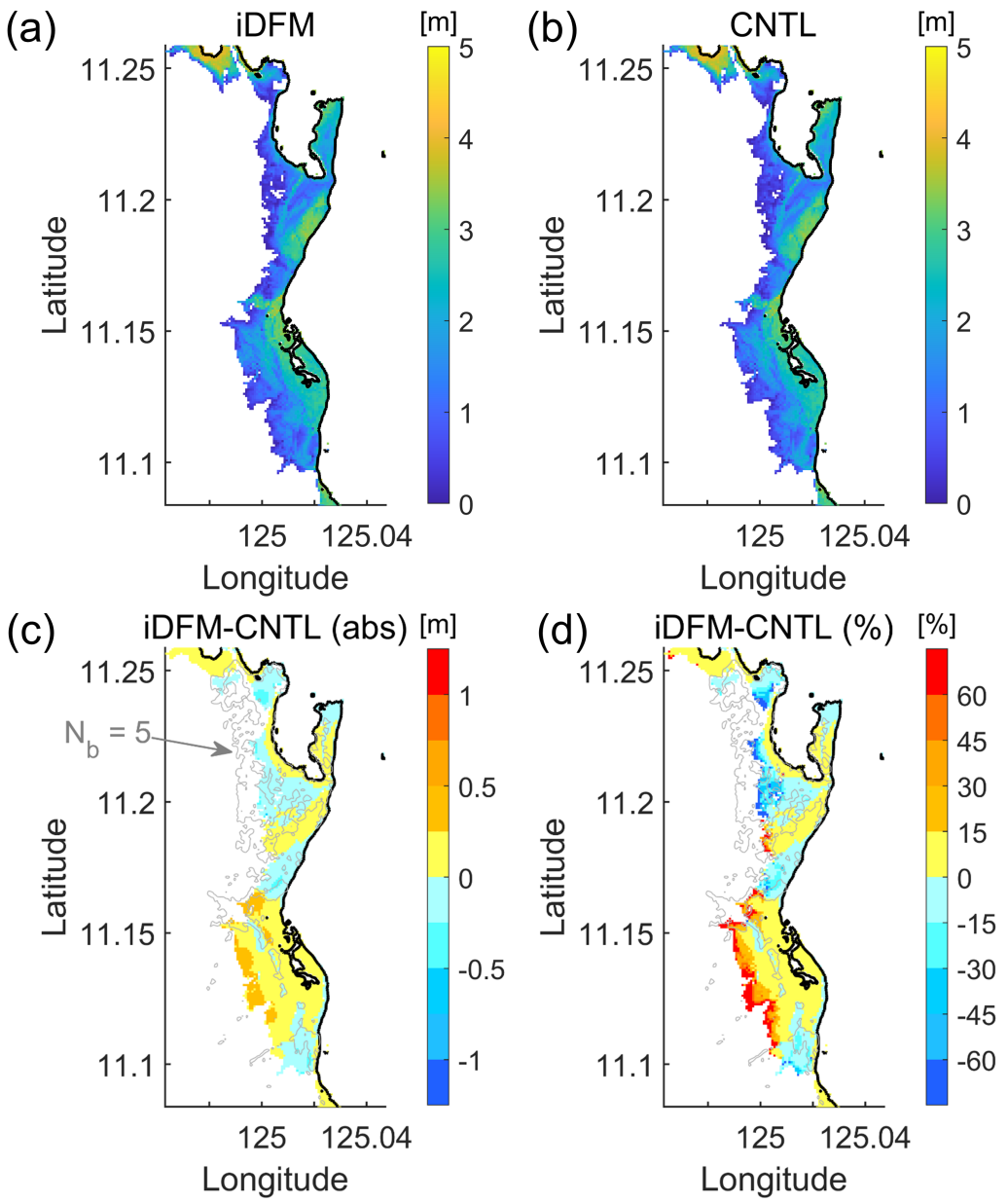

Figure 5.15: Comparison of maximum inundation depths; (a): CNTL and (b): iDFM, and (c): absolute value difference, and (d): relative value difference (black and gray line shows shoreline and contour of $N_b = 5$).

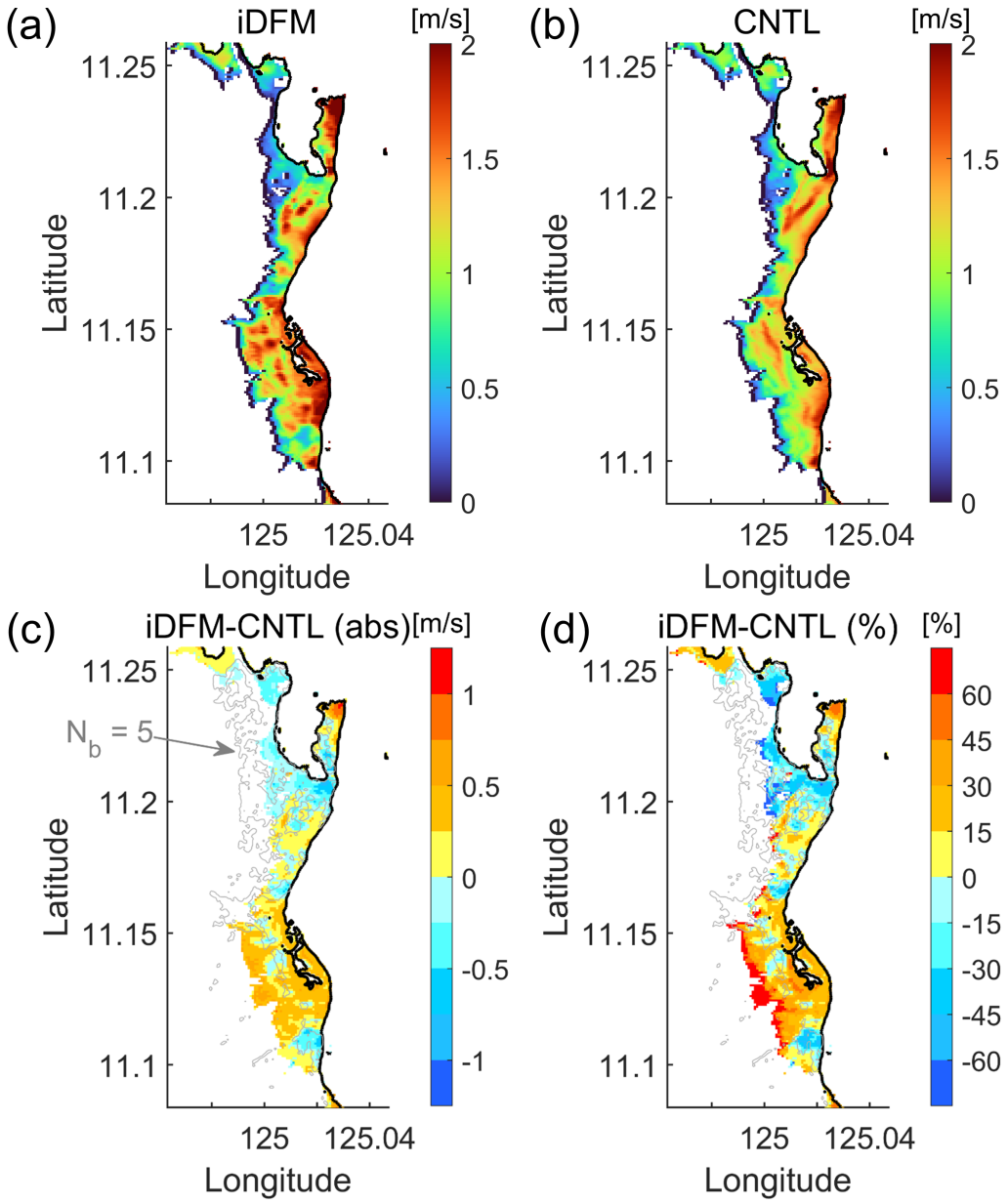

Figure 5.16: Comparison of maximum tsunami fluid velocities; (a): CNTL and (b): iDFM, and (c): absolute value difference, and (d): relative value difference (black and gray line shows shoreline and contour of $N_b = 5$).

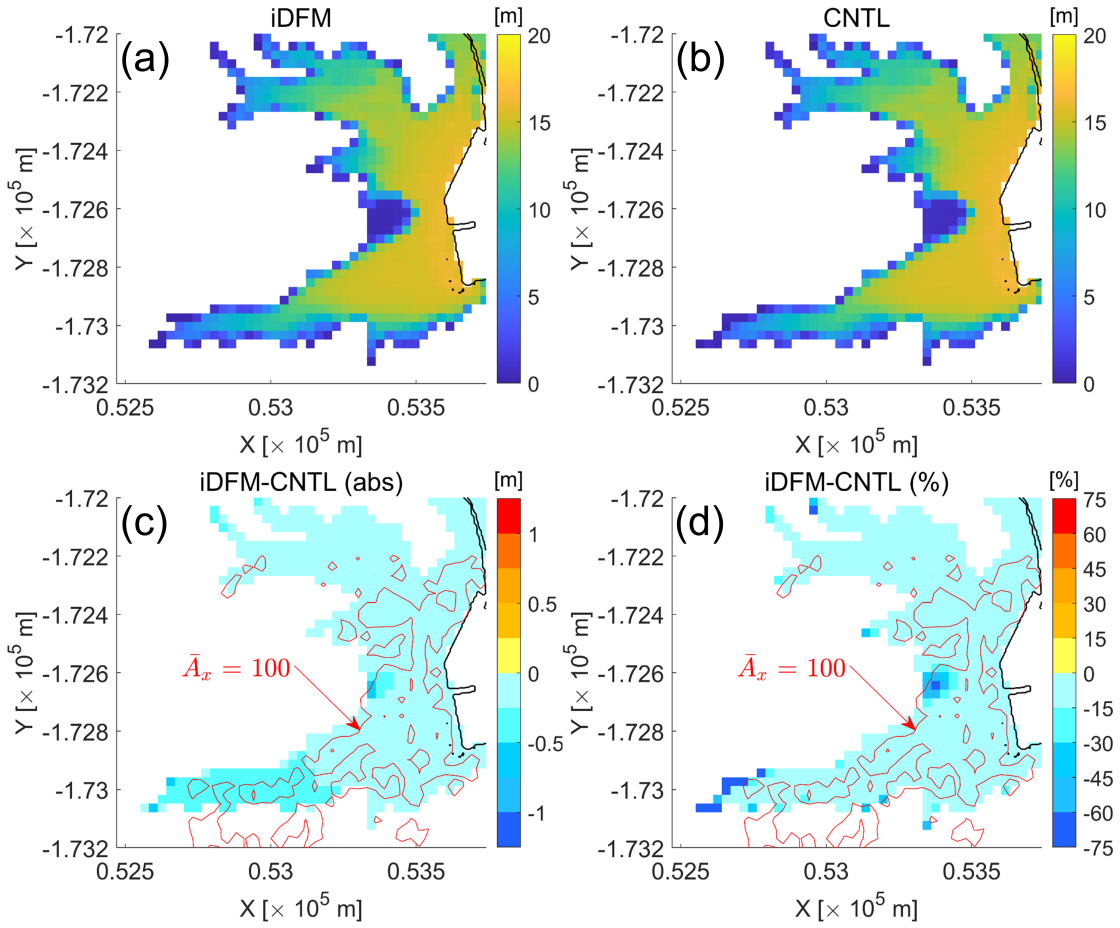

Figure 5.17: Comparison of maximum tsunami inundation depths for Onagawa Case; (a): CNTL (n =0.004 in land area) and (b): iDFM, and (c): absolute value difference, and (d): relative value difference (black and red line shows shoreline and contour of $\bar{A}_x = 100$).

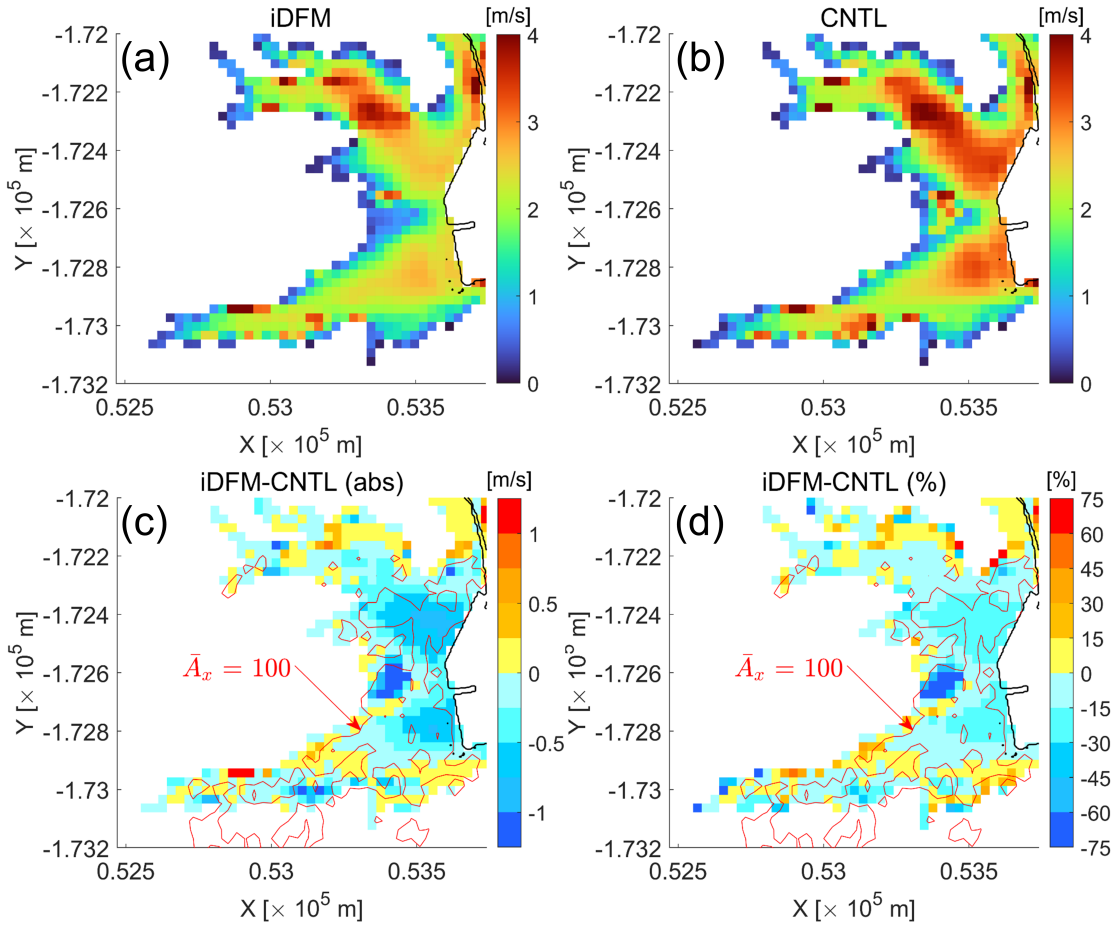

Figure 5.18: Comparison of maximum tsunami fluid velocities for Onagawa Case; (a): CNTL (n =0.004 in land area) and (b): iDFM, and (c): absolute value difference, and (d): relative value difference (black and red line shows shoreline and contour of $\bar{A}_x = 100$).

metropolis where huge number of the buildings are placed complexly to apply the iDFM to coastal hazard assessment.

Chapter 6

Application of Subgrid-scale Modeling of Storm Surge Inundation to Metropolis

6.1 Introduction

In Chapters 4 and 5, the accuracy and error characteristics of the iDFM, an SGS model developed through idealized numerical experiments and application to actual flooding events (2011 Tohoku Earthquake Tsunami and Typhoon Haiyan), are discussed. However, the target area was not a large and heavily populated city, but an urban area with a small number of buildings relatively. On the other hand, as pointed out in Chapter 1, large-scale tsunami and storm surge inundation is expected in the three metropolitan areas adjacent to the three major bays, Tokyo Bay, Osaka Bay, and Ise Bay of Japan, and it is good to examine the inundation simulation in these metropolitan areas.

The purpose of this chapter is to clarify the inundation characteristics reproduced by the drag model iDFM and the conventional domain roughness model for Tokyo, a metropolis with a larger building density than Onagawa and Tacloban, and to organize the differences from the inundation characteristics clarified in the previous chapters in terms of differences in boundary conditions and input building information. First, the storm surge model SuWAT used in Chapter 5 is implemented with the iDFM and regional roughness model to perform the storm surge inundation calculations. In this case, the meteorological field obtained from the pseudo global warming experiment of Typhoon Hagibis in 2019 is used as the target event. Next, the spatio-temporal characteristics of the widely flooded area are clarified by comparing the spatial distributions (maximum values and time series) and point time series of inundation depths and velocities with the roughness model, as before. The differences in characteristics are then discussed in terms of the ratio of drag and advection terms and the difference in total projected area per unit area, including the flooding cases of Onagawa and Tacloban.

6.2 Methodology

6.2.1 Storm surge model

When simulating storm surge inundation for a large city such as Tokyo, where numerous buildings exist over a wide area, it is common to use several domain nesting method using topography and bathymetry with different resolutions, which needs a large computational cost. This study improves computational efficiency using a storm surge model with adaptive mesh refinement (AMR), GeoClaw, (Mandli and Dawson, 2014) for simulating storm surge in ocean. AMR algorithms allows dynamical adjustment of computational cell sizes to track storm surge generation. On the other hand, the storm surge in inner part of the bay and inundation over land are simulated by SuWAT following Chapter 5. This chapter explains only GeoClaw since SuWAT has been already explained in Chapter 5. GeoClaw solves the following 2D-SWE using the finite volume method based on the Riemann solver (details are provided in LeVeque (2002)): The value of the upper limit for wind drag coefficient C_w is set to wind speed 30 m/s. The value of the friction coefficient C_f was determined using the hybrid Chezy-Manning n-type friction law:

$$C_f = \frac{gn^2}{h^{4/3}} \left[1 - \left(\frac{h_{break}}{h} \right)^{\theta_f} \right]^{\frac{\gamma_f}{\theta_f}} \tag{6.1}$$

where n denotes Manning's n coefficient and $h_{break} = 2$, $\theta_f = 10$, and $\gamma_f = 4/3$ control the form of the Chezy-Manning friction law.

The patch-based AMR approach used in GeoClaw employs a set of overlapping logically rectangular grids that correspond to one of many levels of refinement that are enumerated starting at $l = 1$. The first of these levels contains grids that cover the entire domain at the coarsest resolution. The subsequent levels, i.e., $l \geq 2$, represent progressively finer resolutions by a set of prescribed ratios r^l in time and space such that

$$\Delta x^{l+1} = \Delta x^l / r_x^l \tag{6.2}$$

$$\Delta y^{l+1} = \Delta y^l / r_y^l \tag{6.3}$$

$$\Delta t^{l+1} = \Delta t^l / r_t^l \tag{6.4}$$

The refinement criteria for the storm surge simulation include the wind speed and radius of maximum wind speed (RMW) based on the input meteorological field, in addition to the water level and flow velocity calculated at every time step (Mandli and Dawson, 2014). More detailed descriptions and discussions about AMR can be found in LeVeque et al. (2011), Berger et al. (2011), and Mandli and Dawson (2014).

6.2.2 Model setup

(1) Meteorological field based on Typhoon Hagibis 2019

Although there have been no reported cases of storm surge inundation of the coastal areas of Tokyo due to typhoons in the past, there are concerns about storm surge inundation due to increased typhoon intensity in the future climate. In this study, the author used

the results of a pseudo global warming experiment conducted by Kawase et al. (2021) for Typhoon Hagibis in 2019 as the meteorological field used as storm surge forcing. The meteorological field was calculated using Japan Meteorological Agency's Non-Hydrostatic Model (JMA-NHM; Saito et al., 2007). Other numerical setups are shown in Table. 6.1. Here, the SLP and wind speed calculated in the domain in the resolution 2 km are used for input for storm surge models.

The typhoon track and time series of minimum SLP and maximum wind speed are shown in Fig. 6.1. In the meteorological field obtained in this study, the increase in typhoon intensity is small even under warming conditions, which is expected to result in smaller storm surge anomalies and a smaller inundation area not enough to discuss the inundation characteristics modeled by the iDFM. Therefore, the case where the wind speed field is multiplied by 1.5 as a virtual extreme typhoon (hereafter, WS 1.5 case) to increase the inundation area will be discussed.

Table 6.1: Summary of computational setup for JMA-NHM (created based on Kawase et al., 2021)

	Domain (D1)	Domain (D2)
Target typhoon	Typhoon Hagibis (2019)	
Period	06:00, 9th, Oct., 2019 - 00:00, 14th, Oct., 2019 UTC	
Horizontal resolution	5 km	2 km
Horizontal grids	400 × 400	900 × 900
Vertical resolution	50 layers	
Cloud microphysics scheme	Bulk-type cloud microphysics (Ikawa et al., 1991)	

(2) Computational domain and SGS data

Table.6.2 summarizes the numerical setup. The topography, levees, and roughness coefficients are based on the numerical mesh data published by the Central Disaster Management Council. The spatial resolution is 2430, 810, 270, 90, and 30 m for D1 to D5. Fig. 6.2 shows the topography and bathymetry in D1 (Δx = 2430 m) and D5 (Δx = 30 m). GeoClaw solves the domains from D1 to D5 all at once. The refinement criteria used in GeoClaw follow Table. 6.4. On the other hand, SuWAT does in only D5 using the water discharge and surface elevation along the lateral boundaries calculated by GeoClaw. The ground elevation is shifted to consider the sea level rise (SLR) due to the climate change and high tide as the worst scenario. The mean water level increased by SLR uses 1.2 m (5% percentile value in ssp5-8.5 scenario in IPCC-AR6; IPCC, 2021) and the tide height 1.0 m (average high tide in Tokyo Bay) is used. As for the levees, only SuWAT considers the levee boundaries in D5.

The treatment of urban area assumes two patterns; the iDFM and CNTL (using Manning's coefficient according to land usage; see Table. 6.3). The author uses the 3D building shape data by PLATEAU (MLIT, 2021) used for computing SGS parameters. Due to the limitation of data availability and size, the area for entering building information is limited to a part of Koto and Sumida wards (shown in Fig. 6.2(b), where storm surge inundation

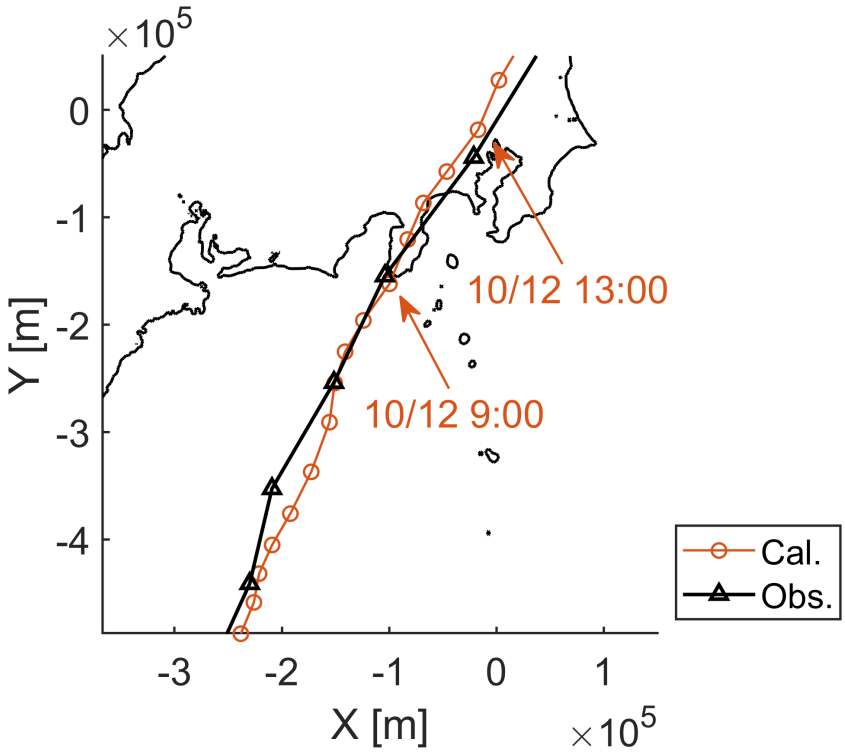

(a) Typhoon track

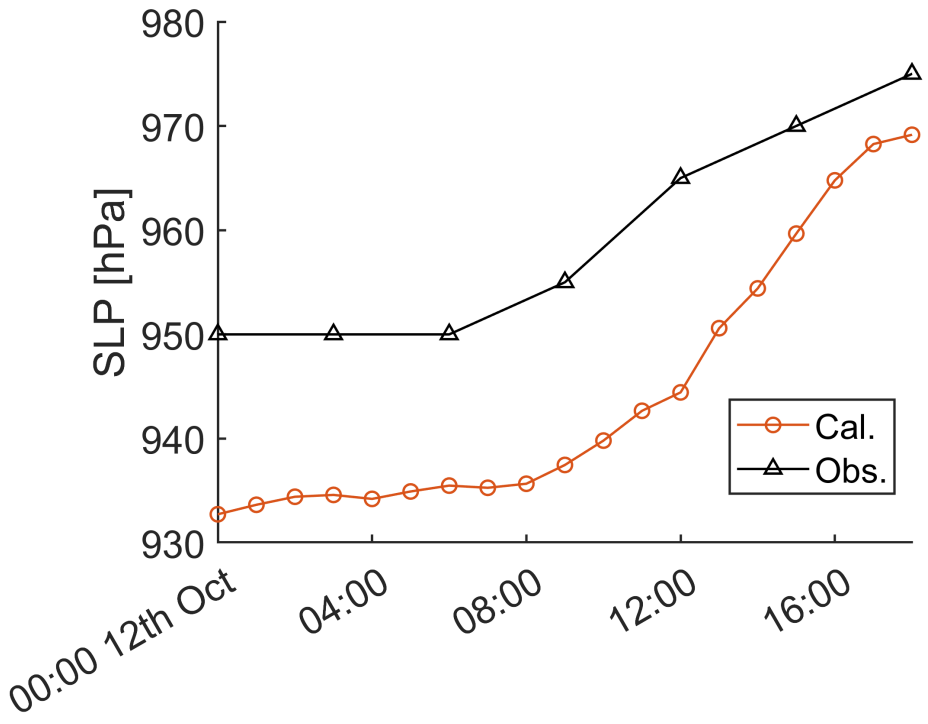

(b) Time series of minimum SLP

Figure 6.1: Typhoon track and intensity (a: track, b: minimum SLP, and c: maximum wind speed) used in storm surge simulation (red line) and observed typhoon data (black line)

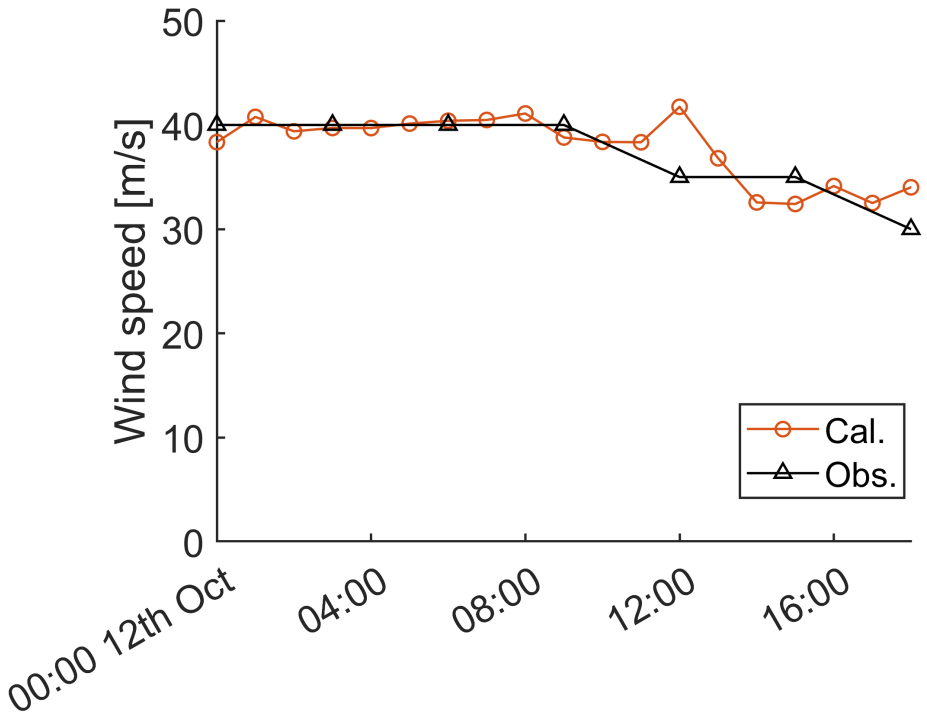

(c) Time series of maximum wind speed

Figure 6.1: Typhoon track and intensity (a: track, b: minimum SLP, and c: maximum wind speed) used in storm surge simulation (red line) and observed typhoon data (black line). (continued)

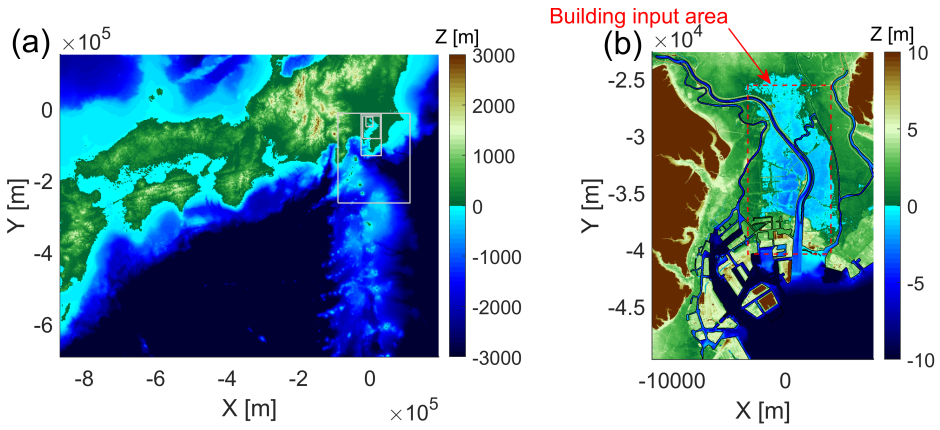

Figure 6.2: Topography and bathymetry in (a): D1 ($\Delta x = 2430$ m) used in GeoClaw and (b): D5 (Tokyo, $\Delta x = 30$ m) used in SuWAT; gray boxes show the nested area D2-4 used in GeoClaw.

is concerned in particular. The building mesh data in 1 m resolution (color shows the building height) and calculated SGS parameters are shown in Fig. 6.3 and 6.4, respectively. In Tokyo, a mega city, buildings are densely arranged in a small area, and there are many areas where the number of buildings in one computational grid N_b is more than five. The manning's coefficient where SGS parameters exist is set to 0.025 in the iDFM so that buildings are not considered twice in the roughness coefficient.

Table 6.2: Numerical setup of two storm surge models; SuWAT and GeoClaw

	GeoClaw	SuWAT
Target area	Whole Japan	Tokyo
Grid size Δx	Adaptive [2430 m, 810 m, 270 m, 90 m, 30 m]	30 m
Time step Δt	Adaptive (CFL ≤ 0.7)	1 s
Manning's coefficient n	0.025	Table. 6.3
Wind drag coefficient C_w (in ocean)	Honda and Mitsuyasu (1980)	
Boundary conditions	Inflow boundary	Radiation boundary
Levee	Implemented	Not implemented
Wave model	Not implemented	
Tide model	Not implemented	

6.3 Results

Before examining inundation characteristics modeled by the iDFM, the computed storm surge anomalies and the scale of inundation were checked. Fig. 6.5 shows the flat distribution of the maximum storm surge anomalies calculated for the original case and the WS 1.5 case. In the original case, the storm surge anomaly is about 1.8-2.0 m, while it is about

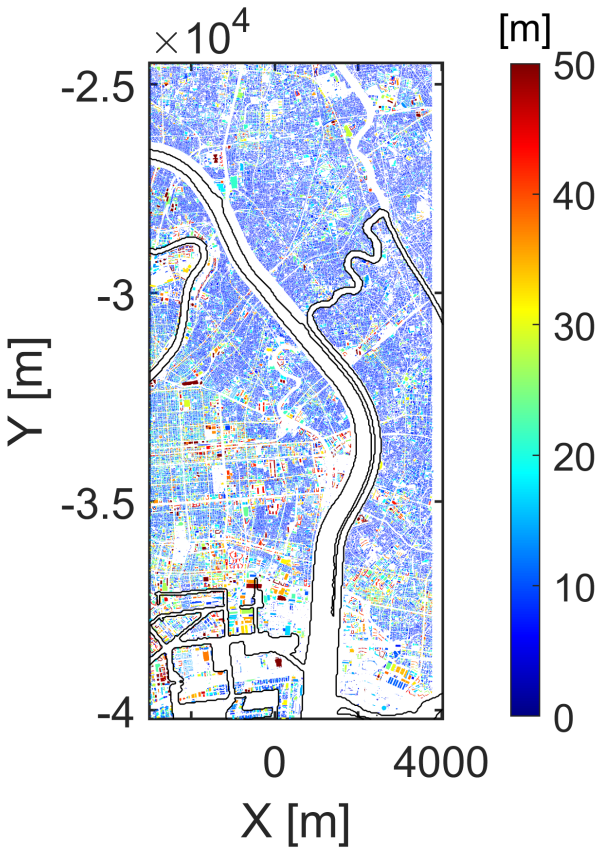

Figure 6.3: Building height calculated from the 3D building shape data from PLATEAU dataset (MLIT, 2021).

Table 6.3: Summary of setup for land area in SuWAT computation

	iDFM	CNTL
Manning's coefficient on land	0.025 (building input area) Kotani et al. (1998) (others)	Kotani et al. (1998)
Wind drag coefficient on land	Honda and Mitsuyasu (1980) ($D \geq \bar{h}_b$) 0 ($D < \bar{h}_b$)	Honda and Mitsuyasu (1980)
Building drag coefficient	Eq. (4.22)	Not implemted

Table 6.4: Refinement criteria for the sea surface height T_{wave}, flow velocity T_{speed}, wind speed T_{wind}, and RMW T_{RMW}

Criteria	
T_{wave} [m]	0.2
T_{speed} [m/s]	[0.25, 0.50, 0.75, 1.0]
T_{wind} [m/s]	[10.0, 20.0, 30.0, 40.0]
T_{RMW} [km]	[200, 100, 50, 25]

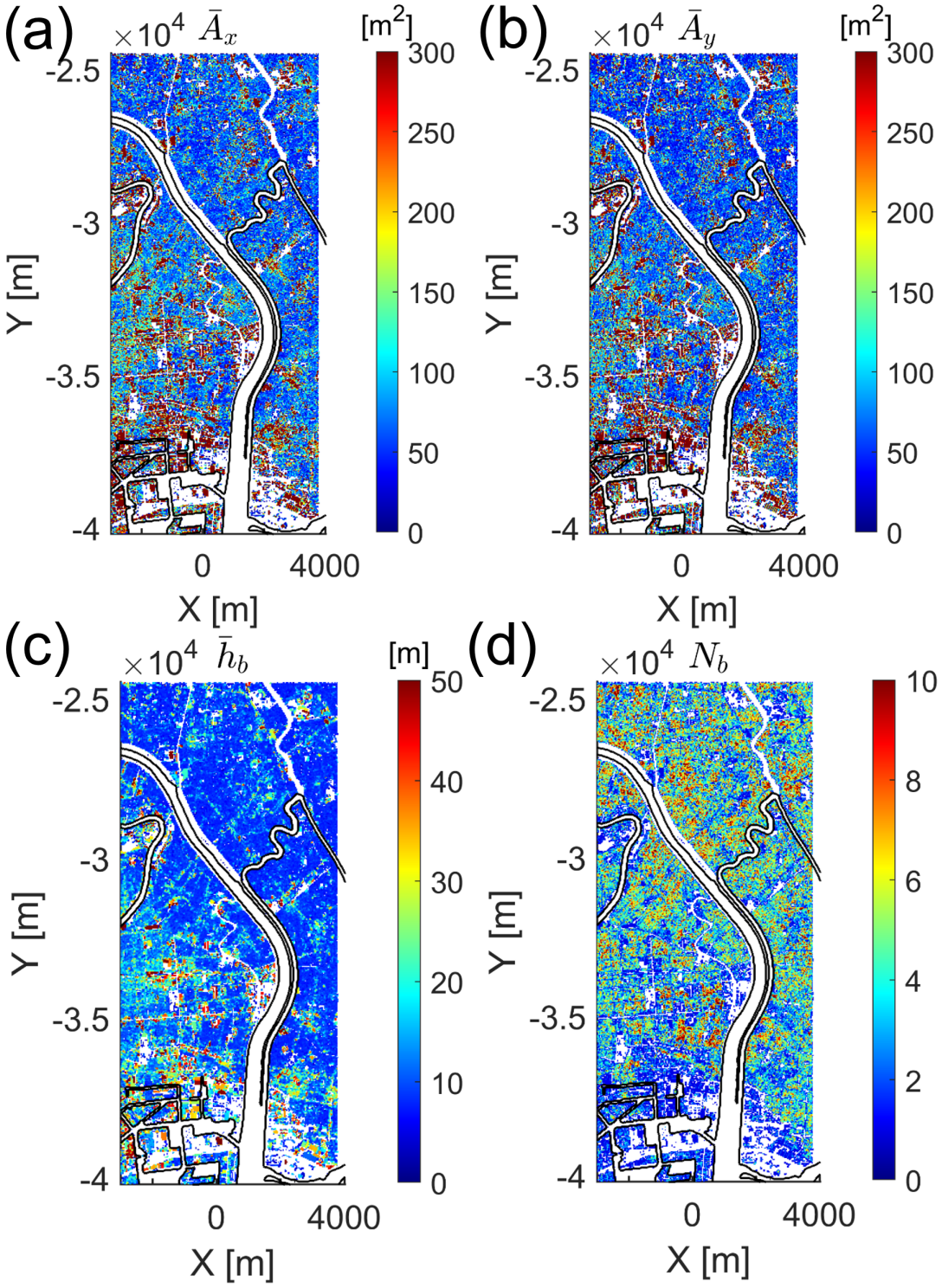

Figure 6.4: SGS parameters in $\Delta x = 30$ m in target area; (a): $\bar{A}_x$ and (b): $\bar{A}_y$, and (c): $\bar{h}_b$, and d: N_b (black line shows shoreline).

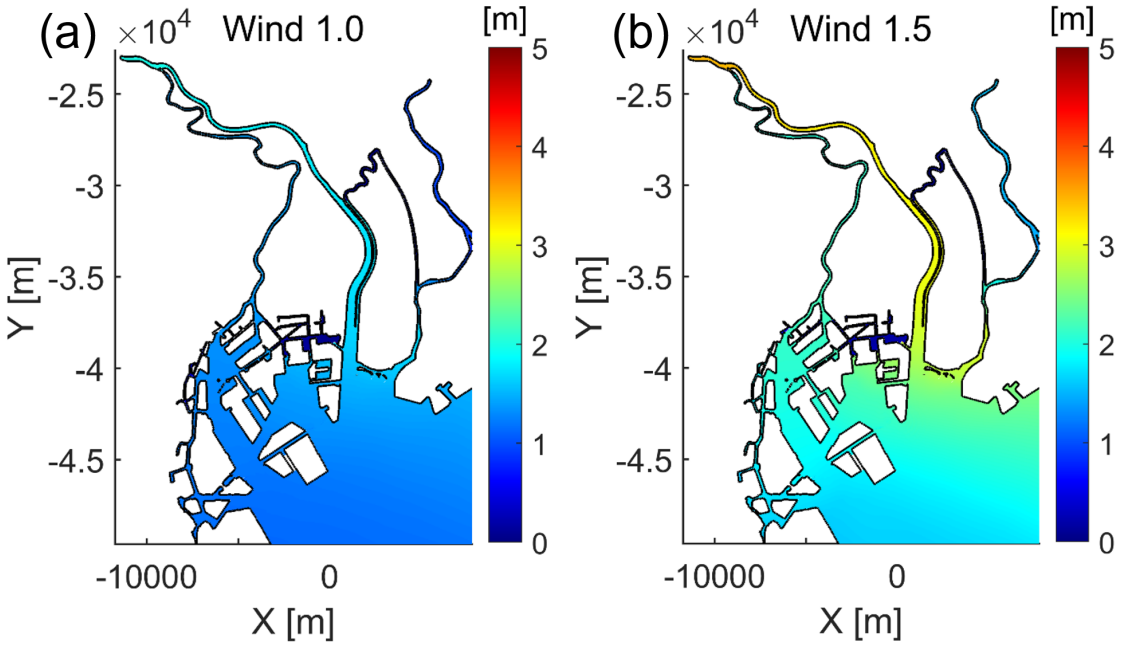

Figure 6.5: Maximum storm surge anomaly in D5 using (a): original meteorological field and (b): meteorological field with 1.5 times wind speed

2.0-3.0 m in the WS 1.5 case. Fig. 6.6 shows the comparison of the maximum inundation area by storm surge for Koto and Sumida wards. The red and blue lines indicate the iDFM and CNTL, respectively. In the original case, the inundation area of both iDFM and CNTL is limited to the northern part of the Sumida River due to the small storm surge anomaly, but in the WS 1.5 case, the inundation area extends from the northern part of the Sumida River to a wide area. In this section, the WS 1.5 case, which has a larger inundation scale, will be used as the main case, and the verification will focus on the northern part of the Sumida River, where building information is included. First, we compare the time series of leading edge of inundation. Fig. 6.7 shows a comparison of the flooded area at 1, 3, 5, 7, and 9 hours after 10:00 on October 12. The red line shows the iDFM and the blue line shows the CNTL, and the background color indicates the elevation. In both models, the inundation area spreads from the higher elevation to the lower elevation after overflowing the northern bank of the Sumida River. The time scales for the run-up are also longer than those in the previous chapter: more than 9 hours for iDFM and 5 hours for CNTL. These differences can be attributed to the fact that the velocity itself is calculated to be small due to the small momentum and mass fluxes entering from the embankment boundary. This point will be discussed as the difference of boundary condition in the following section.

The maximum values of inundation depth and flow velocity are then examined. Fig. 6.8 and 6.9 shows the absolute and relative difference between the maximum inundation depth and velocity and the CNTL in the northern part of the Sumida River (yellow box in Fig. 6.5). Although the inundation area of both iDFM and CNTL is similar, the spatial pattern of inundation depth is different. In the iDFM, the inundation depth is about 2 m around the embankment, which is the entrance to the inundation, while it is about 1 m

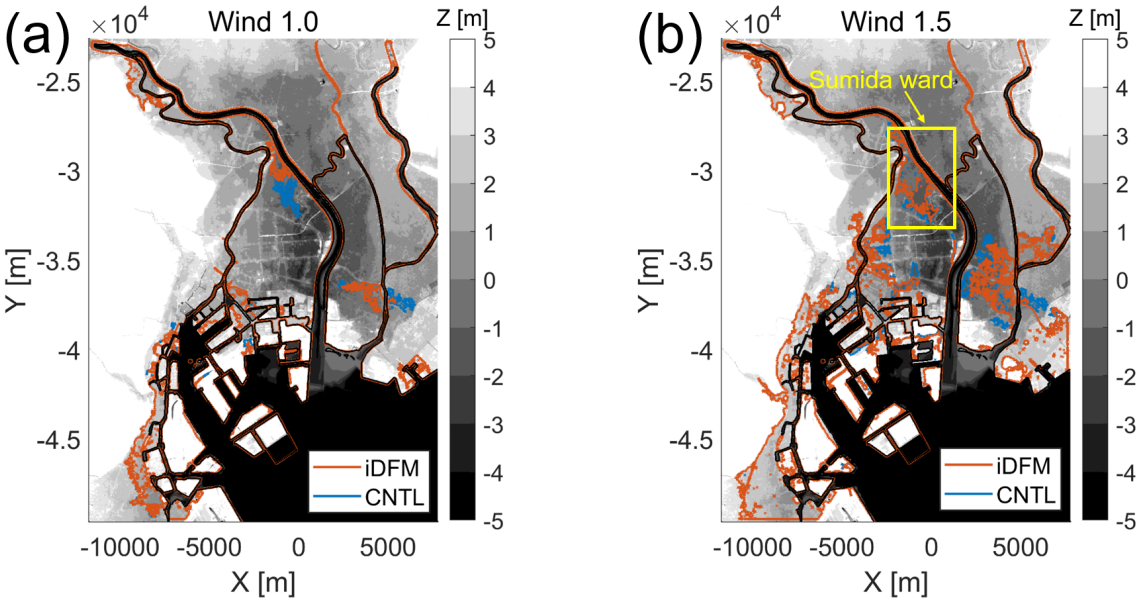

Figure 6.6: Limits of inundation in D5 in the cases of (a): original meteorological field and (b): meteorological field in the WS 1.5 case; colored lines show model difference (red: iDFM and blue: CNTL)

near the edge of the run-up limit. This decrease in inundation depth as the run-up distance increases is similar to the case observed in the Tacloban. On the other hand, in the CNTL, the depth of inundation was about 1.5 m near the bank, and nearly 2 m near the edge of the run-up limit. In the CNTL, the depth of inundation was about 1.5 m near the dike, and nearly 2 m near the edge of the run-up limit. The spatial patterns of the absolute and relative differences are red on the shoreline side, indicating that the inundation depth calculated by iDFM is larger than CNTL near the embankment. The magnitude of the difference increases as one approaches the shoreline, and there are areas where the absolute amount is more than 1 m and the relative amount is more than 50%. On the other hand, the magnitude of the difference reverses from the middle of the inundation area, and there are many areas where the absolute amount is more than 0.5 m and the relative amount is more than 75%. This tendency is not seen in the Onagawa case of Chapter 4 or the Tacloban case of Chapter 5, and the reason for this tendency will be discussed in the following section. When the maximum flow velocity is compared, it is found that most of the regions in the CNTL are above 0.2 m/s, while most of the regions in the iDFM are below 0.1 m/s. When the difference between the two is calculated, the absolute difference is less than 0.25 m/s, but the relative difference is more than 50%. In most areas, the iDFM is smaller than the CNTL for the entire region. Since almost all meshes in this region contain building information, the flow velocity is reduced correspondingly, and this trend is consistent with the results in Chapters 4 and 5.

Next, the spatio-temporal characteristics of inundation depth and velocity. Fig. 6.10 compares the inundation depth, velocity, and momentum flux between iDFM and CNTL. Note that the left panel shows the inundation depth (color) and velocity (arrow), and the right panel shows the momentum flux. Grid cells with inundation depth larger than

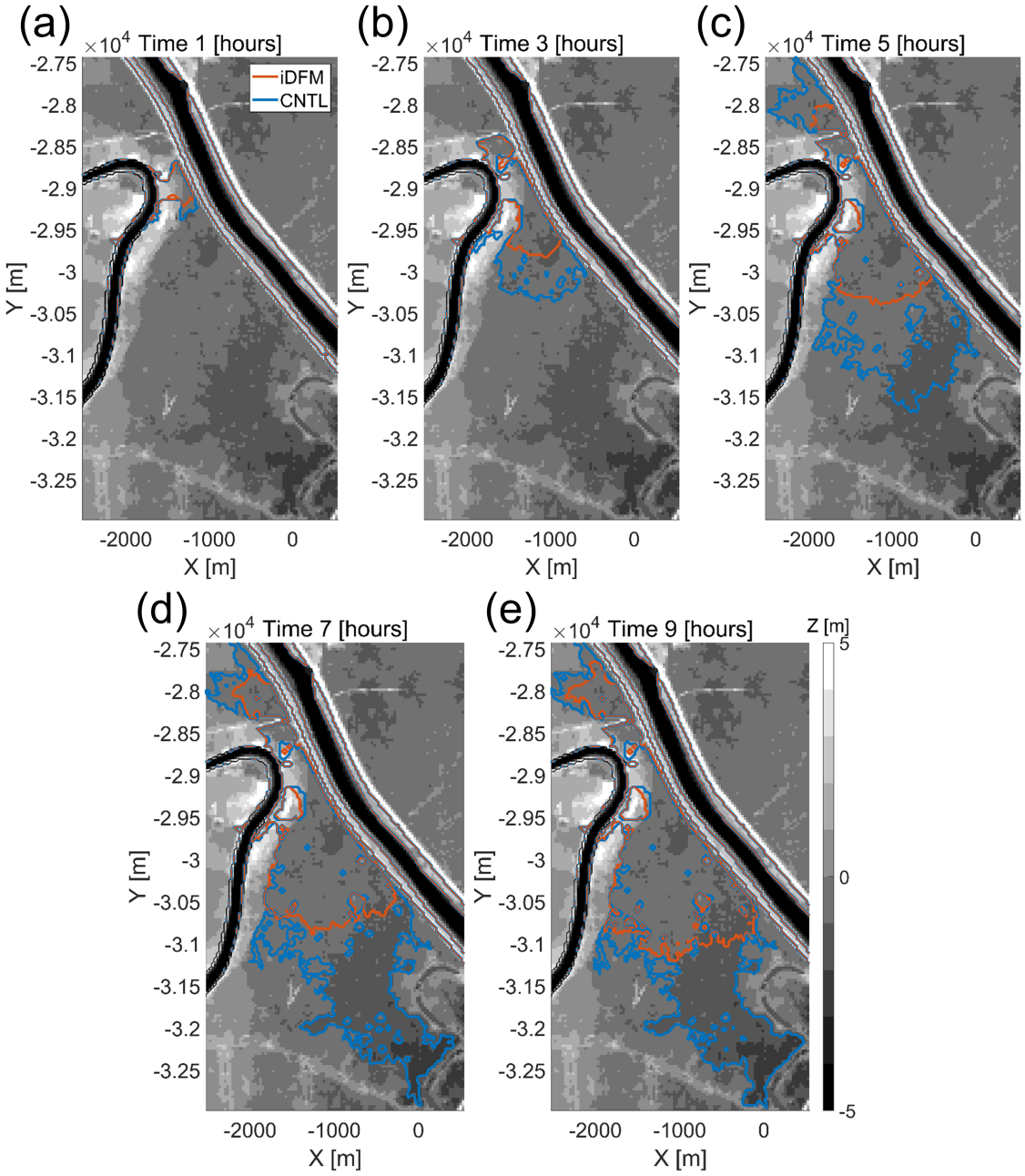

Figure 6.7: Comparison of inundation leading edges between iDFM (WDBuildSub; red line) and CNTL (blue line) every 2 hours; (a): 1 hour, (b): 3 hours, (c): 5 hours, (d): 7 hours, (e): 9 hours after 2019/10/12 10:00 UTC.

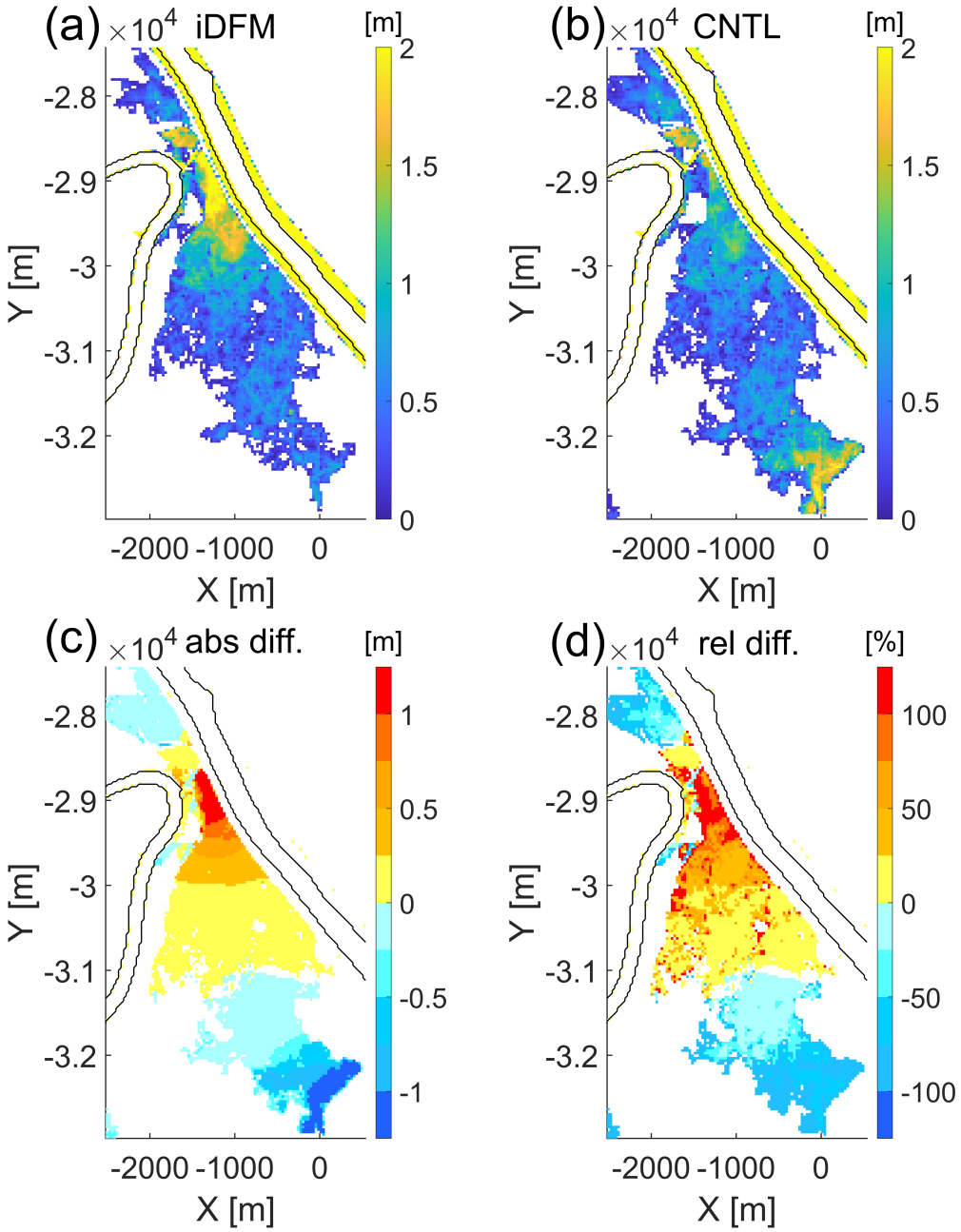

Figure 6.8: Maximum inundation depths modeled by (a): iDFM and (b): CNTL, and (c): absolute and (d): relative differences, respectively (black line shows shoreline).

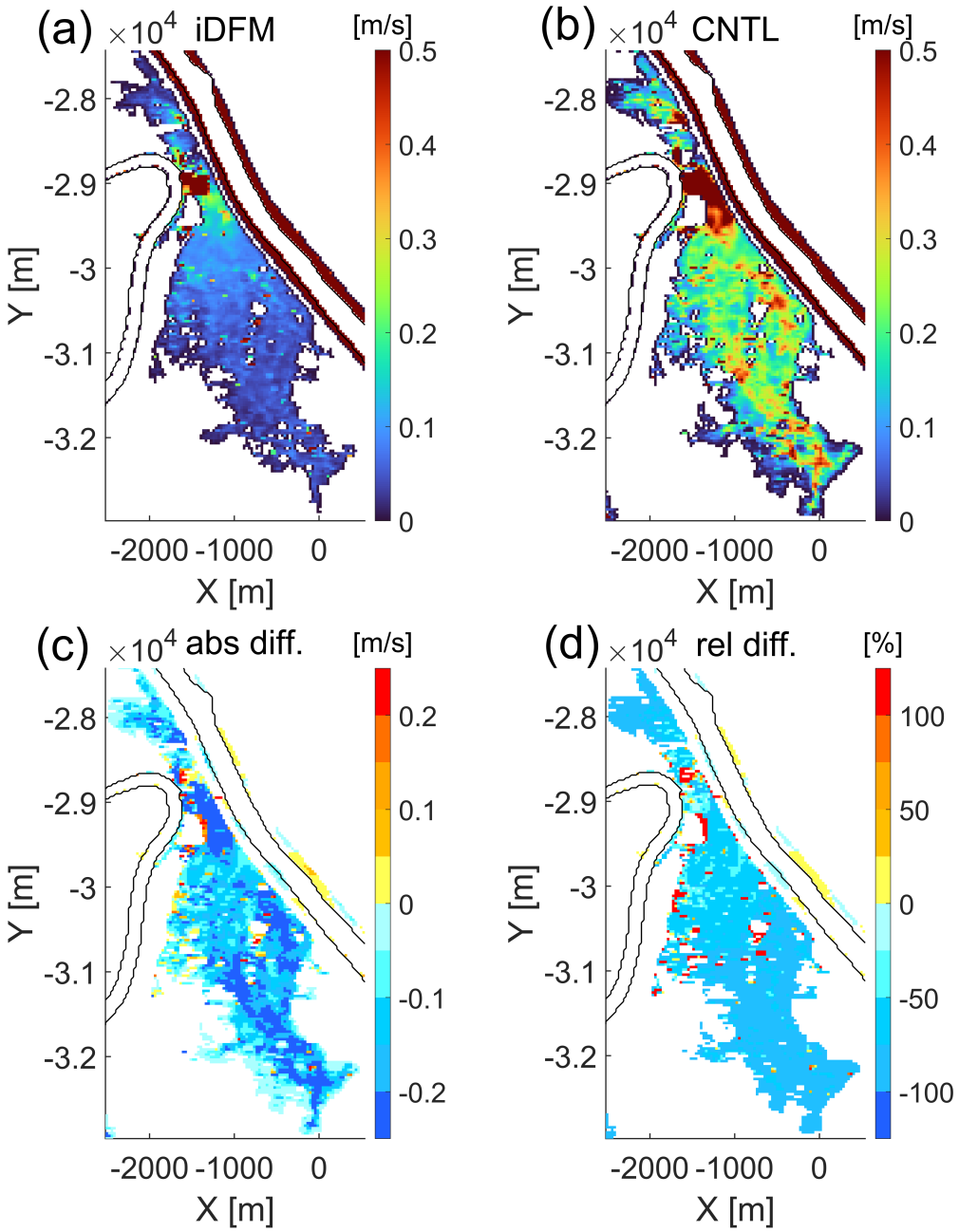

Figure 6.9: Maximum fluid velocities modeled by (a): iDFM and (b): CNTL, and (c): absolute and (d): relative differences, respectively (black line shows shoreline).

1.5 m are observed in the case of the iDFM, while the area with smaller than 1.0 m inundation depth are majority in the case of the CNTL. On the other hand, both velocity and momentum flux by the iDFM are smaller than CNTL in whole the inundated area. Such result means that water is not flowing further inland due to the decrease in flow velocity near the levee boundary.

Futhermore, the time series of the inundation depth, velocity, and flow direction at three point gauges located along the inundation flow path are shown in Fig. 6.11. Note that the top, middle and bottom panel shows the time series of inundation depth, velocity, and flow direction after 10:00 UTC. Station 1 located near river embankment shows similar increase of inundation depth until 150 minutes by both the iDFM and CNTL. However, the iDFM shows approximately 83% larger inundation depth than CNTL after 200 minutes, while the iDFM shows approximately 70% smaller velocity than the CNTL. In addition, the flow direction in the case of the iDFM is in southeast direction, while the one by the CNTL is in south. On the other hand, Station 2 located at middle of the inundated area shows different characteristics from Station 1. The starting time of the inundation is 200 minutes slower than the CNTL and the maximum velocity is much smaller than CNTL. Such decreased velocity is due to the decrease of the momentum flux near river embankment and it causes the increases of inundation depth. Station 3 located near the limit of the inundation shows also different characteristics than other two stations. The starting time of the inundation is more than 800 minutes slower than the CNTL and the inundation depth and velocity are smaller than the CNTL. This is because smaller water amount is transported from the river embankment and the both mass and momentum fluxes decrease.

From the above analyses, it was found that the flow velocity calculated by iDFM is strongly attenuated by buildings near the embankment compared to the CNTL in the entire inundated area and the inundation depth was larger than that of CNTL because water was blocked. In addition, the amount of water flowing in from the river side decreased as the run-up distance is longer, resulting in a smaller inundation depth compared to the CNTL.

6.4 Discussions

In the previous section, the characteristic inundation characteristics calculated by the iDFM were that the flow velocity is reduced near the embankment, the inundation depth is increased compared to the CNTL, and the inflow rate is reduced as the run-up distance is extended. In this section, the differences in inundation characteristics between the tsunami inundation calculation for Onagawa and the storm surge inundation calculation for Tacloban in the previous sections are discussed by focusing on the differences in inflow conditions and building information input.

First, we focus on the drag force and advection terms that act directly on the calculated velocity field. The ratio of the drag force term to the advection term at the time of maximum velocity in the Tokyo, Tacloban, and Onagawa cases (called the DA ratio in this study) is shown in Fig. 6.12 . In all cases, most of the DA ratio is greater than 1, but

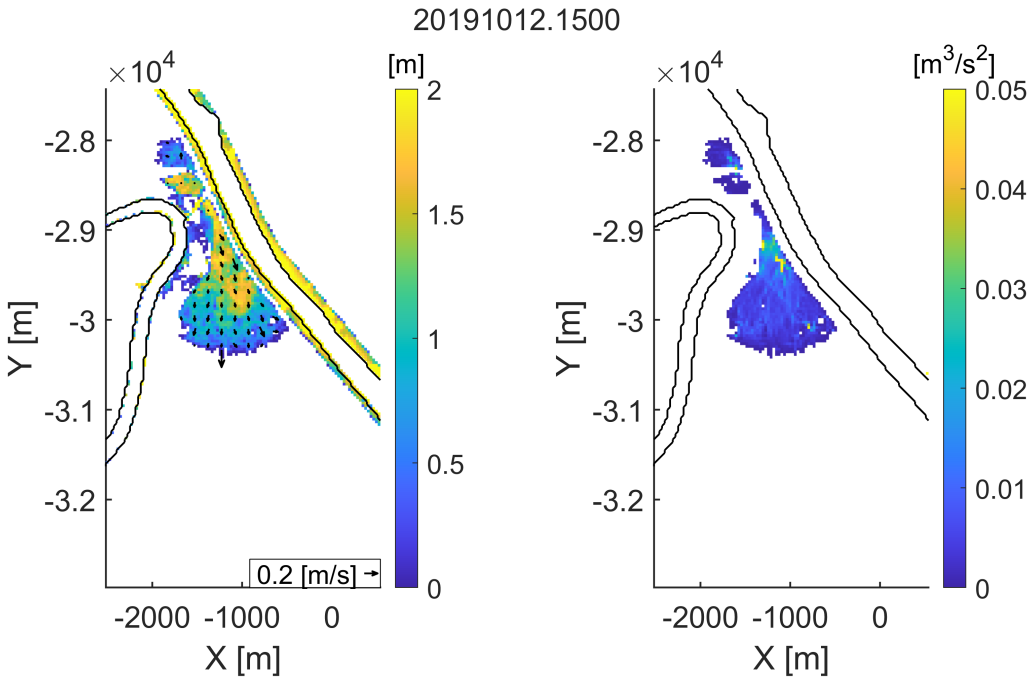

(a) iDFM run

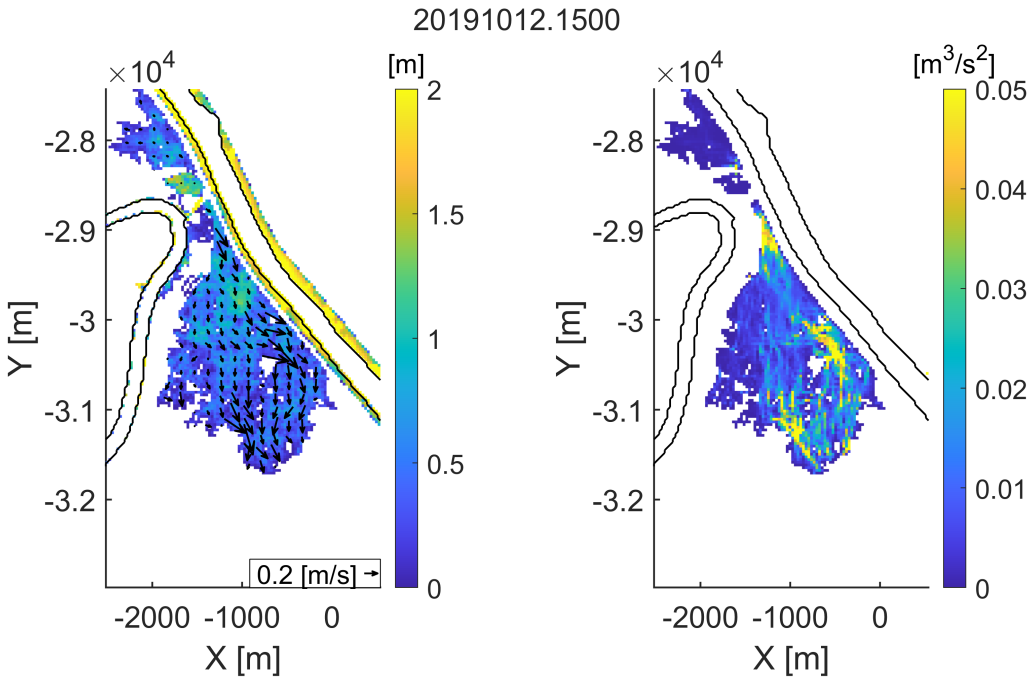

(b) CNTL run

Figure 6.10: Snapshots of inundation depth (color) and velocity (arrow), and momentum flux (color) modeled by (a): iDFM and (b): CNTL at 2019/10/12 15:00 UTC (left: inundation depth and velocity, and right: momentum flux).

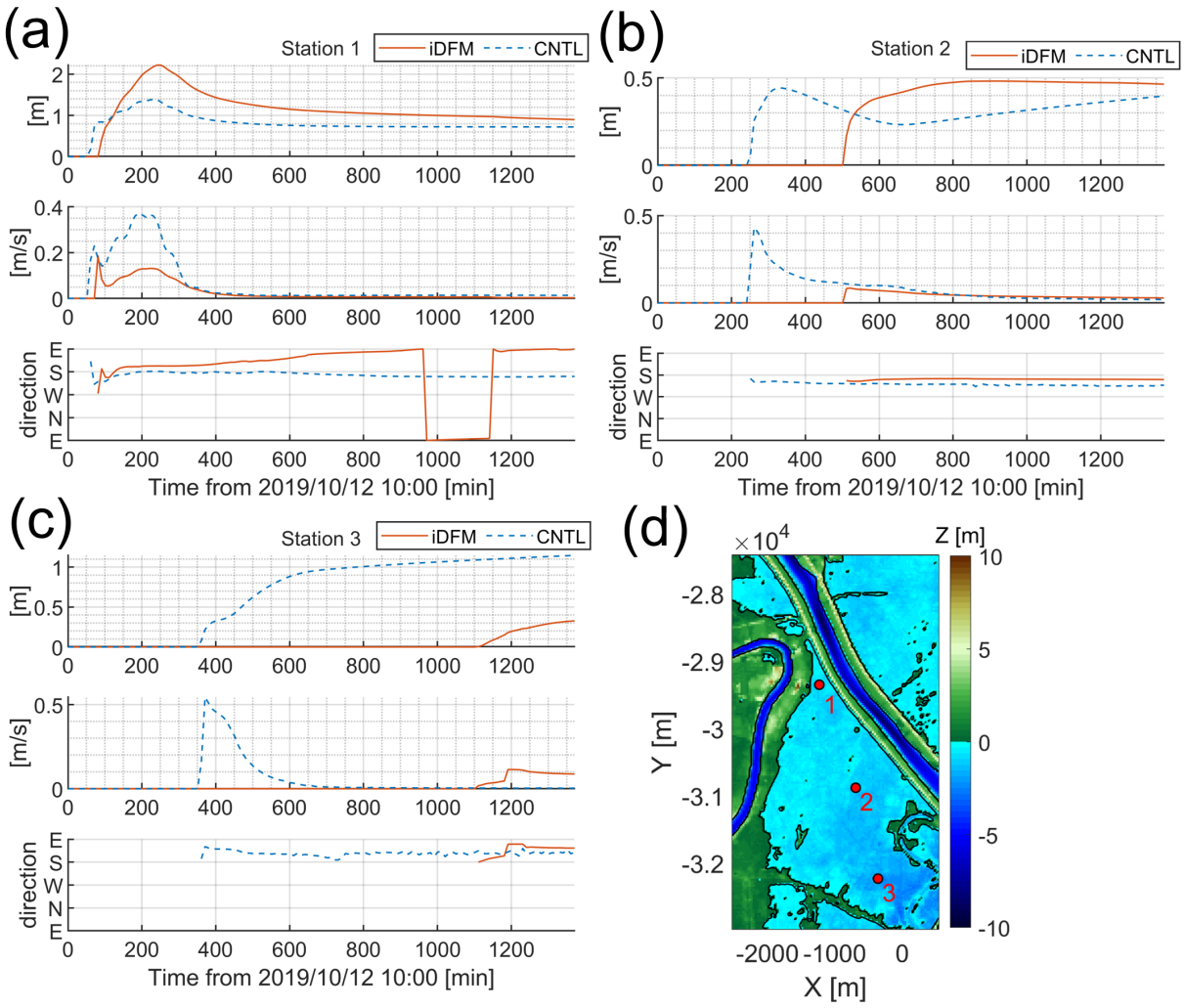

Figure 6.11: Time series of inundation depth, velocity, and flow direction modeled by iDFM (red line) and CNTL (blue dashed line) at three fixed points (Stations a: 1, b: 2, and c: 3) marked with red circle on (d) spatial distribution of topography in Sumida area.

the magnitude of the DA ratio varies from case to case, and the DA ratio of drag force term is in the order of Tokyo > Tacloban > Onagawa. For example, in the Tokyo case, there are many areas with more than 200 DA ratio near the embankment, and many areas with more than 500 DA ratio as the run-up distance increases. In the Onagawa case, the DA ratio is about 30 to 40 near the shoreline, but it is mostly less than 10. On the other hand, in the Tacloban case, the grid cell with the 10 to 50 DA ratio is dominant in the region. These obtained results indicate that the velocity reduction effect by building drag force is larger in storm surge case than tsunami case. Then, next paragraph discusses the relationship between the difference of inflow boundary conditions due to the difference of phenomena (i.e. tsunami or storm surge) and the DA ratio of the drag force term.

Then, the author examines these differences in contribution rates in terms of differences in inflow boundaries and input SGS parameter. Fig. 6.13 are the mass fluxes and momentum fluxes into the northern embankment boundary of Sumida River, Tacloban and Onagawa shorelines, respectively.

$$Q = \sqrt{M^2 + N^2} \tag{6.5}$$

$$\Phi = (U^2 + V^2)D \tag{6.6}$$

where M and N denote discharge per unit width in x and y-direction, U and V denote velocity in x and y-direction, and D denotes the total water depth. Both mass and momentum fluxes are large and small in the order of Tokyo, Tacloban, and Onagawa, indicating the difference in inflow boundary conditions. The time required for inflow also differs among the three sites, being 400, 300, and 10 minutes for Tokyo, Tacloban, and Onagawa, respectively. These results suggest that the advection term increases relatively with the temporal variation of the flux into the land area, which in turn affects the magnitude of the contribution ratio of drag force term as described above.

Next, the author considers the difference in terms of the input building information (i.e., SGS parameters). Here, the product of the projected area per unit area and the number of buildings is defined as the input building information by the following equation. Fig. 6.14 and 6.15 show the product of the projected area and the number of buildings per unit area in each direction, where they are similar to each direction. The area averages are 0.52, 0.073, and 0.26 for x-direction, respectively. These results indicate that the product of the projected area and the number of buildings is larger in large cities where the buildings are densely arranged. Note that although Tacloban is also a city and has many buildings, the projected area is smaller because the height of the buildings is assumed to be 3 m or 6 m.

Furthermore, the relationship between the product of the projected area $\bar{A}_x$ and the number of buildings N_b and the contribution of drag to the advection can be deduced as follows For tsunamis with large momentum and mass fluxes, the drag term contribution is smaller than storm surge regardless of the density of buildings. On the other hand, in the case of storm surges, where the momentum and mass fluxes are smaller than those of tsunamis, the contribution of the drag term is determined by the density of the building.

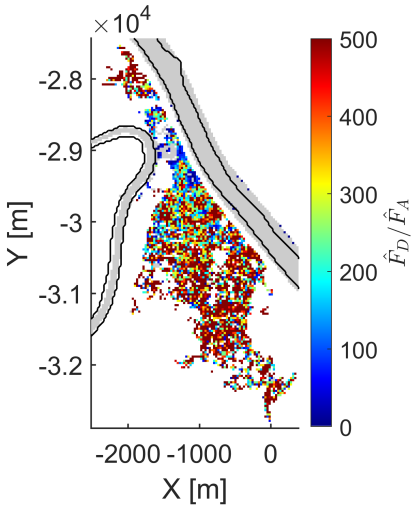

(a) Sumida area

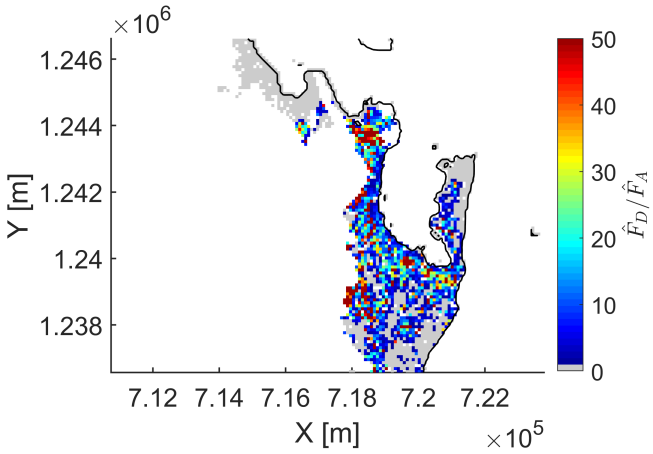

(b) Tacloban area

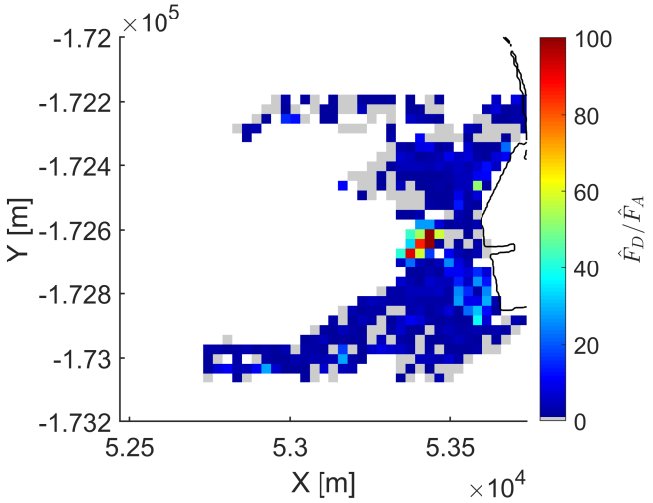

(c) Onagawa area

Figure 6.12: DA ratio of drag force term $\hat{F}_D$ to advection term $\hat{F}_A$ when velocity is maximum (gray patched area indicates grid cells where $\hat{F}_D$ is smaller than $\hat{F}_A$).

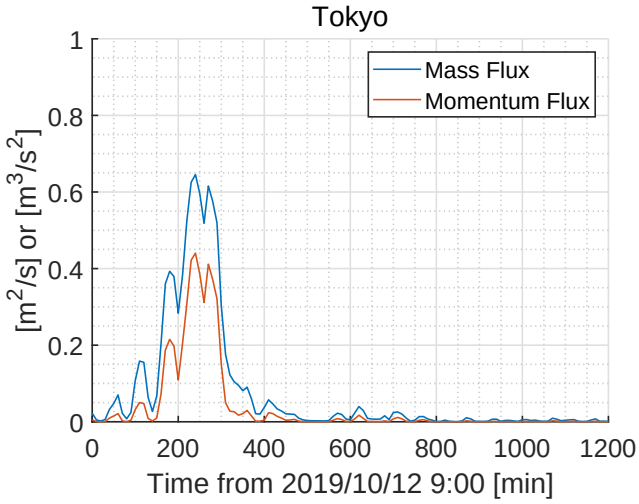

(a) Sumida area

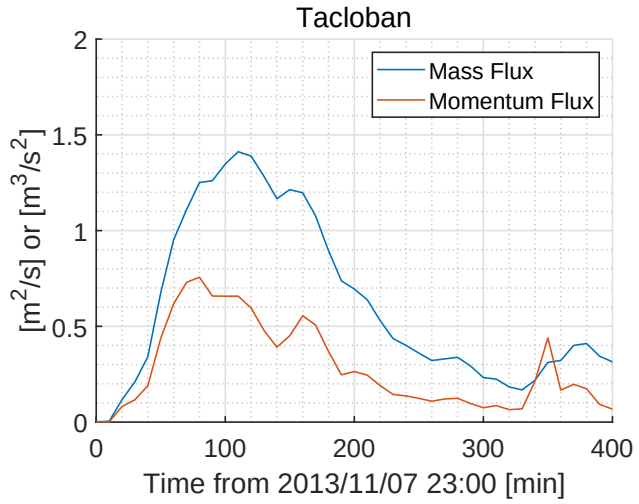

(b) Tacloban area

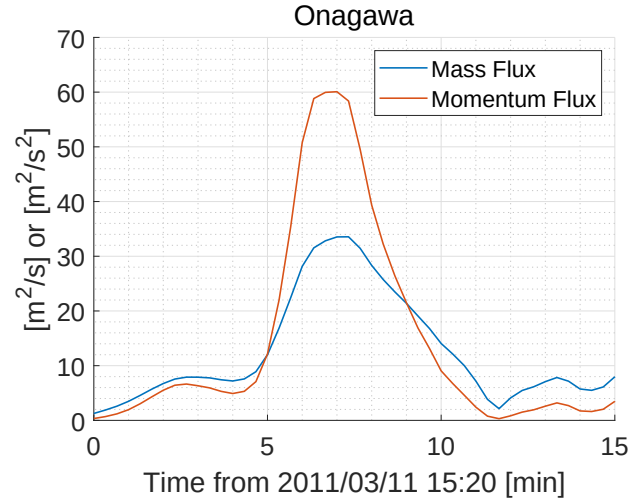

(c) Onagawa area

Figure 6.13: Time series of inflow mass flux Q (blue) and momentum flux Φ (red) from river embankment (Sumida area) or coastline (Tacloban or Onagawa area).

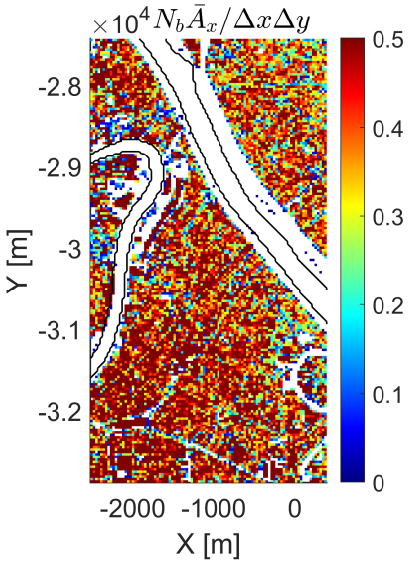

(a) Sumida area

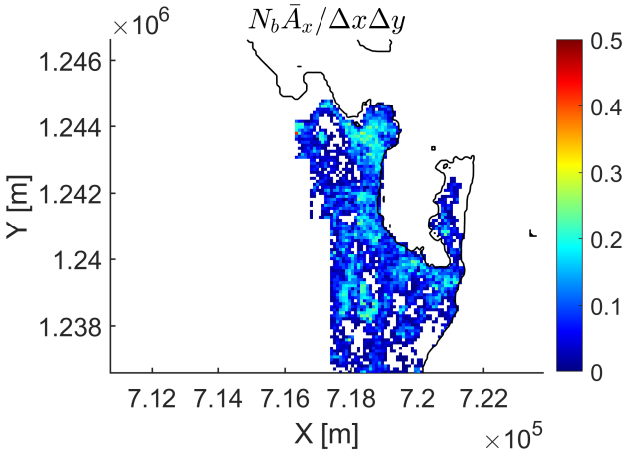

(b) Tacloban area

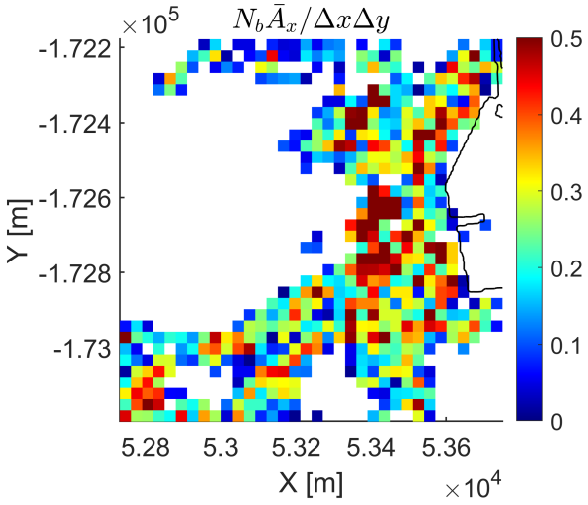

(c) Onagawa area

Figure 6.14: Product of N_b and $\bar{A}_x$ per unit area in (a): Sumida area, (b): Tacloban area, and (c): Onagawa area.

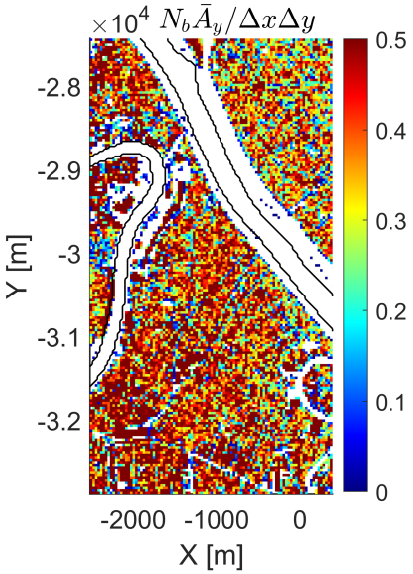

(a) Sumida area

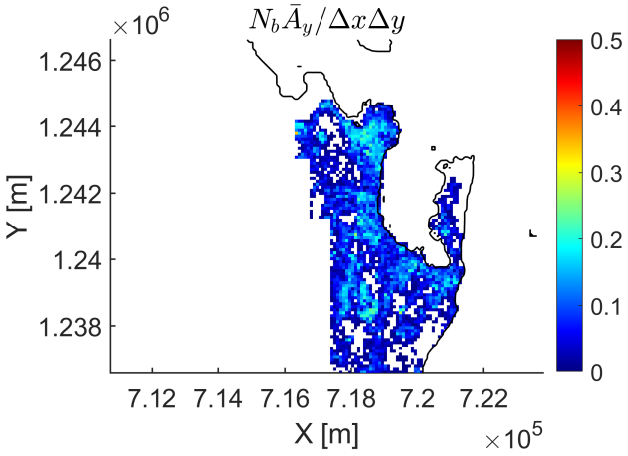

(b) Tacloban area

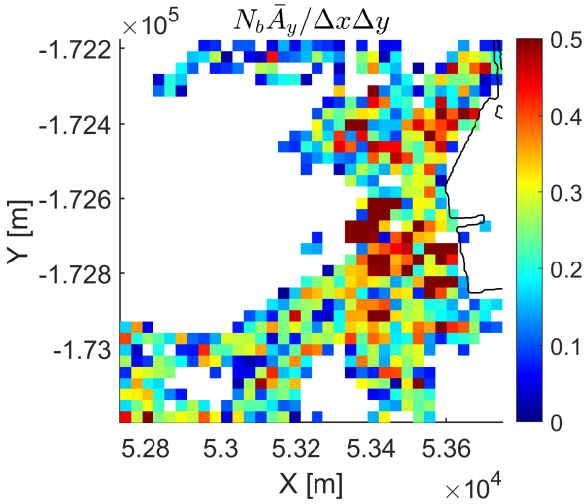

(c) Onagawa area

Figure 6.15: Product of N_b and $\bar{A}_y$ per unit area in (a): Sumida area, (b): Tacloban area, and (c): Onagawa area.

6.5 Summary of Chapter 6

In Chapter 6, storm surge inundation simulations are conducted for Sumida and Koto wards in the coastal areas of Tokyo using typhoons under the assumption of pseudo global warming, and the inundation characteristics such as inundation depth and velocity that appear when iDFM is used in large cities are clarified. In addition, the differences between the Onagawa case in Chapter 4 and the Tacloban case in Chapter 5 are summarized in terms of the magnitude of the ratio of the drag force term to the advection term. The results obtained are as follows.

a) When iDFM is used to calculate storm surge inundation in a large city with a dense array of buildings such as Tokyo, the inundation depth near the sea-land boundary (embankment) is higher than that of the coarse model, and the difference narrows as the run-up distance increases, eventually resulting in a reversal of the relationship. Such a feature was not observed in the previous chapter.

b) Because the majority of the meshes in the domain have buildings as input, the flow velocities, both maximum and time series, are reduced by more than 50% across the domain using iDFM compared to the roughness model, and this difference is consistent with the results in the previous chapters.

c) The contribution of the drag force term to inundating flow is defined as the ratio of the advection term to the drag term at the maximum velocity, the magnitude of which differs more than 10 times in each case (Tokyo: more than 200, Tacloban: less than 50, Onagawa: less than 20). The larger the ratio, the stronger the velocity reduction effect and the more water is held back near the shoreline.

d) One of the factors that determine the size of the contribution is the time variation and absolute value of the momentum and mass fluxes entering the land area. When the absolute value and time variation of the inflowing momentum and mass fluxes are large, as in the case of a tsunami, the contribution rate decreases because the advection term also increases relatively. On the other hand, when the absolute values of the inflowing momentum and mass fluxes are small, as in the case of a storm surge, the value of the advection term is smaller than that of a tsunami, and consequently the contribution increases.

e) One of the factors that determine the size of the contribution is the difference in the input SGS parameters, which increases or decreases depending on the building density. When the building density is defined as the product of the projected area per unit and the number of buildings, the contribution ratio of the storm surge becomes sensitive when the building density is large.

The storm surge model developed in Chapter 6, which combines AMR and SuWAT, can be applied to the long-term assessment of storm surge (and of course, tsunami) nationwide, because it can take buildings into account while reducing the computational cost.

Chapter 7

Conclusions

In this study, for the development of long-term hazard assessment of tsunami and storm surge, the author conducted physical modeling of inundation over coastal city to build benchmark data to validate numerical models of inundations in coastal urban areas. Then, the accuracy of high-resolution inundation simulation was validated by the experiment. Next, the iDFM, which is an subgrid-scale model focusing on the drag force on buildings, was developed and validated to reduce the computational cost with keeping accuracy. The following paragraphs show the main conclusions in each chapter.

In Chapter 2, a physical modeling of inundation using large tsunami flume and physical coastal city model was conducted with advanced visualization techniques. In the experiment, the propagation of inundating waves on land was visualized by flowing water dyed with red paint and tracer particles dyed with yellow fluorescent paint, and the time series of leading edges of inundation and spatial distribution of velocity were successfully estimated by 4K video image analysis. The pathlines and velocities on them were traced using time series of velocity to focus inundation characteristics in local scale in the case of short period waves as an incident wave. Many pathlines affected by buildings were observed and classified mainly in three patterns; 1) reflection, 2) overtopping, and 3) diffraction. The velocity and direction of the flow varied greatly depending on the building, and the importance of inundation calculations that reflected the shape of the building was confirmed.

In Chapter 3, numerical modeling of tsunami inundation in a 3D complex coastal city model including ports and buildings using building-resolving topography in high-resolution grid was conducted and validated using the dataset of leading edges and limit of inundation, flow velocity and inundation depth obtained from the experiment in Chapter 2. Ensemble simulations were performed using four numerical models (TUNAMI, STOC, SGSWE, and JAGURS) based on 2D-SWE to quantify the variations of the inundation depth, velocity, and leading edges or limit of inundation. As a result, it was found that the wide area inundation process (inundation depth, flow velocity, limit of inundation, etc.) could be reproduced using any of the models, but the flow velocity around buildings and the water level rise due to the flow merging at intersections varied among the models.

In Chapter 4, as an alternative approach to the building-resolving simulation with heavy computational cost, an subgrid-scale model iDFM focusing on the drag force on

multiple buildings was developed to reduce the computational load while ensuring accuracy. As a performance evaluation, idealized numerical experiments using simple urban topography with several spatial building layout patterns and hindcast experiments targeting a historical tsunami inundation event for the 2011 Tohoku tsunami were conducted, and the results were compared with those of a tsunami inundation simulation using building-resolving topography in high resolution. As a result, the grid cell size dependency of the limit of inundation, maximum water level, and maximum flow velocity was successfully reduced compared to the existing roughness and drag force models. On the other hand, the accuracy of local phenomena driven by buildings such as surface rising due to blocking and contracting current between structures by the iDFM is clarified as the further challenge.

In Chapter 5, the iDFM developed in Chapter 4 was applied to the historical storm surge inundation (TC Haiyan case) targeting coastal urban area in Leyte island in Philippine using 2D-SWE based storm surge model SuWAT. The implementation of the wind drag coefficient in the land side based on the SGS parameters was also proposed and validated using available survey data. After that, the inundation characteristics such as limit of inundation, inundation depth, and velocity modeled by the iDFM with new implantation of wind drag coefficient were examined in comparison with the survey data and the roughness model used in previous studies. It was found that the influence by the implementation of wind stress change based on building information was large for velocity near limits of inundation, and such velocity reduction leads to smaller inundated area. The inundation limit in Tacloban area was close to the observation, which shows the potential of the model improvement. As a difference between previous roughness model, the flow velocity were sensitively reduced rather than inundation depth near shoreline. On the other hand, the smaller inundation depth and velocity near run-up limit compared to the roughness model because the velocity reduction by buildings was iterated in every time step in momentum conservation as the run-up distance was longer. Such velocity reduction made large difference in leading edges of inundation and this could result in large difference of arrival time.

In Chapter 6, an efficient method for simulating storm surge occurrence and urban inundation over a wide area of Japan was developed by combining the storm surge models SuWAT and iDFM with storm surge model GeoClaw based on the adaptive mesh refinement which changes the computational grid cell size spatio-temporally. Using the developed method, storm surge inundation simulations were conducted for Sumida and Koto wards in the coastal areas of Tokyo using typhoons under the assumption of pseudo global warming, and the inundation characteristics such as inundation depth and velocity that appeared when iDFM was used in large cities were clarified. In addition, the contribution of the drag force term to the advection term was calculated for the simulation of the Tohoku earthquake tsunami, the storm surge caused by Typhoon Haiyan, and the virtual storm surge experiments in Sumida and Koto wards. The ratio of the drag force term to the advection term (DA ratio) was relatively small when the magnitude and time variation of the momentum and mass fluxes into the land was large. And it was also found that the DA ratio increased when the density of buildings in the computational grid cell was high.

As a final remark, the further challenges and visions are mentioned. First challenge is the improvement of accuracy of the hydrodynamic characteristics modeled by the iDFM. The iDFM cannot reflect the building shape directly in topography and mass conservation law cannot consider the building effect. As a result, it is difficult to represent local changes in water levels and velocities due to the porosity and arrangement between buildings, and it is difficult to reproduce the contraction that occurs between buildings and the water surface rising by buildings blocking. This tendency was clearly observed in the idealized numerical experiments described in Chapter 4 and in the reproduction calculation of the Tohoku earthquake tsunami where the DA ratio was relatively small. To improve this point, an approach such as adding a term to the conservation of mass and momentum laws to describe the porosity and arrangement between buildings can be exemplified. After improving the accuracy of the iDFM, this study can be applied to various risk assessment of coastal urban inundation by tsunamis or storm surges.

Acknowledgment

I would like to express my deepest gratitude to Professor Nobuhito Mori, Disaster Prevention Research Institute, Kyoto University, for his kind and careful guidance in achieving this doctoral thesis. I would also like to express my sincere gratitude to Prof. Mori for his many discussions with me and his precise guidance.

Next, I would like to express my gratitude to Professor Tetsuya Hiraishi and Associate Professor Tomoya Shimura for taking on the role of associate reviewers. I would like to thank Professor Hiraishi for his cooperation in the experiments conducted in this research. I apologize for the contamination of the experimental tank with tracer particles. I would also like to express my gratitude to Assistant Professor Takuya Miyashita who, as my advisor and a close colleague in the laboratory, consulted me on a wide range of topics, from how to run the GeoClaw model to how to catch a baseball. I would like to express my gratitude to all staffs in the laboratory for his advice and guidance at every stage of my research, and for providing an environment that made it easy for students to work on their research and ask questions.

I would like to thank Professor Andrew Kennedy (University of Notre Dame), and Associate Professor Tomohiro Yasuda (Kansai University) for their valuable advice and guidance on the experiments conducted in Chapter 2 of this thesis. I also would like to thank Yu Chida (Port and Airport Research Institute), Zhongduo Zhang (University of Notre Dame), Andrew Copp (University of Notre Dame), Takashi Yamamoto (past student in Kansai University), Assistant Professor Che-Wei Chang and Mr. Masato Kamo (DPRI, Kyoto University) for help for conducting tsunami flume experiment. Especially, Yu Chida gave me so much advice about analysis of experiment, making dataset, and numerical simulation.

We are grateful to Associate Professor Sooyoul Kim (Kumamoto University) for his advice on SuWAT, the storm surge model used in Chapters 5 and 6, and for providing the data set. We would like to express our sincere thanks to him.

This work was supported by the Japan Society for the Promotion of Science (JSPS) Fellowships for Young Scientists (19J22429).

I would like to thank all members of the coastal engineering laboratory. Six years in this laboratory with them is a precious experience for me. In particular, Dr. Audrius Sabūnas, Dr. Zuorui Lyu, Dr. Tung-Cheng Ho, and Assistant Professor Masaya Toyoda, (Toyohashi University of Technology) enough for their help in one year, which was as dense as three years. I would also like to express my gratitude to Yuki Imai (JICA) who has been a great help to me from my undergraduate days to the third year of my doctoral

course. I would also like to thank Mr. Maki Chiwata, Taisei Corporation, who was my classmate in the master's course.

I would also like to express my gratitude to Mr. Yuichiro Komori, Sangokushi, who hired me as a part-time worker during my three years of undergraduate and master's degrees and provided me with free dandan noodles after working. The taste of noodle soup after research was the best in the world.

I am sincerely grateful to my family members. My mother's ability to gather and analyze information is something that I can learn from.

Finally, I would like to thank my wife Kyoka and her parents for trusting and marrying me. I would not have been able to meet her without our laboratory. I would like to express my sincere gratitude to all the people who watched over and supported the completion of this thesis. Thank you very much.

本博士論文を取りまとめるにあたり，懇切丁寧にご指導いただいた京都大学防災研究所 森 信人 教授に深く感謝を申し上げます．森先生には，浅学な著者と幾度も議論していただき，的確なご指導を頂きました．また，ご多忙な中で自ら研究を進める森先生から，研究活動の取り組み方についても多くご教示いただきました．

続いて，副査を引き受けてくださった平石哲也 教授，志村智也 准教授に感謝を申し上げます．平石先生には，本研究で実施した実験についてもご協力を頂きました．実験水槽をトレーサ粒子で汚してしまったことについてはお詫びを申し上げます．また，指導教員として，研究室の近い先輩としてモデルの動かし方から野球のボールのとり方まで多岐にわたりご相談に載ってくださった宮下卓也 助教に感謝を申し上げます．研究の各段階で，ご助言・ご指導を頂いた上に，学生が研究に取り組みやすく質問しやすい環境を提供していただきました．

ノートルダム大学の Andrew Kennedy 教授，関西大学の安田誠宏 准教授には，本論文第 2 章で実施した実験について多大なご助言・ご指導を頂きました．また，実験時にご協力を頂いた港湾空港技術研究所 千田 優 氏，ノートルダム大学 張 鐘鐸 氏，ノートルダム大学 Andrew Copp 氏，ハイドロ総合技術研究所 山本剛士 氏，京都大学防災研究所 張 哲維 助教， 加茂正人 技術職員にも感謝いたします．特に，千田 氏には実験後の解析や数値計算時にたくさんアドバイスを頂きました．

熊本大学の金洙列准教授には，第 5, 6 章で用いた高潮モデル SuWAT についてのアドバイス，データセットの提供を頂きました．深くお礼を申し上げます．

また，本研究は日本学術振興会特別研究員奨励費 (19J22429) による成果です．

研究室にて，共に生活した本研究室の研究員，学生や秘書の皆様に感謝いたします．特に，博士課程 3 年間を共に過ごした Audrius Sabūnas 氏，呂 祚叡 氏，何 東政 氏と 1 年間というものの 3 年分の密度でお世話になった豊橋技術科学大学 豊田将也 助教（元学振特別研究員 PD）には感謝してもしきれません．また，学部時代から博士課程 3 年時まで今井優樹 氏にも大変お世話になりました．修士課程在籍時の同期であった大成建設 千綿 蒔 氏にも感謝します．

また，学部・修士の 3 年間にアルバイトとして雇ってくださり，まかないで担々麺を提供してくださった三国志 小森裕一郎さんにも感謝を申し上げます．研究後に食べる担々麺の味は世界一でした．

これまでの，生活を支えてくださった母，兄，伯父に感謝します．母親の情報収集能力，

分析力は私にとっても見習うべき点です．

最後に，著者を信頼し結婚してくれた妻 京香と，妻のご両親に感謝いたします．彼女との出会いは，本研究室無しにはありませんでした．本論文の完成を見守り，支えて頂きました．本当にありがとう．

Bibliography

[1] Aburaya T. and Imamura F. The proposal of a tsunami run-up simulation using combined equivalent roughness. *Proc. Coastal Eng., JSCE*, Vol. 49, pp. 276–280, 2002.

[2] Adriano B., Hayashi S., Gokon H., Mas E., and Koshimura S. Understanding the extreme tsunami inundation in Onagawa town by the 2011 Tohoku earthquake, its effects in urban structures and coastal facilities. *Coastal Engineering Journal*, Vol. 58, No. 04, p. 1640013, 2016.

[3] ASCE . *Minimum design loads and associated criteria for buildings and other structures*. ASCE, 2016.

[4] Baba T., Takahashi N., Kaneda Y., Ando K., Matsuoka D., and Kato T. Parallel implementation of dispersive tsunami wave modeling with a nesting algorithm for the 2011 Tohoku tsunami. *Pure and Applied Geophysics*, Vol. 172, No. 12, pp. 3455–3472, 2015.

[5] Bagherizadeh E., Zhang Z., Farhadzadeh A., Angelidis D., Ghazian A. M., Moghimi S., and Khosronejad A. Numerical modelling of solitary wave and structure interactions using level-set and immersed boundary methods by adopting adequate inlet boundary conditions. *Journal of Hydraulic Research*, pp. 1–27, 2020.

[6] Berger Marsha J., George David L., LeVeque Randall J., and Mandli Kyle T. The GeoClaw software for depth-averaged flows with adaptive refinement. *Advances in Water Resources*, Vol. 34, No. 9, pp. 1195–1206, 2011. New Computational Methods and Software Tools.

[7] Blumberg A. F., Georgas N., Yin L., Herrington T. O., and Orton P. M. Street-scale modeling of storm surge inundation along the New Jersey Hudson River waterfront. *Journal of Atmospheric and Oceanic Technology*, Vol. 32, No. 8, pp. 1486–1497, 2015.

[8] Booij NRRC, Ris R. C., and Holthuijsen L. H. A third-generation wave model for coastal regions: 1. Model description and validation. *Journal of geophysical research: Oceans*, Vol. 104, No. C4, pp. 7649–7666, 1999.

[9] Cabinet Office Goverment of Japan. Report of the Committee for Technical Investigation on Countermeasures for Earthquakes and Tsunamis Based on

the Lessons Learned from the “2011 off the Pacific coast of Tohoku Earthquake”. http://www.bousai.go.jp/kaigirep/chousakai/tohokukyokun/index.html (accessed Nov., 2021), 2011.

[10] Cabinet Office Goverment of Japan. Massive Earthquake Model Review Meeting of the Nankai Trough. http://www.bousai.go.jp/jishin/nankai/model/index.html (accessed Nov., 2021), 2012.

[11] Canny J. A computational approach to edge detection. *IEEE Transactions on pattern analysis and machine intelligence*, No. 6, pp. 679–698, 1986.

[12] Casulli V. A high-resolution wetting and drying algorithm for free-surface hydrodynamics. *International Journal for Numerical Methods in Fluids*, Vol. 60, No. 4, pp. 391–408, 2009.

[13] Charvet I., Suppasri A., Kimura H., Sugawara D., and Imamura F. A multivariate generalized linear tsunami fragility model for Kesennuma City based on maximum flow depths, velocities and debris impact, with evaluation of predictive accuracy. *Natural Hazards*, Vol. 79, No. 3, pp. 2073–2099, 2015.

[14] Chow V. T. *Open-channel hydraulics*. New York: McGraw-Hill, 1959.

[15] Contributers OpenStreetMap. OpenStreetMap. http://openstreetmap.org/. (Accessed on 01/15/2022).

[16] Cox D., Tomita T., Lynett P., and Holman R. Tsunami inundation with macro-roughness in the constructed environment. In *Coastal Engineering 2008: (In 5 Volumes)*, pp. 1421–1432. World Scientific, 2009.

[17] Fukui N., Prasetyo A., and Mori N. Numerical modeling of tsunami inundation using upscaled urban roughness parameterization. *Coastal Engineering*, Vol. 152, p. 103534, 2019.

[18] Goda K., Yasuda T., Mori N., and Mai P. M. Variability of tsunami inundation footprints considering stochastic scenarios based on a single rupture model: application to the 2011 Tohoku earthquake. *Journal of Geophysical Research: Oceans*, Vol. 120, No. 6, pp. 4552–4575, 2015.

[19] Goda K., Yasuda T., Mori N., and Maruyama T. New scaling relationships of earthquake source parameters for stochastic tsunami simulation. *Coastal Engineering Journal*, Vol. 58, No. 3, pp. 1650010–1, 2016.

[20] Goto C., Ogawa Y., Shuto N., and Imamura F. Numerical method of tsunami simulation with the leap-frog scheme. *IUGG/IOC TIME Project Intergovernmental Oceanographic Commission of UNESCO, Manuals and Guides*, Vol. 35, p. 126, 1997.

[21] Hayashi S. and Koshimura S. Measurement of the 2011 Tohoku Tsunami Flow Velocity by the Aerial Video Analysis. *J. Jpn. Soc. Civ. Eng. Coast. Eng.*, Vol. 68, No. 2, pp. I˙366–I˙370, 2012.

[22] Hayashi S., Narita Y., and Koshimura S. Developing Tsunami Fragility Curves from the Surveyed Data and Numerical Modeling of the 2011 Tohoku Earthquake Tsunami. *J. Jpn. Soc. Civ. Eng. B2 (Coast. Eng.)*, Vol. 69, No. 2, pp. I_386–I_390, 2013.

[23] Hiraishi T., Mori N., Yasuda T., Azuma R., Mase H., and Okura S. Characteristics of tsunami generator newly implemented with three generation modes. *J. Jpn. Soc. Civ. Eng. B2 (Coast. Eng.)*, Vol. 71, No. 2, pp. I_349–I_354, 2015.

[24] Honda T. and Mitsuyasu T. Experimental study on the effect of wind on water surface. *Proc. Coast. Eng., JSCE*, Vol. 27, pp. 90–93, 1980.

[25] Hong S. Y. and Lim J. O. J. The WRF Single-Moment 6-Class Microphysics Scheme (WSM6). *JOURNAL OF THE KOREAN METEOROLOGICAL SOCIETY*, Vol. 42, pp. 129–151, 2006.

[26] Ikawa M., Mizuno H., Matsuo T., Murakami M., Yamada Y., and Saito K. Numerical Modeling of the Convective Snow Cloud over the Sea of Japan Precipitation Mechanism and Sensitivity to Ice Crystal Nucleation Rates. *Journal of the Meteorological Society of Japan. Ser. II*, Vol. 69, No. 6, pp. 641–667, 1991.

[27] Imai K., Imamura F., and Iwama S. Advanced tsunami computation for urban regions. *J. Jpn. Soc. Civ. Eng. B2 (Coast. Eng.)*, Vol. 69, No. 2, pp. I_311–I_315, 2013.

[28] Janssen Peter AEM. Wave-induced stress and the drag of air flow over sea waves. *Journal of Physical Oceanography*, Vol. 19, No. 6, pp. 745–754, 1989.

[29] Kaiser G., Burkhard B., Römer H., Sangkaew S., Graterol R., Haitook T., Sterr H., and Sakuna-Schwartz D. Mapping tsunami impacts on land cover and related ecosystem service supply in Phang Nga, Thailand. *Natural hazards and earth system sciences*, Vol. 13, No. 12, pp. 3095–3111, 2013.

[30] Kawase H., Yamaguchi M., Imada Y., Hayashi S., Murata A., Nakaegawa T., Miyasaka T., and Takayabu I. Enhancement of extremely heavy precipitation induced by Typhoon Hagibis (2019) due to historical warming. *SOLA*, pp. 17A–002, 2021.

[31] Kennedy A. B., Wirasaet D., Begmohammadi A., Sherman T., Bolster D., and Dietrich J.C. Subgrid theory for storm surge modeling. *Ocean Modelling*, Vol. 144, p. 101491, 2019.

[32] Kim S., Kumagai K., and Mase H. Inundation Modeling of Typhoon Haiyan Using Sea Surface and Bottom Drags Induced by Wave and Current Interaction. *J. Jpn. Soc. Civ. Eng. B2 (Coast. Eng.)*, Vol. 73, No. 2, pp. I_181–I_186, 2017.

[33] Kim S., Mori N., Mase H., and Yasuda T. The role of sea surface drag in a coupled surge and wave model for Typhoon Haiyan 2013. *Ocean Modelling*, Vol. 96, pp. 65–84, 2015.

[34] Knutson T., Camargo S. J., Chan J.C.L., Emanuel K., Ho C-H., Kossin J., Mohapatra M., Satoh M., Sugi M., Walsh K., and others . Tropical cyclones and climate change assessment: Part ii: Projected response to anthropogenic warming. *Bulletin of the American Meteorological Society*, Vol. 101, No. 3, pp. E303–E322, 2020.

[35] Kotani M., Imamura F., and Shuto N. Tsunami run-up simulation and damage estimation by using GIS. *Proc. Coast. Eng., JSCE*, Vol. 45, pp. 356–360, 1998.

[36] Le T. A., Takagi H., Heidarzadeh M., Takata Y., and Takahashi A. Field surveys and numerical simulation of the 2018 Typhoon Jebi: impact of high waves and storm surge in semi-enclosed Osaka Bay, Japan. *Pure and Applied Geophysics*, Vol. 176, No. 10, pp. 4139–4160, 2019.

[37] LeVeque R. J. and others . *Finite volume methods for hyperbolic problems*, Vol. 31. Cambridge university press, 2002.

[38] LeVeque Randall J., George David L., and Berger Marsha J. Tsunami modelling with adaptively refined finite volume methods. *Acta Numerica*, Vol. 20, pp. 211–289, 2011.

[39] Lin I-I, Pun Iam-Fei, and Lien Chun-Chi. “category-6” supertyphoon Haiyan in global warming hiatus: Contribution from subsurface ocean warming. *Geophysical Research Letters*, Vol. 41, No. 23, pp. 8547–8553, 2014.

[40] Lynett P. J. Precise prediction of coastal and overland flow dynamics: a grand challenge or a fool's errand. *Journal of disaster research*, Vol. 11, No. 4, pp. 615–623, 2016.

[41] Lynett P. J., Gately K., Wilson R., Montoya L., Arcas D., Aytore B., Bai Y., Bricker J. D., Castro M. J., Cheung K. F., and others . Inter-model analysis of tsunami-induced coastal currents. *Ocean Modelling*, Vol. 114, pp. 14–32, 2017.

[42] Mai P. M. and Thingbaijam K. K. S. SRCMOD: An online database of finite-fault rupture models. *Seismological Research Letters*, Vol. 85(6), pp. 1348–1357, 2014.

[43] Mandli K. T. and Dawson C. N. Adaptive mesh refinement for storm surge. *Ocean Modelling*, Vol. 75, pp. 36–50, 2014.

[44] Miyashita T., Mori N., and Goda K. Uncertainty of probabilistic tsunami hazard assessment of Zihuatanejo (Mexico) due to the representation of tsunami variability. *Coastal Engineering Journal*, Vol. 62, No. 3, pp. 413–428, 2020.

[45] Mizobata Y., Yasuda T., Okumura Y., Mori N., Mase H., and Shimada H. Resistance capacity assessment of local communities against tsunami inundations by continuous increase in tsunami intensity. *J. Jpn. Soc. Civ. Eng. B2 (Coast. Eng.)*, Vol. 70, No. 2, pp. I_1326–I_1330, 2014.

[46] MLIT . Guide to Determining the Potential Tsunami Inundation Ver 2.10. https://www.mlit.go.jp/river/shishin˙guideline/kaigan/tsunamishinsui˙manual.pdf (accessed Nov., 2021), 2019.

[47] MLIT . Guide to Creating Storm Surge Inundation Area Maps Ver 2.10. https://www.mlit.go.jp/river/shishin˙guideline/kaigan/takashioshinsui˙manual.pdf (accessed Nov., 2021), 2021.

[48] MLIT . PLATEAU. https://milt.go.jp/plateau (accessed Nov., 2021), 2021.

[49] Mori N., Cox D. T., Yasuda T., and Mase H. Overview of the 2011 Tohoku earthquake tsunami damage and its relation to coastal protection along the Sanriku Coast. *Earthquake Spectra*, Vol. 29, No. 1_suppl, pp. 127–143, 2013.

[50] Mori N., Kato M., Kim S., Mase H., Shibutani Y., Takemi T., Tsuboki K., and Yasuda T. Local amplification of storm surge by Super Typhoon Haiyan in Leyte Gulf. *Geophysical research letters*, Vol. 41, No. 14, pp. 5106–5113, 2014.

[51] Mori N., Shibutani Y., Takemi T., Kim S., Yasuda T., Niwa T., Tsujio D., and Mase H. Forecast and Hindcast of Storm Surge Modeling by Typhoon Haiyan in 2013. *J. Jpn. Soc. Civ. Eng. B2 (Coast. Eng.)*, Vol. 70, No. 2, pp. I_246–I_250, 2014.

[52] Mori N., Takahashi T., Yasuda T., and Yanagisawa H. Survey of 2011 Tohoku earthquake tsunami inundation and run-up. *Geophysical research letters*, Vol. 38, No. 7, 2011.

[53] Mueller C., Power W., Fraser S., and Wang X. Effects of rupture complexity on local tsunami inundation: Implications for probabilistic tsunami hazard assessment by example. *Journal of Geophysical Research: Solid Earth*, Vol. 120, No. 1, pp. 488–502, 2015.

[54] Oceans (GEBCO) Dataset of General Bathymetric Chart. Gridded Bathymetry Data (General Bathymetric Chart of the Oceans) GEBCO2014. https://www.gebco.net/, 2014.

[55] Oishi Y., Imamura F., Sugawara D., and Furumura T. Invesitgation of Reliable Tsunami Inundation Model in Urban Areas Using a Supercomputer. *J. Jpn. Soc. Civ. Eng. B2 (Coast. Eng.)*, Vol. 72, No. 2, pp. I_409–I_414, 2016.

[56] Okada Y. Surface deformation due to shear and tensile faults in a half-space. *Bulletin of the seismological society of America*, Vol. 75, No. 4, pp. 1135–1154, 1985.

[57] Park H., Cox D. T., Lynett P. J., Wiebe D. M., and Shin S. Tsunami inundation modeling in constructed environments: A physical and numerical comparison of free-surface elevation, velocity, and momentum flux. *Coastal Engineering*, Vol. 79, pp. 9–21, 2013.

[58] Prasetyo A., Yasuda T., Miyashita T., and Mori N. Physical modeling and numerical analysis of tsunami inundation in a coastal city. *Frontiers in built environment*, Vol. 5, p. 46, 2019.

[59] Pringgana G., Cunningham L. S., and Rogers B. D. Influence of Orientation and Arrangement of Structures on Tsunami Impact Forces: Numerical Investigation with Smoothed Particle Hydrodynamics. *Journal of Waterway, Port, Coastal, and Ocean Engineering*, Vol. 147, No. 3, p. 04021006, 2021.

[60] Qin X., Motley M. R., and Marafi N. A. Three-dimensional modeling of tsunami forces on coastal communities. *Coastal Engineering*, Vol. 140, pp. 43–59, 2018.

[61] Qin X., Motley M., LeVeque R., Gonzalez F., and Mueller K. A comparison of a two-dimensional depth-averaged flow model and a three-dimensional RANS model for predicting tsunami inundation and fluid forces. *Natural Hazards and Earth System Sciences*, Vol. 18, No. 9, pp. 2489–2506, 2018.

[62] Reduction National Disaster Risk and Council management . Effects of Typhoon " Yolanda " . http://www.ndrrmc.gov.ph, 2014.

[63] Roshko A. Experiments on the flow past a circular cylinder at very high Reynolds number. *Journal of fluid mechanics*, Vol. 10, No. 3, pp. 345–356, 1961.

[64] Saito K., Ishida J., Aranami K., Hara T., Segawa T., Narita M., and Honda Y. Nonhydrostatic atmospheric models and operational development at JMA. *Journal of the Meteorological Society of Japan. Ser. II*, Vol. 85, pp. 271–304, 2007.

[65] Sarjamee S., Nistor I., and Mohammadian A. Large eddy simulation of extreme hydrodynamic forces on structures with mitigation walls using OpenFOAM. *Natural Hazards*, Vol. 85, No. 3, pp. 1689–1707, 2017.

[66] Satake K., Fujii Y., Harada T., and Namegaya Y. Time and space distribution of coseismic slip of the 2011 Tohoku earthquake as inferred from tsunami waveform data. *Bulletin of the seismological society of America*, Vol. 103, No. 2B, pp. 1473–1492, 2013.

[67] Schiermeier Q. Did climate change cause Typhoon Haiyan. *Nature*, Vol. 11, , 2013.

[68] Skamarock W. C., Klemp J. B., Dudhia J., Gill D. O., Barker D. M., Wang W., and Powers J. G. A description of the Advanced Research WRF version 3. NCAR Technical note-475+ STR. 2008.

[69] Sogut E., Sogut D. V., and Farhadzadeh A. Effects of building arrangement on flow and pressure fields generated by a solitary wave interacting with developed coasts. *Advances in Water Resources*, Vol. 134, p. 103450, 2019.

[70] Sogut E., Sogut V. D., and Farhadzadeh A. Overland Wave Propagation and Load Distribution among Arrays of Elevated Beachfront Structures. *Journal of Waterway, Port, Coastal, and Ocean Engineering*, Vol. 146, No. 4, p. 04020016, 2020.

[71] Suppasri A., Charvet I., Imai K., and Imamura F. Fragility curves based on data from the 2011 Tohoku-oki tsunami in Ishinomaki city, with discussion of parameters influencing building damage. *Earthquake Spectra*, Vol. 31, No. 2, pp. 841–868, 2015.

[72] Suppasri A., Shuto N., Imamura F., Koshimura S., Mas E., and Yalciner A. C. Lessons learned from the 2011 Great East Japan tsunami: performance of tsunami countermeasures, coastal buildings, and tsunami evacuation in japan. *Pure and Applied Geophysics*, Vol. 170, No. 6, pp. 993–1018, 2013.

[73] Tajima Y., Yasuda T., Pacheco B. M., Cruz E. C., Kawasaki K., Nobuoka H., Miyamoto M., Asano Y., Arikawa T., Ortigas N. M., and others . Initial report of JSCE-PICE joint survey on the storm surge disaster caused by Typhoon Haiyan. *Coastal Engineering Journal*, Vol. 56, No. 1, pp. 1450006–1, 2014.

[74] Takagi H., Li S., Leon de M., Esteban M., Mikami T., Matsumaru R., Shibayama T., and Nakamura R. Storm surge and evacuation in urban areas during the peak of a storm. *Coastal Engineering*, Vol. 108, pp. 1–9, 2016.

[75] Tanioka Y. and Satake K. Tsunami generation by horizontal displacement of ocean bottom. *Geophysical research letters*, Vol. 23, No. 8, pp. 861–864, 1996.

[76] TIME . The Typhoon's Toll. *TIME Magazine*, Vol. 182, No. 22, 2013.

[77] Tomiczek T., Prasetyo A., Mori N., Yasuda T., and Kennedy A. Physical modelling of tsunami onshore propagation, peak pressures, and shielding effects in an urban building array. *Coastal Engineering*, Vol. 117, pp. 97–112, 2016.

[78] Tomita T. and Kakinuma T. Storm surge and tsunami simulation in oceans and coastal areas (STOC). *Report of the Port and Airport Research Institute*, Vol. 44, No. 2, pp. 83–98, 2005.

[79] Verma V., Kumar R., and Hsu S. 3d building detection and modeling from aerial lidar data. In *2006 IEEE Computer Society Conference on Computer Vision and Pattern Recognition (CVPR'06)*, Vol. 2, pp. 2213–2220. IEEE, 2006.

[80] Wang H., Mostafizi A., Cramer L. A., Cox D., and Park H. An agent-based model of a multimodal near-field tsunami evacuation: Decision-making and life safety. *Transportation Research Part C: Emerging Technologies*, Vol. 64, pp. 86–100, 2016.

[81] WGI IPCC-AR6. Contribution of Working Group I to the Sixth Assesment Report of the Intergovernmental Panel on Climate Change. https://www.ipcc.ch/report/ar6/wg1/ (accessed Nov., 2021), 2021.

[82] WGI IPCC-AR6. Special Report on the Ocean and Cryosphere in a Changing Climate (SROCC). https://www.ipcc.ch/srocc/ (accessed Nov., 2021), 2021.

[83] Yasuda T., Imai K., Shigihara Y., Arikawa T., Baba T., Chikasada N., Eguchi Y., Kamiya M., Minami M., Miyauchi T., and others . Numerical Simulation of Urban Inundation Processes and Their Hydraulic Quantities–Tsunami Analysis Hackathon Theme 1–. *Journal of Disaster Research*, Vol. 16, No. 7, pp. 978–993, 2021.

[84] Yasuda T., Miyaue D., Prasetyo A., Kamo M., Mori N., Hiraishi T., Mase H., and Shimada H. Tsunami inundation experiment using coastal city model. *J. Jpn. Soc. Civ. Eng. B2 (Coast. Eng.)*, Vol. 72, No. 2, pp. I_385–I_390, 2016.

Appendix A

Results of idealized numerical experiments in other cases

This appendix attaches the results (time series of leading edges, maximum surface elevation, and maximum velocity) of idealized numerical experiment in other building layouts; Regular, Random 01-03.

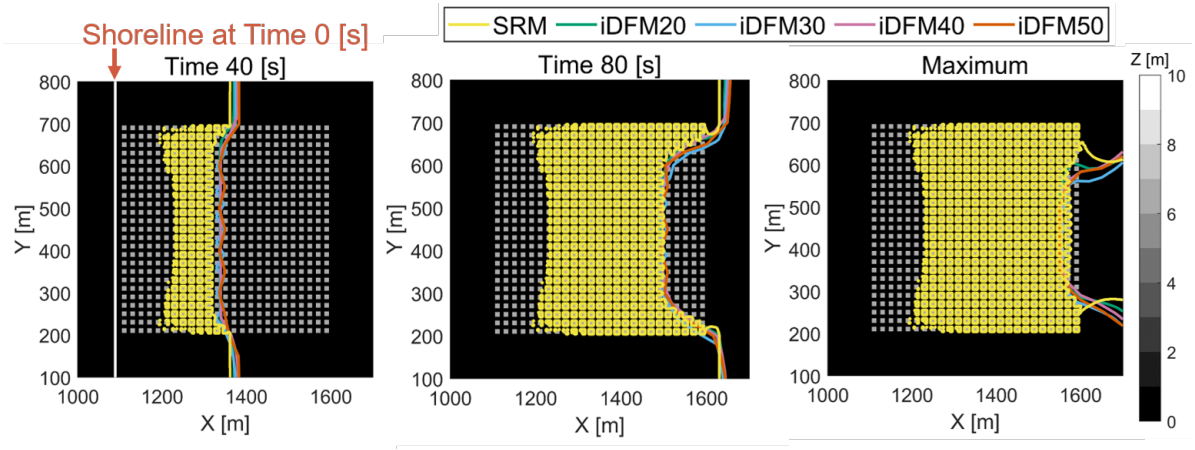

(a) Wave S075 case: ($\eta = 7.5$ m, $T = 136$ s)

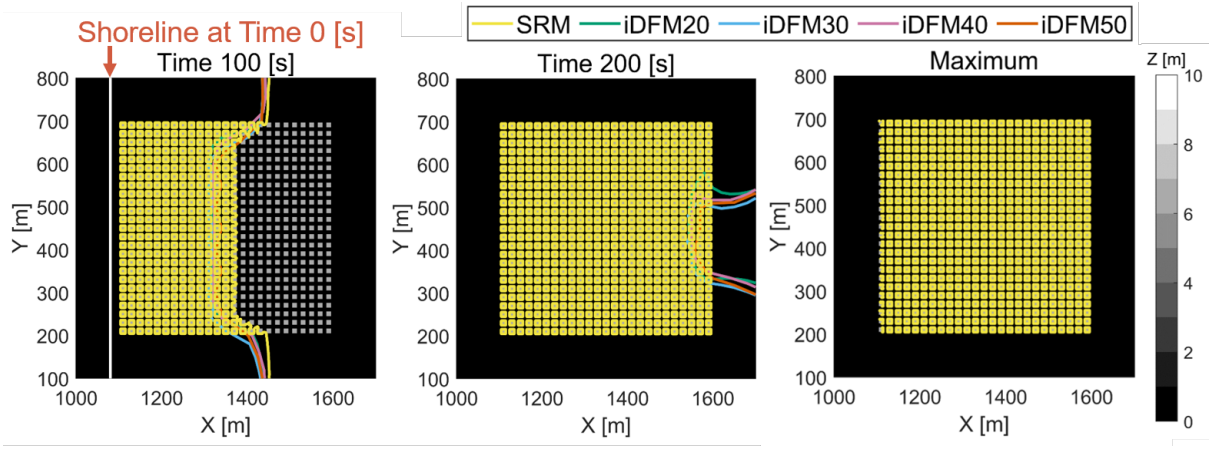

(b) Wave L15 case: ($\eta = 15$ m, $T = 4000$ s)

Figure A.1: Time series of the inundation leading edge since inundation starts modeled by the iDFM (colors indicate the cell sizes for computation or the SRM; green: $\Delta x = 20$ m, cyan: $\Delta x = 30$ m, magenta: $\Delta x = 40$ m, red: $\Delta x = 50$ m, and yellow: SRM) in the Regular topography.

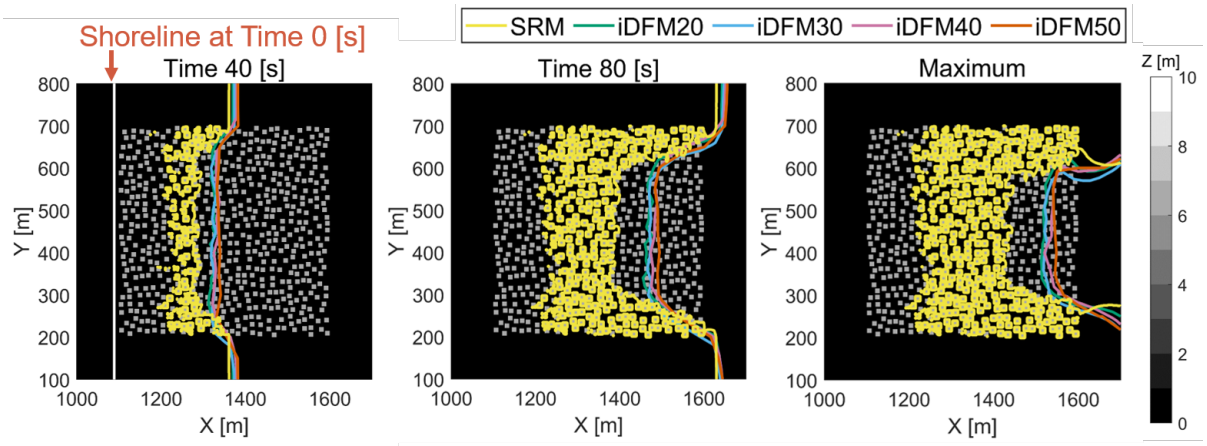

(a) Wave S075 case: ($\eta = 7.5$ m, $T = 136$ s)

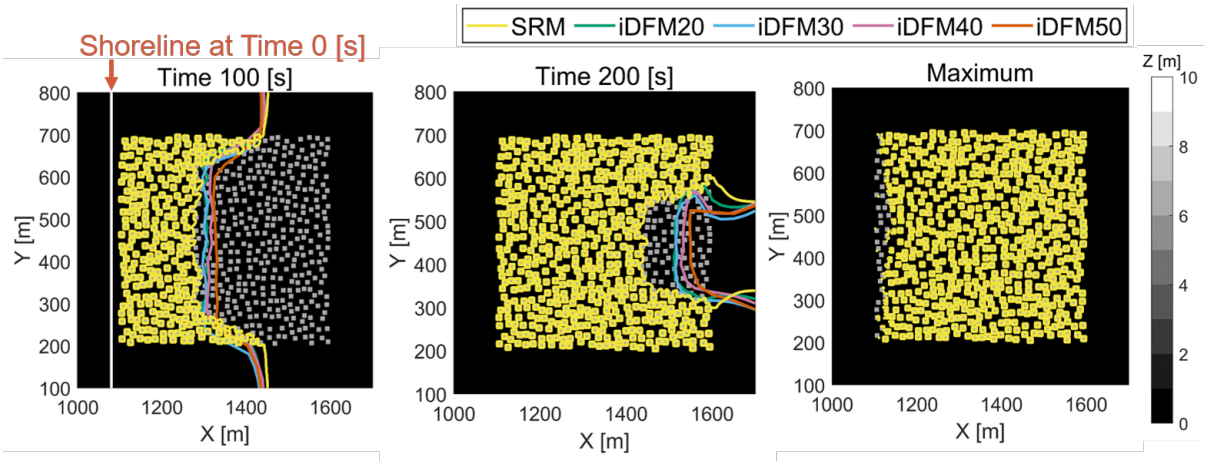

(b) Wave L15 case: ($\eta = 15$ m, $T = 4000$ s)

Figure A.2: Time series of the inundation leading edge since inundation starts modeled by the iDFM (colors indicate the cell sizes for computation or the SRM; green: $\Delta x = 20$ m, cyan: $\Delta x = 30$ m, magenta: $\Delta x = 40$ m, red: $\Delta x = 50$ m, and yellow: SRM) in the Random 01 topography.

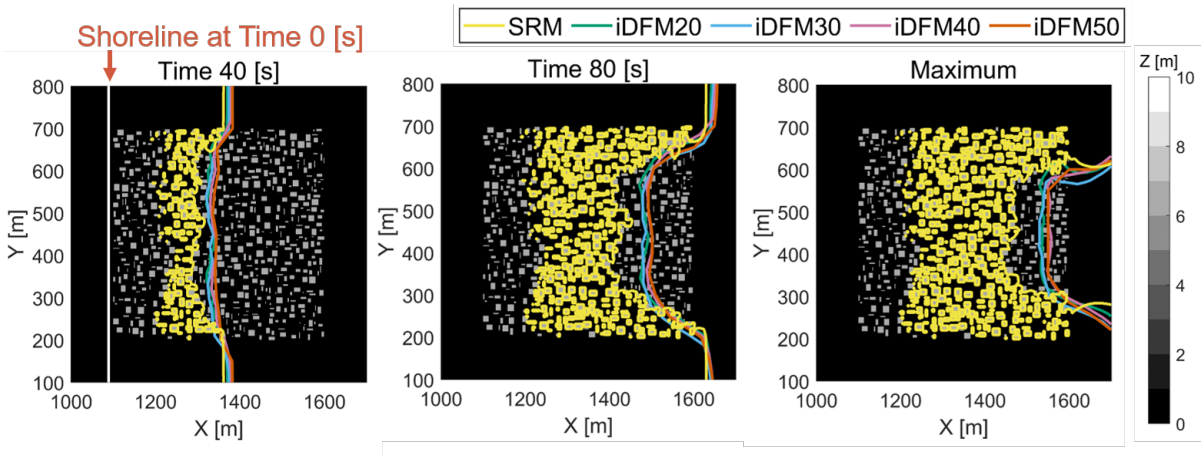

(a) Wave S075 case: ($\eta = 7.5$ m, $T = 136$ s)

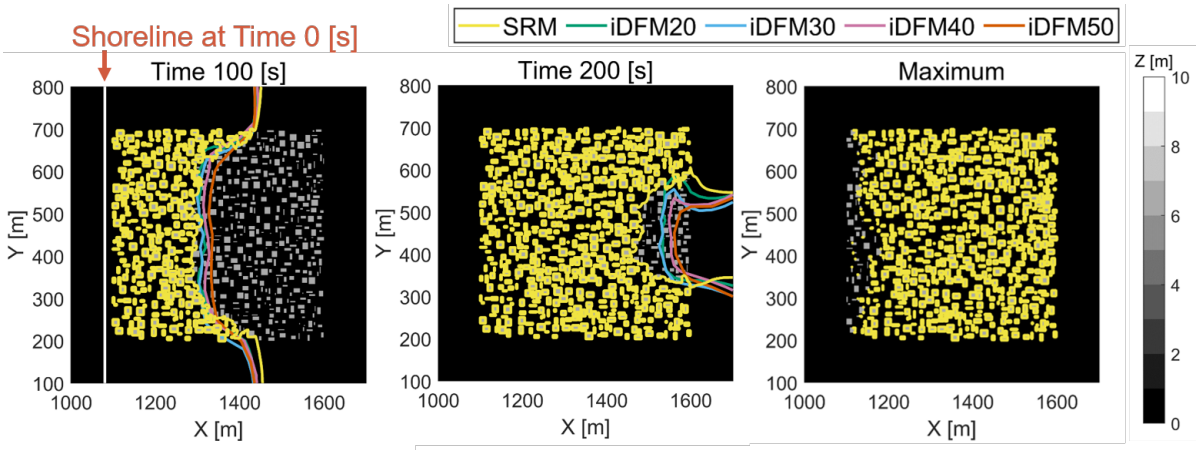

(b) Wave L15 case: ($\eta = 15$ m, $T = 4000$ s)

Figure A.3: Time series of the inundation leading edge since inundation starts modeled by the iDFM (colors indicate the cell sizes for computation or the SRM; green: $\Delta x = 20$ m, cyan: $\Delta x = 30$ m, magenta: $\Delta x = 40$ m, red: $\Delta x = 50$ m, and yellow: SRM) in the Random 02 topography.

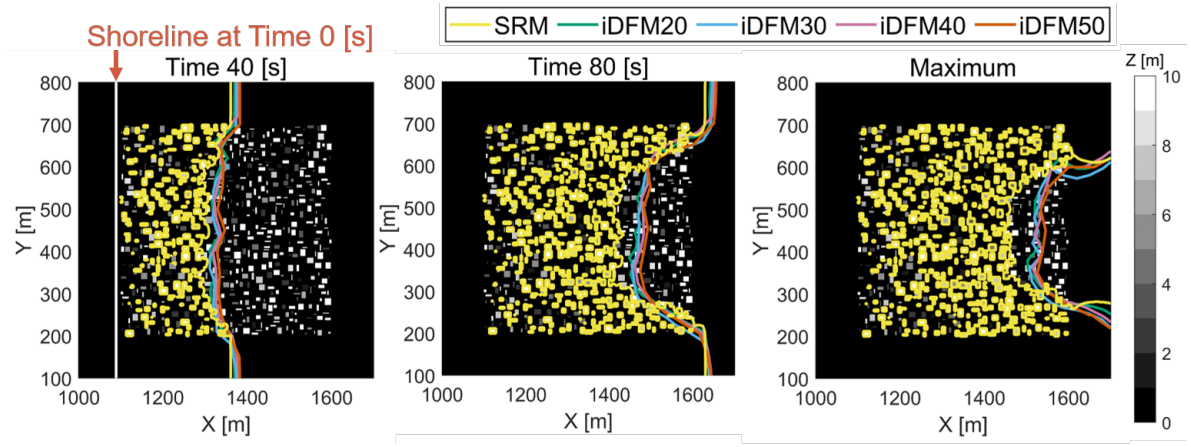

(a) Wave S075 case: ($\eta = 7.5$ m, $T = 136$ s)

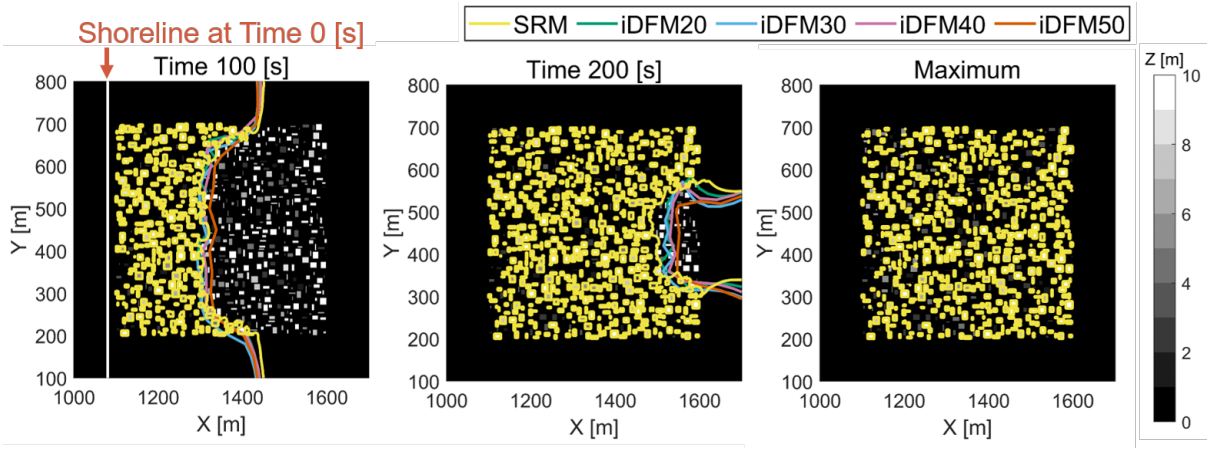

(b) Wave L15 case: ($\eta = 15$ m, $T = 4000$ s)

Figure A.4: Time series of the inundation leading edge since inundation starts modeled by the iDFM (colors indicate the cell sizes for computation or the SRM; green: $\Delta x = 20$ m, cyan: $\Delta x = 30$ m, magenta: $\Delta x = 40$ m, red: $\Delta x = 50$ m, and yellow: SRM) in the Random 03 topography.

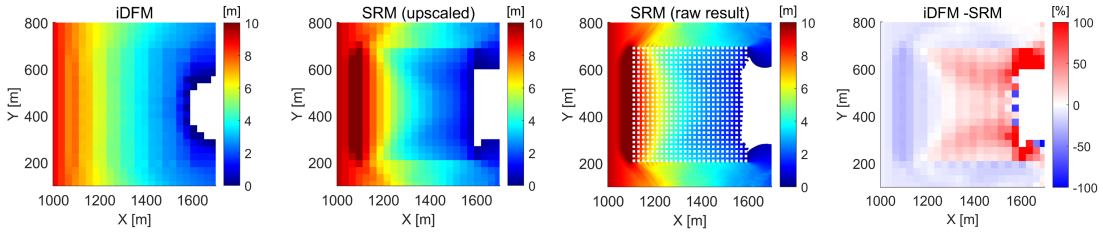

(a) Maximum surface elevation

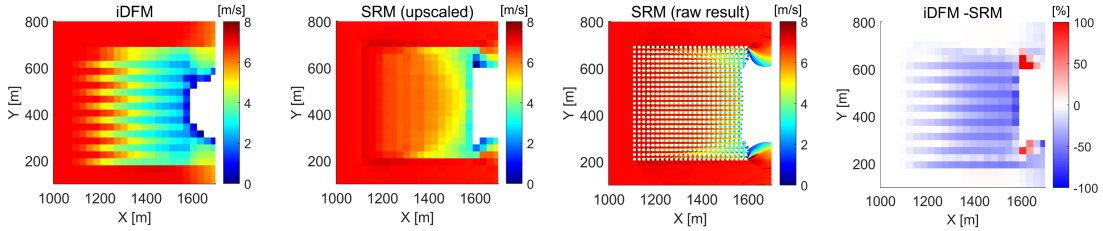

(b) Maximum fluid velocity

Figure A.5: Difference of (a) maximum surface elevation and (b) maximum fluid velocity between the iDFM ($\Delta x = 30$ m) and SRM results with the Regular topography in the Wave S075 case (1st panel from left: iDFM, 2nd panel: cell-averaged value for SRM, 3rd panel: raw results of SRM, and 4th panel: error between iDFM and SRM).

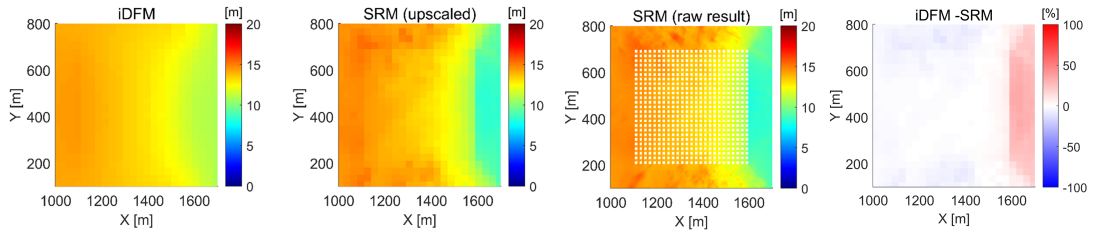

(a) Maximum surface elevation

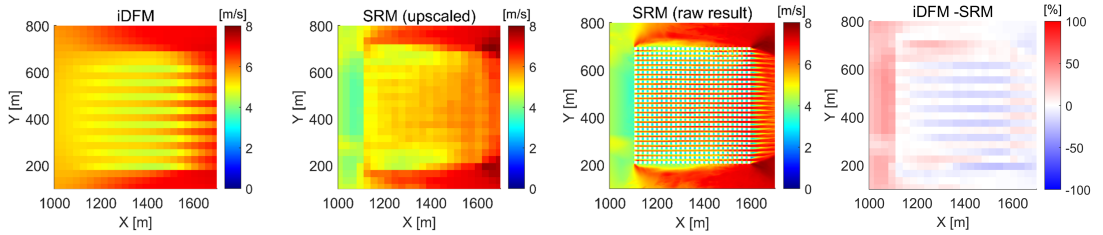

(b) Maximum fluid velocity

Figure A.6: Difference of (a) maximum surface elevation and (b) maximum fluid velocity between the iDFM ($\Delta x = 30$ m) and SRM results with the Regular topography in the Wave L15 case (1st panel from left: iDFM, 2nd panel: cell-averaged value for SRM, 3rd panel: raw results of SRM, and 4th panel: error between iDFM and SRM).

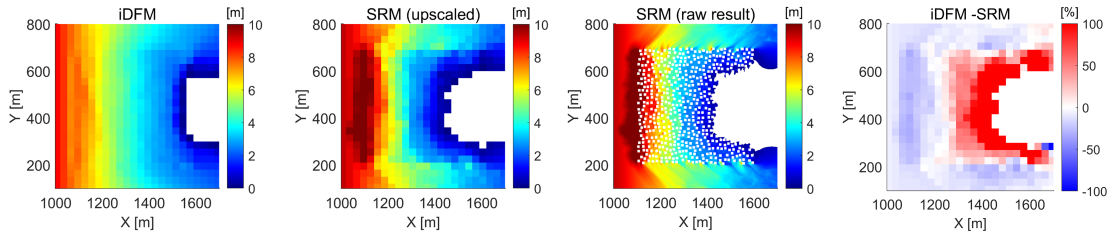

(a) Maximum surface elevation

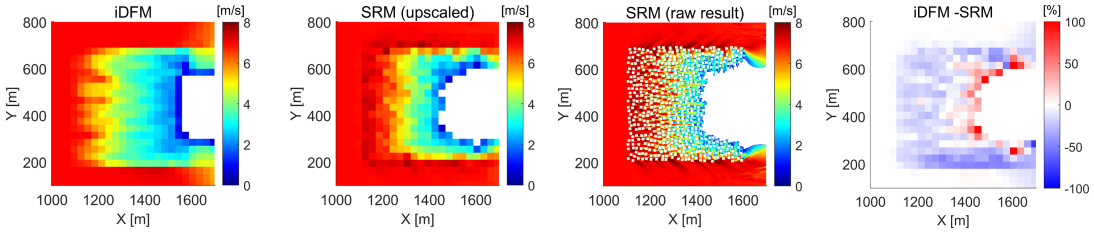

(b) Maximum fluid velocity

Figure A.7: Difference of (a) maximum surface elevation and (b) maximum fluid velocity between the iDFM ($\Delta x = 30$ m) and SRM results with the Random 01 topography in the Wave S075 case (1st panel from left: iDFM, 2nd panel: cell-averaged value for SRM, 3rd panel: raw results of SRM, and 4th panel: error between iDFM and SRM).

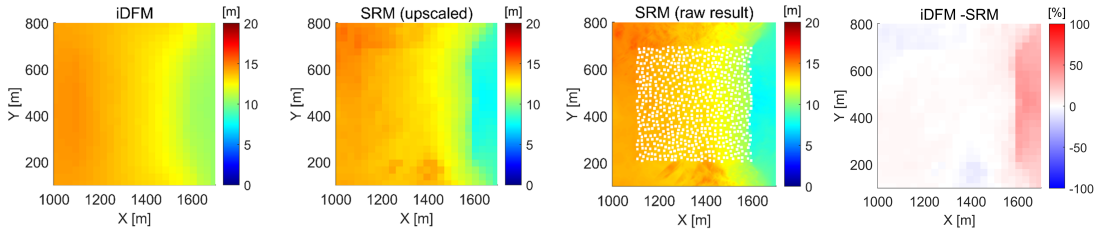

(a) Maximum surface elevation

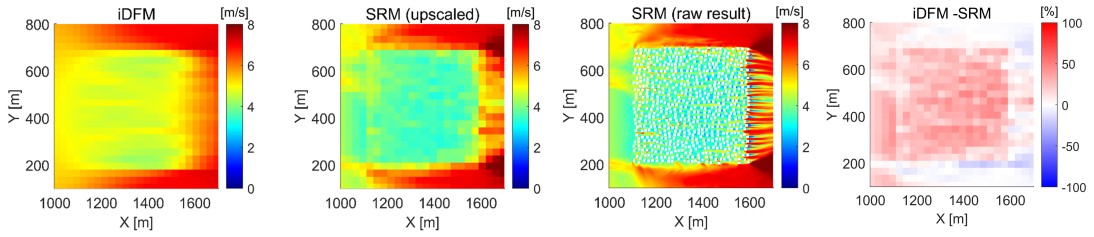

(b) Maximum fluid velocity

Figure A.8: Difference of (a) maximum surface elevation and (b) maximum fluid velocity between the iDFM ($\Delta x = 30$ m) and SRM results with the Random 01 topography in the Wave L15 case (1st panel from left: iDFM, 2nd panel: cell-averaged value for SRM, 3rd panel: raw results of SRM, and 4th panel: error between iDFM and SRM).

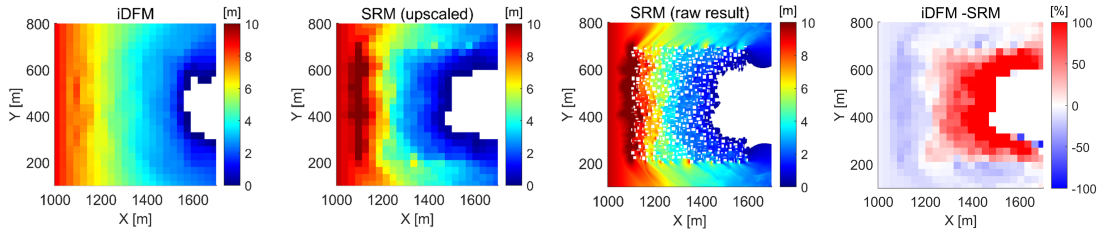

(a) Maximum surface elevation

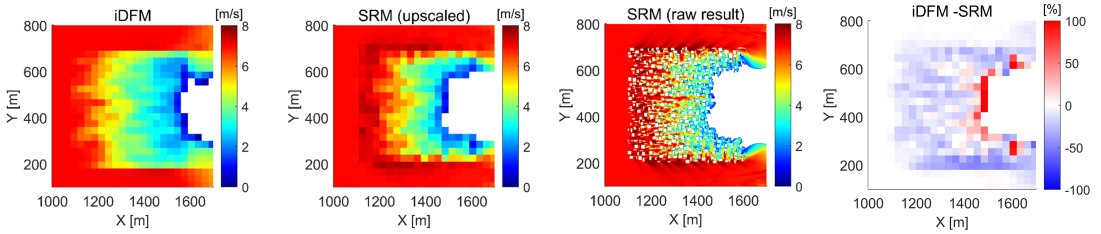

(b) Maximum fluid velocity

Figure A.9: Difference of (a) maximum surface elevation and (b) maximum fluid velocity between the iDFM ($\Delta x = 30$ m) and SRM results with the Random 01 topography in the Wave S075 case (1st panel from left: iDFM, 2nd panel: cell-averaged value for SRM, 3rd panel: raw results of SRM, and 4th panel: error between iDFM and SRM).

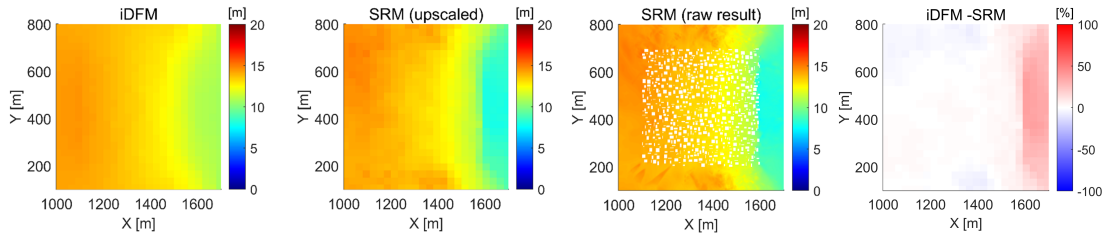

(a) Maximum surface elevation

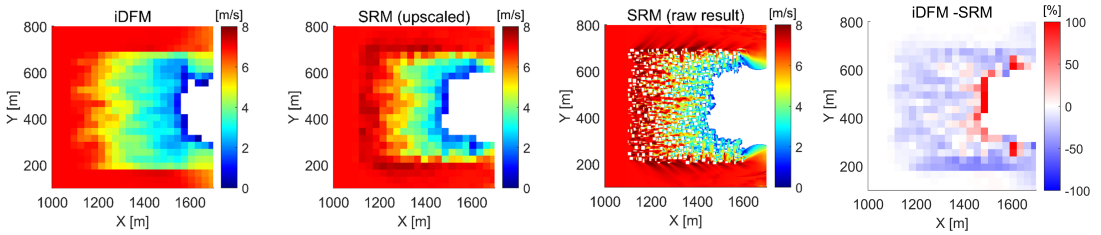

(b) Maximum fluid velocity

Figure A.10: Difference of (a) maximum surface elevation and (b) maximum fluid velocity between the iDFM ($\Delta x = 30$ m) and SRM results with the Random 02 topography in the Wave L15 case (1st panel from left: iDFM, 2nd panel: cell-averaged value for SRM, 3rd panel: raw results of SRM, and 4th panel: error between iDFM and SRM).

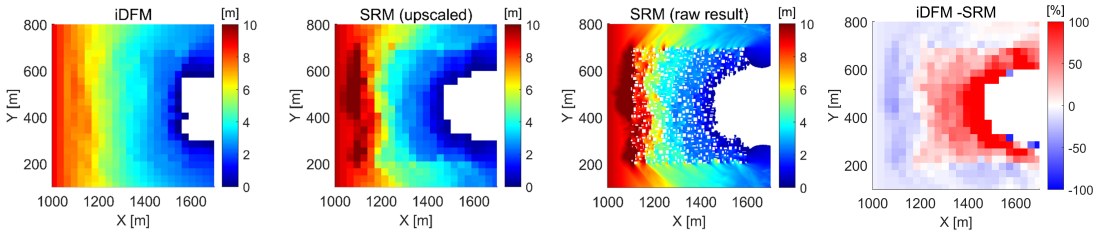

(a) Maximum surface elevation

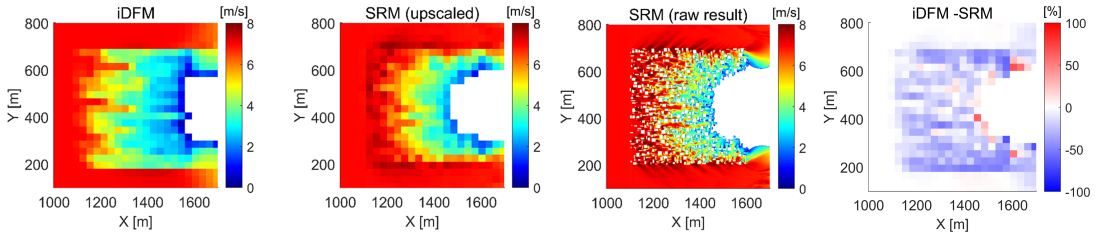

(b) Maximum fluid velocity

Figure A.11: Difference of (a) maximum surface elevation and (b) maximum fluid velocity between the iDFM ($\Delta x = 30$ m) and SRM results with the Random 03 topography in the Wave S075 case (1st panel from left: iDFM, 2nd panel: cell-averaged value for SRM, 3rd panel: raw results of SRM, and 4th panel: error between iDFM and SRM).

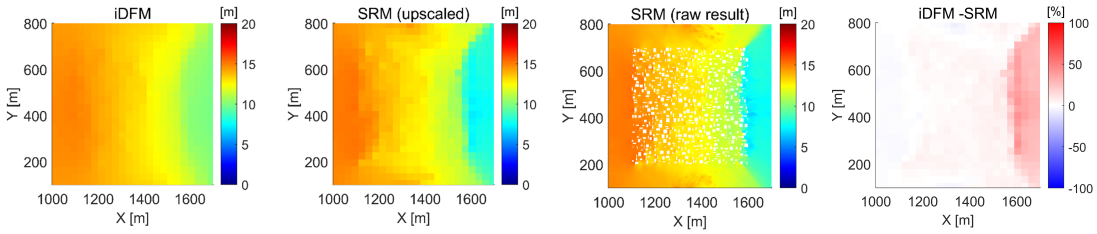

(a) Maximum surface elevation

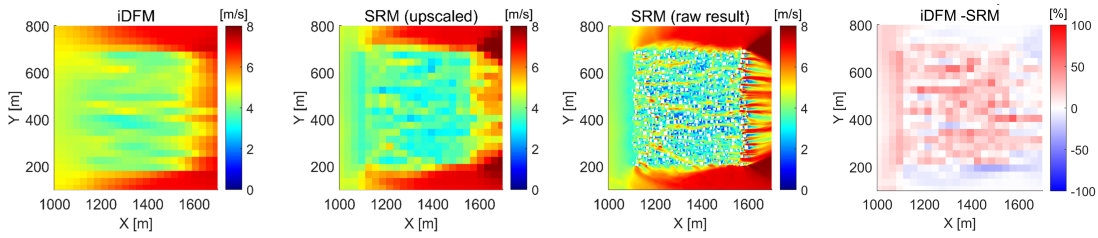

(b) Maximum fluid velocity

Figure A.12: Difference of (a) maximum surface elevation and (b) maximum fluid velocity between the iDFM ($\Delta x = 30$ m) and SRM results with the Random 03 topography in the Wave L15 case (1st panel from left: iDFM, 2nd panel: cell-averaged value for SRM, 3rd panel: raw results of SRM, and 4th panel: error between iDFM and SRM).